SCHOOL OF APPLIED SCIENCE

Department of Applied Physics

MICROSTRUCTURAL DESIGN AND CHARACTERISATION OF ALUMINA/ALUMINIUM TITANATE COMPOSITES

Posman Manurung

This thesis is presented as part of the requirements for the award of the Degree of Doctor of Philosophy of the Curtin University of Technology

August 2001

ACKNOWLEDGMENTS

I would like to express my most sincere gratitude to my principal supervisor Dr Jim Low for his encouragement, consistent support, advice and tremendous knowledge that he has shared with me, not only in materials science, but also in all aspects in reviewing and polishing the many drafts of my thesis.

Special thanks are also due to Professor Brian O'Connor, Associate Supervisor, for proof reading the thesis, expert advice on diffraction and Rietveld analysis. Thanks to Dr Brendan McGann for his assistance and efforts as thesis committee chairperson.

Next I would like to thank my family. Without them, this PhD would not be possible. They have provided me with the love and understanding especially during my undergraduate studies. Special thanks are also due to my wife, Tetty Asteria Samosir, for her support during the writing of thesis.

The financial support provided by the Development of Undergraduate Education (DUE) Project via LPIU – The University of Lampung is greatly acknowledged. Without that support, it is impossible to submit this PhD project.

Thanks also to Dr. Shane Kennedy and Dr. Andrew Studer of the Neutron Scattering Group at ANSTO for their assistance with collection of neutron diffraction data and invaluable contribution in interpreting the data. The financial assistance of the Australian Institute of Nuclear Science and Engineering (AINSE) and the Australian Synchrotron Research Program (ASRP) are greatly acknowledged.

Many other staff and colleagues at the School of Applied Science, Curtin University of Technology have assisted with technical support. Special thanks to Prof. H. Tsubakino of the Himeji Institute of Technology, Japan, for providing facilities to conduct TEM. Thanks also to all my colleagues at the University of Lampung who have supported me during this study.

Lastly, I would like to thank everyone once again, and also to anyone that I have forgotten to mention, who in one way or another have helped me make this thesis possible. It has been a tremendous experience completing my PhD program and it will definitely go down in my diary as one of the best chapters ever. Thank you very much from the bottom of my heart.

Posman Manurung
August, 2001

ABSTRACT

A new but relatively simple processing study was conducted to investigate the microstructure-property relationships of alumina/aluminium titanate (AAT) composites. The objectives of this study were: (a) to develop a process for fabricating AAT and β-spodumene modified AAT composites using a solid-state reaction method and functionally-graded AAT using an infiltration technique, and (b) to evaluate the effects of dispersed aluminium titanate (AT) on the phase relations, microstructure and mechanical properties of alumina-based composites. The study has revealed that the processing procedures played an important rule in the microstructural development of AAT composites. The microstructure and properties of AAT composites have been found to be strongly influenced by the presence of dispersed AT.

The phase relations in the AAT system have been characterised by x-ray diffraction (XRD) and neutron diffraction (ND). Rietveld analysis showed that the AT content increased in proportion with the amount of rutile added. The dynamic ND study showed that AT commenced to form at ~1310°C. The presence of AT caused a reduction of hardness but an improvement in fracture toughness. In addition, the presence of AT hindered the processes or kinetics of sintering and densification.

The use of β-spodumene has been investigated as a liquid-phase-sintering aid for the densification of AAT composites. XRD, ND, differential thermal analysis (DTA), scanning electron microscopy (SEM), transmission electron microscopy (TEM) and Vickers indentation were used to characterise the effect of β-spodumene on the phase relations, densification, microstructure and mechanical properties of AAT composites. The presence of β-spodumene was found to have a profound influence on the phase relations, densification, microstructure and properties of AAT composites. The addition of β-spodumene caused a small reduction of AT content and a commensurate increase of alumina phase.

Functionally-graded AAT composites have been successfully synthesised through infiltration of porous alumina preform with a solution containing $TiCl_4$. The infiltration kinetics of liquid into porous alumina preform has also been investigated and modelled. It was found that the infiltration rate equation proposed by Washburn

was proven to be suitable for describing the kinetics of infiltration in terms of preform sintering temperature, viscosity, and multiple infiltrations. The influence of applied pressure was consistent with the model proposed by Travitzky and Shlayen, where the applied pressure enhanced the rate of infiltration. Pre-sintering of alumina preform at 900, 1000 and 1100°C for 2 h resulted in different rates of infiltration which may be attributed to a varying degree in tortuosity of the pore channels.

The graded composition character of functionally-graded AAT composites has been determined by XRD and grazing incidence synchrotron diffraction (GISRD). Graded compositions from Rietveld refinement analysis showed that the concentration of AT decreased with depth. In contrast, the α-Al_2O_3 content increased with depth. Microstructural examination by SEM showed that the content of AT grains was the most abundant near the surface and decreased gradually with an increase in depth. The hardness results showed that FGM had a soft graded-region (AT rich) but hard non-graded alumina region. The lower hardness in the graded region can be attributed to the presence of intrinsically soft AT phase. The presence of graded AT caused a considerable improvement in damage tolerance.

The isothermal decomposition of AT at 1100°C both in air and vacuum has been studied. Both *ex-situ* and *in-situ* studies have been conducted to examine the effect of environment on the decomposition behaviour of AT. The addition of MgO was effective in enhancing the thermal stability of AT against decomposition both in air and in vacuum.

TABLE OF CONTENTS

LIST OF FIGURES

LIST OF TABLES

CHAPTER ONE

INTRODUCTION

1.1 BACKGROUND

Ceramics have been defined as the art and science of making and using solid articles. Essentially, they are non-metallic, inorganic solid materials produced by thermal treatment. Compared to metals and plastics, ceramics are generally hard, non-combustible and temperature resistant. They can be used in severe high temperature and corrosive environments.

Intrinsically, ceramics usually have high melting points and are therefore generally described as highly refractory. For example, the melting point of aluminium titanate (AT) is ~1860°C (Nagano *et al.* 1999; Bhattacharyya & Sen 1963). They are also brittle and chemically inert. In recent years, attempts have been made to divide ceramic materials into two categories, namely traditional and advanced ceramics. Traditional ceramics bear a close relationship to those materials that have been developed since the earliest civilizations. Advanced ceramics are sometimes also referred as functional or structural materials. Using a different approach, Kenny and Bowen (1983) have classified the high technology ceramics according to their functions. Much of the emphasis on powder processing for structural ceramics in the past years has been focused on obtaining powders of controlled particle size (Rhodes 1981).

The properties of ceramics are determined by the properties of each phase present in the sample. There are several factors that determine the phase distribution and how they operate in ceramic systems. Preparation methods also play a key role in the properties of sintered ceramics. Ohya, Hamano and Nakagawa (1983) showed that reducing the grain size of AT increases its mechanical strength. Parker and Rice (1989) reported that there is a correlation between grain size and thermal expansion for aluminum titanate materials.

Aluminium oxide is mostly prepared from the mineral bauxite by the Bayer process (Adamson 1970), which involves the selective leaching of the alumina by caustic soda, followed by the precipitation of aluminium hydroxide. There are a breadth of applications for alumina. Demand lies mainly in ceramic, refractory and

abrasive industries. High thermal conductivity, hardness, wear resistance and electrical resistivities are some properties of alumina that are considered better than other substances. Because of its superiority, alumina is frequently incorporated with other materials to obtain specific properties and microstructures such as $Al_2O_3/LaAl_{11}O_{18}$ (Yasuoka *et al.* 1995; Chen and Chen 1992), $Al_2O_3/LaMgAl_{11}O_{19}$, $Al_2O_3/Mg_2NaAl_{15}O_{25}$ systems (Chen and Chen 1992), Al_2O_3/Ce-TZP (Cutler *et al.* 1991) and Al_2O_3/Al_2TiO_5 (Padture, Bennison and Chan 1993).

An enhancement in fracture toughness and crack growth resistance can be realised for many ceramics through microstructural control (Evans 1990). SrO addition to Ce-TZP decreased the ZrO_2 grain size with a corresponding decrease in toughness from ~13 to ~6 $MPa.m^{1/2}$ (Cutler *et al.* 1991). The simultaneous addition of Al_2O_3 and SrO to Ce-TZP leads to the formation of strontium hexaluminate platelets within the Ce-TZP matrix. The toughness of Ce-TZP/Al_2O_3 compositions increased from ~8 to ~14 $MPa.m^{1/2}$ by virtue of the formation of strontium aluminate platelets within the microstructure.

It is now well established that ceramics with heterogenous microstructures exhibit improved toughness, principally via crack stabilisation from grain bridging (Bennison and Lawn 1989). The fracture toughness of ceramic such as Si_3N_4 and Al_2O_3-SiC_w is improved by the presence of elongated grains or second phases in the microstructure, promoting crack deflection and crack bridging (Becher 1991). From the processing perspective, the modification of microstructure can be achieved by dispersing a suitable second phase within a matrix. Whiskers or platelets can be incorporated into the matrix by mixing them mechanically with the raw powder before sintering (Wei and Becher 1985; Sakai, Matsuhiro and Furuse 1991). In the case of alumina/SiC-whisker composites, fracture toughness values in excess of 6 $MPa.m^{1/2}$ have been reported (Wei and Becher 1985). However, the same internal microstructural weaknesses that promote bridging also have a tendency to reduce the intrinsic strength (An, Chan and Chan 1998). Recently, Yasuoka *et al.* (1995) reported that fully-dense alumina composites containing 20 vol% $LaAl_{11}O_{18}$ showed increases in both strength and fracture toughness due to the crack bridging effect of anisotropically grown alumina grains, while the lanthanum-aluminate grains play an important role in hindering the alumina growth.

As a ceramic, AT has interesting properties due to its low coefficient of thermal expansion (Morishima *et al.* 1986; Parker 1990). Sintered AT has a

relatively low thermal expansion coefficient (1 x 10^{-6}/°C). The excellent thermal shock resistance of AT makes it attractive as a refractory material and for applications in metallurgy and automotive engineering. It is these properties that make AT suitable for high temperature applications where thermal shock resistance and thermal insulation is required such as port liners, piston crowns and turbo-charger manifolding. Practical applications for AT however remain uncertain because of its low strength. Both properties are attributed to the strong thermal anisotropy (Buessen, Thielke and Sarakauskas 1952) and another problem is that AT decomposes to Al_2O_3 and TiO_2 below 1200°C (Lang, Filmore and Maxwell 1952). Several studies showed that by adding some MgO to AT, the synthesized material did not decompose after annealing for 250 hours in the range 900-1175°C (Buscaglia *et al.* 1997). Kim, Zografou and Kroenert (1993) added some mullite to AT and after a decomposition test at 1100°C and cyclic decomposition test at 750-1400-750°C for 100 hours, AT was stabilized 80% by the presence of mullite.

The alumina-AT (AAT) system is another material that offers high temperature and thermal shock resistance. Alumina is excellent for wear resistance but poor thermal shock. On the other hand, AT is superior in thermal shock but lacks mechanical toughness. It follows that through the marriage of both materials, superior properties may be tailored in the system Al_2O_3-Al_2TiO_5. Generally, the AAT system can be produced by both solid-state reaction and sol-gel processing. In this thesis, the AAT system was prepared by both solid-state reaction and infiltration methods.

In the AAT system, both alumina and AT can be considered as an additive depending on which is the minority phase in the system. If the alumina is present as an additive in the AAT system, it can affect several properties of AT (Hamano *et al.* 1981). Ohya, Hamano and Nagakawa (1986) reported that some additives influence the microstructure and bending strength of AT. Furthermore, it was reported that the addition of 5% MgO, Fe_2O_3 or ZrO_2 also affects grain size, microcracking, crystalline phases present and thermal expansion.

The microstructure of AAT composites can also be designed with a graded composition using the infiltration processing. These functionally-graded materials (FGMs) are a new generation of manufactured materials where the microstructural details are spatially varied through non-uniform distribution of phases. The

introduced phase will change the properties of host body (Hirai 1996). The resultant material exhibits a progressive change in composition, structure and properties. This method has been well demonstrated in various graded ceramic systems such as alumina/mullite (Marple & Green 1990 and 1993), mullite/ZTA (Low *et al.* 1993; Low, Skala & Li 1993) and alumina/calcium hexaluminate (Asmi *et al.* 1998, 1999, Asmi 2001). Tu & Lange (1995) showed that Si_3N_4 powder compacts infiltrated with Zr(Y)-nitrate increased both fracture toughness and strength. Figure 1.1 shows one of the continuously types of functionally-graded microstructure.

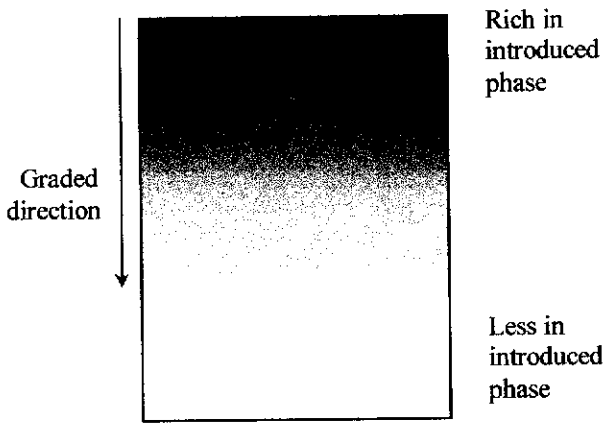

Figure 1.1. Schematic of a continuously graded FGM.

This idea can be applied to produce graded AAT composites where the host body or preform is either AT or alumina. If an alumina preform is used then the introduced phase should be AT and vice versa. In this research, the alumina preform was chosen as the host body and the introduced phase was TiO_2. The latter formed as a result of the hydrolysis of $TiCl_4$ and the subsequent decomposition process during drying. The overall reaction can be written as:

$$TiCl_4 + 2H_2O \rightarrow TiO_2 + 4HCl \qquad (1.1)$$

The introduced TiO_2 will then react with the alumina preform at approximately 1300°C to form AT.

In recent years, functionally-graded alumina-based composites have been extensively studied by the Materials Research Group at Curtin University. Low and co-workers (1998-2000) synthesized layered and graded AAT composites by infiltrating alumina preforms with tetraethyl-orthotitanate (TEOT). Depth-profiling results showed that the abundance of AT decreased but the hardness increased with depth. Microstructural evaluation showed that the grain size of alumina increased with depth indicating that the presence of AT in the graded AAT system had a beneficial effect in controlling the grain growth behaviour of alumina. The presence of AT also imparted considerable improvement in fracture and damage resistance of the system. This unique mechanical performance of both damage tolerance and wear resistance has been well demonstrated in other graded systems such as AT/ZTA (Low, Skala and Zhou 1996; Pratapa and Low 1996; Pratapa, O'Connor & Low 1997), mullite/ZTA (Low *et al.* 1993) and alumina/calcium hexaluminate (Asmi 2001). The heterogeneous layer of graded AT/ZTA, mullite/ZTA and alumina/calcium-hexaluminate provides excellent toughness whereas the homogeneous alumina retains strength and wear resistance.

The complex processes of liquid infiltration kinetics into alumina preforms are not well understood. Manurung, Low & Buckley (2000) investigated the infiltration kinetics of liquid into porous alumina preforms under various experimental conditions. They showed that the rate of infiltration was strong dependent on various parameters such as pre-sintering temperature of preform, type of infiltrant, pressure, and multiple infiltrations. In a related study, Buckley, Manurung & Low (2000) found that the effective pore radius in the preform is an order of magnitude smaller than the average pore size determined from SEM and porosimetry.

1.2 RESEARCH OBJECTIVES

The primary objective of this research project was to produce novel AAT composites with high mechanical performance through microstructural control. The presence of AT in the system was expected to improve the mechanical properties. The specific objectives of the research were:

(1) To study the phase compositions and developments of reaction-sintered AT, AAT, β-spodumene-modified AAT and functionally-graded AAT composites.

(2) To study the isothermal decomposition characteristics of AT at 1100°C both in air and in vacuum. The effectiveness of MgO as a stabiliser for AT was also to be studied.

(3) To conduct a feasibility study on the use of β-spodumene as a sintering aid for AAT composites. The effect of β-spodumene on the phase composition, microstructure, and properties was also to be studied.

(4) To study the various parameters that control the infiltration kinetics of liquids into alumina preforms. Modelling of the complex infiltration process was also to be conducted.

(5) To design alumina-based ceramic matrix composites with graded dispersion of AT.

(6) To characterise the graded composition profiles, microstructures, and properties of functionally-graded AAT composites.

(7) To compare the phase developments, microstructures, physical and mechanical properties for AAT system produced by both solid-state reaction and infiltration method.

1.3 RESEARCH PLAN

In order to fulfil the objectives, the following research plan was formulated:

(1) Selection and evaluation of raw materials to produce reaction-sintered AAT, β-spodumene-modified AAT and functionally-graded AAT composites.

(2) Fabrication of AT and alumina/AT (AAT) composites using solid-state reaction and functionally-graded AAT composites using infiltration technique.

(3) Study the isothermal decomposition behaviour of AT and the effectiveness of MgO as a stabiliser.

(4) Characterisation of phase development and graded composition profiles for the composites using room temperature x-ray diffraction (XRD) and neutron diffraction (ND), high temperature neutron diffraction (HTND) and grazing incidence synchrotron radiation diffraction (GISRD).

(5) Study the kinetics of infiltration of liquids into porous alumina preforms.

(6) Evaluation of physical and mechanical properties such as density, porosity, shrinkage, thermal expansion and shrinkage behaviour, hardness and fracture toughness.

(7) Evaluation of microstructure using scanning electron microscopy (SEM) and transmission electron microscopy (TEM).

1.4 STRUCTURE OF THESIS

This thesis is concerned primarily with the processing and characterisation of Al_2O_3-AT composites using both the conventional solid-state reaction and an infiltration process. The background, research objectives, research plan and structure of research are presented in chapter 1. Chapter 2 provides an introductory overview of the various ceramic systems, the FGM concept and the various methods that can be used for the production of FGMs. The production of graded ceramics from the infiltration method is also considered. In chapter 3, the detailed experimental procedure on the fabrication of AAT and FGM systems is described.

The characteristics and complex processes of isothermal thermal decomposition of AT in both air and vacuum are described in Chapter 4. The effectiveness of MgO as a stabiliser is also discussed. Chapter 5 involves the characterisation of AAT (0-45 wt% AT). This serves as comparison to AAT prepared by the infiltration method. Both XRD and HTND data were collected to elucidate the phase relations and reaction kinetics. Chapter 6 deals with the use of β-spodumene (0-15 wt%) as a sintering aid for the densification of AAT (30 wt% AT) composites. The phase relations, microstructure and properties are also described. Chapter 7 describes the use of infiltration processing to design a graded AAT system. The chapter discusses the kinetics and modelling of the complex infiltration processes. The effects of pressure and other parameters are also explored to explain the infiltration behaviour of liquid into the alumina preform. Depth-profiling of

physical and mechanical properties in the graded AAT system was characterised using a multitude of analytical techniques.

Finally, the conclusions and further work are outlined in Chapter 8.

CHAPTER TWO

LITERATURE REVIEW

2.1 INTRODUCTION

This chapter is concerned primarily with the fundamentals and theoretical aspects of alumina, AT and functionally-graded materials (FGMs). The approach taken is to outline the fundamentals of the structure and properties of these materials. This chapter also provides an introductory overview of the various methods that can be used to fabricate FGMs. Theoretical models describing the infiltration process for FGMs are also presented.

2.2 ALUMINA (Al_2O_3)

Like all ceramics, alumina is intrinsically hard and strong in compression, but has low toughness and tensile strength. Due to its high melting point, alumina is usually processed in powder form. Sintered alumina ceramics are recognized as important industrial materials. In addition, aluminas are also widely used as catalytic supports in chemical reactions (Marturano, Aglietti and Ferretti 1997).

Stoichiometric Al_2O_3 has a molecular weight of 101.96 and exists in various crystallographic forms *eg.* α, β, δ and γ (Wefers and Misra 1987). The most prevalent and stable single phase of the material is denoted as α-Al_2O_3 and occurs as the corundum crystal structure (space group $R\bar{3}c$) which contains two formula units per rhombohedral unit cell (Hübner 1984). The structure model of α-Al_2O_3 was first proposed by Bragg and Bragg (1916), followed by Pauling and Hendricks (1925). A refined structure model was published by Newham and DeHaan (1962), and then Lewis, Schwarzenbach and Flack (1982) reported further improved structural parameters. Maslen *et al.* (1993) refined the structure model using synchrotron radiation powder diffraction data. The crystal structure of α-Al_2O_3 has hexagonal cell containing six formula units per hexagonal unit cell with lattice parameters a and c of 4.754(1) and 12.982(1) Å, respectively as shown in Figure 2.1 based on Maslen *et al.* (1993). This model has been used in this thesis because it gives better refinement results than other models.

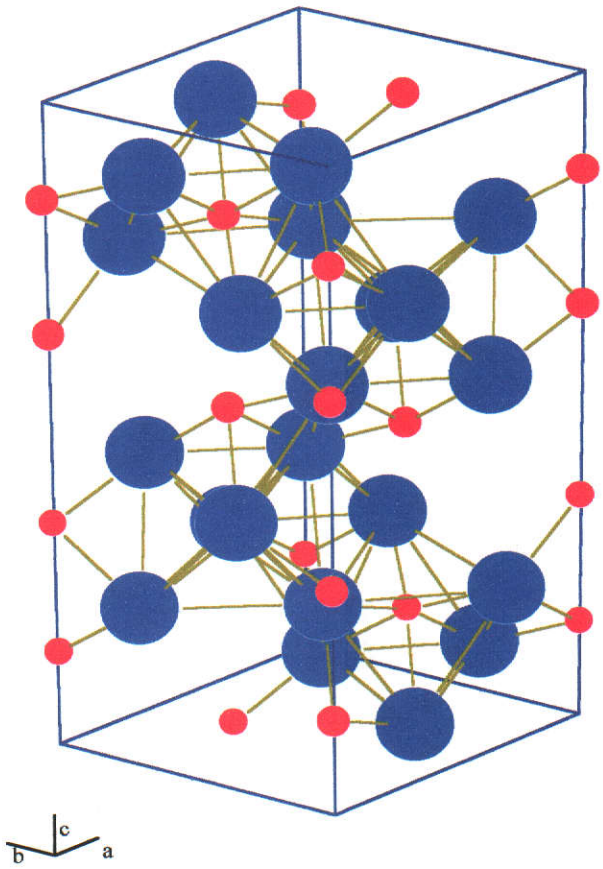

Figure 2.1. Crystal structure of α-alumina (α-Al_2O_3). The parameters are based on Maslen *et al.* (1983) model (ICSD # 73725). The *PowderCell* software package (Kraus and Nolze 1999) was used to construct the figure. The ionic radii are proportional to 0.55 Å for Al^{3+} (red) and 1.35 Å for O^{2-} (blue).

The structure of α-Al_2O_3 consists of planes of close-packed oxygen ions in the A-B-A-B sequence interleaved with planes of aluminium ions in an a-b-c-a-b-c sequence. In each aluminium plane, the aluminium ions occupy only two-thirds of the available octahedral sites. In this way, α-Al_2O_3 maintains charge neutrality with four Al^{3+} for every six O^{2-}. A hexagonal crystallographic cell is formed from the repeating sequence A-a-B-b-A-c-B-a-A-b-B-c (Munro 1997). Some other properties of Al_2O_3 are listed in Table 2.1 (Schneider 1994).

Table 2.1. Some properties of Al_2O_3 (Schneider 1994).

Crystal structure	Hexagonal
Theoretical density	3.97 g/cm^3
Vickers hardness	18-23 GPa
Transverse rupture strength	276–1034 MPa
Fracture toughness	2.7–4.2 MPa.m$^{1/2}$
Young's modulus	380 GPa
Poisson's ratio	0.26
Thermal expansion coefficient	(7.2–8.6) × 10^{-6}/K
Thermal conductivity	27.2 W/mK at 400 K
Melting temperature	2050°C

Some properties, as listed in Table 2.1, can vary according to starting materials and processing method. Latella and O'Connor (2000) reported that hardness of high-purity Al_2O_3 was 18.0 GPa for fine-grained and 14.1 GPa for coarse-grain microstructures while the hardness of liquid-phase sintered Al_2O_3 was 12.0 GPa. Krell and Schädlich (2001) showed that the hardness of alumina is indentation-size or load-dependent, in that it increased to ~30 GPa with a low load of 0.2 N. The fracture plane can have a strong influence on the value of fracture toughness in alumina. Kirchner and Gruver (1980) showed that the fracture toughness of alumina for the fracture plane of *0001* was 5.6 and for *1010* was 2.4 MPa.m$^{1/2}$. Considerable effort has been made to increase both strength and toughness of alumina ceramics by incorporating various dispersed phases. When zirconia is dispersed in the alumina matrix, the fracture toughness and strength increase to 10 MPa.m$^{1/2}$ and 1.2 GPa from 3.5 MPa.m$^{1/2}$ and 0.5 GPa, respectively, as reported by (Claussen 1976; Green, Hannink and Swain 1989).

2.3 ALUMINUM TITANATE (AT)

2.3.1 Crystal Structure

Aluminium titanate or *tialite* (AT) exists in two forms, α and β. The α-form is stable up to ~1820°C and the β-form at ~1320-1400°C (Sekar and Patil 1994). Sintered AT has a relatively low thermal expansion coefficient. The excellent

thermal shock resistance of *β-tialite* makes it attractive as a refractory material and for applications in metallurgy and automotive engineering. AT is a popular engineering material where thermal insulation is required. Practical applications for AT however remain limited because of its low strength which resulted from its strong thermal anisotropy (Buessen, Thielke and Sarakauskas 1952). Another problem is that AT decomposes to Al_2O_3 and TiO_2 at the temperature range of 1200-900°C (Lang, Filmore and Maxwell 1952).

The structure of AT is not unambiguously defined in the literature. Discrepancies in the peak positions and intensities have been found between the models available and the measured data. The crystal structure of AT is reported to be isomorphous with the mineral *pseudobrokite* (Austin and Schwartz 1953) and it has the general formula A_2BO_5, represented by the homologous Fe_2TiO_5. In the Al_2TiO_5 structure, each Al^{3+} or Ti^{4+} cation is surrounded by six oxygen ions forming distorted oxygen octahedra. These AlO_6 or TiO_6 octahedra form (*001*) oriented double chains weakly bonded by shared edges. This structured feature with CMCM space group is responsible for the strong thermal anisotropy, which creates a complicated system of localised internal stresses during cooling from the firing temperature. These stresses can, and frequently do, exceed the intrinsic fracture strength of the material, resulting in severe microcracking. The microcracking is responsible for the mechanical weakness of ceramic compacts and explains the quoted low thermal expansion coefficient (Segadães, Morelli and Kiminami 1998). The AT crystal structure is illustrated in Figure 2.2 using the '*PowderCell*' sofware package program version 2.3 for windows (Kraus and Nolze 1999). The input parameters were taken from Epicier *et al.* (1991) model with unit-cell parameters *a*, *b* and *c*, of 3.591, 9.429 and 9.636 Å, respectively.

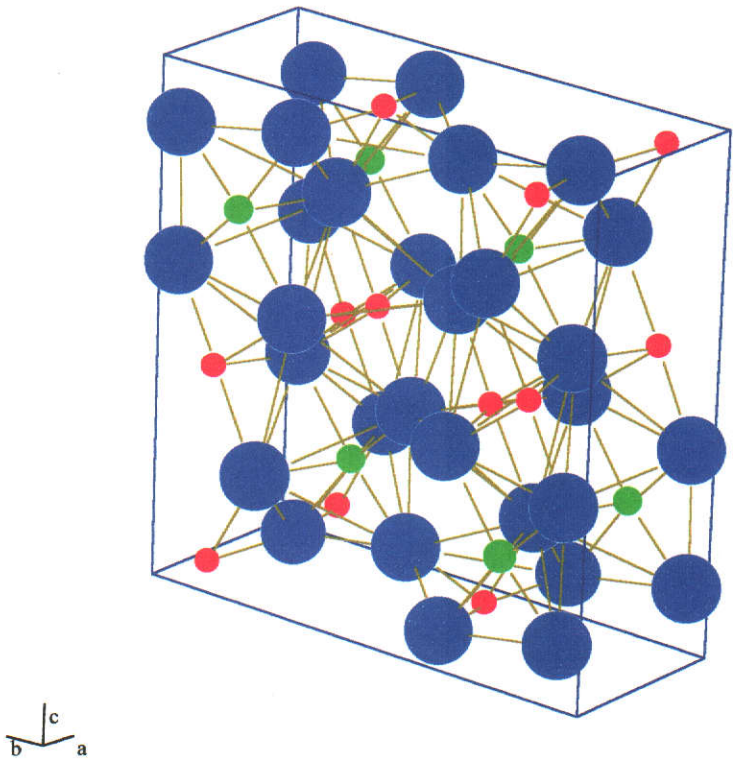

Figure 2.2. Illustration of the orthorhombic crystal structure of aluminium titanate (AT). The input parameters were based on Epicier *et al.* (1991) model. The *PowderCell* tool of Kraus and Nolze (1999) was used to draw the model. The ionic radii are proportional to 0.55 Å for Al^{3+}, 1.35 Å for O^{2-} and 0.64 Å for Ti^{4+}, respectively. Legend: red is Al, green is Ti and blue is O.

Austin and Schwartz (1953) proposed the orthorhombic space group CMCM for the structure of AT, with axes *a*, *b* and *c* of 3.557(2), 9.436(5) and 9.648(5) Å, respectively. Then, Hamelin (1958) published crystal data for Al_2TiO_5 (Tieilite) synthesized at 1600°C for 6 hours. It was proposed essentially the same model as that Austin and Schwartz (1953) with *a* and *b* axes interchanged with *a* = 9.360(30), *b* = 3.560(20) and *c* = 9.680(50) Å. Later, Morosin and Lynch (1972) studied the structure of AT at room temperature and 600°C, and proposed the same model again, with space group BBMM being proposed, with *a* = 9.429(2), *b* = 9.636(2) and *c* = 3.591(1) Å. Holcombe and Coffey (1973) calculated x-ray powder diffraction data

for Al_2TiO_5 and obtained *a*, *b* and *c* of 3.591(1), 9.429(2) and 9.636(2) for the CMCM orthorhombic system. The latest published data are from Epicier *et al.* (1991) with CMCM orthorhombic system, where *a*, *b* and *c* are 3.591, 9.429 and 9.636 Å, respectively. It seems that the Morosin model is the same as Epicier where *a*, *b* and *c* axes in Epicier are interchanged to *b*, *c* and *a* in Morosin. The atomic coordinates of *x*, *y* and *z* are also interchanged to *y*, *z* and *x*.

The atom coordinates *x* in the models of Austin and Schwartz (1953) and Epicier *et al.* (1991) are zero with the number of the atoms of 5 and 7, respectively. The number of the atoms results in the difference of site occupancies for Al and Ti atoms. Both Hamelin (1958) and Austin and Schwartz (1953) models used 5 atoms to determine the atom coordinates. The number of space group (63) and *Wyck* for both models are the same and thus result in the same site occupancies. Hamelin (1958) used zero for *y*-coordinate whereas Austin and Schwartz (1953) used zero for the *x*-coordinate. The interchange in atom coordinates results in interchange in lattice parameters. Both models by Epicier *et al.* (1991) and Morosin and Lynch (1972) proposed the number of atoms as 7 and thus the same site occupancies. In both models, the position of zero was interchanged from *x* to *z*.

Recently, Skala (2000) modified the space group of AT structure from BBMM to CMCM in refining the high temperature neutron diffraction data. The slight discrepancies between the atomic coordinates were reported especially in site occupancies of the cationic atoms. He reported that two metal sites M1 (Ti, Al) and M2 (Ti, Al) have octahedral coordination with each site surrounded by 6 oxygen atoms.

2.3.2 Physical Properties

Thermal Properties

Most solid materials expand upon heating and contract when cooled. In many materials, the value of linear coefficient of thermal expansion is anisotropic which means that it depends on the crystallographic direction along which it is measured. AT has attractive thermal properties *viz.* its low thermal expansion coefficient, high melting point and low thermal conductivity. Table 2.2 provides linear thermal expansion data for AT.

Table 2.2. Linear thermal expansion of aluminium titanate (AT).

Temperature range (°C)	Linear thermal expansion coefficient, α ($\times 10^{-6}$/K)			Reference
	α_a	α_b	α_c	
Room temperature	9.8	20.6	-1.4	Morosin and Lynch (1972)
Up to 1000	11.8	19.4	-2.6	Buessem, Thielke and Sarakauskas (1952)
Up to 1020	-3.0	11.8	21.8	Bayer (1971)
25 - 1200	-2.4	12.0	20.8	Skala (2000)

The thermal expansion of AT exhibits anisotropy because the values of α in directions a, b and c axes are not the same. From an atomic perspective, thermal expansion reflects an increase in the average distance between the atoms when a substance is being heated. From Table 2.2, the thermal expansion of each axis in Bayer (1971) work is close to that of Skala (2000). The unusual expansion anisotropy in AT appears to be a structure related property. The highest thermal expansion coincides with the direction of the double chains of strongly distorted (MeO_6)-octahedra (direction c-axis). The smallest or even negative expansion occurs in the direction of the a-axis (the shortest axis) where its length corresponds to the height of the distorted (MeO_6)-octahedra (Bayer 1971).

Activation Energy

Considering the energy required for an atom to jump from one lattice site to another, there is an intermediate stage of higher energy that separates one site from another. For an atom to pass from one interstitial site to another, the lattice must be distorted. Only some of the atoms will have sufficient energy to surmount this energy barrier and the magnitude of the energy that must be supplied in order to surmount the energy barrier is the activation energy.

The activation energy can be determined in various ways. For pure AT and AT with additives, the activation energy can vary. Table 2.3 shows the activation energy of AT obtained by various researchers.

Table 2.3. Activation energy of AT.

Preparation method	Additive	Method	Activation energy (kJ/mole)	Reference
Mixed powder via Al and Ti alkoxides		DTA	380.7	Yamaguchi, Hitoshi and Shimizu (1981)
Solid state reaction via: $Al_2O_3 + TiO_2$	0.5-7 mole % Fe_2O_3		205.8	Sakabe *et al.* (1970)
Solid state reaction via: $Al_2O_3 + TiO_2$		Kinetic equation	279.1	Kato, Kobayashi and Daimon (1979)
Solid state reaction	Mullite	DTA	243 to 282	Dos-Santos and Kiminami (1997)

The kinetic method in table 2.3 refers to the rate constant, k, which has the temperature (T) dependence according to:

$$k = A\exp(-E/RT) \tag{2.1}$$

where A is the frequency factor, E is the activation energy and R is the numerical gas constant = 8.314 J/Kmol. The activation energy can be determined graphically from experimental determination of the rate constant through an Arrhenius plot.

2.3.3 Mechanical Properties

The problem limiting the use of AT is attributed to the extensive microcracking occurring during cooling the sintered body. Bush and Hummel (1959) explained that the microcracks were associated with thermal anisotropy. Ohya, Nakagawa and Hamano (1987) explained the grain boundary microcracking of AT by measuring the change in the length of the sample and acoustic emissions during heating and cooling. They suggested that the critical grain size of AT is dependent on the sintering temperature. The critical grain size increases with temperature. The presence of extensive cracks severely lowers the mechanical strength.

To overcome this limitation, several additives such as MgO and ZrO_2 have been used to reduce grain growth (Thomas and Stevens 1989). The presence of spinel or zirconia serves to inhibit grain growth and reduce microcracking. SiO_2 of concentration less than 3 wt% has also been shown to improve the strength.

Hamano *et al.* (1981) reported that introducing additives for instance MgO and SiO_2, could increase the strength of AT. Preparation techniques either rapid heating or addition of a small amount of synthesized AT powder decreased the crack size and thus increased the strength (Hamano, Ohya and Nakagawa 1983). Addition of 5% of MgO, Fe_2O_3 or ZrO_2 has also been shown to improve the bending strength of AT (Ohya, Hamano and Nakagawa 1986).

2.3.4 Decomposition Behaviour of AT

Because of its high melting temperature (Lang, Filmore and Maxwell 1952) and low thermal expansion coefficient (Morosin and Lynch 1972), aluminium titanate can be used in high-temperature structural applications. Lejus, Goldberg and Revcolevschi (1966) reported that AT was unstable between 800-1280°C and decomposed into alumina and rutile by an eutectoid-like modification. Kato, Daimon and Takahashi (1980) determined the decomposition temperature as 1281(1)°C. It is known that the thermal decomposition of AT can be controlled by adding MgO, ZrO_2, and SiO_2 (Hamano *et al.* 1981). The free energy change in the thermal decomposition of AT is increased by both alloying and dispersing these oxides. Therefore Ishitsuka *et al.* (1987) studied the solubility limit and thermal stability of AT synthesized as a single-phase compound by substituting Al or Ti ions with Mg, Zr, or Si ions. This results in the substitution of Al^{3+} by Si^{4+} and $2Al^{3+}$ by Mg^{2+} and Ti^{4+} and the concomitant reduction of the thermal decomposition rate. Furthermore they showed that the substitution of more than 20 mol% of Al by Mg and Ti can completely prevent the thermal decomposition of AT. Similar results have also been shown by Demaestri *et al.* (1989) where MgO addition to AT was found to increase its thermal stability and mechanical strength but its thermal expansion coefficient was degraded.

The thermal decomposition of AT composites can also be controlled microstructurally through cyclic annealing (Kamiya and Bowen 1988). The density of the material increased significantly after decomposing more than 2 times.

Irregularly shaped and interwinded grains were observed to form after the annealing cycles that serve to impart better mechanical properties.

Besides MgO, Fe_2O_3 is also a good candidate for stabilising AT as iron acts as a redox buffer and thus prevents the reduction of Ti^{4+} to Ti^{3+} (Duran, Wohlfromm and Pena 1994). As the content of iron decreases, the reduction of the titanium occurs. The appearance of large quantities of Ti^{3+} can indicate the beginning of the decomposition of AT.

The decomposition of AT doped with TiO_2 has been reported by Hwang, Nakagawa and Hamano (1993). The presence of TiO_2 was found to accelerate the decomposition, but the residual thermal stresses decreased. Decomposition of Al_2TiO_5 was accompanied by the formation of fine rutile grains and pores at the interfaces with corundum grains.

2.4 CERAMIC SYSTEMS CONTAINING ALUMINUM TITANATE (AT)

Based on its low thermal expansion coefficient and low thermal conductivity, AT is a versatile engineering material. However, it has poor mechanical properties in terms of strength, hardness and fracture toughness. Hwang and Chang (1996) prepared ZTA with the addition of TiO_2 to enhance its mechanical properties. XRD results showed evidently the presence of AT. Bending strength and fracture toughness increased with the increase of rutile content which was related to residual thermal stress, grain size and the density of the specimen.

Other ceramic systems that contain AT were reported by Lee, Jeong and Lee (1997) in investigating the effects of additives on the properties. They found that adding mullite and alumina to AT limited grain growth, prevented microcracking and increased the density, strength and thermal expansion coefficient. Shi and Low (1998) investigated the effect of β-spodumene additions on the sintering and densification of AT. The presence of up to 15 wt% β-spodumene improved the sintering kinetics and thus the densification of AT.

As a low-thermal-expansion material, Parker (1990) prepared AT ceramic composites containing ZrTiO4 and ZrO_2. The average thermal expansions was found to be -2×10^{-6}/K from 24 to 1000°C with excellent in high-temperature stability. The low expansion is due to the microcracking by the titanate phases and a contractive phase transformation by the ZrO_2. In the system of aluminium titanate-

mullite composites prepared by a gel-coated powder processing method showed that both the mechanical strength and the thermal expansion coefficient increased with mullite content (Huang, Senos and Baptista 2000). The mechanical strength showed a strong dependence on the grain size of aluminium titanate. Inhibitation of AT grain growth is due to the presence of the mullite phase. The thermal shock resistance tended to decrease with an increase of mullite content.

2.4.1 Aluminium Titanate (AT) –MgO Systems

Zografou *et al.* (1988) investigated the use of MgO as an additive for AT and found that MgO increased its thermal durability and mechanical properties. Hiroshi (1990) reported that the presence of MgO could improve the high temperature resistance of AT. Furthermore, Washmuht, Recht and Kroenert (1991) showed that MgO can act as a stabiliser to improve the thermal shock resistance of AT. It is believed that the presence of MgO forms a spinel ($MgAl_2O_4$) as shown in Figure 2.3. Suvorov *et al*, (1987) also reported that the presence of 70-80% spinel in AT increased its thermal stability and heat resistance.

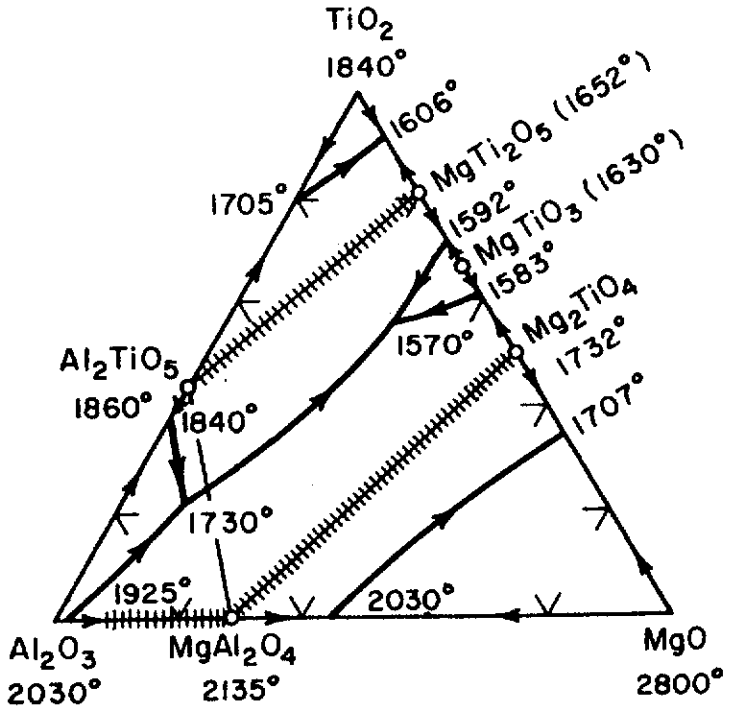

Figure 2.3. The primary phases in the system Al_2O_3-TiO_2-MgO. The cross-hatched lines are solid solutions (After Levin, Robbins and McMurdie 1964).

The formation of spinel by the solid phase reaction can occur in the system MgO-TiO_2, CaO-SiO_2, as well as in AT-MgO. A spinel is formed with the addition of MgO to AT. Buscaglia *et al*, (1996) reported that the spinel ($MgAl_2O_4$) affects the mechanism of AT formation by providing active nuclei for the growth of new phase. AT-spinel is formed by reaction between spinel and rutile at temperatures above 1150°C. When AT and MgO powders are sintered, AT reacts with MgO to form the spinel, Al_2MgO_4. Addition of 0.25 wt% MgO provided beneficial effect on both the densification rate and full density (Coble 1961).

2.4.2 Alumina-AT Systems

The process to form alumina-AT (AAT) systems is based on the reaction-sintering of alumina and rutile with an excess of alumina. The relevant phase diagram is shown in Figure 2.4.

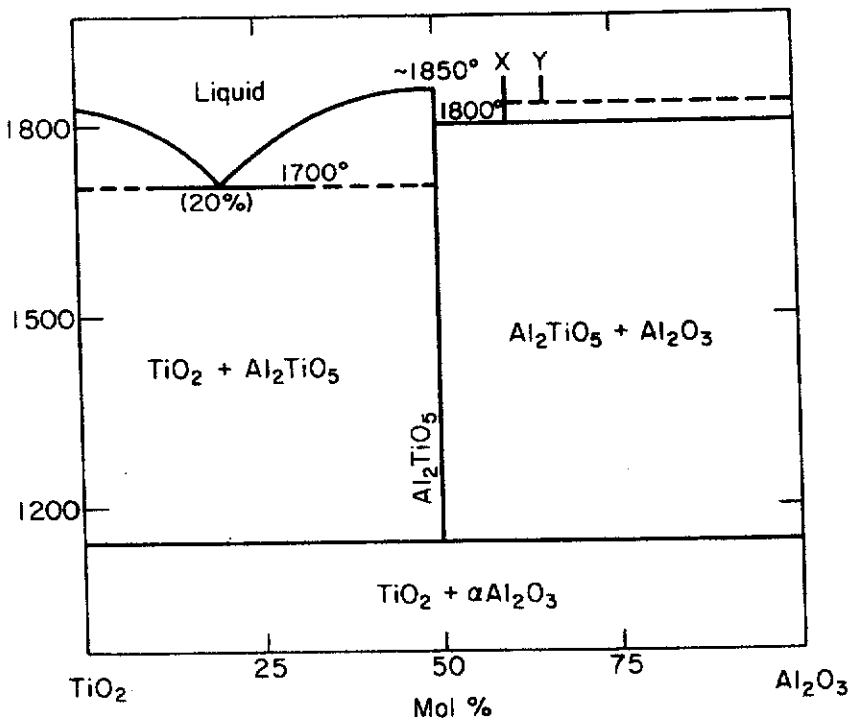

Figure 2.4. Phase diagram of Al_2O_3-TiO_2 system (After Levin, Robbins and McMurdie 1964).

The crystal structure of rutile is depicted in Figure 2.5 using the '*PowderCell*' software package program version 2.3 for windows (Kraus and Nolze 1999). The atom positions were taken from the model of Howard, Sabine and Dickson (1991) with unit cell parameters *a* and *c* of 3.594 and 2.959 Å, respectively.

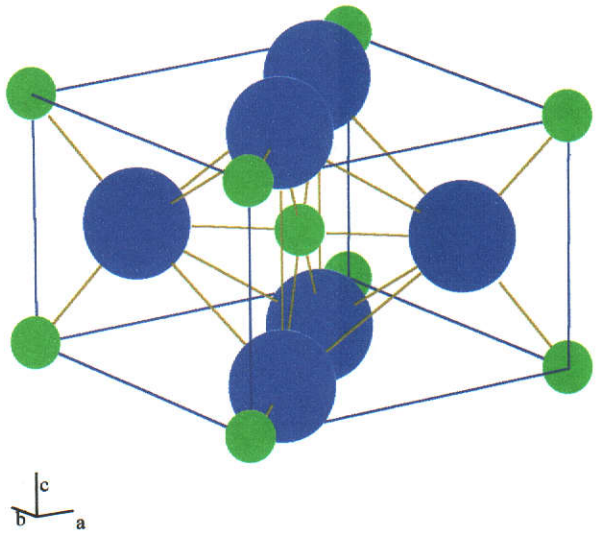

Figure 2.5. Illustration of the tetragonal crystal structure of rutile (TiO_2). The atom positions are from Howard, Sabine and Dickson (1991) model. The *PowderCell* program of Kraus and Nolze (1999) was used. The ionic radii are proportional to 0.64 Å for Ti^{4+} and 1.35 Å for O^{2-}. Legend: green is Ti, and blue is O.

Alumina and AT are two materials that have superior engineering properties. AT is superior in thermal shock but lacks mechanical strength and toughness. On the other hand, alumina is superior for wear resistance but poor thermal shock. Hence, by combining both to form alumina/AT (AAT) composites may result in a system that offers better mechanical properties with desirable thermal shock resistance. AAT composites can be fabricated either through a solid-state or sol-gel reaction followed by sintering. The alumina and AT will distribute homogeneously in the sintered product. A schematic microstructural design of this system is shown in Figure 2.6.

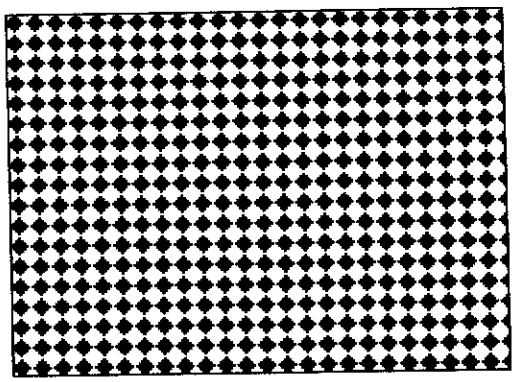

Figure 2.6. Schematic microstructural design of an AAT duplex two phases. ♦ = aluminium titanate.

AAT composites can also be formed using the laminar to achieve unique mechanical properties. For example, this approach has been used in the tape casting of a laminated Al_2O_3/ZrO_2 composite (Boch, Chartier and Huttepain 1986). Similarly, a trilaminate composite consisting of outer layers of a strong material with a flaw-tolerant inner layer has been produced (Harmer, Chan and Miller 1991). An *et al.* (1996) produced damage-resistant alumina-based layered composites consisting of three layers of alumina/calcium-hexaluminate. There was significant grain bridging which is indicative of R-curve behaviour or damage tolerance. Hertzian contact damage analysis of the tri-layer composites structure showed that the generation of shear-fault damage zones inhibited cracking in the outer polycrystalline alumina layer. A schematic diagram of the microstructural design for laminates is shown in Figure 2.7.

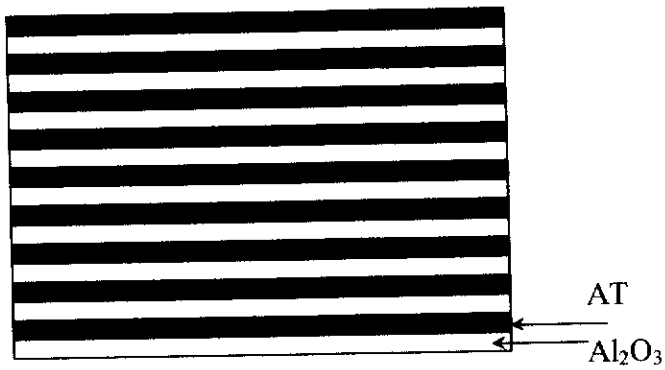

Figure 2.7. Schematic microstructural design of a multilayer laminate consisting of alumina and AT.

Hasselman *et al.* (1993) prepared AAT composites with a relative phase abundance of 72.0 wt% AT, 7.6 wt% alumina, 3.4 wt % titania and the remainder consisting of the various stabilizers. A study was conducted of the temperature dependence of the thermal diffusivity and thermal expansion of an alumina-aluminium titanate composite heated from room temperature to 1200°C followed by cooling to room temperature. Healing to temperatures above 600°C resulted in a hysteresis behaviour in which the data on cooling differed from the data obtained during heating. For both the thermal diffusivity and thermal expansion, the degree of hysteresis increased with maximum temperature. On return to room temperature, following heating to a temperature of about 1200°C, the thermal diffusivity exhibited a significant decrease, with a corresponding increase in specimen size. This effect was attributed to an increase in microcrack density over the corresponding value prior to heating.

Padture, Bennison and Chan (1993) prepared AAT composites with 20-30 wt% AT via duplex and duplex-bimodal powder. The duplex powder was prepared by mixing AT and fine alumina powders. The duplex-bimodal powder was prepared by mixing AT and fine alumina powders with spray-dried alumina after wet-ball-milling. They found that a high level of residual stresses developed due to the

presence of AT. These stresses were thought to be responsible for enhancing the display of crack-closure stresses in the bimodal AAT (20 wt% AT) sample. However, it was found that the duplex-bimodal AAT (30 wt% AT) system had better flaw-tolerance than bimodal AAT (20 wt% AT). They suggested that the improved flaw-tolerance could be attributed to the combined influences of increased internal residual stresses and increased microstructural coarseness due to the presence of large alumina grains. The internal residual stresses were thought to arise from the thermal expansion mismatch between AT and the matrix.

The flaw-tolerant behaviour of AAT composites has been studied by various researchers (Runyan and Bennison 1991; Padture, Bennison and Chan 1993; Braun, Bennison and Lawn 1992). The major toughening mechanisms responsible for the observed flaw tolerance were attributed to interphase debonding and grain-localized bridging (Evans 1990).

The third method to form AAT composites is by infiltration. The infiltration method has been successfully used by various researchers to introduce secondary phases into a host ceramic body. Glass and Green (1987) have incorporated alumina into yttria-stabilised tetragonal zirconia polycrystal (Y-TZP) and mullite into alumina. Similarly, functionally-graded AAT materials have been developed by Low and co-workers (1996) using infiltration.

2.4.3 β-Spodumene Modified Ceramic Systems

Beta-spodumene is useful for making glasses and ceramics which is harder, smoother, chemical and thermal shock resistant. Spodumene has been used as a liquid-phase sintering aid for alumina (Latella, Burton and O'Connor 1995; Bayususeno, Latella and O'Connor 1999), mullite (Low, Suherman and Phillips 1997; Low *et al.* 1997), alumina-calcium hexaluminate (Asmi *et al.* 1998) and AT (Shi and Low 1998; Low and Shi 2000). Shi and Low (1998) have investigated the effect of β-spodumene additions on the sintering and densification of AT. The presence of up to 15 wt% β-spodumene improved the mechanical properties of AT as a result of enhanced sintering kinetics and densification.

Rabinovich (1985) proposed that β-spodumene has a tetragonal di-pyramid crystal structure. The structure consists of rigid Si-O and Al-O tetrahedra arranged around a four-fold screw axis. This is a common characteristic of materials that

possess anisotropic thermal expansion. The structural crystal of β-spodumene is depicted in Figure 2.8 using the '*PowderCell*' software package program version 2.3 for windows (Kraus and Nolze 1999). The atomic positions are from Clarke and Spink (1969) with unit cell parameters *a* and *c* of 7.534 and 9.158 Å respectively.

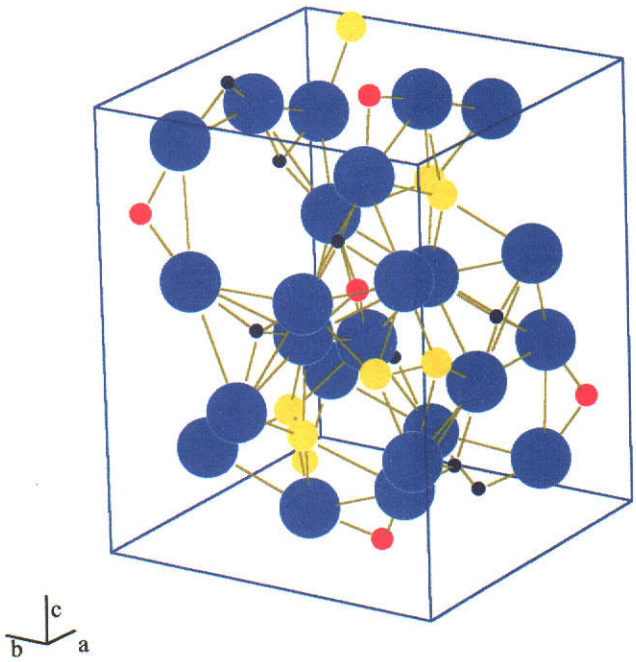

Figure 2.8. Illustration of the tetragonal crystal structure of β-spodumene ($Li_2O.Al_2O_3.4SiO_2$). The atom positions are from Clarke and Spink (1969) model. The *PowderCell* program of Kraus and Nolze (1999) was used. The ionic radii are proportional to 1.55 Å for Li^+, 0.55 Å for Al^{3+}, 0.4 Å for Si^{4+}, and 1.35 Å for O^{2-}, respectively. Legend: red is Al, yellow is Li, black is Si, and blue is O.

2.5 FUNCTIONALLY-GRADED MATERIALS (FGM)

2.5.1 Concept

Japanese scientists first proposed the concept of functionally-graded materials (FGMs) in 1984 (Koizumi 1997). The idea was based on the demand for thermal barrier materials that led to the development of high performance heat-

resistant materials. The growing interest in FGMs is evidenced by the large number of recent conferences and specials issues of technical journals devoted to the analysis, design and fabrication of these materials (Ilschner and Cherradi 1995).

Graded materials are not new in that the concepts for synthesising materials containing microstructural gradients in nature and also through processing. Dental implants are examples of biomaterial FGMs (Takahashi, Watari and Nishimura 1992; Takahashi *et al.* 1992; Takahashi 1993). The new and interest about FGMs are the realization that gradients can be designed at the microstructural level to tailor a material for the specific functional and performance requirement of an intended application. Recent advances in processing are opening up the possibility for extending the graded materials concept to new materials systems and engineering problems. Figure 2.9 shows the schematic concept for a typical microstructure of a functionally-graded material.

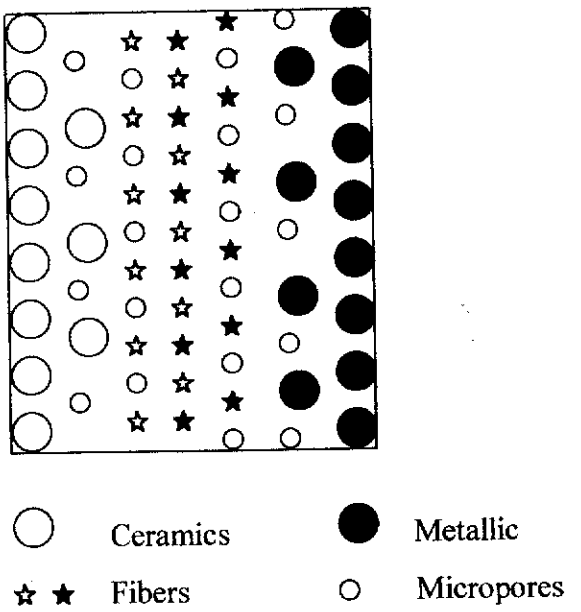

Figure 2.9. Conceptual diagram of FGMs (After Koizumi and Niino1995).

FGMs can be designed in various ways to produce several type of continuous component change (Hirai 1996). *Type one* exhibits a continuous change in state, where the material has a very dense surface in one side and porous surface on the other side. *Type two* exhibits continuous change in concentration with phase

abundance, density and shrinkage vary in every depth. Commonly, most FGMs show this behaviour. *The third type* has a continuous change in morphology, where on one side consists of spherical particles and on the other side consists of fiber-like particles. *The fourth type* has a continuous change in crystallinity, which represents the different behaviour in terms of crystallinity and amorphous. The different types of functionally-graded microstructures with ceramic and metallic phases are shown in Figure 2.10(a), (b) and (c).

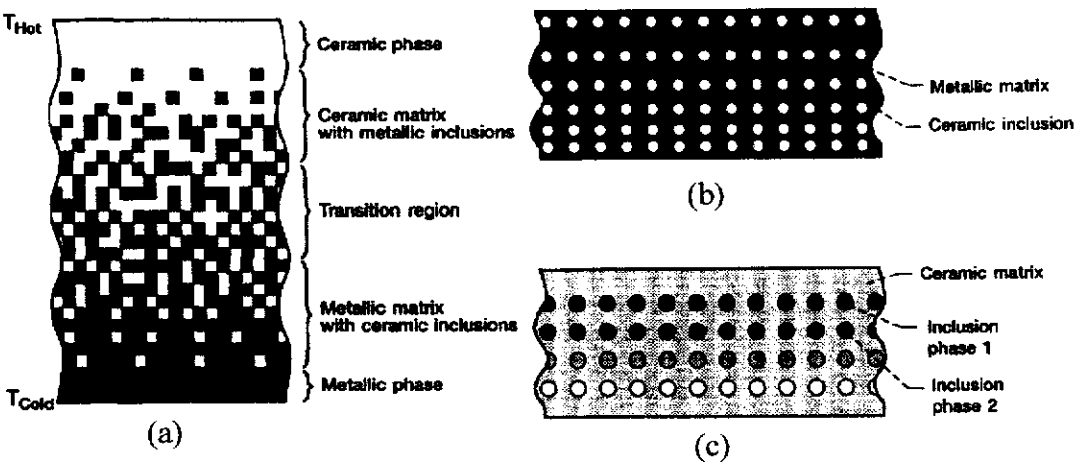

Figure 2.10. Different types of functionally graded microstructures (a) Continuously graded microstructure, (b) Discretely graded microstructure and (c) Multi-phase graded microstructure (After Aboudi, Pindera and Arnold 1999).

2.5.2 Processing Methods

Many processing methods have been used to fabricate the graded structures, *eg.* coating (Tsuchida *et al.* 1998), thermal spray, powder processing (Tomsia *et al.* 1998), chemical vapor deposition (CVD) (Takanori *et al.* 1999), novel jet vapor deposition (JVD) (Wadley, Hsiung and Lankey 1995), physical vapor deposition, self propagating high temperature synthesis, diffusion treatment and sedimentation. Recently, the infiltration technique has emerged as a popular method for fabricating FGMs because of its simplicity and versatility. Infiltration is conducted in various ways. For instance, processing of metal matrix composites (MMCs) is usually

conducted by liquid metal penetration (Schwartz 1984). Graded MMCs of Al-Cu-Mg-Ag/δ-Al_2O_3 were reported by Morelli *et al.* 1998. Travitzky and Shlayen (1998) infiltrated Cu-O molten into alumina preform to fabricate Al_2O_3/Cu-O composites. Chemical vapour infiltration (CVI), reactive melt infiltration (RMI) (Einset 1998; Sheelak 1998) and reactive metal penetration (RMP) (Loehman, Ewsuk and Tomsia 1998; Fahrenholtz *et al.* 1998) are other examples of infiltration methods. Tables 2.4 - 2.6 list preparation methods reported in the literature.

Table 2.4. FGMs prepared by combustion synthesis (After Gregory 1995).

Material System	Processing Method
TiC/Ni	Hydrostatic pressing
TiC/Ni_3Al	Hot pressing
Cr_3C_2/Ni	Hydrostatic pressing
TiB_2/Ni	Hydrostatic pressing
TiB_2/Cu	Hydrostatic pressing
(Ti-Si-O)/Ti	Hydrostatic pressing
(TiB_2-ZrO_2)/Cu	Hot pressing
$MoSi_2$-SiC)TiAl	Hydrostatic pressing
(Al_2O_3-SiC)(Al_2O_3-TiC)/Al	Hydrostatic pressing

Table 2.5. FGMs prepared by chemical vapour deposition (CVD) (After Hirai 1995).

System	Materials
Carbide	ZrC/C, SiC/C, TiC/C, SiC/TiC, SiC/TiC(SiC) C/B_4C/SiC
Oxide	SiO_2/SiO_2(GeO_2)
Nitride	BN/Si_3N_4

Table 2.6. Fabrication methods for FGMs (After Hirai and Sasaki 1989).

Phase	Process	Method	System
Gas	Chemical	Chemical vapour deposition	SiC/C, SiC/TiC, TiC/C, C/C-C composite, C/ceramics
	Physical	Ion plating Plasma spraying Ion mixing	TiN/Ti, TiC/Ti, ZrO_2/Cu, C/Cr, YSZ/NiCrAlY, YSZ/Ni-Cr, diamond/TC, YSZ/Cu
Liquid (melt)	Chemical	Electrodeposition	Ni/Cu
	Physical	Plasma spraying Eutectic reaction	YSZ/NiCrAlY, YSZ/Ni-Cr $Si/ZrSi_2$
Solid	Chemical	Self heating system	TiBe/Cu, TiBe/Ni, TiC/Ni, $MoSi_2$-SiC/TiAl
		Smearing	ZrO_2/Ni, PZT/Ni, PZT/Nd
	Physical	Sintering	YSZ/SOS_3O_4, YSZ/Mo, YSZ/Nb, Si_3H_4/Ni, W/Cu
		Diffusion	Ni/Al

From Table 2.6, the gaseous method provides the material in the form of film or plate directly without melting or sintering process. The gaseous method is also easiest for controling the concentration of the dispersed phase in terms of thickness. Solid and liquid methods require further sintering in order to obtain bulk materials.

2.5.3 Infiltration

In this research, the infiltration method was used to fabricate FGMs. The technique is relatively simple and involves the pressing of powder mixture to form a porous preform suitable for infiltration. Pre-sintering of preform is essential to impart the necessary strength required. However it is very important to make sure that the porosity is not less than 10%. Otherwise the porosity may consist of isolated pores that cannot contribute to infiltration process. Treatment before infiltration is also very important; for example degassing in vacuum can enhance the kinetics of infiltration. The infiltrant should be non-viscous so that it can penetrate the preform. Full or partial infiltration can be used depending on the aims of processing. Marple and Green (1990 and 1993) used the full infiltration technique fabricating the alumina/mullite system. Low, Skala and Zhou (1996) synthesized functionally-graded alumina/AT composites using the full infiltration method. Glass and Green

(1987) used partial infiltration to fabricate alumina/Y-TZP. The subsequent reaction during sintering produces the introduced phase in the host body that forms the matrix. This technique produces a graded amount of introduced phase within the sample. Table 2.7 lists some infiltration techniques for producing FGMs. Figure 2.11 shows the steps during the preparation of FGMs by infiltration.

Table 2.7. List of infiltration techniques for producing FGMs.

Technique	Reference
Partial infiltration	Glass and Green (1987) Low (1998)
Full infiltration	Marple and Green (1993) Low, Skala and Zhou (1996)
Microwave processing	Skamser *et al.* (1995)
Chemical vapor infiltration	Skamser, Jennings and Johnson (1997)
Centrifugal casting	Fukui, Yamanaka and Enokida (1997)
Constant current electrophoretic deposition	Sarkar, Datta and Nicholson (1997)
Chemical vapor deposition	Takanori *et al.* (1999)

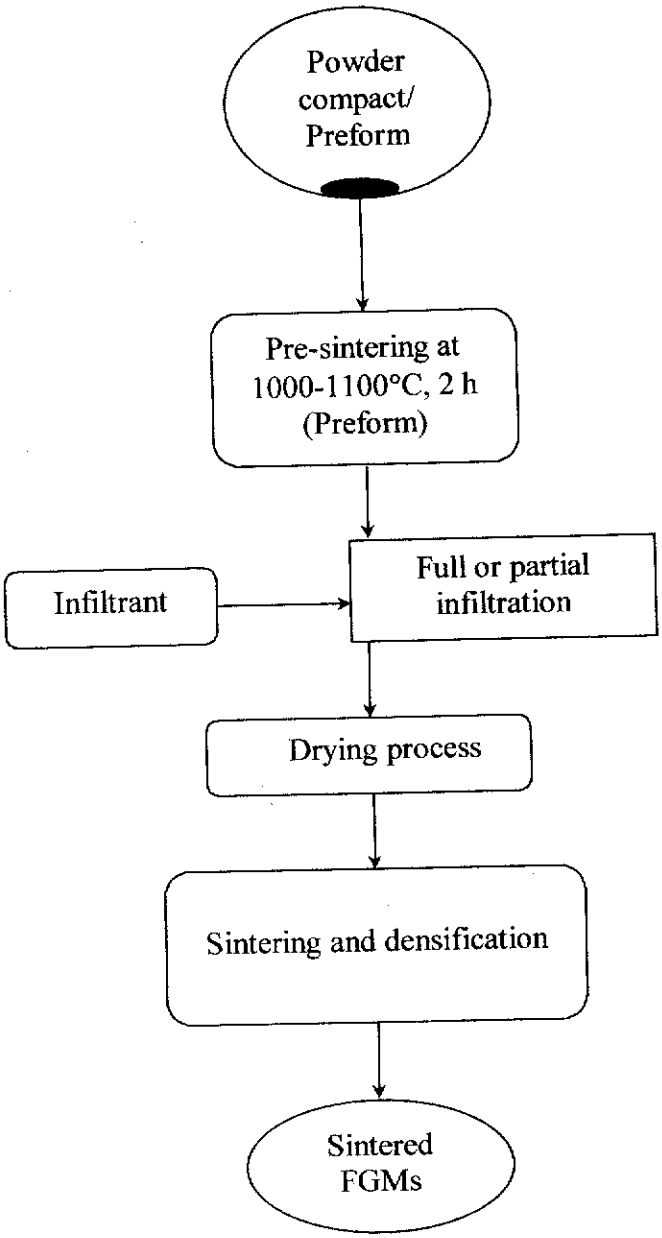

Figure 2.11. The steps involved in the fabrication of FGMs by infiltration technique.

2.5.4 Modeling Infiltration Kinetics

There are a number of formulae which are relevant for modeling the infiltration kinetics of a liquid into preforms. The first equation to calculate the height of infiltration against time was formulated by Washburn (1921):

$$h = \left(\frac{\gamma r \cos\theta}{2\eta} \right)^{1/2} t^{1/2} \qquad (2.2)$$

where h and t are the height of liquid and time, respectively. Symbols γ, θ, r and η are the surface tension, contact angle, pore radius and viscosity, respectively. Hence, the rate of infiltration (*ie.* h/t) is a function of surface tension, contact angle, pore radius and viscosity.

Another model proposed by Yokota *et al.* (1980) involves tortuosity, T, and shape factors, C_s:

$$h = \frac{2}{T} \left(\frac{C_s p \gamma r \cos\theta}{\eta} \right)^{1/2} t^{1/2} \qquad (2.3)$$

The value for T is normally 1.4142 and C_s is 0.4. When water wets the preform completely and liquid is spreading, the contact angle θ is 0° (Yokota *et al.* 1980). A schematic of tortuosity can be seen in Figure 2.12.

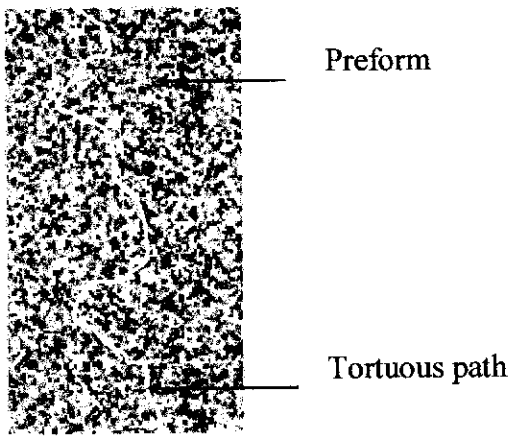

Figure 2.12. Tortuous path through a packed powder bed (After Lowell and Shield 1984).

A third formula was proposed by Travitzky and Shlayen (1998):

$$h = r\left(\frac{P_{net}}{2\eta}\right)^{1/2} t^{1/2} \tag{2.4}$$

where the net pressure, P_{net} is given by:

$$P_{net} = \frac{2\gamma\cos\theta}{r} - \rho g h - P_{atm} \tag{2.5}$$

Here ρ is the density of the infiltrant, g is the acceleration due to gravity (9.8 m/s^2) and P_{atm} is the pressure of the surrounding space above the liquid infiltrant. This model is useful for predicting the influence of pressure on the rate of infiltration.

Another formula is the Kozeny-Carman (Carman 1956) equation:

$$h\frac{dh}{dt} = \frac{k}{T} \tag{2.6}$$

where T is tortuosity of the capillary tube and k is a constant.

Since FGMs were first fabricated in 1984, the best theoretical approach for explaining the phenomenon is still not clear. Many researchers have only focused on the synthesis and characterisation of the material. Tai and Chou (1989) developed an analytical model for chemical vapor infiltration (CVI) in the fabrication of ceramic composites. This model was applied to study the growth of alumina from chemical reaction of $AlCl_3$, H_2 and CO_2 within a SiC fibre bundle which is situated in an isothermal hot-wall reactor. The pore space between the fibres is simulated by cylindrical capillary tubes. Figure 2.13 shows a control volume in cylindrical coordinates (r, θ, z) where N is the molar flux (mol/m^2s).

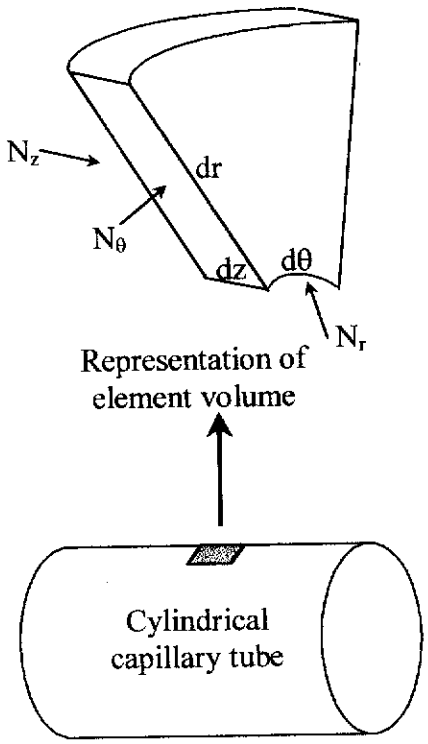

Figure 2.13. Control volume for the unidirectional fibre preform under CVI (After Tai and Chou, 1989).

Mass conservation in the unsteady state leads to the following equation.

$$\frac{\partial C}{\partial t} r dr d\theta dz = (N_\theta - N_{\theta+d\theta}) dr dz + (N_r - N_{r+dr}) d\theta dz + (N_z - N_{z+dz}) d\theta dr \tag{2.7}$$

where C is the mole total of vapour per unit volume (mol/m^3) and t is the time (s). N_r, N_θ and N_z are the molar flux in r, θ and z directions (mol/m^{2}s). Equation (2.7) can be simplified by using symmetry and the result is:

$$\frac{\partial C}{\partial t} + \frac{1}{r}\frac{\partial r N_r}{\partial_r} + \frac{\partial Nz}{\partial z} = 0 \tag{2.8}$$

By introducing the diffusivity, D (m^2/s), the relationship between the molar flux N and the mole fraction x of a given vapour species is

$$N_j = -CD\frac{\partial x}{\partial j} \qquad (j = r, z) \tag{2.9}$$

By combining equations (2.8) and (2.9), the equation for the ith species of a multicomponent system becomes

$$\frac{\partial C_i}{\partial t} - \frac{CD}{r}\frac{\partial}{\partial r}\left(r\frac{\partial x_i}{\partial r}\right) - CD\frac{\partial^2 x_i}{\partial z^2} = 0 \tag{2.10}$$

where $x_i(C_i/C)$ is the mole fraction of the ith species.

Equation (2.10) represents the differential equation for the mole fraction of ith species, mole total of vapour and diffusivity in terms of the t, r and z variables. By using a separation of variables technique with a modified Bessel function, the mole fraction, mole total and diffusivity can be found. From this model, the growth rate is higher near the ends of the fibre bundle than in the middle section. The growth rate decreases with time and the reaction rate is sensitive to temperature.

Tai and Chou (1990) proposed the modelling of an improved CVI process for ceramic composites fabrication. The model is based upon the premise that discontinuous fiber mats and three-dimensional woven fabrics can be regarded as porous media. This model takes into account the reactant properties, preform structure and flow phenomena. In terms of fluid flow, the preform is assumed to obey Darcy's law.

A more physical approach to the modelling of FGMs was proposed by Markworth, Ramesh and Park (1995). The models are concerned with the microstructure-dependent thermophysical properties and the design, processing and performance of FGMs. A semiquantitative theory has long been used for predicting the properties of heterogeneous materials that is called the Rule of Mixture. Let the phases of mixture be A and B and the particular properties for pure A be P_A and for B be P_B. The equation for property of compound, P is given by:

$$P = f_A P_A + f_B P_B \tag{2.11}$$

where P is an effective value. Equation (2.11) is known as a Voigt-type rule or arithmetic mean. Another equation describing the property of compound, P is given by:

$$\frac{1}{P} = \frac{f_A}{P_A} + \frac{f_B}{P_B} \tag{2.12}$$

Equation (2.12) is known as a Reuss-type rule or harmonic mean. For a more general expression, Markworth, Ramesh and Park (1995) modified equation (2.11) to allow for parameter correlations:

$$P = f_A P_A + f_B P_B + f_A f_B Q_{AB} \tag{2.13}$$

where Q_{AB} is a function that depends on f_A, f_B, P_A, and P_B as well as microstructure-dependent quantities.

Using a different approach, Skamser *et al.* (1995) proposed a model for microwave processing of compositionally changing ceramic systems. His interest in this process is based on an unique but cost-effective way for processing ceramic materials. Microwave heating provides a rapid heating rate and volumetric heating, in contrast to the slow heating rates and surface heating obtained with conventional heating. A finite-difference model was used to simulate the temperature and composition distribution produced inside a specimen heated with microwave energy during a process involving a change in composition.

Skamser, Jennings and Johnson (1997) proposed another model for chemical vapour infiltration using temperature gradients. The model simulates the deposition of alumina matrix within fibres wrapped around a tube. A simple one-dimensional approach was used. They took into account the temperature, pressure and porosity profiles. The governing equation for heat conservation in cylindrical coordinates with $dT/dz = 0$ is

$$\Phi \rho C_p \frac{\partial T}{\partial t} = \frac{1}{r}\frac{\partial}{\partial r}\left(r K_{eff} \frac{\partial T}{\partial r} \right) + \Omega S_v \Delta H_f \tag{2.14}$$

where Φ is porosity, ρ is density of alumina, C_p is heat capacity of alumina as a function of temperature (J/g°C), K_{eff} is the effective thermal conductivity (W/m°C), Ω is reaction rate (mol/m^{2}s), S_v is the internal surface area density and ΔH_f is the heat of reaction (J/mol). Heat is generated only at the internal surface of the coating. The equation governing mass conservation in cylindrical coordinates is

$$\Phi \frac{\partial\left(\frac{P_i}{RT}\right)}{\partial t} = \frac{1}{r}\frac{\partial}{\partial r}(rN_i) - \Omega S_v \qquad (2.15)$$

where P_i is the partial pressure of each gas component involved in the chemical reaction, R is the universal gas constant and N_i is the flux of each gas component (mol/m^{2}s). From this model, it was established that a temperature gradient in which the interior is hotter than the exterior can result in denser composite coating. A thin coating should be used so that only a small temperature gradient and a short process time is required. For thick coating, the process is more diffusion controlled because the temperature gradient required is decreasingly smaller for increasingly thicker samples.

In a recent work, Aboudi, Pindera and Arnold (1999) proposed a volumetric model for FGMs. They used boundary and interfacial conditions between the subvolumes to characterise the FGMs. This model was then implemented in a new higher-order micromechanical theory. Both Skamser *et al.* (1997) and Aboudi *et al.* (1999) included the volumetric term in their modelling.

2.5.5 Properties

The study of Glass and Green (1987) on the mullite-alumina system indicated that the infiltration depth is dependent on the square root of time, and with the content of mullite decreasing from the surface towards the interior. Marple and Green (1991) infiltrated tetra-ortho-silicate (TEOS) to alumina preforms. The elastic modulus of the composite decreased with an increase in the lower-modulus mullite content. The strength and fracture toughness of samples rich in mullite were higher than samples lack in mullite. This phenomenon may be caused by (i) a change of flaw population during processing, (ii) effect of mullite on crack propagation, and

(iii) the presence of residual compressive stresses at the surface during cooling. In another study, Marple and Green (1992) showed that the major contributor to the improvements of the strength and fracture toughness is compressive surface stresses, formed by the thermal expansion mismatch between mullite and alumina.

Low (1998) reported that the presence of AT phase in functionally-graded AAT composites has a strong influence on thermal expansion coefficient, elastic modulus and microhardness. The hardness in the graded region increased with reduction in the AT content. Similar results were reported by Skala (2000) and Pratapa & Low (1998) in graded alumina-based systems. The resultant composites were found to be damage tolerant and exhibited graded mechanical properties.

In a separate study, Asmi (2001) and Asmi & Low (1998) prepared graded alumina/calcium-hexaluminate composites using the infiltration method. They found that the hardness of the graded layer was lower than that of the alumina layer. The content of calcium hexaluminate (CA_6) decreased with an increase in depth. A plate-like morphology of CA_6 was observed in the graded region.

Sarkar, Datta and Nicholson (1997) used electrophoretic deposition to fabricate graded alumina/zirconia composites. They reported that these materials exhibited increasing hardness but decreasing fracture toughness from the zirconia-rich layer to the alumina-rich layer. The compositional change of zirconia and of alumina was consistent with the microstructural observations. By using the plasma spraying technique, functionally-graded ZrO_2 (8% Y_2O_3)/NiCrAlY with a thickness of 0.4 mm was prepared on a SUS310 substrate. The cross-sectioned hardness was found to increase with increasing ZrO_2 (8% Y_2O_3) content (Fukushima, Kuroda and Kitahara 1990). Other properties of FGMs are given in Table 2.8.

Table 2.8. Properties of selected FGMs (After Hirai and Sasaki 1989).

	Material	Density (kg/m^3)	Melting point (K)	Thermal Conductivity (W/mK)	Thermal expansion coefficient ($10^{-6}/K$)	Young's modulus (GPa)
High-temperature side	SiC	3220	>2473	135	4.2 (20-800°C)	320
	TiC	4940	3430	25.1 (100°C) 5.9 (1000°C)	7.4	315 to 450
	TiN	5430	3223	5.7 (500°C) 12.1(1000°C)	9.3	251
	TiB_2	4520	3193	35 (24°C) 50 (500°C)	8.6 (300-1000°C)	345 to 428
	ZrO_2 (PSZ)	5400	2988	1.9 (20°C)	11.3 (20-1000°C)	186
	SiO_2 (quartz)	1950	1823	1.3 (25°C)	0.54 (25-300°C)	172
Low-temperature side	C	1780	3873	9.5	9.3	2.8
	Ti	4500	1933	21.9	9-10 (20-800°C)	106
	Cu	8960	1356	398	17.5 (20-300°C)	
	SUS-304	8060	1872 to 1727	21.5 (500°C) 16.2 (100°C)	17.3 (0-100°C)	193
	Ni	8900	1723	90.5	16.5 (300-600°C)	204

CHAPTER THREE

EXPERIMENTAL METHODS

3.1 INTRODUCTION

In order to achieve the objectives described in Chapter One, the experimental methods are described in this chapter. The experimental procedures are primarily concerned with the processing of alumina/aluminium-titanate (AAT) composites using both solid-state and infiltration methods as well as the characterisation of their properties. Material's characterisation involved the use of various analytical techniques, notably included: differential thermal analysis (DTA), dilatometry, x-ray diffraction (XRD), high temperature neutron diffraction (HTND), grazing-incidence synchrotron radiation (GISRD), scanning electron microscopy (SEM), transmission electron microscopy (TEM), and Vickers indentation.

3.2 MATERIALS PROCESSING

3.2.1 Raw Materials

The starting materials used in this work consisted of alumina (α-Al_2O_3), titanium dioxide (TiO_2), β-spodumene ($Li_2O.Al_2O_3.4SiO_2$) powders and titanium chloride ($TiCl_4$). The alumina powder was reactive alumina from AES-11C, Mandoval Ltd., United Kingdom, (99.9% purity and mean particle size of 0.4 μm). β-spodumene ($Li_2O.Al_2O_3.4SiO_2$) powder was supplied by Gwalia Consolidated Ltd, Western Australia. Both titanium dioxide (TiO_2) powder and titanium chloride ($TiCl_4$) liquid were supplied by BDH Limited Poole, England. The chemical analysis results for these powders are shown in Table 3.1. The median particle size for as-received β-spodumene powders was 19 μm. No milling trials were performed on the alumina powder because the particle size (0.4 μm) was considered to be acceptable.

Table 3.1. Chemical composition (wt%) of starting raw materials provided by suppliers.

Composition	Alumina	Rutile	β-spodumene
Al_2O_3	99.90		27.00
Na_2O	0.03		0.19
SiO_2	0.04		64.00
Fe_2O_3	0.01		0.16
MgO	0.04		0.02
CaO	0.02		0.04
LOI	0.10		0.30
H_2O	0.20		
TiO_2		98	0.02
K_2O			0.05
Li_2O			8.10
P_2O_5			0.11
SO_4		0.05	
As		0.0005	
Pb		0.005	
Fe		0.005	
Water-soluble matter		0.5	

LOI: loss on ignition

3.2.2 Alumina/Aluminium-Titanate (AAT) System

Samples of alumina/AT composites (AAT) were synthesized using the solid-state powder reaction between alumina and rutile. The samples were formulated in five compositions with AT content of 0, 8, 15, 30 and 45 wt% (Table 3.2).

Figure 3.1 shows the flowchart for the processing of the AAT composites. The powders were initially mixed for 15 min using a mortar and pestle. The powder mixture was then wet mixed in ethanol using a Turbula mixer for 1 h. The slurry was then dried in an oven, initially for 24 h at 60°C and the followed by 100°C for a further 24 h. The dried powder mixture was then uniaxially pressed in a metal die at 100 MPa to yield cylindrical pellets with dimensions 0.3 cm in height and diameter of 1.92 cm. Rectangular bar samples 5 × 10 × 60 mm^3 were also fabricated for thermal expansion testing and high temperature neutron diffraction (HTND). These samples were subsequently sintered in air at 1600°C for 4 h.

Pure AT pellets were also prepared for thermal decomposition study at 1100°C (considered as a critical condition for engineering application). Decomposition studied by *ex-situ* x-ray diffraction (XRD) and *in-situ* HTND, with the XRD work being conducted at ambient temperature. For comparison purposes, MgO-stabilised AT samples were also fabricated to study the influence of MgO addition on the decomposition behaviour of AT under both atmospheric and vacuum conditions.

Table 3.2. Formulations of AAT composites used in the study.

Sample	Alumina (wt%)	AT (wt%)
AAT0	100	0
AAT8	92	8
AAT15	85	15
AAT30	70	30
AAT45	55	45

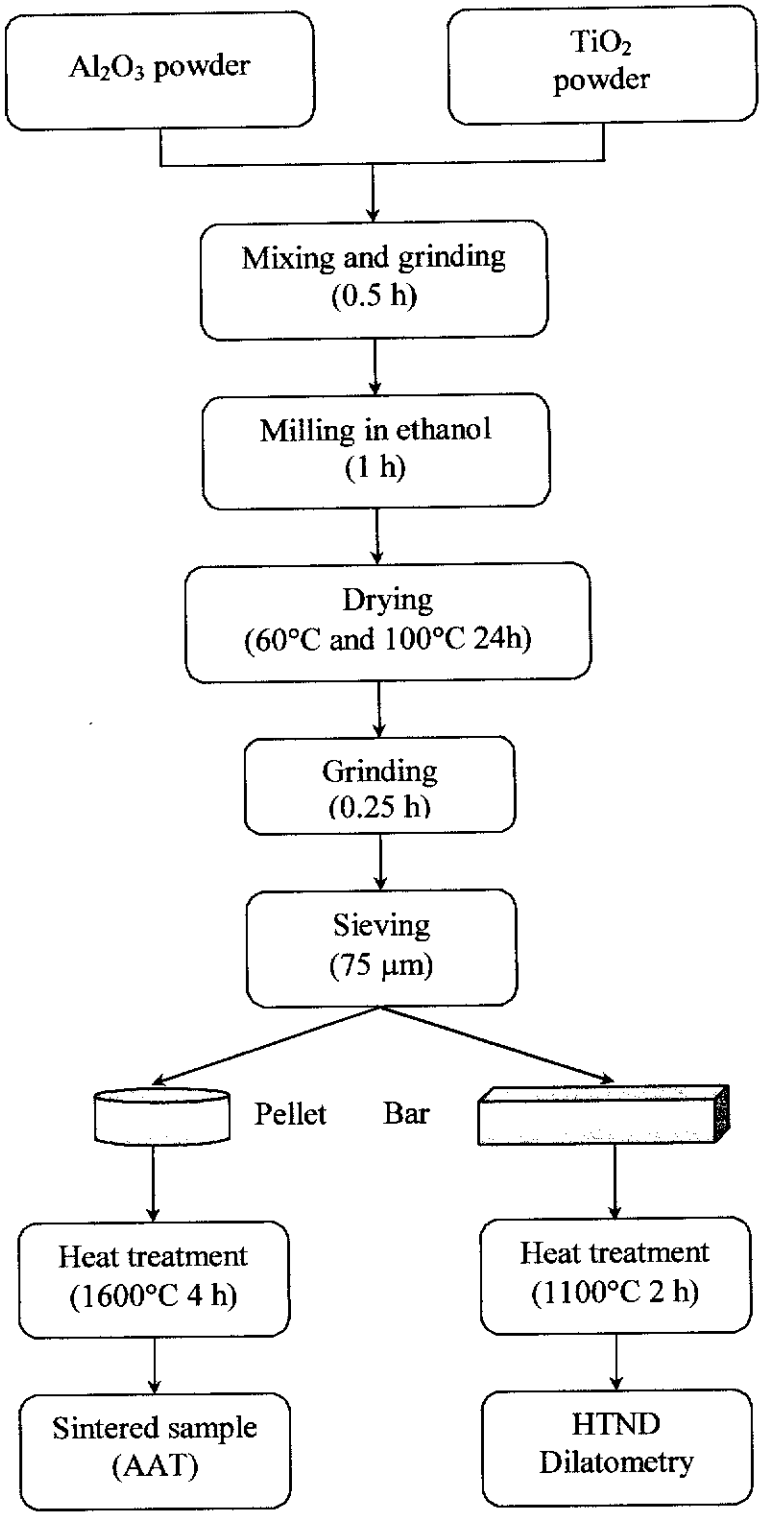

Figure 3.1. Processing of AAT composites.

3.2.3 β-Spodumene-modified AAT System

Five AAT samples with a fixed 30 wt% AT and 0 - 15 wt% β-spodumene were fabricated using solid-state powder reaction. The formulations of these samples are shown in Table 3.3.

Table 3.3. Formulation of β-spodumene modified AAT composites (30 wt% AT) samples.

Sample	Wt% β-spodumene
AATS0	0
AATS2	2
AATS5	5
AATS10	10
AATS15	15

The powder for each composition was mechanically-mixed in ethanol using a Turbula mixer for 1 h. After drying in an oven, initially at 60°C for 24 h and then a further 24 h at 100°C, the powder was uniaxially-pressed at 150 MPa into cylindrical pellets and rectangular bars. Cylindrical pellets were then pressureless-sintered at 1600°C for 4 h. These samples were prepared for XRD and physical property studies. Rectangular bar samples were pressureless-sintered at 1100°C for 2 h for use in dilatometry and HTND studies. The flowchart for the processing of β-spodumene modified AAT composites is shown in Figure 3.2.

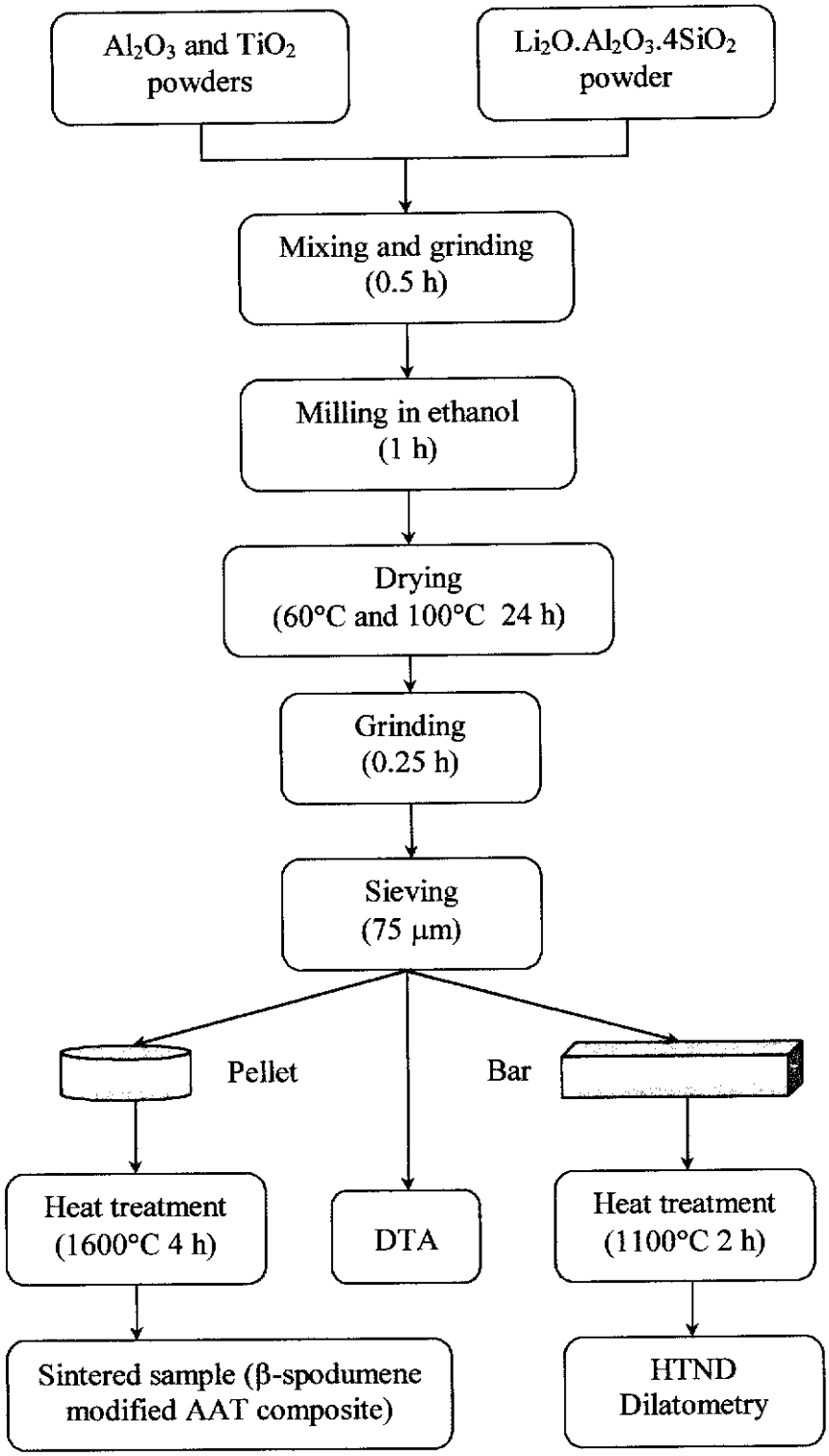

Figure 3.2. Processing of β-spodumene modified AAT composites.

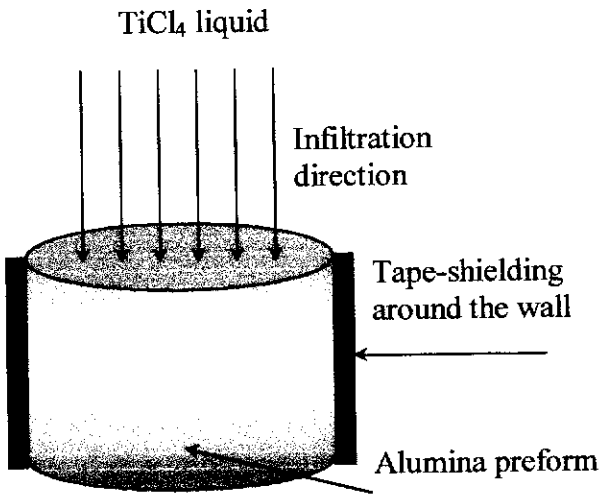

Figure 3.3. The alumina preform with plastic tape-shielding for uni-directional infiltration of liquid.

The uni-directional infiltration was conducted twice for 15 h each. After the first infiltration, the preform was dried at 40°C for 15 h before the second infiltration was performed. Samples were weighed before and after infiltration to calculate the mass increase due to infiltration. The infiltrated samples were calcined initially at 1350°C for 10 h, followed by final sintering at 1600°C for 6 h. In all cases the heating and cooling rates were 3°C /min.

3.3 MATERIALS CHARACTERISATION

3.3.1 Infiltration Kinetics

Alumina powder was used for the fabrication of alumina porous preforms. The powder was uni-axially pressed at 50 MPa to form rectangular bars (0.5 × 1.2 × 6) cm^3. These bars were then pre-sintered at 1000°C for 2 h. In order to study the effect of pre-sintering temperature, the bars were also treated at 900 and 1100°C for 2 h.

The kinetics of infiltrating a liquid precursor into alumina preforms were studied using water and $TiCl_4$. Infiltration of preforms was performed either in vacuum (10^{-3} torr) or under ambient conditions. The height of infiltrant rise was

recorded visually as a function of time at room temperature. The effects of preform sintering temperature, liquid type, vacuum and non-vacuum, and multiple infiltrations on the infiltration behaviour were also investigated. After each cycle the sample was dried at room temperature for 24 h. The flowchart for the infiltration kinetics study is shown in Figure 3.4.

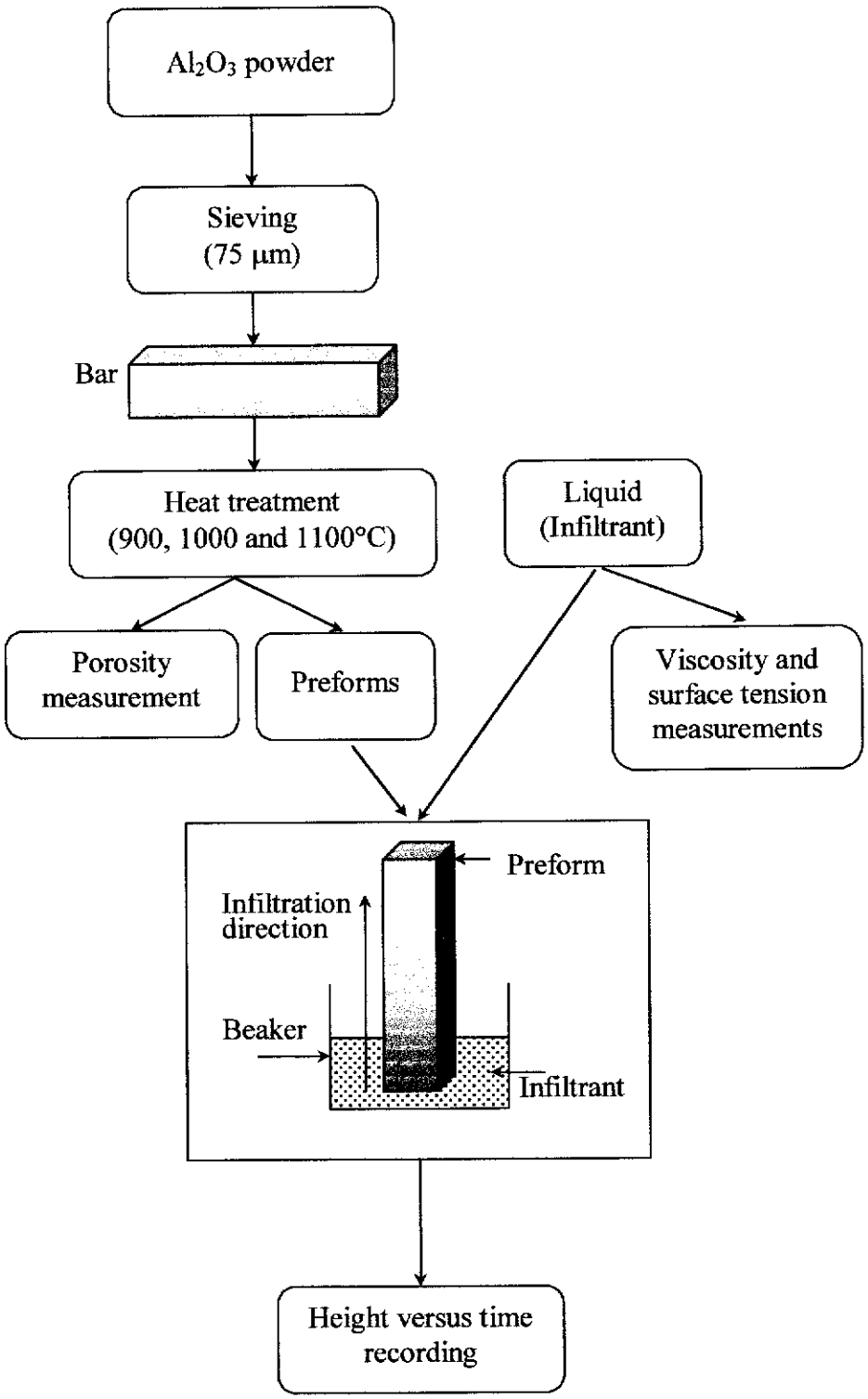

Figure 3.4. The flowchart for the infiltration kinetics study.

3.3.2 X-Ray Diffraction (XRD)

Analysis of phases formed was performed under ambient conditions with a Siemens D500 X-ray diffractometer for all heat-treated samples. The operating conditions used were CuKα radiation (λ = 1.5418 Å) produced at 40 kV and 30 mA. The receiving slit for the goniometer was set at 0.15° so that the beam as fully recovered by the specimen over the defined 2θ-range. The patterns were collected over the 2θ range 15-120°. Both the polishing and slicing of the samples methods were used to construct the graded composition profiles. For the thermally decomposed AT samples, emery paper was used to polish away the surface material to depths of 0.1, 0.2, 0.3, 0.4 and 0.5 mm. A high-precision diamond blade cutter was used to obtain 1 mm thin-slices of FGM samples. The XRD data were collected on both surfaces of each slice. Samples for data collection were mounted in a sample holder using bluetack (Bostik Australia PTY. Ltd.).

3.3.3 Neutron Diffraction (ND)

High temperature neutron diffraction was used to monitor the evolution of phase transformations in alumina/AT (AAT30), β-spodumene modified alumina/AT (AATS15) and pure AT systems. Neutron diffraction data collection was performed at the Australian Nuclear Science and Technology Organisation (ANSTO) using a high temperature neutron diffraction (HTND) with 32 detectors. The operation conditions were λ of 1.667 Å, 2θ range of 4-138° with step of 0.1°. The neutron flux (4×10^5 n/cm^{2}s) was produced from HIFAR research located at Lucas heights, NSW. The measurement time for each temperature was 2 h to obtain acceptable counting statistics. Data were collected at room temperature, 1200, 1290, 1310, 1330, 1350, 1370 and 1390°C. HTND was also conducted to study the isothermal decomposition behaviour of AT at 1100°C as a function of time (2-12 h).

3.3.4 Grazing Incidence Synchrotron Radiation Diffraction (GISRD)

Use of synchrotron radiation has a number of advantages over x-ray tube radiation (Parish and Hart 1985). Beside the higher intensity, the wavelength can be selected to avoid fluorescence background in order to maximise the peaks to background ratio.

The grazing incidence SRD measurements were conducted on infiltrated bar samples with the BIGDIFF instrument (O'Connor *et al.* 1997; Garret *et al.* 1995) located at the Australian National Beamline Facility (ANBF) in Tsukuba, Japan. The incident beam dimensions were set at a length of 10 mm and a width of 0.8 mm. Four erasable imaging plates were used to obtain the diffraction patterns with an exposure time of 15 min. The monochromator was set to deliver a wavelength of 1 Å. The grazing incidence measurements were conducted with incidence angles (α) of 0.1, 0.3, 0.5, 1, 2, 3 and 5°.

In θ:2θ mode (conventional X-ray diffraction), the reflection occurs from planes parallel to the surface 2θ. In the grazing incidence mode, reflection takes place from planes inclined to the surface so that the angle between the Bragg plane and the surface is (θ - α) where α is the grazing incidence angle (Figure 3.5a and b).

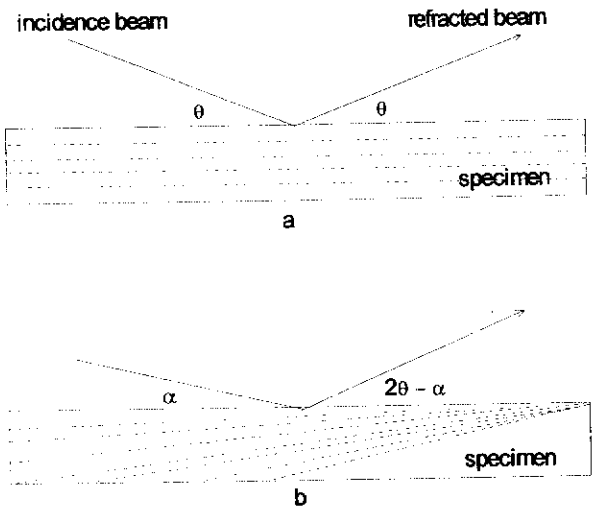

Figure 3.5. Schematic for (a) reflection from parallel planes, θ:2θ recording and (b) reflection from planes inclined to the surface (grazing incidence angle α).

3.3.5 Qualitative Phase Analysis

The phase compositions for the AAT, β-spodumene modified AAT, and functionally-graded AAT systems were determined using XRD and ND on the as-fired surface. Preliminary qualitative phase analysis was performed by comparing

the diffraction lines with Powder Diffraction File (PDF) data. Table 3.4 lists the PDF files for each of the phases formed.

Table 3.4. PDF numbers used for qualitative phase analysis of the XRD, ND and SRD patterns.

Phase	PDF files
α-Al_2O_3 (Corundum)	43-1484
Al_2TiO_5 (Aluminium Titanate)	41-0258
TiO_2 (Rutile)	21-1276
$Li_2O.Al_2O_3.4SiO_2$ (β-spodumene)	35-0797

3.3.6 Rietveld Phase Composition Analysis

The Rietveld method was developed to refine crystal structures by comparing the measured diffraction pattern with that calculated from a known crystal structure. Least-squares refinement is used to optimise the structure parameters by minimising the residual (X) summed over n points in pattern for which data was measured (Rietveld 1969),

$$X = \sum_{i=1}^{n} w_i (y_{io} - y_{ic})^2 \qquad (3.1)$$

where y_{io} and y_{ic} are the observed and calculated intensity and w_i is the weight of each observation. By using Bragg-Brentano optics to infinitely thick specimen, the calculated intensity, y_{ic} is formulated by (Warren 1969),

$$y_{ic} = \left(\frac{K}{\mu}\right) \sum_{jk} m_{jk} L_{jk} \left|F_{jk}\right|^2 G_{ijk} P_{jk} \left(\frac{C_k}{V_k^2}\right) + y_{ib} \qquad (3.2)$$

where K and μ are the instrumentation constant and linear attenuation coefficient, respectively. Term m_{jk} is multiplicity factor, L_{jk} is Lorentz-polarisation factor, F_{jk} is structure factor, G_{ijk} is normalised peak profile, P_{jk} is preferred orientation, C_k is volume fraction of k, V_k is cell volume and y_{ib} is the background contribution all for Bragg peak j of phase k.

The peak profile function, G_{ijk}, is selected from a menu of analytical shape functions which include Gaussian, Lorentzian, Pseudo-Voight, Pearson VII and Voight. The Pseudo-Voight function were tested by Young and Wiles (1982) with the equation (equation 3.3),

$$G_{ijk} = \frac{C_0^{1/2}\gamma}{\pi H_k}\left[1 + C_0\frac{(2\theta_i - 2\theta_k)^2}{H_k^2}\right]^{-1} + \frac{(1-\gamma)C_1^{1/2}}{\pi^{1/2}H_k}exp\left[-C_1\left(\frac{(2\theta_i - 2\theta_k)^2}{H_k^2}\right)\right] \tag{3.3}$$

was used exclusively in this study. The constants C_0 and C_1 are 4 and 4ln2, respectively. The mixing parameter γ which varies from 0 to 1 represents the fraction of Lorentzian character in this composite function.

The full-width-at-half-maximum (FWHM), H_k, for Bragg reflection was proposed by Caglioti, Paoletti and Ricci (1958) for Debye-Scherer optics,

$$H_K = \left(U\tan^2\theta + V\tan\theta + W\right)^{1/2} \tag{3.4}$$

where U, V and W are refineable parameters.

Peak asymmetry can be modelled using the semi-empirical function (Rietveld, 1969).

$$A_{ik} = 1 - AS[sign(2\theta_i - 2\theta_k)](2\theta_i - 2\theta_k)^2\cot\theta_k \tag{3.5}$$

where AS is asymmetry parameter determined from refinement.

Dollase (1986) proposed the correcting the intensities I_k of Bragg peaks for preferred orientation using the preferred correction (PO).

$$P_k = \left(r^2 \cos^2 \alpha_k + r^{-1} \sin^2 \alpha_k\right)^{-3/2} \tag{3.6}$$

where r is the refineable PO parameters.

A polynomial was used to fit the background of data collection. For many refinement order 3 was sufficient, but sometimes order 4 or higher was needed depending on data behaviour whether collected from XRD, SRD or ND,

$$y_{bi} = B_0 + B_1(2\theta_i) + B_2(2\theta_i)^2 + B_3(2\theta_i)^3 \tag{3.7}$$

Hence, B_0, B_1, B_2 and B_3 are the polynomial coefficients and 2θ is diffraction angle.

The application of the Rietveld refinement procedure or strategies for phase composition has been demonstrated in powdered mixtures (O'Connor and Raven 1988; O'Connor and Li 2000a; O'Connor and Li 2000b). Quantitative phase analysis was performed on the multi-phase samples using the expression described by Hill and Howard (1987).

$$W_k = \frac{S_k (ZMV)_k}{\sum_i S_i (ZMV)_i} \tag{3.8}$$

where W_k is the weight fraction of phase k, S_k is the Rietveld scale factor, Z is the number of formula per unit cell, M is the mass of the formula unit, and V is the unit-cell volume. The values of the parameter estimated standard deviations (esds), σ_j were calculated from the expression:

$$\sigma_j = \left[M_{jj}^{-1} \frac{\sum_{i=1}^{N} w_i (y_{io} - y_{ic})^2}{N - P} \right] \tag{3.9}$$

where N and P are the number of observations and the number of parameters being refined. M_{jj} is the diagonal element of the inverse of the matrix M_{jk}, which is given by:

$$M_{jk} = -\sum_i w_i \left[(y_{io} - y_{ic}) \frac{\partial^2 y_{ic}}{\partial x_j \partial x_k} - \frac{\partial y_{ic}}{\partial x_j} \frac{\partial y_{ic}}{\partial x_k} \right] \tag{3.10}$$

where x_j and x_k are adjustable parameters.

In relation to checking the figures-of-merit or R-values after refining, some formulae are used according to Young (1993) and Kisi (1994). Those formulas are presented as follows.

Profile R factor:

$$R_p = \frac{\sum_0^i |y_{io} - y_{ic}|}{\sum y_{io}} \tag{3.11}$$

Weighted profile R factor:

$$R_{wp} = \left[\frac{\sum w_i (y_{io} - y_{ic})^2}{\sum w_i y_{io}^2} \right]^{1/2} \tag{3.12}$$

Expected R factor:

$$R_{exp} = \left[\frac{N - P}{\sum w_i y_{io}^2} \right]^{1/2} \tag{3.13}$$

where N is the number of observations and P is the number of least-squares parameters being estimated.

The goodness-of-fit (GOF):

$$GOF = \left(\frac{R_{wp}}{R_{exp}} \right)^2 \tag{3.14}$$

Ideally, based on equation (3.14), the value of GOF should be 1.0. Kisi (1994) suggested that value should be less than four for phase analysis.

Bragg R factor for every phase:

$$R_B = \frac{\sum |I_{ko} - I_{kc}|}{\sum I_{ko}} \tag{3.15}$$

where I_{ko} and I_{kc} are observed and calculated intensities for Bragg reflection k.

The difference plots between the observed and the calculated patterns is an important for assessing the degree of refinement. The two patterns should give a flat difference for a well-refined model. The difference plots may show indication of the presence of undetected phases or inaccuracies in the background or peak shape modelling.

The models used to calculate the relative phase abundance for XRD, SRD and HTND data were Maslen *et al.* (1993) for alumina, Epicier *et al.* (1991) for AT, Howard, Sabine and Dickson (1991) for rutile and Clarke and Spink (1969) for β-spodumene. The software used to refine the data was the *Rietica* program (Hunter 1997).

3.3.7 Optical Microscopy

An Olympus PMG3 microscope was used to observe the general microstructural details of polished samples using a 1 μm surface finish.

3.3.8 Scanning Electron Microscopy (SEM)

A Phillips XL30 scanning electron microscope was used to examine the microstructures of both as-fired and polished surfaces. Polishing of samples to 1 μm surface finish was conducted with an automated polishing machine (Struers Pedemat, Denmark). The polished surfaces were then thermally-etched at 1400°C for 15 min, followed by gold-coating prior to examination. A field-emission SEM (Hitachi S-900) located at the Himeji Institute of Technology (Japan) was also used to observe the microstructures of the graded AAT samples.

3.3.9 Transmission Electron Microscopy (TEM)

A transmission electron microscope (JOEL HRTEM), coupled with the selected area diffraction (SAD) and energy dispersive spectrum (EDS) facilities, was used to observe and analyse the microstructures of the β-spodumene modified AAT samples. TEM examination was conducted at the Department of Materials Science and Engineering, Himeji Institute of Technology, Japan.

3.4 MATERIALS PROPERTIES

3.4.1 Density, Porosity and Shrinkage

Density and porosity were measured according to the Australian Standard (AS 1774.5-1989). The mass of the sample was measured using a digital balance (Denver Instrument Company, USA) to an accuracy of 0.3 mg. The bulk density (D_b) and apparent porosity (P_a) were measured using the boiling water method and calculated by the following formulae:

Bulk density,
$$D_b = \frac{m_D}{m_s - m_i} \text{ x } D_i \tag{3.16}$$

Apparent porosity,
$$P_a = \frac{m_s - m_D}{m_s - m_i} \text{ x } 100 \tag{3.17}$$

where m_D, m_i, m_s, and D_i are the dried mass, mass of the specimen saturated and suspended in water, mass of the specimen saturated and suspended in air, and the density of the immersion medium.

The dimensions of the samples were measured using a vernier caliper (Mitutoyo, Japan) to an accuracy of 0.02 mm. The shrinkage (S) was determined from the percent reduction in the diameter of the green compact (D_o) relative to the sintered sample (D_s) using the formula:

$$S = \frac{D_s - D_o}{D_o} \text{ x } 100 \tag{3.18}$$

3.4.2 Dilatometry

Bar samples with dimensions 4 × 4 × 10 mm^3 were prepared to study the thermal expansion behaviour. Theta 160 dilatometer was used to characterise the *in-situ* shrinkage or densification behaviour of the alumina/AT and β-spodumene modified alumina/AT samples in air over the temperature range 20-1500°C. The measurements were conducted at the Materials Division of ANSTO at Lucas Height, Sydney. Sapphire was used as a reference in the equipment for examining the standard measurement.

3.4.3 Surface Tension and Viscosity

The surface tensions of $TiCl_4$ and H_2O were measured using the plate removal method. The method is based on the force required to remove a lens plate from the liquid. The measurement was conducted at the Department of Physics, Curtin University of Technology.

The viscosities were measured with an Oswald viscometer. The instrument is based on the driving force of the liquid through the capillary, which is proportional to density. Therefore, for two different liquids the equation is:

$$\frac{\eta_1}{\eta_2} = \frac{\rho_1 t_1}{\rho_2 t_2} \tag{3.19}$$

where η_1, ρ_1, t_1, η_2, ρ_2 and t_2 are viscosity, density and flow time for liquids 1 and 2 respectively (Partington 1955).

By comparing the flow time of the two liquids where one was used as a standard, the viscosity of the other can be calculated. Methanol was used as standard in this experiment. The measurement was conducted at the Department of Chemistry, Curtin University of Technology.

3.4.4 Mercury Porosimetry

Mercury porosimetry is more widely used than the gas adsorption method for the porosity determination. Mercury porosimetry is based on the phenomenon of capillary rise. A liquid that wets the walls of a narrow capillary will climb up the

walls of the capillary. However, for nonwetting liquid like, such as mercury, pressure must be applied to cause the liquid to flow up the capillary to the level of the reservoir.

The porosimetry measurements were conducted at the University of New South Wales, Sydney with a Micromeritics 92220II mercury porosimeter at a pressure up to 414 MPa. The alumina preform sample was prepared by pre-sintering temperature at1000°C for 2 h. The formula to calculate the pore diameter of the preform, d is:

$$d = \frac{4\gamma \cos\theta}{P} \tag{3.20}$$

where γ, θ and P are surface tension (485 dyne/cm), contact angle (130°) and applied pressure of mercury, respectively (Washburn 1921).

3.4.5 Differential Thermal Analysis (DTA)

DTA/TG is useful for characterising phase changes, thermal decomposition and loss or gain in weight of a sample during heating. It can also show whether the reaction mechanism is endothermic or exothermic. Both endothermic and exothermic reactions correspond to thermal energy changes within the sample.

DTA measurements on the powder mixture were carried out on a Stanton Redcroft STA-780 in a nitrogen atmosphere. DTA data were collected on the β-spodumene modified AAT samples with heating rate of 20°C/min. Heating rates of 5, 10 and 15°C/min were also used on samples AAT30 and AT for the purpose of calculating the activation energy of AT. The data were collected at the temperature range of 20-1500°C with a flow rate of 60 cm^3/min. The crucible used was alumina with empty reference.

3.4.6 Mechanical Properties

The indentation half-diagonal lengths and the surface crack lengths were measured directly using a Zwick microhardness tester. All the specimens used for the indentation tests were from diamond polished to 1 μm surface finish. The specimens were indented using a load 10 kg for the AAT solid-state and β-

spodumene modified AAT, and 3 kg for decomposed AT and AAT FGMs. The number of indents made for each load was three The average half-diagonal lengths and the surface crack lengths were used to calculate hardness and fracture toughness (Figure 3.6). The hardness and fracture toughness were calculated using the following formulae (Evans and Charles 1976):

Hardness, $$H_v = 1.8544 \text{ x } \frac{P}{(2a)^2} \text{ x } \frac{9.8}{1000} \quad \text{(GPa)} \qquad (3.21)$$

Fracture Toughness, $$K_{IC} = 0.0824 \text{ x } \frac{P}{c^{3/2}} \text{ x } \frac{9.8}{\sqrt{1000}} \quad \text{(MPam}^{1/2}\text{)} \qquad (3.22)$$

where H_v is Vicker's hardness, K_{IC} is fracture toughness, P is applied load (kg), a is half-diagonal (mm) and c is the crack length (mm).

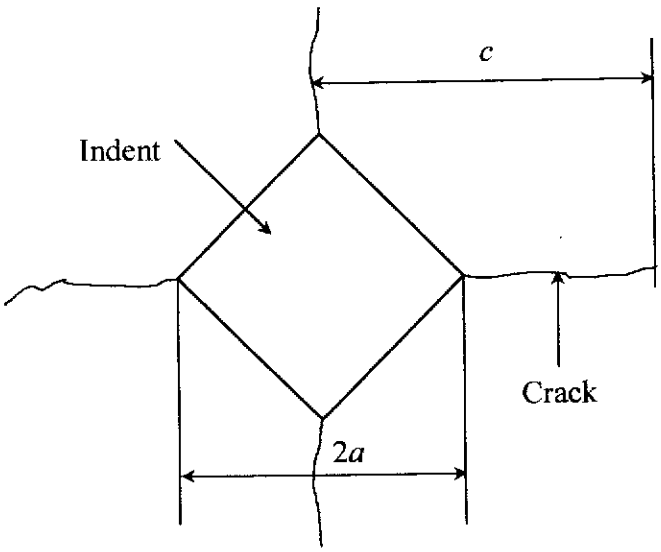

Figure 3.6. Schematic diagram of crack formation for Vickers indentation.

CHAPTER FOUR

THERMAL CHARACTERISTICS AND STABILITY OF ALUMINIUM TITANATE

4.1 INTRODUCTION

Aluminium titanate (Al_2TiO_5) may be formed through an equimolar reaction of alumina (Al_2O_3) and rutile (TiO_2). The formation commences at ~1300°C and reaches completion at ~1450°C. Based on differential thermal analysis, Lang, Filmore and Maxwell (1952) obtained 1380°C as the reaction temperature; and Yamaguchi, Hitoshi and Shimizu (1981) reported a formation temperature of ~1320-1400°C. Various researchers have reported different values of enthalpy and formation temperature for AT. Widely different values for enthalpy of 272 kJ/mol and 25.1 kJ/mol for AT were published by Sleepetys & Vaughan (1969) and Gani & McPherson (1973).

Aluminium titanate (AT) is thermally unstable over the range ~900-1250°C where it decomposes into the parent oxides α-Al_2O_3 and TiO_2 by an eutectoid reaction (Kato, Daimon and Takahashi 1980). Lang, Filmore and Maxwell (1952) reported that this material is thermodynamically stable from ~1280°C to the melting temperature (T_m = 1860°C). Buscaglia and Nanni (1998) found that the decomposition rate of AT is relatively low below ~800°C. Demaestri *et al.* (1989) reported that addition of MgO to AT can increase thermal stability and mechanical strength. It is also known that the thermal decomposition of AT can be controlled by adding MgO (Hamano *et al.* 1981).

The addition of 5% of MgO, Fe_2O_3 or ZrO_2 has been shown to affect the microstructure but improve the bending strength of AT (Ohya, Hamano and Nakagawa 1986). Wook, Jik and Lim (1999) investigated the bicomponent additives of 2, 5 and 10 mol% of equimolar MgO/ZrO_2, SiO_2/ ZrO_2 and MgO/SiO_2 mixture to stabilise AT from decomposition at 1150°C for 24 h. The MgO/SiO_2 was the most effective in suppressing thermal decomposition due to substitution of Al^{3+} by Mg^{2+}.

In this study, AT was isothermally decomposed at 1100°C both in air and in vacuum. This temperature was chosen because AT is known to be most unstable.

The phase relations, microstructure and mechanical properties were characterised by neutron diffraction, X-ray diffraction, SEM and Vickers indentation. The effect of MgO addition on the stability of AT was also studied.

4.2 RESULTS AND DISCUSSION

4.2.1 Differential Thermal Analysis

DTA data were collected for aluminium titanate (AT) powder prepared by the solid-state reaction of α-Al_2O_3 and TiO_2 (rutile) in stoichiometric proportions (see section 3.2.1). Measurements were made between room temperature and 1500°C on the basis that the formation temperature of AT is between 1340 and 1375°C (Gani and McPherson 1973). The DTA measurement procedure is described in section 3.4.1. The DTA data provided information on the activation energy by using different heating rates as seen in Figure 4.1. The endothermic peaks in Figure 4.1 were assumed as the formation temperature of AT and the plot is shown in Figure 4.2.

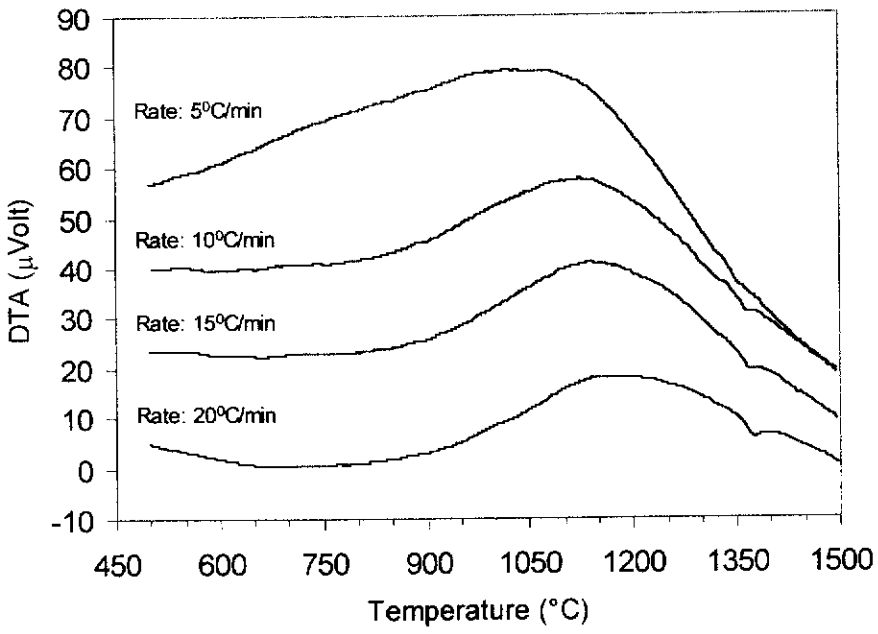

Figure 4.1. DTA analysis of AT powder prepared by solid-state reaction with heating rates of 5, 10, 15 and 20°C/min.

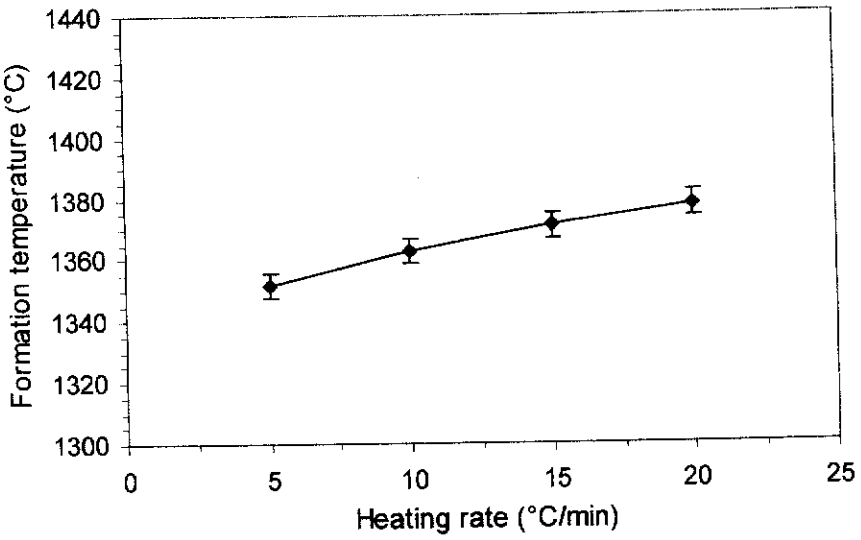

Figure 4.2. The formation temperature of AT for different heating rates. The error bars were based on the accuracy of the temperature.

In Figure 4.2, the formation temperature of AT varies from 1352 to 1378°C depending on the heating rate. The formation temperature increases with heating rate. Lower heating rates tend to decrease the formation temperature because time is longer. These results are consistent with the formation temperature range of 1360-1400°C, depending on the preparation route of the precursor mixture, reported by Segadaes, Morelli and Kiminami (1998) from DTA data. Generally, the peak temperature shifts to lower temperature with a decrease of heating rate.

For an atom to pass from one interstitial site to another, the lattice must be distorted in the intermediate position in order for the atom to squeeze between the lattice atoms in its way. Only a certain fraction of the atoms will have sufficient energy to surmount this energy barrier and the magnitude of the energy that must be supplied in order to surmount the energy barrier is the activation energy.

Solid-state reactions such as the crystallisation of AT can be described empirically by the Avrami (1939) law which may be used to calculate the activation energy from DTA data. Kissinger (1957) estimated the activation energy of magnesite, calcite, brucite, kaolinite and halloysite from DTA patterns. Then Anderson, Besch and Haberland (1977) examined the best-known kinetic evaluation

methods for DTA curves. The method of Kissinger (1957) was formulated by the equation:

$$\text{Kissinger:} \quad \ln\left(\frac{q}{T_m^2}\right) = -m\frac{E}{RT_m} \tag{4.1}$$

The method of Bansal *et al.* (1983) has been employed in this study for calculating the activation energy of AT.

$$\text{Bansal } et\ al.: \quad ln\left(\frac{T_m^2}{q}\right) = ln\left(\frac{E}{R}\right) - \ln A + \frac{E}{RT_m} \tag{4.2}$$

where q is the heating rate (°/min), T_m is the temperature for the endothermic/exothermic event (K), E is the activation energy, R is the universal gas constant (8.314 J/Kmol) and A is the frequency factor in Arrhenius expression, $k = A\ exp(-E/kT)$. By using equation (4.2) and the data from Figure 4.2, the activation energy was calculated as shown in Table 4.1.

Matusita and Sakka (1980) suggested the crystal growth dimension, m, should be considered carefully when using the Kissinger equation. Then Xu, Ray and Day (1991) proposed that m = 1 should be used when surface crystallization predominates and m = 3 for predominantly bulk crystallisation. For a constant heating rate, a broad crystallization peak indicates surface crystallization, whereas a sharp peak signifies a bulk crystallization process (Ozawa 1971). Based on this interpretation, the endothermic peak in Figure 4.1 shows that bulk crystallization is dominant in the sample. On this basis, the activation energy for m = 3 is 389(2) kJ/mole. This value is comparable to that Yamaguchi, Hitoshi and Shimizu (1981), 380.7 kJ/mole. Sakabe *et al.* (1970) reported that the activation energy of AT is 205.8 kJ/mole

Table 4.1. Activation energy of aluminium titanate for solid state reaction of α-Al_2O_3 and TiO_2 (rutile).

Additives	Method	Activation Energy (kJ/mol)	Reference
none	DTA	389(2)*	This study
0.5-7 mole % Fe_2O_3	Kinetic	205.8	Sakabe *et al.* (1970)
none	Kinetic	380.7	Yamaguchi *et al.* (1981)

* The number in the parenthesis is mean deviation based on the best-fit data and model.

The kinetic method in table 4.1 refers to the rate constant, k, which has the temperature (T) dependence as explained in section 2.3.2.

4.2.2 Densification

The density, porosity, and shrinkage of sintered pure AT and MgO-AT were measured according to Archimedes principle (Australian Standard AS 1774.5 - 1989). The addition of MgO to AT was conducted to gauge the influence of MgO on the thermal stability and mechanical strength of compound (Demaestri *et al.* 1989). The results are shown in Table 4.2.

Table 4.2. Density, porosity and shrinkage of pure AT and MgO-AT after firing at 1600°C for 6 h.

Sample	Density (g/cm^3)	Porosity (%)	Shrinkage (%)
AT	2.751(10)	23.4(7)*	2.6(1)
MgO-AT	3.382(8)	6.7(2)	10.7(1)

*Number in parenthesis is estimated standard deviation (σ).

Table 4.2 shows that the density of AT is lower than theoretical (3.700 g/cm^3) due to high porosity and small shrinkage. In contrast, the density of MgO-AT is higher than AT due to low porosity and high shrinkage. The porosity decreases 3.5 times whereas shrinkage increases 4 times compared to AT. This indicates that MgO

can reduce the porosity because of its ability to form a liquid phase during sintering (Rahaman 1995).

4.2.3 XRD and ND Characterisation

Room-temperature x-ray and neutron diffraction (XRD and ND) analysis were used to characterise the AT material. The preparation procedure was described in section 3.2.1.

AT was the only phase observed in both XRD and ND patterns indicating that α-Al_2O_3 and rutile have reacted completely to form AT (see the Rietveld difference plots in Figure 4.3). Since the wavelengths used for XRD and ND are similar, corresponding peaks occur similar angles. The relative for corresponding peaks are very different for the two patterns due to the differences in the scattering factors for x-rays and neutrons.

The diffraction data were further analysed by Rietveld analysis. The model of Epicier *et al.* (1991) gave the most acceptable refinements for the various models reported in the literature (section 2.3.1), according to the difference plots and figures-of-merit obtained. The pseudo-Voigt function was used to model the shape of diffraction peaks. The parameters refined were the background profile parameters (*B's*), 2θ-zero, scale factor (s), profile broadening parameters (*U*, *V*, *W*), lattice parameters (*a*, *b*, *c*), preferred orientation factor (*PO*), asymmetry factor (*As*), mixing parameter (γ) and atom isotropic thermal parameters (*T*). The atom coordinates (*x,y,z*) were not refined. The two difference plots are shown in Figure 4.3, and the lattice parameters and figures-of-merit are given in Table 4.2.

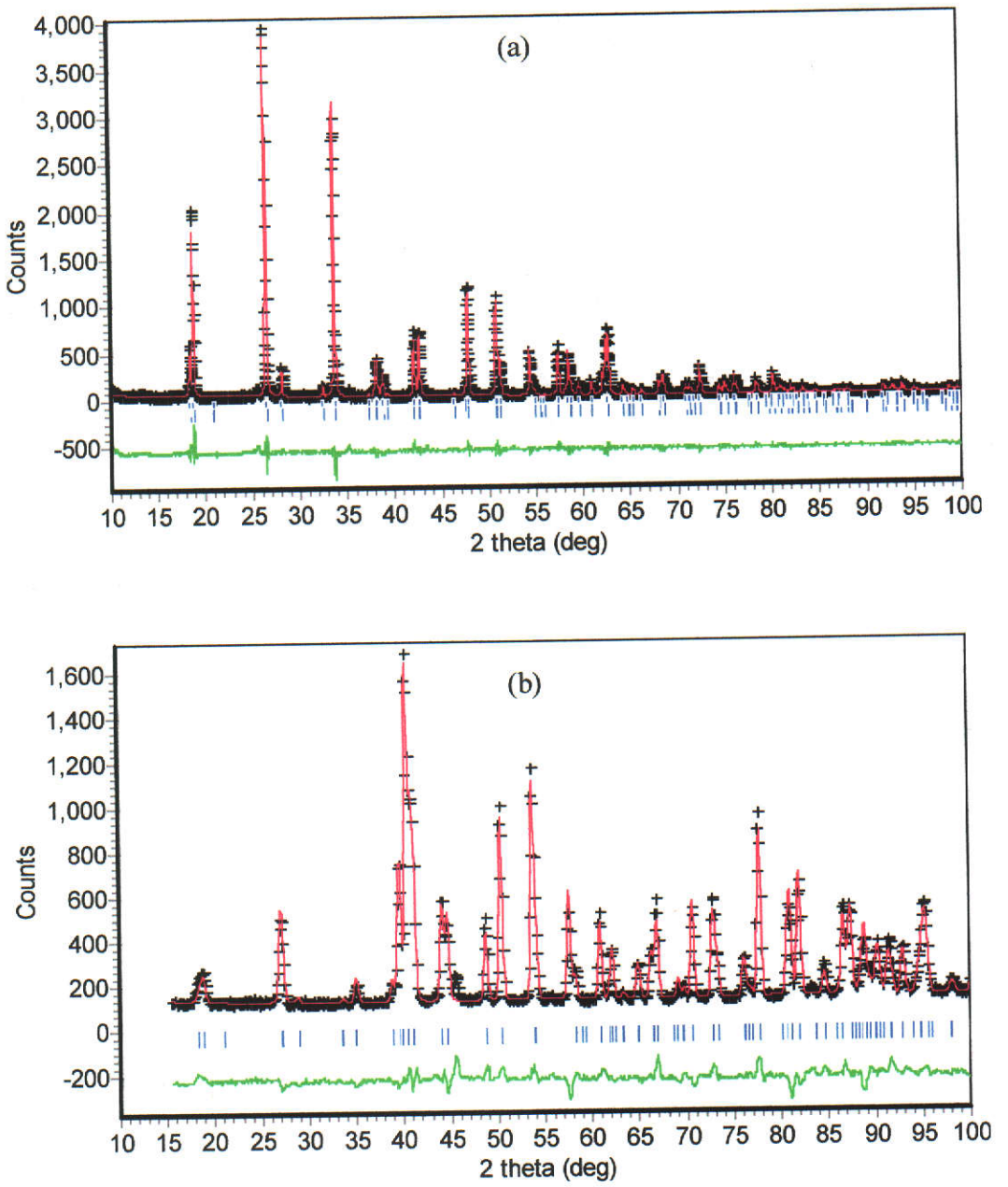

Figure 4.3. (a) XRD and (b) ND difference plots for AT after Rietveld refinement with the Epicier *et al.* (1991) model. The measured and calculated patterns are indicated by crosses (black) and solid lines (red), respectively. The green line is the difference plot. Vertical bars (blue) represent the Bragg peak positions for AT. Wavelengths for XRD and ND = 1.5418 and 1.666 Å, respectively.

Table 4.3. Lattice parameters and figures-of-merit for Rietveld AT refinements with XRD and ND room-temperature data.

Study	Space group	*a* (Å)	*b* (Å)	*c* (Å)	Rwp	GOF	R_B
XRD-this study	Cmcm	3.5930 (1)*	9.4311 (2)	9.6385 (2)	12.0	2.0	5.1
ND-this study	Cmcm	3.5972 (4)	9.4441 (10)	9.6531 (10)	7.5	5.5	5.0
Epicier *et al.* (1991)	Cmcm	3.591	9.429	9.636	n	n	6.0

*Note: Number in parenthesis is estimated standard deviation (σ), n = no information.

4.3 ISOTHERMAL DECOMPOSITION OF AT

4.3.1 Decomposition at 1100°C in Air and in Vacuum

A green sample of diameter of 1.92 cm was compacted at 150 MPa. The material was then sintered at 1600°C for 6 h. A sample of AT containing 10 wt% MgO was also prepared for the tests described in section 4.4. Samples decomposition tests were conducted by heating at 1100°C for 5 h in both air and vacuum (10^{-5} Torr). The decomposition behaviour was studied by XRD and ND (section 3.2.1)

In order to examine whether or not there is a mass change (Δm) during decomposition, the sample was measured before (m_b) and after (m_a) decomposition. The mass of AT after decomposition at 1100°C for 5 h was measured.

Table 4.4. The mass of AT after heating at 1100°C for 5 h.

Treatment	m_b (g)	m_a (g)	Δm (%)
Air	1.9557(2)	1.9532(2)*	+ 0.13
Vacuum	1.4239(2)	1.4233(2)	+ 0.04

*Number in parentheses is estimated standard deviation (σ).

Table 4.4 shows that the mass change after decomposition in atmosphere and vacuum is very small (less than 1%) which is consistent with the formula:

$Al_2TiO_5 \rightarrow Al_2O_3 + TiO_2$.

4.3.2 *In-situ* ND KineticDecomposition Study

In this experiment, AT was decomposed at 1100°C in air as a function of time. The purpose was to study the influence of time on the decomposition process at a fixed temperature. The ND data at each temperature were collected over 2 h in order to obtain adequate intensity statistics. The isothermal decomposition behaviour of AT measured in this way is shown in Figure 4.4.

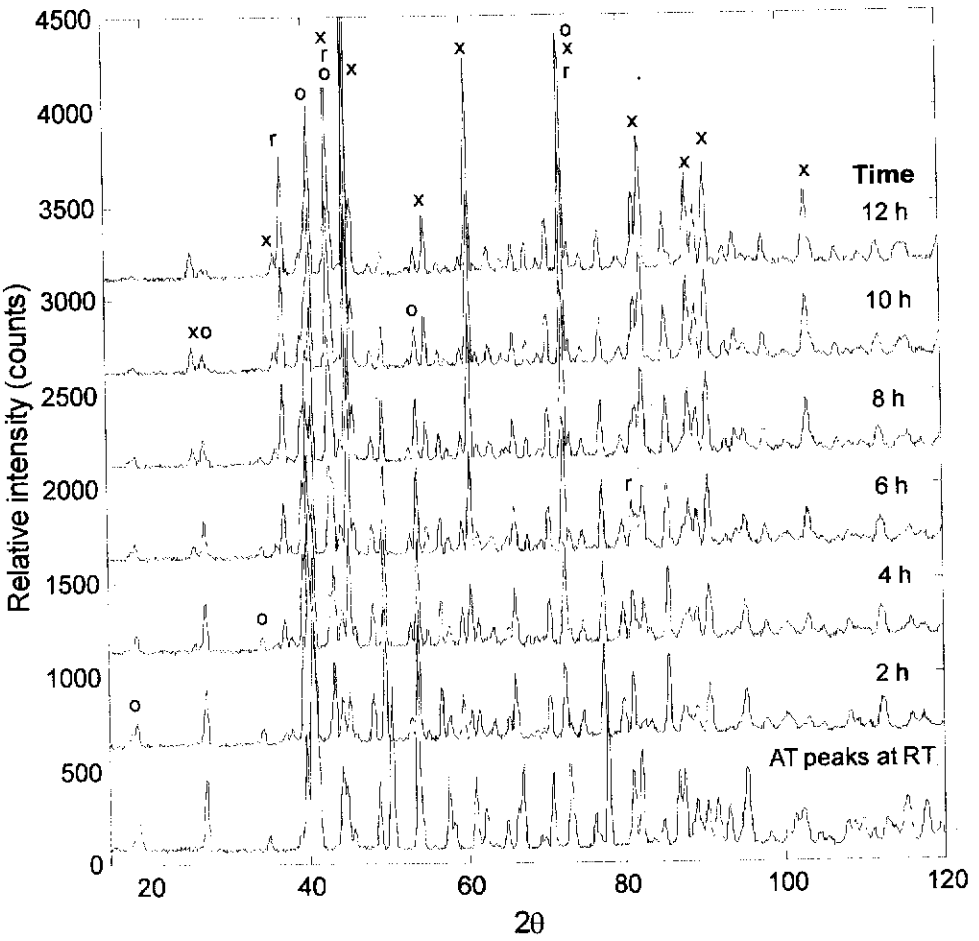

Figure 4.4. Decomposition of AT in air at 1100°C. The pattern for pure AT at room temperature before decomposition is also shown. Legend: x = alumina, o = AT, and r = rutile. Wavelength for ND = 1.666 Å.

Figure 4.4 shows the *in-situ* decomposition of AT to parent oxide *ie*. alumina and rutile as a function of time. The relative phase abundance from patterns was calculated using Rietveld analysis as explained in section 3.3.6. Figure 4.5 depicts shows the relative phase abundance in mol% for AT, alumina and rutile for every 2 h after decomposing at 1100°C.

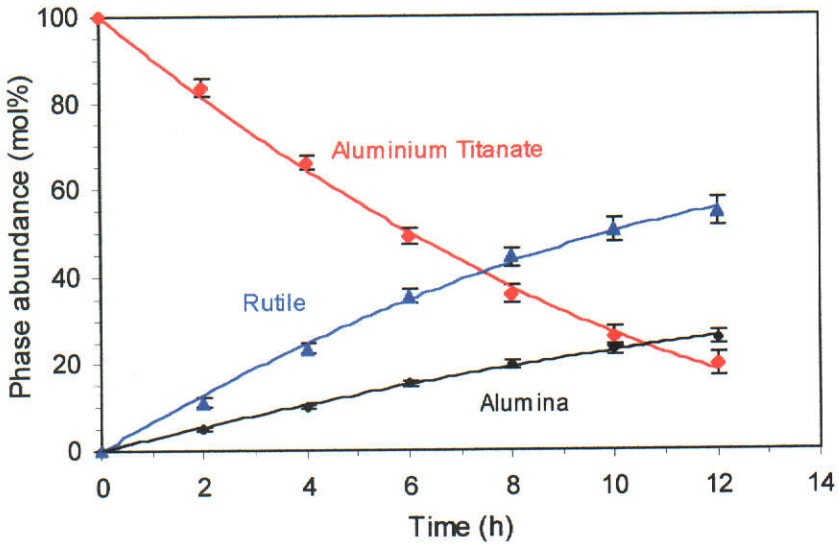

Figure 4.5. *In-situ* relative phase abundance of AT as a function of time. The decomposition was conducted in air at 1100°C. Error bars indicate two estimated standard deviations (2σ).

From Figure 4.5, the best-fit curves for AT, alumina and rutile obey the second-order polynomial. This allows one to predict the phase abundance at any time. The temporal change in phase abundances show that AT dissociates with time as expected.

4.3.3 *Ex-situ* XRD Decomposition Study

The decomposition of samples was conducted at 1100°C under two conditions, *ie*. in air and in vacuum for 5 h. The purpose of this study was to

understand the influence of oxygen partial-pressure on the decomposition process. In addition, the study aimed to ascertain whether the decomposition process was surface-initiated or a bulk phenomenon. Depth-profiling analysis of phase composition was conducted by polishing the surface to selected depths (section 3.3.1). The ambient-temperature diffraction patterns for the decomposition in air study are shown in Figure 4.6.

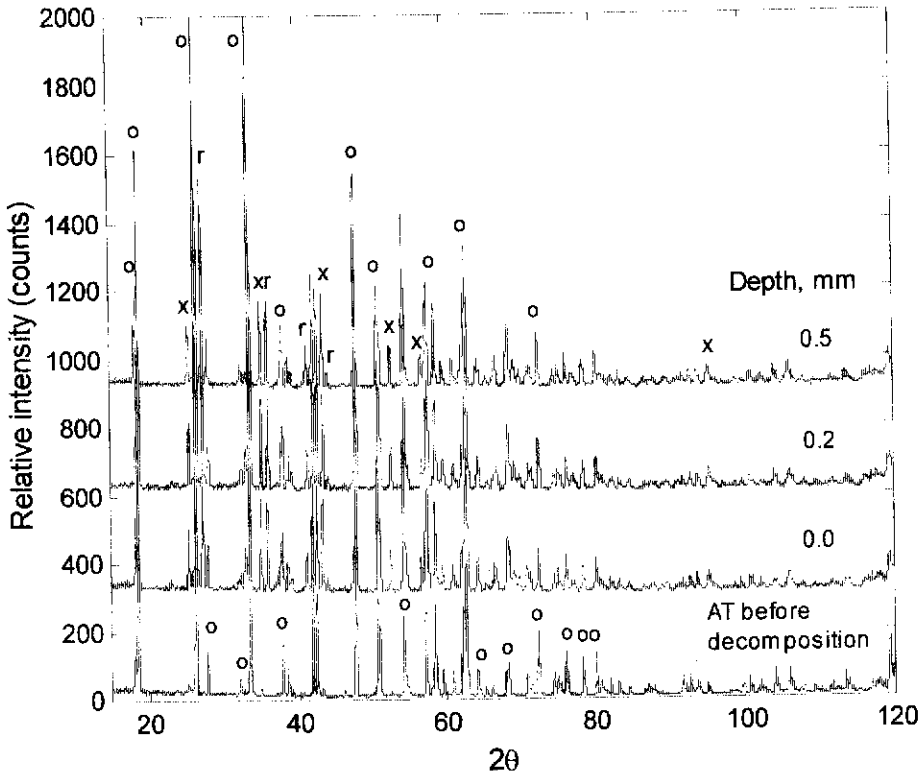

Figure 4.6. Ambient temperature XRD patterns for AT before and after decomposition in air at 1100°C for 5 h depths of 0.0, 0.2 and 0.5 mm. Legend: x = alumina, o = AT and r = rutile. Wavelength = 1.5418 Å.

Figure 4.6 shows that both alumina and rutile formed following decomposition in air at 1100°C for 5 h. When polished to depths of 0.2 and 0.5 mm, the relative phase abundances remained the same *ie.* were depth independent (Figure 4.7), indicating that the decomposition of AT was not surface-initiated but a bulk phenomenon.

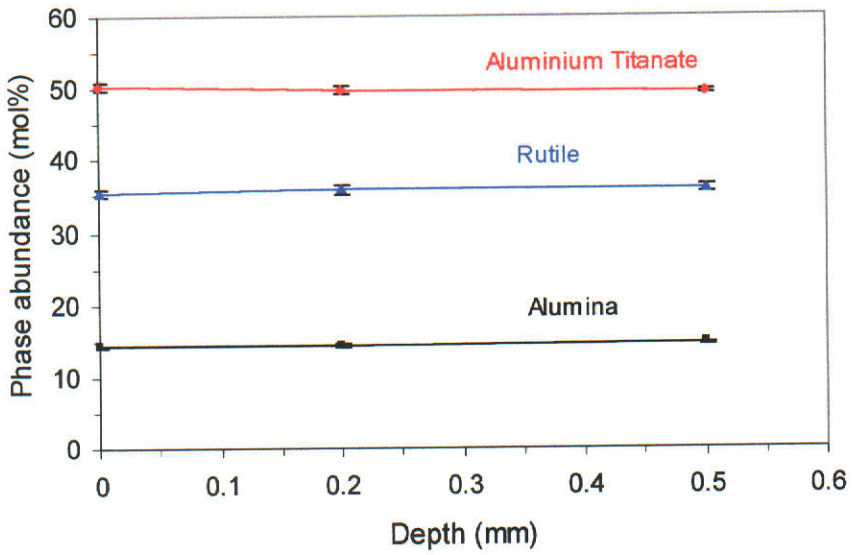

Figure 4.7. The relative mol percentages of alumina, AT and rutile phases after decomposition of AT in air at 1100°C for 5 h. Sample was polished to depths of 0.2 and 0.5 mm. Error bars indicate two estimated standard deviations (2σ). Wavelength = 1.5418 Å.

Figure 4.7 shows that the relative phase abundance of AT on surface after decomposing for 5 h at 1100°C is 50.3(5) mol%. At the same time, the relative phase abundance of AT based on *in-situ* decomposition is 57.1 mol% (see Figure 4.5). Therefore, the phase abundances from the *ex-situ* and *in-situ* experiments are close indicating that decomposition in air is a bulk phenomenon since the neutron data provide bulk information.

In order to study the influence of oxygen partial-pressure on decomposition, the AT sample was also isothermally decomposed at 1100°C for 5 h in vacuum (10^{-5} Torr). The sample was placed in the vacuum furnace as shown in Figure 4.8.

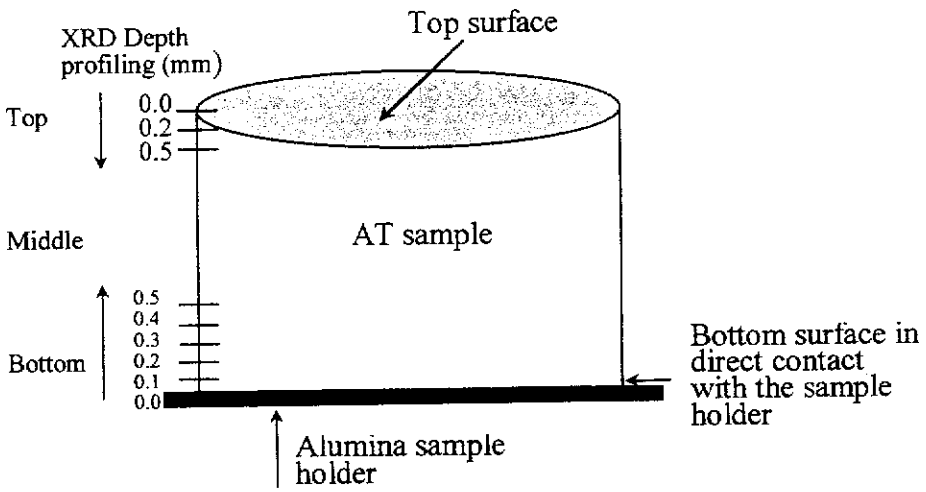

Figure 4.8. Schematic sketch showing AT sample in vacuum furnace during decomposition study. The top surface of sample was exposed to vacuum and the bottom surface was in direct contact with alumina sample holder.

The XRD patterns for the decomposition behaviour of AT in vacuum are shown in Figures 4.9 and 4.10 for top and bottom surfaces, respectively. Figure 4.9 shows the XRD patterns for surface polishing to depths of 0.0, 0.2 and 0.5 mm, and Figure 4.10 shows patterns for depths of 0.0, 0.1, 0.2, 0.3, 0.4 and 0.5 mm.

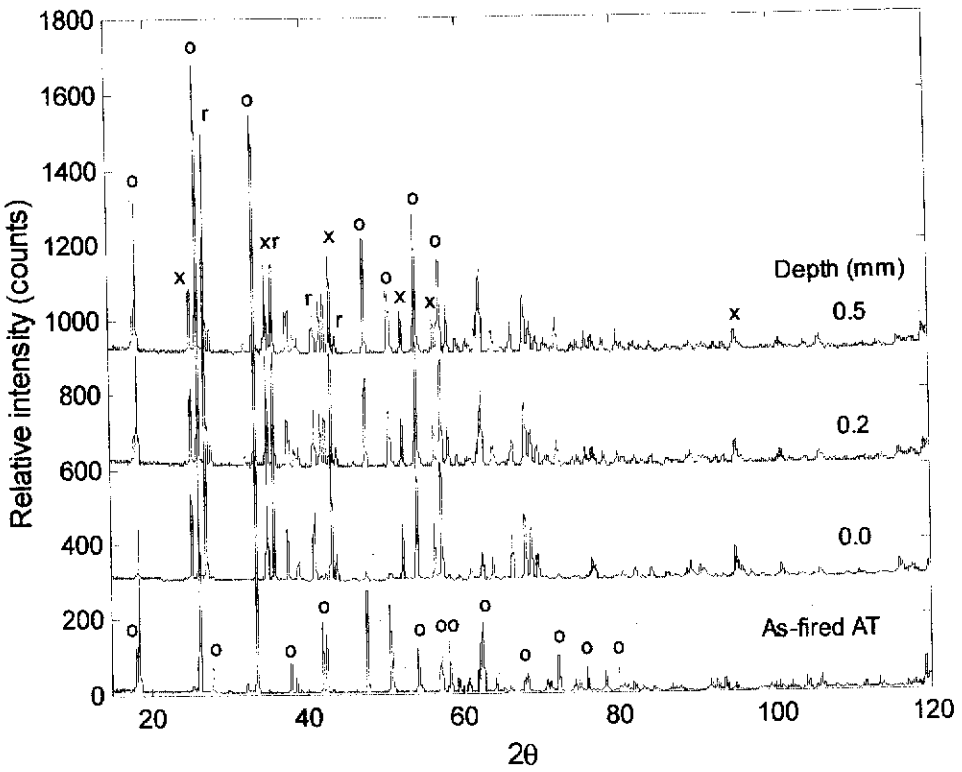

Figure 4.9. XRD patterns for AT before and after decomposition in vacuum (10^{-5} Torr) at 1100°C for 5 h for depths of 0.0, 0.2 and 0.5 mm (top). Legend: x = alumina, o = AT and r = rutile. Wavelength = 1.5418 Å.

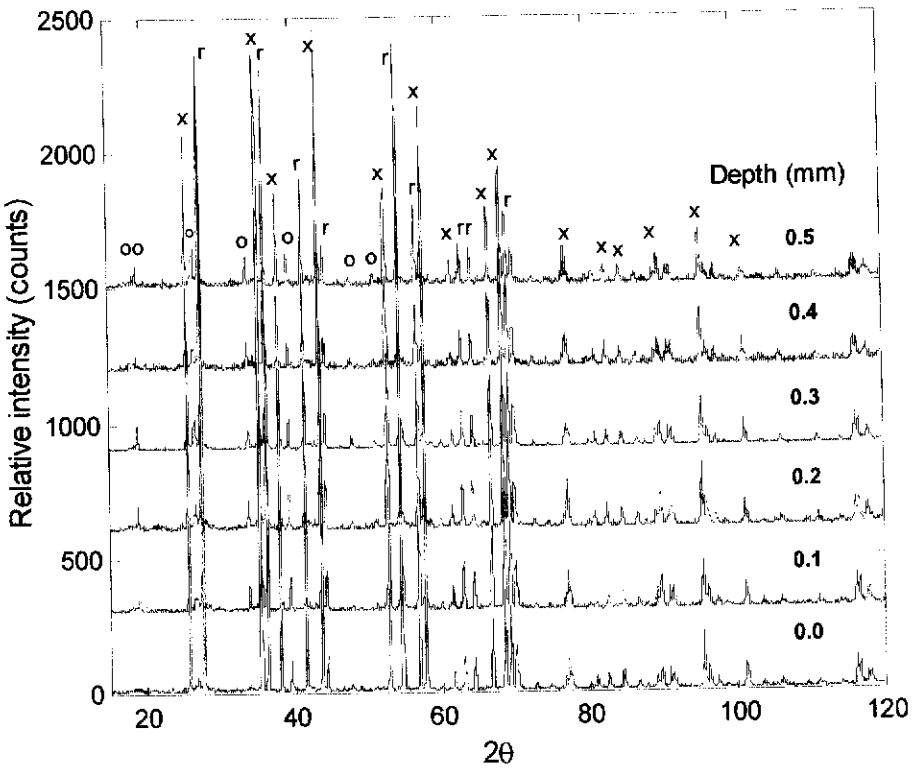

Figure 4.10. Decomposition behaviour for AT in vacuum at 1100°C for 5 h for the bottom surface polished to depths of 0.0, 0.1, 0.2, 0.3, 0.4 and 0.5 mm. Legend: x = alumina, o = AT and r = rutile. Wavelength = 1.5418 Å.

The relative phase abundances for top and bottom surfaces were calculated with Rietveld phase analysis and the results are presented in Figures 4.11 and 4.12, respectively.

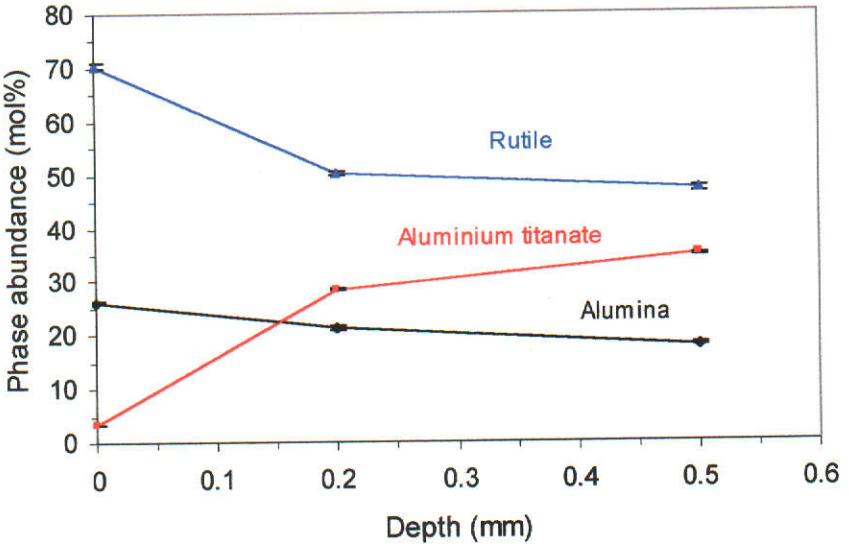

Figure 4.11. The relative mol percentage of AT, alumina and rutile phases after decomposition of AT in vacuum (10^{-5} Torr) at 1100°C for 5 h (top). The sample depth of 0, 0.2 and 0.5 are shown. Error bars indicate two estimated standard deviations (2σ).

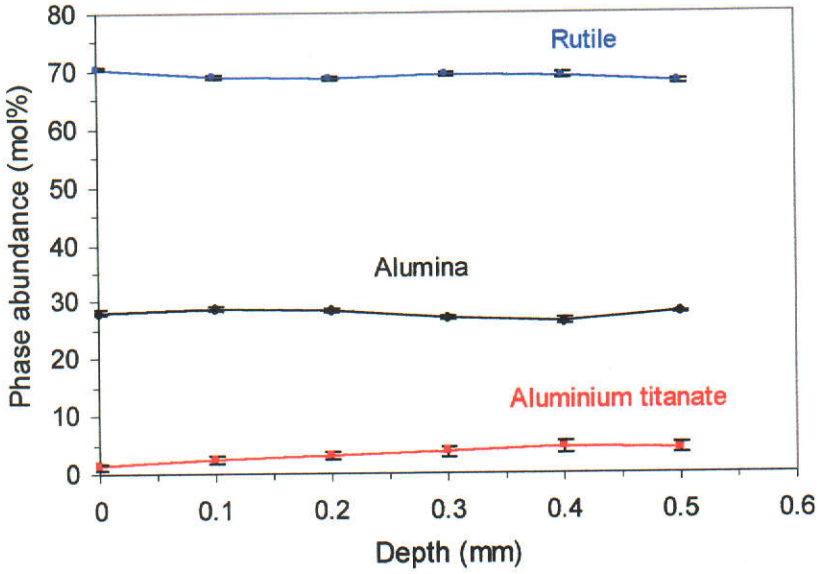

Figure 4.12. The relative mol percentage of AT, alumina and rutile phases after decomposition of AT in vacuum (10^{-5} Torr) at 1100°C for 5 h (bottom). The sample depth of 0, 0.1, 0.2, 0.3, 0.4 and 0.5 are shown. Error bars indicate two estimated standard deviations (2σ).

The results in Figures 4.7, 4.11 and 4.12 suggest that the decomposition behaviour of AT is different depending on the atmosphere environment, especially the oxygen partial pressure. As the oxygen partial pressure is reduced, as in vacuum, the rate of decomposition on the surface increases. This may be attributed to the susceptibility of rutile to lose its oxygen, causing non-stoichiometry in the compound which expedites the decomposition process. In air, the rate of decomposition is lower but it involves bulk transformation rather than surface-initiation. However, the overall decomposition in air is larger than in vacuum. It is also interesting to note that the difference in the nature and degree of decomposition in vacuum between the top and bottom surfaces of the sample. Figure 4.11 shows the more gradual and graded variation of phase compositions than the bottom surface decomposed in vacuum. This difference may be attributed to the slight variation in oxygen partial pressure experienced by both surfaces during vacuum decomposition.

The exciting discovery from this decomposition study is the possibility of designing functionally-graded AT through a novel high-temperature vacuum heat-treatment. This offers a new approach in the design of layered and graded AT system where an alumina-rich layer imparts hardness, strength and wear-resistance to the otherwise soft and weak AT.

4.3.4 Scanning Electron Microscopy

SEM micrographs of AT decomposed in vacuum are shown in Figures 4.13 - 4.16. Figure 4.13 shows clearly the cross-sectional graded microstructure behaviour of AT from top to bottom regions. There is a distinct contrast in microstructures between the top and the middle regions. This verifies that the decomposition process in vacuum is surface-initiated, leading to a graded composition as indicated by XRD depth-profiles (Figures 4.11 and 4.12).

Figure 4.14 shows a magnified view of the top region in higher magnification. To further confirm the graded behaviour in the sample, the SEM was taken at the boundary between the middle and the top regions (Figures 4.15) and at the middle region (Figure 4.16) in higher magnifications. The microstructure in the middle region appears more porous than that of the top region.

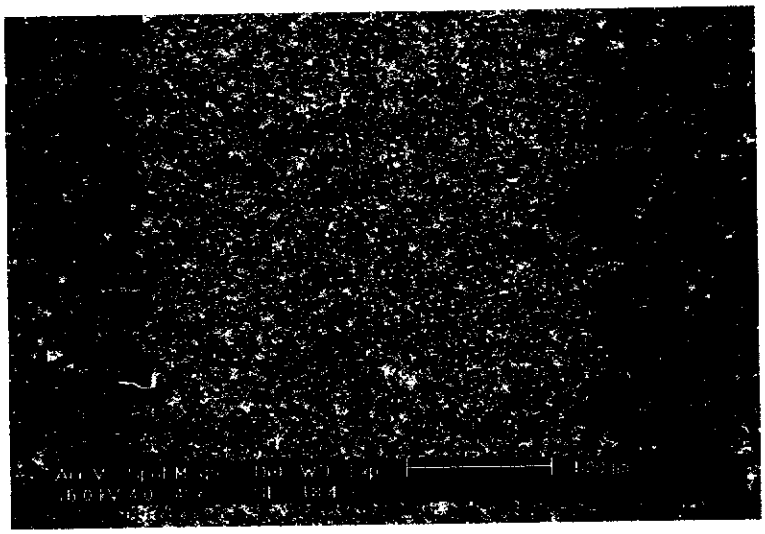

Bottom Middle Top

Figure 4.13. SEM image showing a cross-sectional view from top to bottom surfaces of the sample decomposed in vacuum.

Figure 4.14. SEM image showing a magnified view of the top surface.

Figure 4.15. SEM image showing the microstructure at the boundary between the top and middle regions.

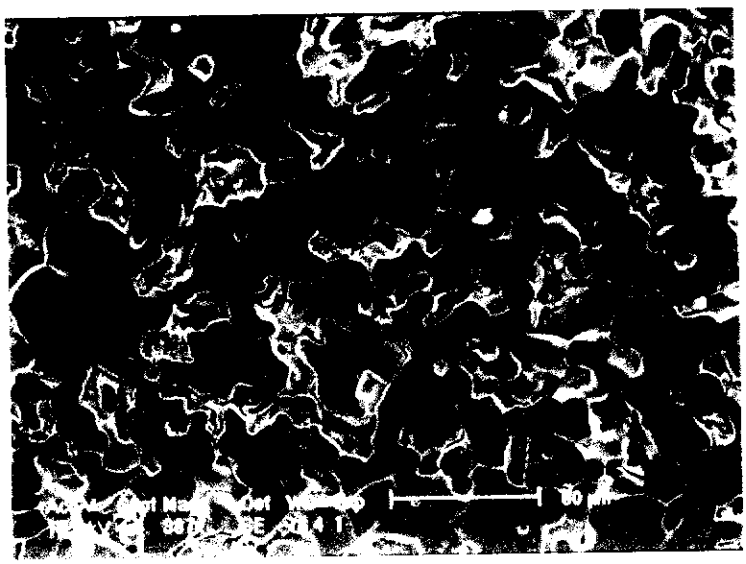

Figure 4.16. SEM image showing a magnified view of the microstructure in the middle region.

4.3.5 Hardness

The variation of cross-sectional hardness was measured on polished surfaces using Vickers indentation with a load of 3 kg (see section 3.4.6). The hardness depth-profiles were measured according to Figure 4.17 and the results are shown in Figure 4.18.

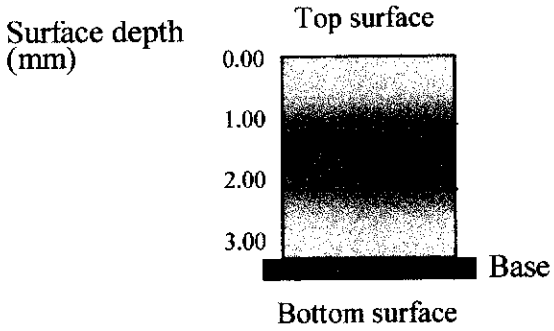

Figure 4.17. Schematic sketch showing the measurement of cross-sectional hardness depth-profiles of the sample.

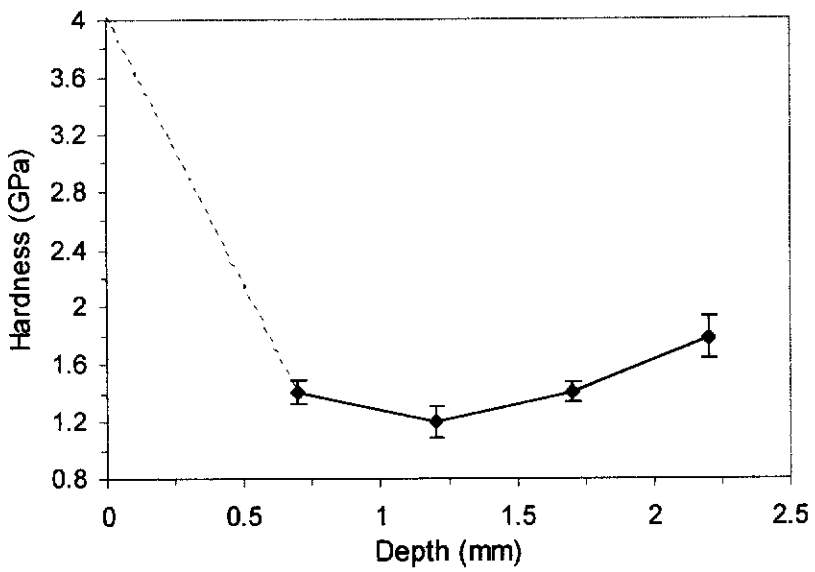

Figure 4.18. Cross-sectional plot of hardness as a function of depth. Error bars indicate two mean deviations (±). Dotted line is extrapolated value.

The results show that the decomposed alumina-rich layers have higher hardness than the inner core of AT. This is consistent with alumina being much harder and stronger material than AT. Hence, the presence of this layer can serve to impart both strength and wear resistance while the inner AT core retains its excellent thermal shock resistance.

Figures 4.19 and 4.20 show the appearance of the Vickers indent at two locations. In both cases, there is a display of pronounced microdamage within and in the vicinity of the indent but the presence of radial cracks are not apparent. It is unclear whether this apparent damage-tolerance behaviour was due to the effect of vacuum heat-treatment.

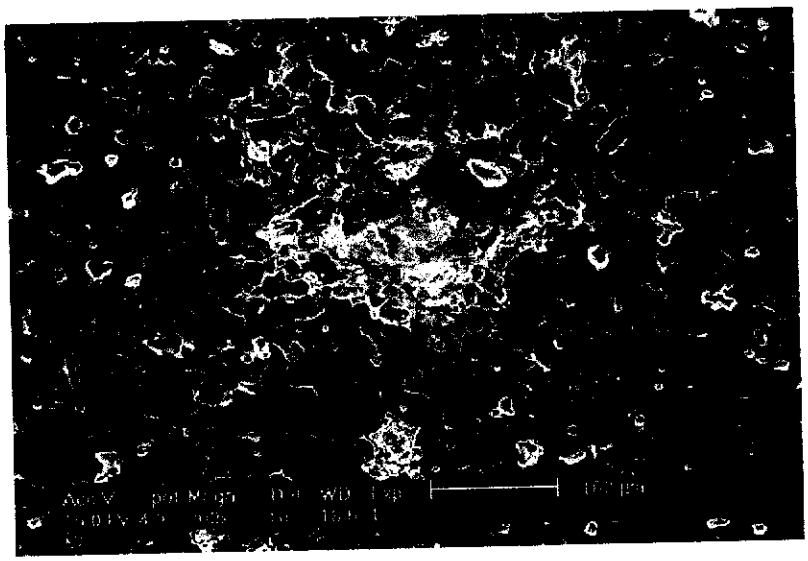

Figure 4.19. Scanning electron micrograph showing the Vickers indent at the top surface region. Note the absence of radial cracks.

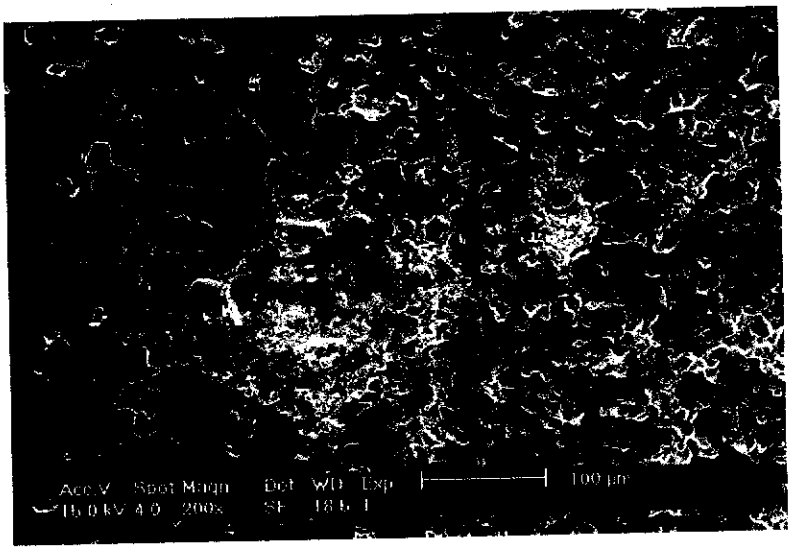

Figure 4.20. Scanning electron micrograph showing the indent at the boundary between the middle and top regions. Note the absence of radial cracks.

4.4 EFFECT OF MgO-ADDITION ON THE AT

Various investigations have shown that the thermal shock resistance (Wasmuht, Recht and Kroenert 1991), heat resistance or thermal durability (Zografou *et al.* 1988), and mechanical properties of AT can be significantly improved through the addition of MgO (Liu and Perera 1998; Martinez *et al.* 2001). The formation of spinel, $MgAl_2O_4$, in AT has been found to have a favorable effect on thermal shock resistance. Suvorov *et al.* (1987) also reported that the presence of spinel in AT increased its thermal stability and heat resistance.

In order to understand the decomposition characteristics of MgO-stabilised AT, XRD data were collected on the as-sintered sample (see section 3.3.2) which was in air and vacuum at 1100°C for 5 h. The XRD patterns for both conditions are shown in Figure 4.21.

Figure 4.21 shows the presence of spinel in MgO-stabilised AT after sintering at 1600°C for 10 h. Spinel peaks can be clearly seen at 2θ values of 31.23,

44.83 and 65.33°. After decomposition in air, the intensities of these peaks decrease. A similar behaviour was observed for the sample decomposed in vacuum although the spinel peaks here decreased more.

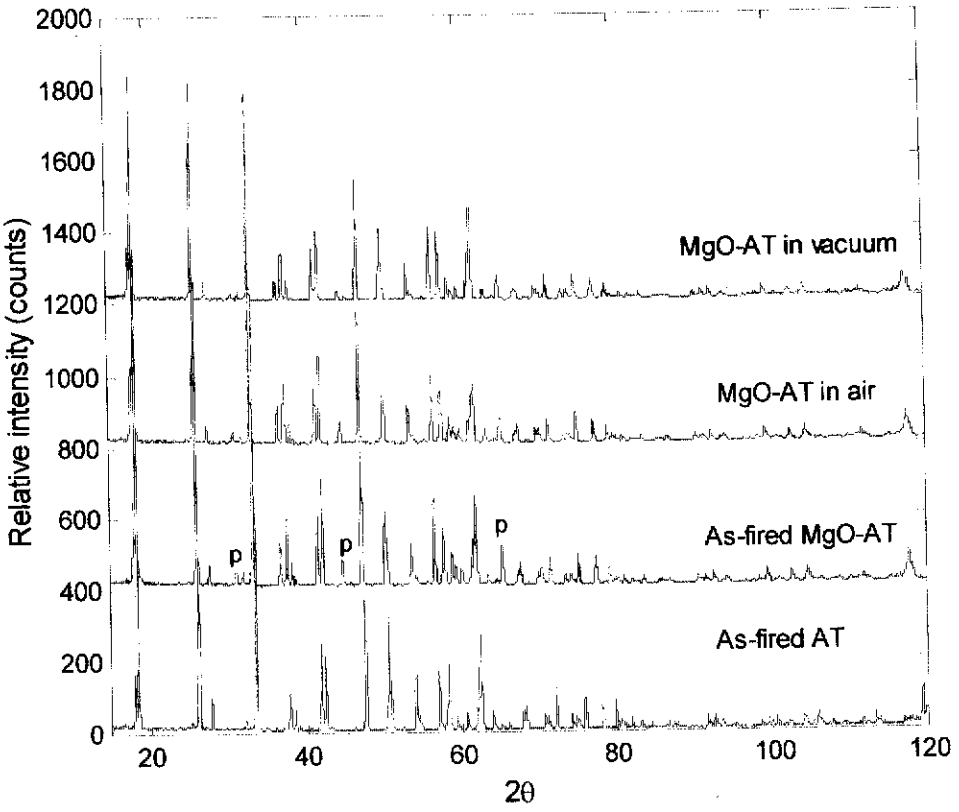

Figure 4.21. XRD patterns for pure AT and MgO-stabilised AT following decomposition in air and vacuum at 1100°C for 5 h. Legend: p = spinel. Wavelength = 1.5418 Å.

The Rietveld method was used to calculate the relative phase abundances of phases formed. The model used for spinel was that of Sawada (1995). The presence of spinel in the samples is evident. When MgO was added to AT powder and then sintered at 1600°C for 10 h, AT formed together with spinel. Buscaglia *et al.* (1996) reported that $MgAl_2O_4$ can affect the mechanism of AT formation by providing active nuclei for growth of new phase. Table 4.5 shows the relative phase abundances of AT and spinel after Rietveld analysis.

Table 4.5. Relative phase abundances for MgO-stabilised AT before and after decomposition.

Condition	Relative weight percentage, %	
	AT	Spinel
As-Sintered 1600°C, 10 h	92.1(1.0)*	7.9(0.2)
Decomposed in air at 1100 °C for 5 h	91.9(1.0)	8.1(0.3)
Decomposed in vacuum at 1100°C for 5 h	95.2(1.0)	4.8(0.2)

*Number in the parentheses indicates the estimated standard deviation (σ).

Table 4.5 shows that the weight percentage of AT and $MgAl_2O_4$ after sintering to 1600°C for 10 h was ~92 and 8% respectively. When the sample was decomposed in air, the weight percentages of AT and $MgAl_2O_4$ remained virtually unchanged. But when sample was decomposed in vacuum, the weight percentage of AT increased to 95% and $MgAl_2O_4$ decreased to 4.9%. It is of interest that decomposition in vacuum can decrease the weight percentage of spinel and increase the AT phase concentration. There was no indication of any apparent decomposition of AT both in air and vacuum indicating that the presence of MgO in AT hinders decomposition process that commonly occurs in pure AT. Thus, MgO can act as AT stabiliser (Takayuki and Tsuneo 1995).

4.5 SUMMARY

The density and shrinkage of pure AT were considerably lower than the corresponding value for MgO-AT indicating that MgO can enhance the densification process of AT probably through liquid-phase sintering.

The formation temperature of pure AT sample was found to depend on the heating rate. By assuming bulk crystallisation (*ie.* m of 3), the activation energy of AT was calculated as 495 kJ/mol. The activation energy of AT depends on the preparation method and purity (Table 2.7 in Chapter 2).

The Rietveld refinement method has been used to examine and characterise the thermal decomposition of AT-based ceramics. X-ray and neutron data were used to collect the diffraction data.

Both XRD and ND were used to study the isothermal decomposition of pure-AT and MgO-AT in both air and vacuum at 1100°C for 5 h. The ND study showed that decomposition of AT to alumina and rutile commenced during the first 2 h. The decomposition process was time-dependent.

Depth-profiling studies using XRD showed that decomposition of AT in air was uniform through the bulk. In contrast, the decomposition was not uniform in vacuum but surface-initiated which resulted in the formation of a graded surface layer rich in alumina. This phenomenon offers a novel approach for designing layered and graded AT with a layer rich in alumina to impart strength and wear resistance.

The addition of 10 wt% MgO to AT resulted in considerably better densification and thermal stability in both air and vacuum.

CHAPTER FIVE

SYNTHESIS AND CHARACTERISATION OF ALUMINA-ALUMINIUM TITANATE COMPOSITES

5.1 INTRODUCTION

Alumina and aluminum titanate (AT) have markedly different properties. Alumina has high strength and hardness, and excellent resistance to oxidation and chemical corrosion. In contrast, AT has high temperature and low thermal expansion materials (Kato, Daimon and Takahashi 1980; Dworak and Fingerle 1987). In principle, combining these two materials should lead to ceramics which have the advantages of both materials.

Alumina-AT (AAT) composites may be formed by reaction-sintering between TiO_2 (rutile) with an excess of α-Al_2O_3:

$$\alpha\text{-}Al_2O_3\,(\text{excess}) + TiO_2 \rightarrow \alpha\text{-}Al_2O_3 + \beta\text{-}Al_2TiO_5 \qquad (5.1)$$

Several authors prepared AAT composites using different processing routes (Wohlfromm *et al.* 1990; Low, Skala and Zhou 1996; Gutierrez-Alejandre *et al.* 1998). With plasma-sprayed alumina-titania composites, the hardness of AAT containing 3, 13 and 40 wt% of aluminium titanate (AT) is 5.2, 4.2 and 2.9 GPa, respectively (Ajit-Prasad, Mayuram and Krishnamurthy 1999). Low (1998) prepared layered and graded AAT using partial infiltration of a porous alumina preform with titanium ethoxide. The AT content and hardness decreased with an increase of depth. Commonly, the hardness of AAT increases with a decrease of AT content.

Furthermore, Padture, Bennison and Chan (1993) reported that the flaw-tolerance of AAT with either duplex or duplex-bimodal microstructure increased with the addition of 20-30 wt% AT. For both duplex-bimodal and duplex composites, *in-situ* SEM observation of crack growth provides direct evidence for grain-localised bridging in the crack wake. The fracture toughness of alumina may increase by incorporating with AT. In AAT containing ~5 vol% AT, the fracture toughness of the composite is 5 $MPa.m^{1/2}$ (Bartolome *et al.* 1995). This is higher than fracture toughness of alumina which ranges 2.7-4.2 $MPa.m^{1/2}$ (Schneider 1994).

In this study, AAT composites were prepared with 0-45 wt% AT. The effects of AT addition on the physical and mechanical properties were characterised by differential thermal analysis (DTA), dilatometry, x-ray diffraction (XRD), high-temperature neutron diffraction (HTND) for kinetics of reaction for the phase development in the AAT and Vickers indentation. Quantitative phase compositions of AAT composites were analysed using Rietveld refinement method.

5.2 RESULTS AND DISCUSSION

5.2.1 Porosity, Shrinkage and Bulk Density

The samples were prepared by reaction-sintering rutile and an excess of alumina (section 3.2.2) to achieve AAT composites with 0-45 wt% AT. The measurement of porosity, density and shrinkage of sintered samples was conducted using Archimedes principle (Australian Standard 1989). The results of these measurements for the compositions AAT0, AAT8, AAT15, AAT30 and AAT45 are shown in Figures 5.1, 5.2 and 5.3.

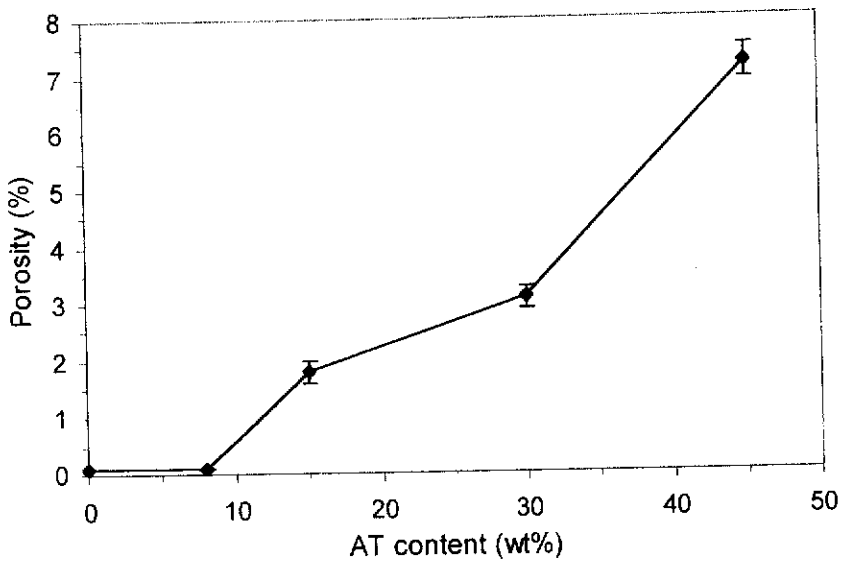

Figure 5.1. Porosity as a function of AT content for AAT0, AAT8, AAT15, AAT30 and AAT45 samples. Error bars indicate two estimated standard deviations (2σ).

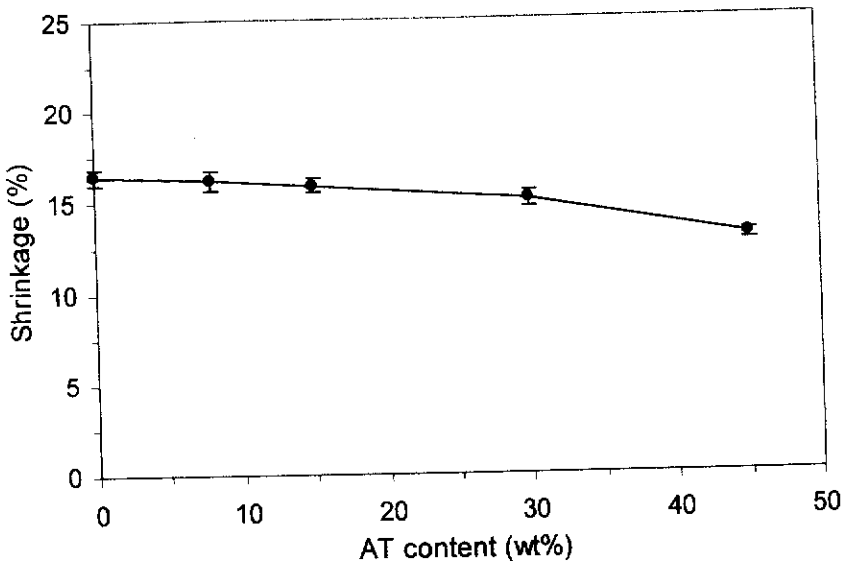

Figure 5.2. Shrinkage as a function of AT content for AAT0, AAT8, AAT15, AAT30 and AAT45. Error bars indicate two estimated standard deviations (2σ).

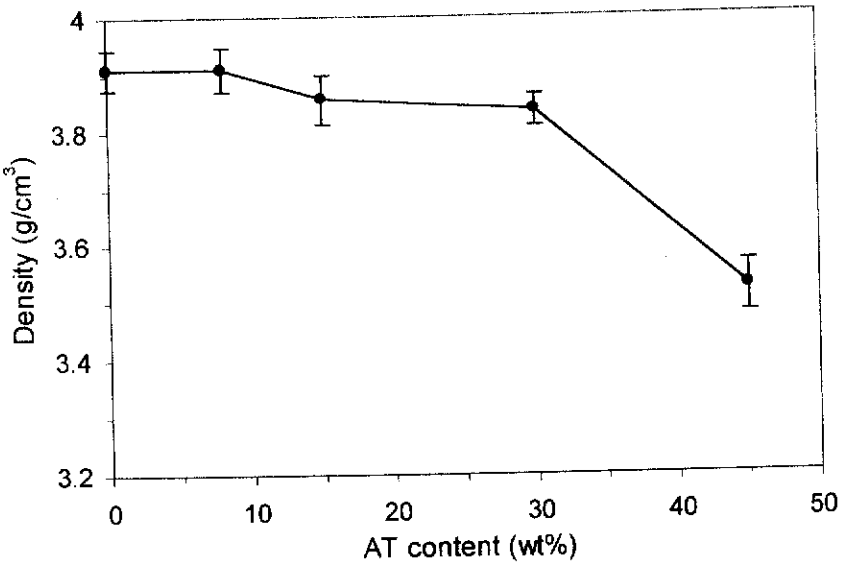

Figure 5.3. Density as a function of AT content for AAT0, AAT8, AAT15, AAT30 and AAT45. Error bars indicate two estimated standard deviations (2σ).

The results show that the radial shrinkage (Figure 5.2) of samples decreased with AT content increased. The maximum radial shrinkage was 16.4 % for pure alumina, suggesting that the lower the alumina content in AAT composites the

smaller the radial shrinkage. This means that the presence of AT resulted in lower shrinkage due to volumetric expansion associated with its formation at ~1300°C.

One of the problems of ceramists in processing material is the difference of density between theoretical and experimental results. The density of theoretical value is usually larger than the experimental value. Use of longer sintering time and finer powders would increase the experimental density (Rahaman 1995). The bulk density of sintered AAT samples is lower when the AT content increases (Figure 5.3). This can be attributed to (a) the presence of lower density AT (3.700 g/cm^3) and (b) an increase in the porosity (Figure 5.1) of the sample. If the content of AT increases, then the compound density of the sample will decrease.

The lowest apparent porosity was found for pure alumina indicating high densification. As the content of AT increased, so was the value of porosity within the sample. Porosity usually arises from poor densification which in turn leads to the lowering of the true density of sample. In essence, shrinkage, bulk density and apparent porosity are inter-related to each other.

5.2.2 Thermal Expansion Behaviour

As explained in section 2.4.2, the AAT offers the prospect of high temperature and thermal shock resistance. Therefore, it is important to understand the thermal expansion behaviour of AAT. In this study, the AAT (30 wt% AT) sample was examined because of its optimum microstructure and mechanical properties (Padture, Bennison and Chan (1993). The linear coefficient of thermal expansion, $\alpha = \frac{1}{L}\cdot\frac{dL}{dT}$, may be approximated by the cumulative expansion coefficient,

$$\alpha = \frac{1}{L_O}\left(\frac{L_T - L_O}{T - T_O}\right) \qquad (5.2)$$

assuming that α is independent of temperature. Here L is the lattice parameter; T is the temperature, and the subscript, o, denotes the reference temperature. From equation (5.2), and the data of Morrosin and Lynch (1972), the calculated thermal expansion coefficients of AT in the temperature range 20-600°C are 9.62 x 10^{-6},

18.47 x 10^{-6}, and -3.89 x 10^{-6}/°C for *a*, *b*, and *c*-axis, respectively. The corresponding volume coefficient of thermal expansion is 24.3 × 10^{-6}/°C.

The lattice parameters of AT at room temperature are a = 9.429, b = 9.636 and c = 3.591 Å (Morosin and Lynch (1972). At 600°C, these parameters are a = 9.481, b = 9.738 and c = 3.583 Å, with the a and b axes increasing but the c axis decreasing. The thermal expansion of AT is therefore anisotropic. The cell volume at room temperature is 326.3 $Å^3$ and 330.8 $Å^3$ at 600°C.

Dilatometry data were collected from 20 to 1500°C (section 3.4.2). Sapphire was used as a standard. Data were recorded for the thermal expansions of the sapphire and test sample to determine the mean thermal expansion per °C. The alumina sample AAT0 (0 wt% AT) was chosen as control to provide a comparison of the thermal expansion and densification behaviour with the AAT30 sample. Figure 5.4 shows the *in-situ* thermal expansion and contraction results.

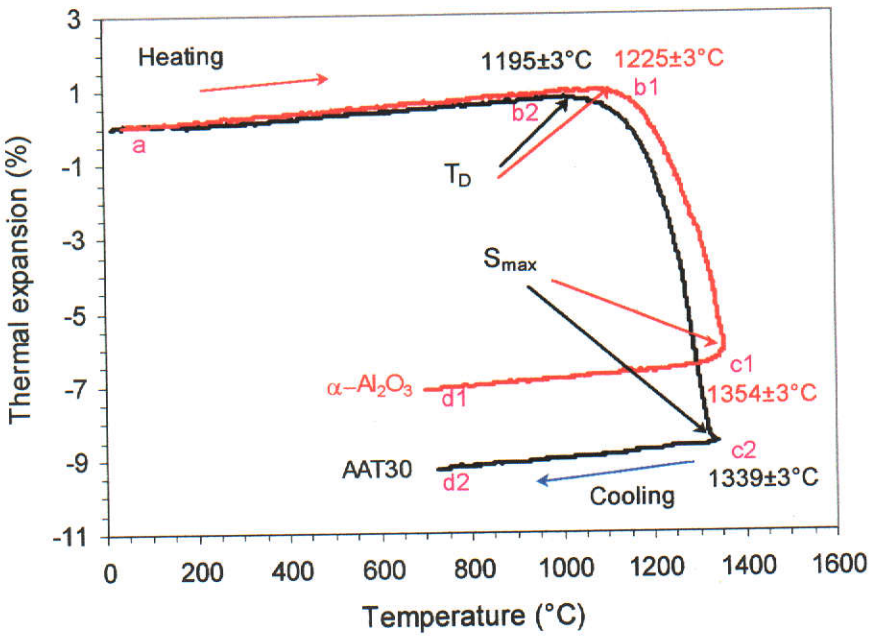

Figure 5.4. Dilatometry data showing the thermal expansion and contraction behaviour of sample AAT30 as compared with sample AAT0. T_D and S_{max} denote the densification temperature and maximum shrinkage, respectively.

The initial stage of each dilatometry trace (a → b1 for α-Al_2O_3 and a → b2 for AAT30) shows the expected thermal expansion prior to sintering which initiates densification. It is interesting to note that α-Al_2O_3 commenced densifying at ~1225°C, but the onset of densification for AAT30 occurred at a significantly lower temperature *viz.* 1195°C. Therefore, the presence of AT lowered the initial sintering temperature by ~30°C. This can be attributed to liquid-phase sintering in AAT30.

The densification-related shrinkage of the AAT30 composite continued until ~1339°C which is marginally lower than the corresponding temperature for α-Al_2O_3, 1354°C. The shrinkage of sample AAT30 at the maximum temperature 1339°C was 9.4% compared with 6.9% for sample AAT0. Therefore the presence of AT enhanced sintering and densification. Note that the radial shrinkage of the sintered sample at 1600°C was 15.1% (Figure 5.2) compared with 16.4% for α-Al_2O_3. The difference is probably due to the difference in sintering temperature. The values of thermal expansion coefficient for AAT30 and control samples are shown in Table 5.1. The AAT30 sample has a lower thermal expansion coefficient than α-Al_2O_3 thus indicating that the presence of 30 wt% AT can improve its thermal shock resistance.

Table 5.1. Average thermal expansion coefficient for AAT30 composite produced by *in-situ* reaction sintering, compared with the alumina control sample, for the range 20–1000°C.

Sample	Average thermal expansion coefficient ($\times 10^{-6}$/°C)
Control	9.0
AAT30	7.6

5.3 ANALYSIS OF PHASE DEVELOPMENT

5.3.1 DTA Study

Data were collected over the temperature range of 20-1500°C at heating rates of 5, 10, 15 and 20°C/min using empty alumina crucible as reference. The atmosphere was air and the flow rate was 60 cm^3/min. Figure 5.5 shows the plots for sample AAT30 for a range of heating rates.

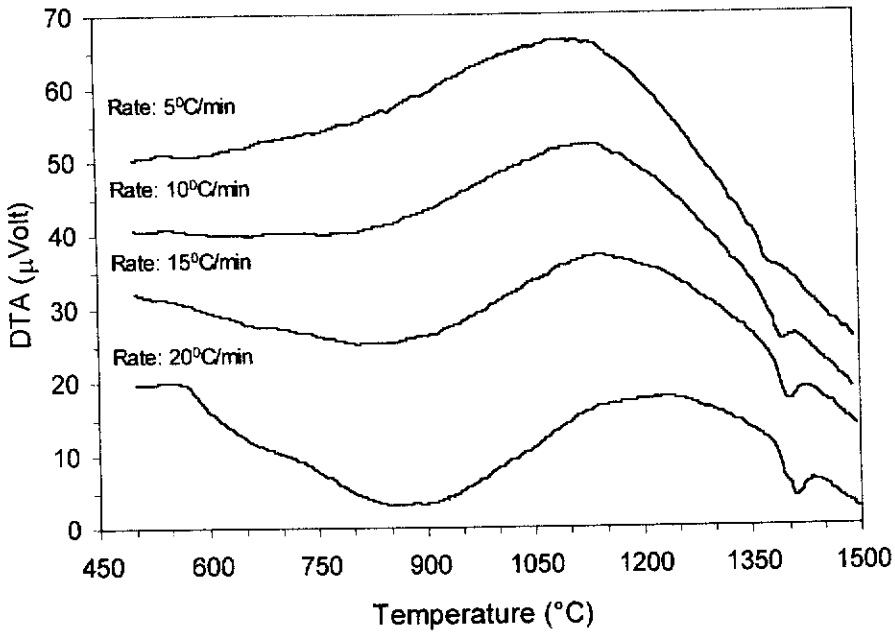

Figure 5.5. DTA analysis of sample AAT30 at different heating rates.

The results show that the formation temperature of AT varies significantly with heating rate. A similar effect was reported by Wendlandt (1964) for clay materials. The excess of alumina in AAT30 raised the endothermic peak with heating rate when compared with pure AT (section 4.2.1) as shown in Figure 5.6. This indicates that the presence of alumina constraints the crystallisation of AT by raising the activation energy.

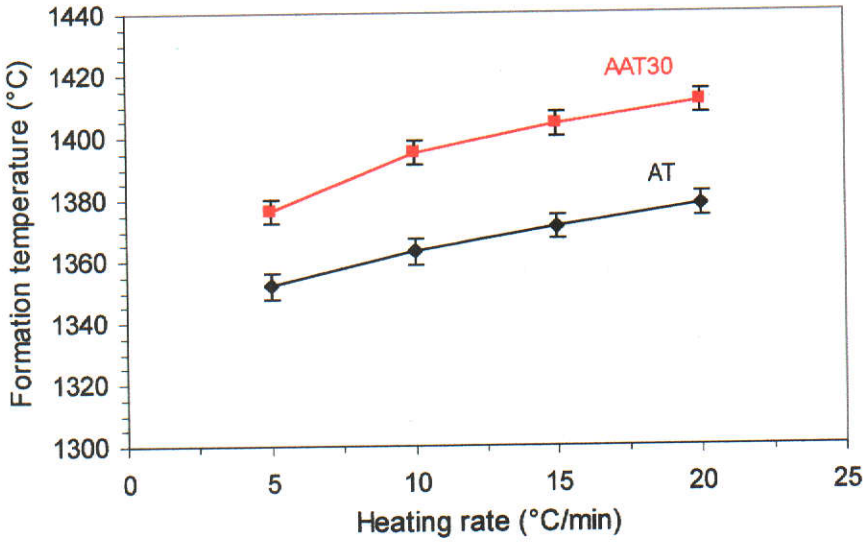

Figure 5.6. The formation temperature of AT in sample AAT30 compared with that for pure AT, for different heating rates. The error bars were based on the accuracy of the temperature.

The formation temperature of AT for sample AAT30 as shown in Figure 5.6 ranged from 1376±4 to 1411±4°C depending on heating rate. In general, the peak temperature shifts to lower temperature with a decrease in heating rate and the peak shape becomes broader due to an increase in the crystal growth dimension. It is also found that an increase in heating rate increases the peak temperature, and often increases peak area to a small extent.

From the DTA data, it is possible to calculate the activation energy for AT formation. The method of Bansal *et al.* (1983) was employed in this study for calculating the activation energy of AT as explained in section 4.2.1. By using equation (4.2) and the data from Figure 5.6, the AT activation energy for sample AAT30 was calculated as shown in Table 5.2.

Table 5.2. The activation energy for AT formation for sample AAT30 and pure AT.

Wt% AT	Preparation Method	Activation Energy (kJ/mol)
30	Solid-state reaction: Excess Al_2O_3 + TiO_2	295(2)*
100	Stoichiometric: α-Al_2O_3 + TiO_2	389(2)

*The number in the parenthesis is mean deviation based on the best-fit data and model.

The higher value obtained for this study may be attributed to the presence of alumina which acted as a constraint to the crystallization of AT. In the absence of matrix constraints, as in pure AT, lower values of activation energy may be result.

Hennicke and Lingerberg (1986) observed that the formation temperature of AT occurred in two stages. Phase nucleation was found to occur within the range 1230 and 1280°C, and grain growth above 1280°C. Beyond 1280°C, formation of AT occurs in an oxidizing atmosphere (Kato, Daimon and Takahashi 1980). Buscaglia *et al.* (1996) reported that in the range 1280–1400°C, the chemical driving force is too small in comparison with the strain energy associated with bulk nucleation of the new phase. As a consequence, titania formation can start only at a limited number of 'easy-to-nucleate' sites with growth of quite large Al_2TiO_5 crystals.

5.3.2 *In-situ* Neutron Diffraction (ND) Measurement of Phase Development

High temperature neutron diffraction analysis was conducted with AAT30 to monitor the *in-situ* phase developments (section 3.3.3). Phase identification analysis with PDF files 43-1848 for α-Al_2O_3, 41-0258 for Al_2TiO_5 and 21-1276 for TiO_2 (rutile) accounted for all peaks of every pattern. Rietveld analysis was subsequently employed to calculate the relative phase abundance of the phases present. Because the average temperature formation of AT is ~1375°C (Figure 4.2), the study of phase development was monitored at 1200, 1290, 1310, 1330, 1350, 1370 and 1390°C. Figure 5.7 shows the measured ND patterns.

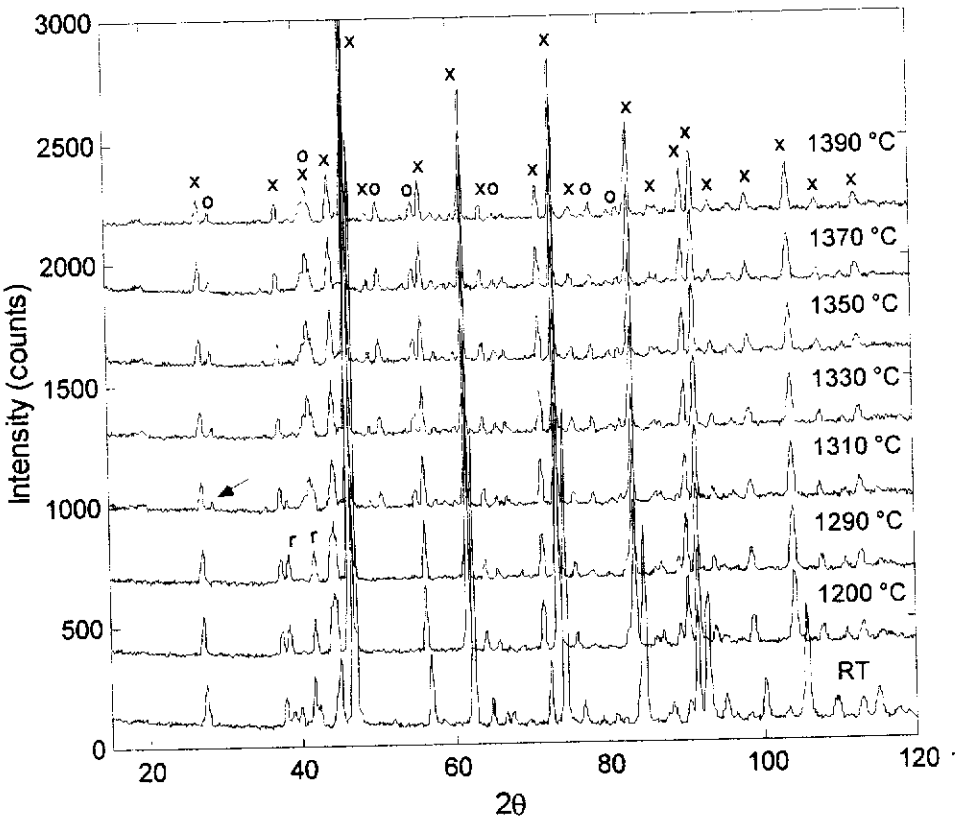

Figure 5.7. High-temperature ND patterns for sample AAT30. The holding time at each temperature was 2 h to increase the counting statistics. The arrow indicates the start of AT formation. Legend: x = alumina, o = AT, r = rutile, RT = room temperature. Wavelength = 1.666 Å.

From room temperature (RT) to 1200°C, the diffraction peaks shifted to lower Bragg angles due to thermal expansion. After Rietveld refinement, the thermal expansion coefficients of alumina and rutile along *a* axis from RT to 1200°C were $(8.61\pm0.02) \times 10^{-6}$/°C and $(5.82\pm0.07) \times 10^{-6}$/°C, respectively. These values agree reasonably well with the values 8.3 and 6.8×10^{-6}/°C, respectively reported by Kingery, Bowen and Uhlmann (1976).

At 1290°C, there were only two phases in the sample *ie.* α-alumina and rutile. At 1310°C, AT commenced to form even though the rutile had not reacted completely. The peaks due to AT formation intensified with increase in temperature. In contrast, rutile co-existed with AT at 1310°C but had eventually disappeared by

1390°C. Therefore, the reaction between rutile and alumina to form AT occurred at 1290-1310°C.

The relative phase abundances for each of the diffraction patterns were performed by the Rietveld method (section 3.3.6). The crystal structure models used were ICSD # 73725 for alumina, 27681 for AT and 63710 for rutile taken from the Inorganic Crystal Structure Data Base (Fach Informations Zentrum and Gmelin Institut, Germany). The Rietveld parameters refined were background and 2θ-zero, scale factors, peak profile parameters including mixing parameters, lattice parameters, preferred orientation, asymmetry factor and thermal parameters. Figure 5.8 shows a typical Rietveld plot for sample AAT30 at 1310°C. The phases formed and their abundances from 1200 to 1390°C are presentedin Figure 5.9.

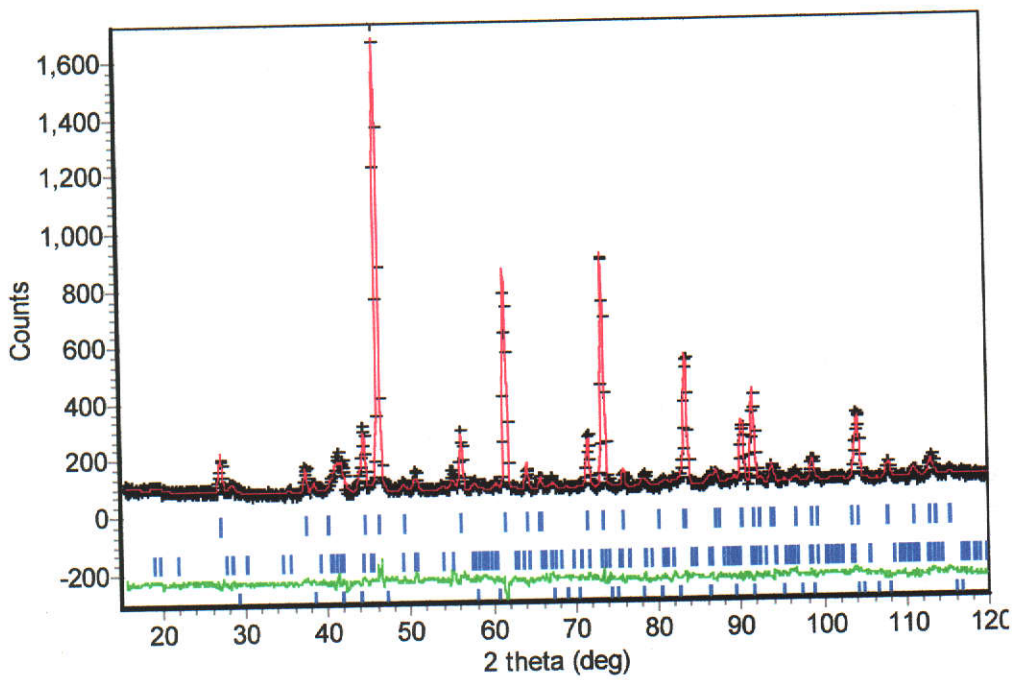

Figure 5.8. Neutron diffraction profile plots for the AAT30 sample measured at 1310°C. The measured and calculated patterns are indicated by crosses (black) and solid line (red) respectively. The difference plot for the measured and calculated patterns is shown in green. Vertical bars (blue) represent the Bragg peak positions for each of the phases (from top to bottom: alumina, AT and rutile). Wavelength = 1.666 Å.

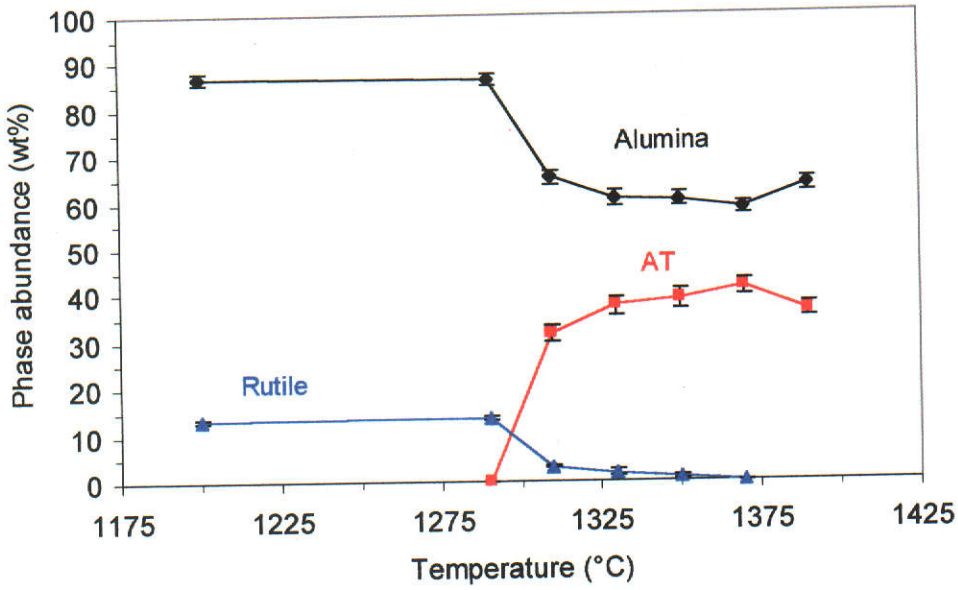

Figure 5.9. Relative phase abundance levels (wt%) for sample AAT30 from 1200 to 1390°C. Error bars indicate two estimated standard deviations (2σ).

Above 1200°C, the concentrations of both alumina and rutile decrease with an increase of temperature. AT appears at 1310°C and increases in concentration with increase of temperature. At 1370°C, rutile reacted completely with alumina to form AT. Figure 5.9 shows that the growth of AT is temperature-dependent. It is worth noting that AT forms and grows rapidly at a small temperature range of 1290-1310°C but after 1310°C the growth becomes more sluggish indicating that the formation of AT is not spontaneous but a diffusion-controlled process.

5.4 X-RAY DIFFRACTION

Room temperature XRD data were also used to examine the phase compositions of sintered AAT samples with different AT content. The preparation of samples is described in section 3.2.2. A search and match procedure using the PDF files numbers 43-1848 for α-Al_2O_3, 41-0258 for Al_2TiO_5, and 21-1276 for TiO_2 was employed to identify the individual peaks in each pattern prior to Rietveld analysis.

The models used for analysing each pattern are from Maslen *et al.* (1993) for alumina, Epicier *et al.* (1991) for AT and Howard, Sabine and Dickson (1980) for rutile as described in section 3.3.6. The measured XRD patterns are shown in Figure 5.10. Data for pure alumina are also presented for comparison.

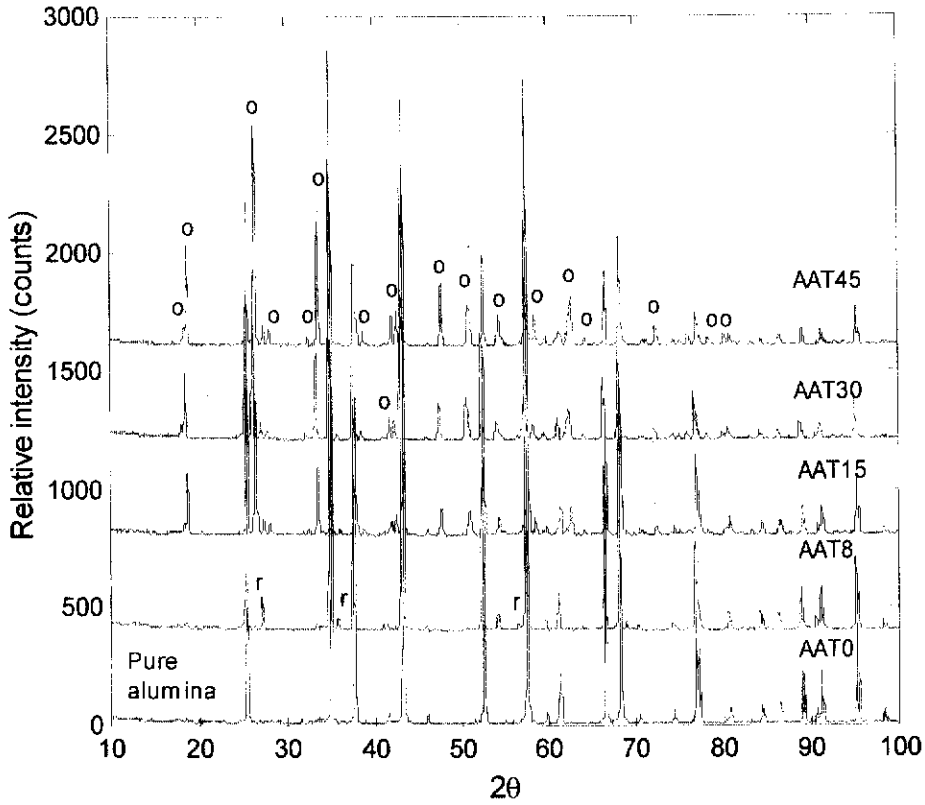

Figure 5.10. XRD plots for as-sintered AAT samples containing 0 – 45 wt% AT. Legend: o = AT, r = rutile with the remaining peaks being alumina. Wavelength = 1.5418 Å.

Search/match analysis were used to identify the peaks in the patterns. The AT peaks for 2θ angles 18.04, 18.45 and 28.22° are obvious. These peaks increased from sample AAT8 to sample AAT45 due to the presence of more AT.

Figure 5.11 shows a typical difference plot of sample AAT45 after Rietveld refinement. The small goodness-of-fit index (*ie.* 1.7) obtained for the refinement is acceptable as it should be in the range 1 - 4 for phase analysis (Kisi 1994).

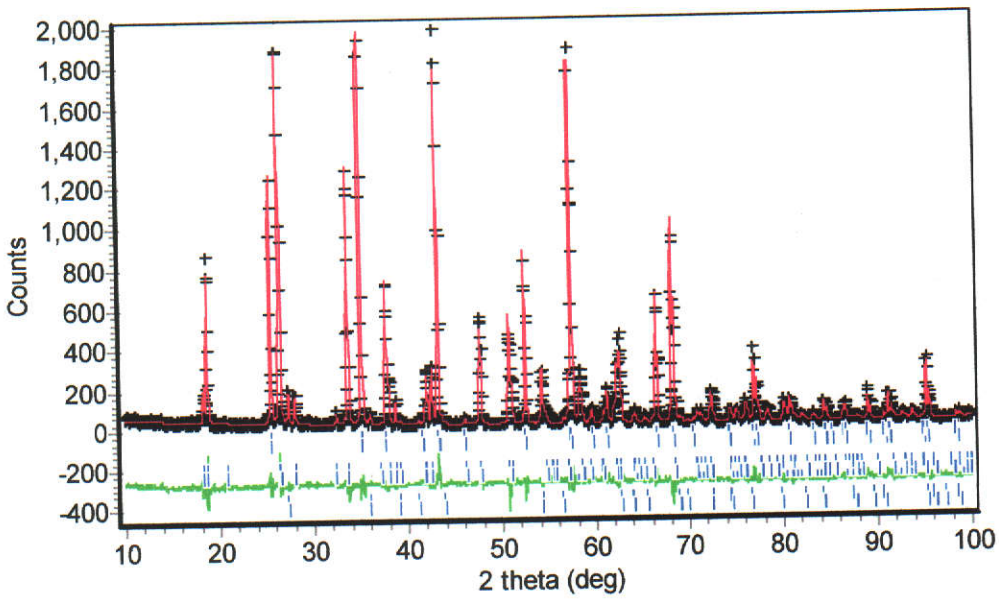

Figure 5.11. XRD profile plot for sample AAT45. Measured and calculated patterns are indicated by crosses (black) and solid line (red) respectively. Intensity differences between the two patterns are shown along the bottom of the plot (green). Vertical bars (blue) represent the allowable peak positions for each of the phases (from top to bottom: alumina, AT, and rutile).

The analysis of relative phase abundance in each sample was calculated using *Rietica* (Hunter 1997). The crystalline phase concentrations were normalised to 100%. The results are shown in the Figure 5.12.

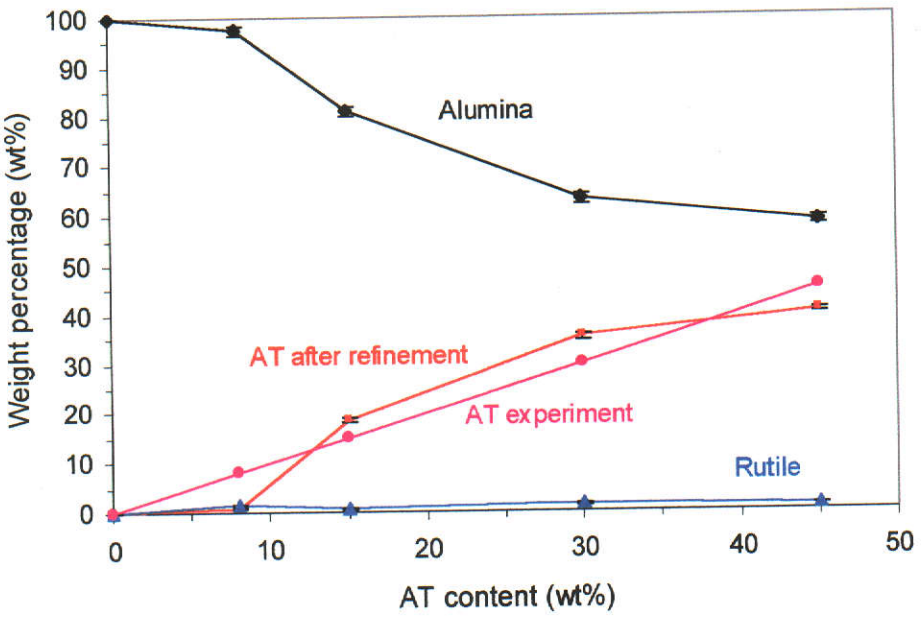

Figure 5.12. Relative weight percentage (wt%) of phases for the AAT samples after Rietveld analysis with XRD data. Error bars indicate two estimated standard deviations (2σ).

Figure 5.12 indicates that the weight percentage of AT in samples AAT15, AAT30 and AAT45 is close to the experimental values. The difference is probably due to the well-known underestimation of uncertainties in Rietveld analysis. It is interesting to note that there is ~1 wt% rutile in every sample except for sample AAT15 indicating that complete reaction was not achieved in those samples. This may be caused by the use of insufficient temperature or sintering time. In addition, decomposition of AT may have occurred during furnace cooling from 1600°C to room temperature. As previously mentioned, below 1280°C, AT tends to decompose into the parent oxides α-Al_2O_3 and TiO_2 (Martinez *et al.* 2001).

5.5 MECHANICAL PROPERTIES

It is well known that microstructure strong influences the mechanical performance of alumina-based ceramics. An *et al.* (1996) added calcium carbonate to form calcium-hexaluminate ($CaAl_{12}O_{19}$) platelets for self-strengthening and toughening of alumina. Braun, Bennison and Lawn (1992) dispersed 20-30wt% AT particles in alumina and obtained considerable improvement in flaw-tolerance, and Padture, Bennison and Chan (1993) also reported that addition of AT to alumina results in an improvement in flaw tolerance of the duplex alumina-AT composites over single-phase aluminas, based on the observation of a strong T-curve.

The indentation half-diagonal lengths and the radial-crack lengths were measured directly using a Zwick microhardness tester (section 3.4.6). Values of hardness and fracture toughness were calculated using the equations of Evans and Charles (1976). Figures 5.13 and 5.14 show the hardness and fracture toughness results, respectively.

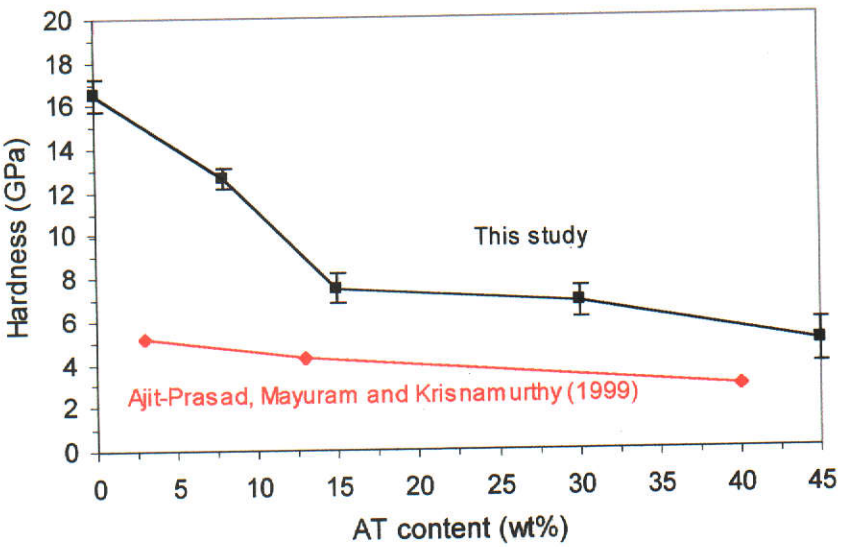

Figure 5.13. Hardness of AAT samples as a function of AT content compared to Ajit-Prasad, Mayuram and Krishnamurthy (1999). The load used was 10 kg. Error bars indicate two mean deviations (±).

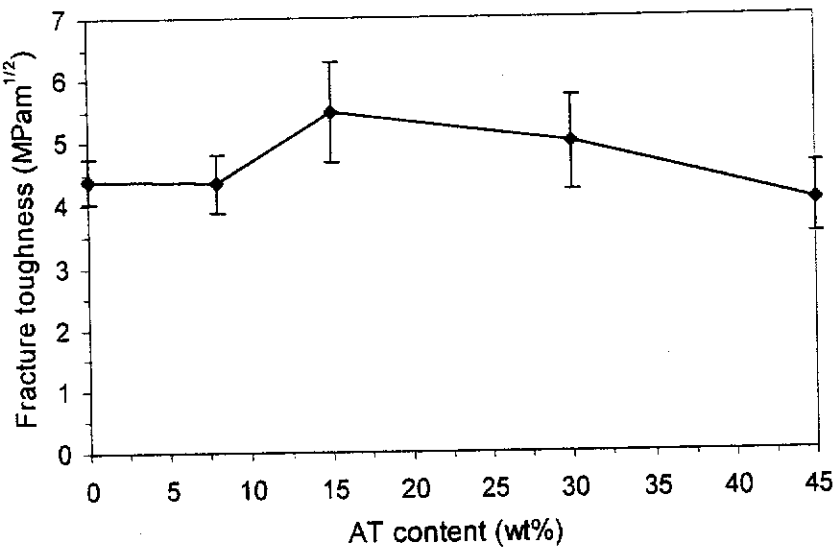

Figure 5.14. Fracture toughness of AAT samples as a function of AT content. The load used was 10 kg. Error bars indicate two mean deviations (±).

From Figure 5.13, the hardness of AAT decreases with increase in AT content. This trend is consistent with that found by Ajit-Prasad, Mayuram and Krishnamurthy (1999) who reported that the hardness AAT containing aluminium titanate (AT) concentrations of 3, 13 and 40 wt% is 5.2, 4.2 and 2.9 GPa, respectively. Figure 5.13 shows that the hardness values from this study substantially higher than those of Ajit-Prasad, Mayuram and Krishnamurthy (1999) probably due to starting material and preparation method.

The fracture toughness values for samples AAT15 and AAT30 are higher than that of the control (Figure 5.14) indicating that the presence of AT can increase the fracture toughness of AAT composites. This agrees well with the work of Padture, Bennison and Chan (1993) where 20-30 vol% AT provided much improved flaw-tolerance due crack-bridging which is attributed to the large thermal expansion mismatch between alumina and AT. In AAT containing ~5 vol% AT, the fracture toughness of the composite is 5 MPa.m$^{1/2}$ (Bartolome *et al.* 1995). This is higher than fracture toughness of alumina quoted by Schneider (1994) which ranges 2.7-4.2 MPa.m$^{1/2}$. Furthermore, the fracture toughness of AAT with AT content of 3, 13 and 40 wt% reported by Ajit-Prasad, Mayuram and Krishnamurthy (1999) is 3.6, 4.0 and

4.9 MPa.m$^{1/2}$, respectively. Therefore the fracture toughness of AAT increases with the presence of AT.

Typical optical micrographs of the indentation sites are shown in Figure 5.15 for samples AAT0, AAT8, AAT15, AAT30 and AAT45. Cracking in AAT0 is very clear indicating that the sample is brittle. For sample AAT8, cracking is also clear and there is evidence of micro-damage around the indent due to grain-debonding and grain push-out. The hardness of sample AAT15 decreased rapidly due to the presence of AT content (*ie.* 15 wt%). The cracks formed in this sample are not easy to observe due to extensive degree of micro-damage in the vicinity of the indent which indicates high damage-tolerance. Sample AAT30 also shows no damage area formed indicating that sample is damage tolerant. Similar damage behaviour is observed for sample AAT45.

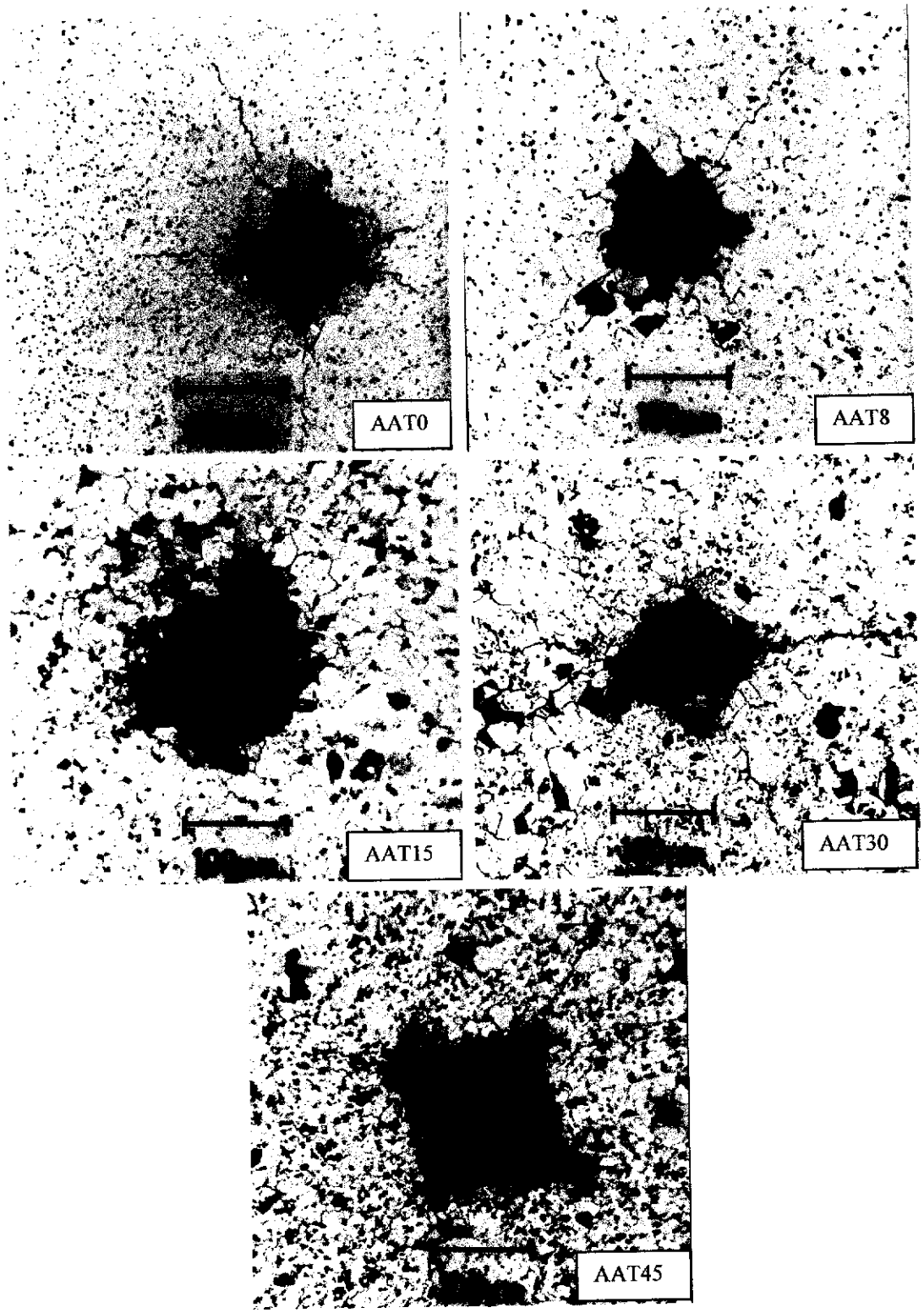

Figure 5.15. Optical micrographs of Vickers indentations for samples AAT0, AAT8, AAT15, AAT30 and AAT45.

5.6 MICROSTRUCTURE EVALUATION

Optical micrographs of the polished samples AAT0, AAT8, AAT15, AAT30, and AAT45 are shown in Figure 5.16. The white phase is AT and the grey phase is alumina. As expected, the abundance of AT increases from sample AAT0 to sample AAT45 due to the increase in AT. The black phase is porosity or grain pull-out from polishing.

It is very clear that the porosity increases with an increase of AT content due to mismatch between alumina and AT. This observation agrees with the porosity found by measurement (Figure 5.1).

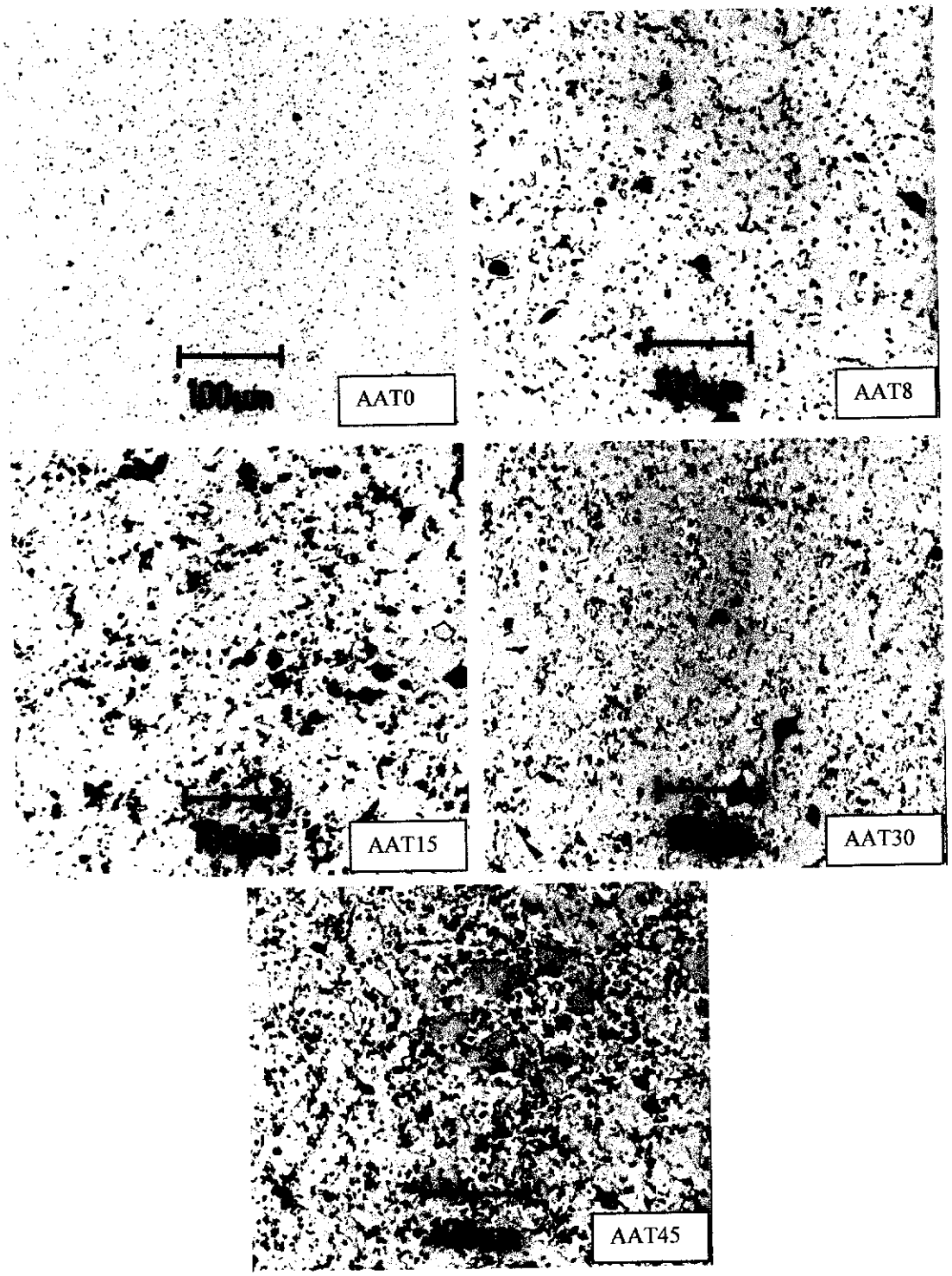

Figure 5.16. Optical micrographs of polished AAT samples. The grey phase is alumina, white phase is AT and the dark regions are either pores or grain pull-outs.

Figures 5.17 shows SEM micrographs for sample AAT8 and AAT30. The existence of microcracks due to the presence of AT is readily observed in AAT30. These microcracks are formed probably as a result of strong thermal expansion anisotropy associated with AT.

The grain size of alumina for small AT content (AAT8) is relatively large whereas for large AT content (AAT30) it is relatively small. The presence of more AT in AAT samples not only reduces the alumina grain-size but also increases the porosity as shown in sample AAT30 (Figure 5.17). This agrees with the porosity results obtained by Archimedes measurement for sample AAT30, ie. ~3% (see Figure 5.1).

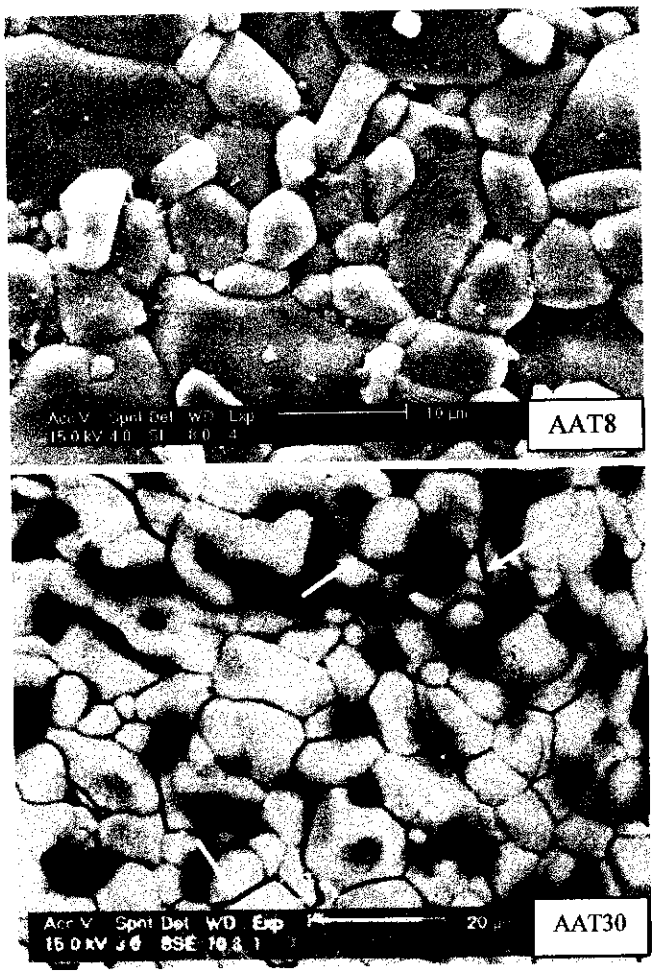

Figure 5.17. SEM images showing the microstructures of samples AAT8 and AAT30. The presence of microcracks (marked with arrows) is evident within certain AT grains. The dark regions represent porosity or grain pull-out from polishing.

5.7 SUMMARY

The synthesis of alumina/aluminium titanate (AAT) composites containing 0-45 wt% AT through reaction sintering of alumina and rutile has been examined. The presence of AT in the alumina matrix significantly effects the physical properties. Both radial shrinkage and bulk density decreased with an increase in AT content whereas the porosity increased.

The formation temperature of AT in AAT30 samples measured by DTA is heating-rate dependent, varying between 1376-1411°C. The activation energy of AT in AAT30 was 295 kJ/mol which was lower than pure AT (389 kJ/mol).

The thermal expansion and densification behaviour of alumina and AAT30 were quite different. Sample AAT30 commenced to densify at a lower temperature than that of the control alumina sample, thus indicating that the presence of AT may serve to enhance the kinetics of densification. The average thermal expansion coefficient of sample AAT30 in the range 20–1000°C was lower than the control due to the presence of AT. A similar lowering of thermal expansion was also observed by Morishima *et al.* (1986) and Parker (1990).

The *in-situ* phase formation in sample AAT30 was monitored using high-temperature ND. Rutile and alumina reacted to form AT at ~1310°C. The phase level of AT increased with temperature indicating that the phase abundance of AT was temperature-dependent and diffusion-controlled. Room temperature XRD analysis showed a residual small concentration in the sintered samples which could be due to the decomposition of AT during cooling from 1600°C to room temperature.

Scanning electron micrographs of polished sample AAT30 revealed the presence of microcracks within AT grains and debondings between AT and alumina grains. These microcracks and debondings formed as the result of pronounced thermal expansion anisotropy associated with AT and the mismatch in thermal expansion between aluminium titanate and alumina. The microcracks are responsible for the high thermal shock resistance of this material (Hasselman 1969). The grain size of alumina decreased with an increase in AT content.

The hardness of the AAT ceramics decreased with AT content. Similarly, porosity also increased with AT content, thus indicating that the reduction in hardness was caused by an increase of porosity. Although the presence of AT caused the reduction of hardness, the fracture toughness of AAT30 improved relative to the

alumina control. The fracture toughness of AAT15 was superior to those others because the cracks were relative small in the site of indentation. Padture, Bennison and Chan (1993) reported that the flaw-tolerance of AT improved by adding 20-30 wt% due to crack bridging phenomenon.

Typical optical micrographs for the indentation sites showed a large degree of localised microcracking and damage zone. AAT15 is superior in fracture toughness compared to other compositions but not resistance-damage. The improved damage-tolerance behaviour was attributed to the combined influences of increased internal residual stresses due to the presence of AT in the alumina matrix (Padture, Bennison and Chan 1993). The damage zone decreased with AT content due to weak bonding between AT and alumina.

CHAPTER SIX

SYNTHESIS AND CHARACTERISATION OF β-SPODUMENE MODIFIED ALUMINA/ALUMINIUM TITANATE COMPOSITES

6.1 INTRODUCTION

Monoclinic α-spodumene ($Li_2O.Al_2O_3.4SiO_2$) is stable under ambient conditions and transforms irreversibly at 1080°C to a tetragonal β polymorph which melts at 1423°C. Spodumene has been widely used in the glass and ceramic industry for decades as a lithia-bearing flux and low-expansion filler in whiteware bodies. It is also commonly used for making glasses and ceramics, which are harder, smoother, chemical and thermal shock resistant. The mean thermal expansion coefficient of β-spodumene is 9×10^{-7}/°C in the temperature range 20-1000°C (McMillan 1964). Smoke (1951) and Hummel (1951) reported a negative thermal expansion coefficient for β-spodumene which may be due to anisotropy whereby the *c*-axis expands linearly whereas the *a*–axis contracts parabolically with an increase of temperature (Ostertag, Fischer and Williams 1968).

Spodumene has been used as a second phase for fabricating composites (see section 2.4.3). Recently, Low and Shi (2000) showed that by adding AT with spodumene and zirconia significantly reduces porosity, lower thermal expansion, improves densification, hardness and thermal stability, without degradation of thermal shock resistance.

This chapter describes the use of β-spodumene for liquid-phase-sintering of AAT composites. The composition examined in the study was the AAT30 system containing 0-15 wt% β-spodumene. AAT30 means alumina and aluminium titanate contents are 70 and 30 wt%, respectively. The physical characteristics and properties have been studied using room temperature x-ray diffraction (XRD), high temperature neutron diffraction (HTND), dilatometry, differential thermal analysis (DTA), scanning electron microscopy (SEM), transmission electron microscopy (TEM), optical microscopy and Vickers indentation. Rietveld refinement was used to quantify the relative abundance of phases present.

6.2 RESULTS AND DISCUSSION

6.2.1 Density, Shrinkage and Porosity

Densification measurements involved shrinkage, density and porosity. The measurements were conducted according to Archimedes principle (Australian standard 1989) as explained in section 3.4.1. The preparation of samples was described in section 3.2.3. Figures 6.1, 6.2 and 6.3 show the shrinkage, density and porosity results for samples sintered at 1600°C for 4 hours.

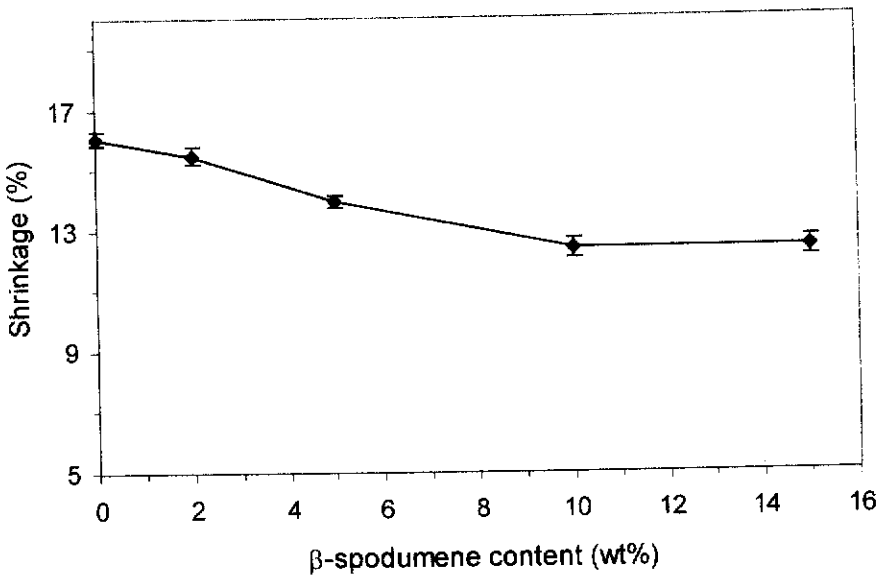

Figure 6.1. Variation of shrinkage as a function of β-spodumene content for samples AATS0, AATS2, AATS5, AATS10 and AATS15. Error bars indicate two estimated standard deviations (2σ).

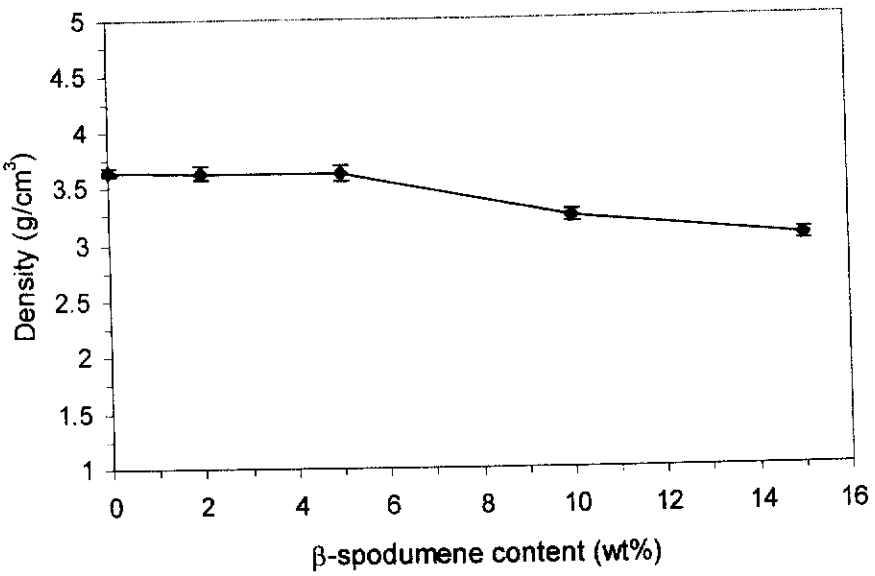

Figure 6.2. Variation of density as a function of β-spodumene content for samples AATS0, AATS2, AATS5, AATS10 and AATS15. Error bars indicate two estimated standard deviations (2σ).

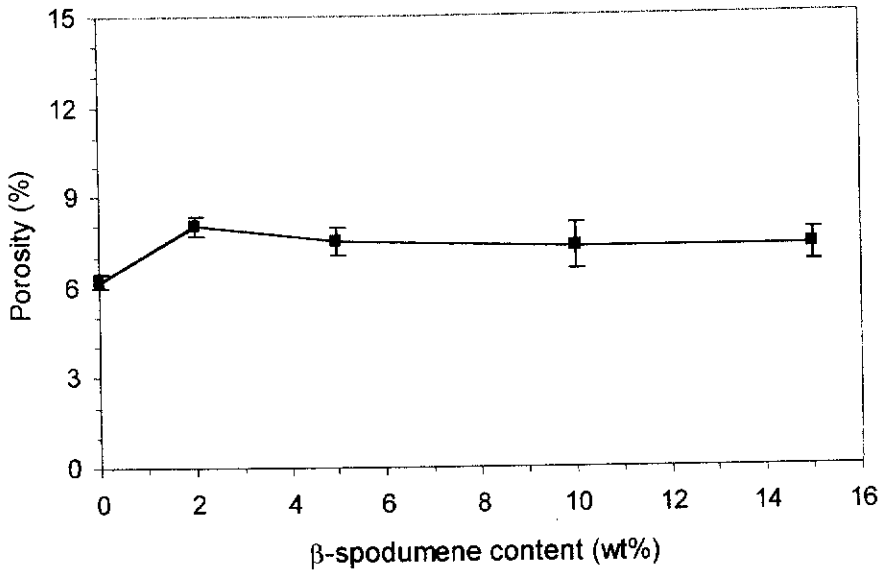

Figure 6.3. Variation of porosity as a function of β-spodumene content for samples AATS0, AATS2, AATS5, AATS10 and AATS15. Error bars indicate two estimated standard deviations (2σ).

In Figure 6.1, the shrinkage decreases with the increase of β-spodumene indicating that only a small amount β-spodumene (< 2 wt%) is needed for liquid-phase-sintering. Excess spodumene may have resulted in formation of glassy phase and recrystallisation of β-spodumene during cooling. Like the shrinkage results, density (Figure 6.2) also follows the same trend because spodumene has a lower density of 2.377 g/cm^3 (National Bureau Standard, US 1984) than alumina. The theoretically density of AATS0 is 3.8963 g/cm^3 since the density of alumina and AT are 3.987 (Swanson *et al.* 1953) and 3.700 g/cm^3 (Holcombe and Coffey 1973), respectively. The difference between theoretical and the experimental values is 6.4 %. The lowest porosity occurred in sample AATS0 (Figure 6.3) indicating that β-spodumene is not effective in the process of pore-filling during sintering. Most ceramics produced by solid-state sintering retain some residual porosity.

6.2.2 Differential Thermal Analysis (DTA)

The influence of β-spodumene on the endothermic reactions for samples AATS0, AATS2, AATS5, AATS10 and AATS15 is shown by the thermograms in Figure 6.4. The endothermic peaks for the melting of β-spodumene and the corresponding formation temperature of AT are depicted in Figure 6.5. It is interesting to note the presence of two endothermic peaks for samples containing ≥ 10 wt% spodumene, *ie.* for AATS10 and AATS15.

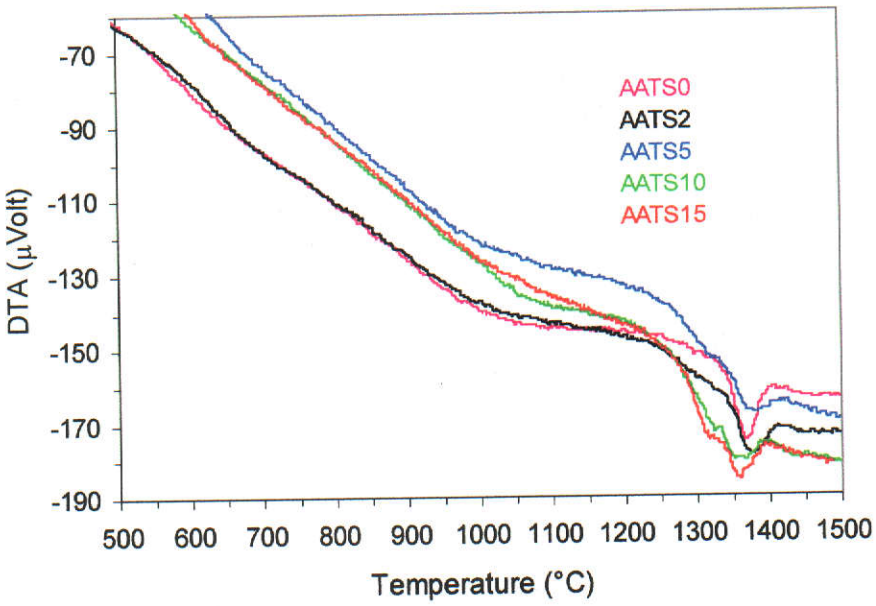

Figure 6.4. Thermograms for β-spodumene modified samples AATS0, AATS2, AATS5, AATS10 and AATS15.

Figure 6.4 shows the endotherms for samples AATS0, AATS2 and AATS5, with peak temperatures of 1368, 1374 and 1383, respectively. This endothermic reaction can be attributed to the formation of AT. It is noted that the presence of 2 and 5 wt% spodumene has raised the peak temperature but broadened the endotherm. Samples AATS10 and AATS15 each have two endothermic peaks at 1317 and 1358°C, and 1324 and 1366°C, respectively. In both samples, the first endotherm is attributed to the melting of β-spodumene while the second is due to the formation of AT. It is interesting to note here that the peak temperature for AT formation is strongly dependent on the content of spodumene. For spodumene content ≥ 10 wt%, the peak temperature is lowered and vice versa for content ≤ 5 wt%.

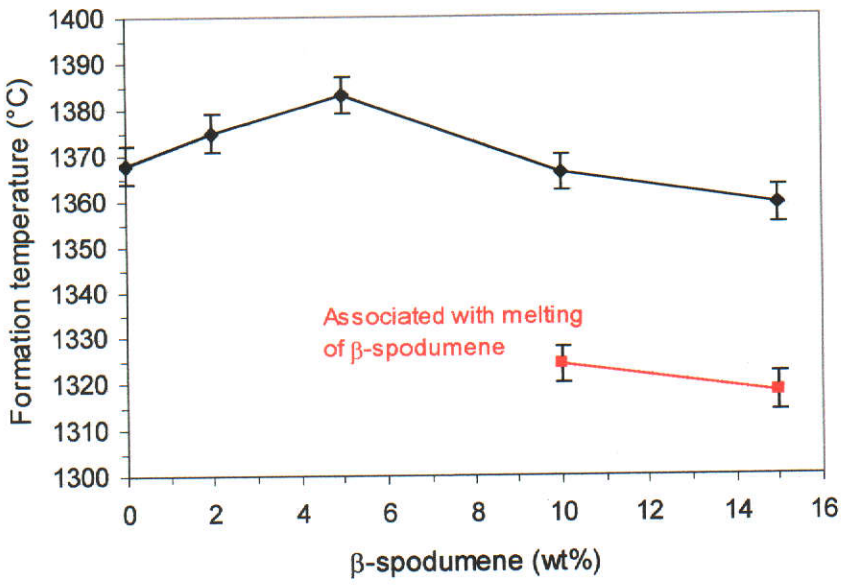

Figure 6.5. Formation temperature as a function of β-spodumene content for samples AATS0, AATS2, AATS5, AATS10 and AATS15. The red line is associated with the melting of β-spodumene. The error bars were based on the accuracy of the temperature.

The peak temperature associated with the formation of AT in all samples occurred in the range of 1358 and 1383°C, although the onset temperature remained fairly constant at ~1310°C. This agrees well with the work of Wohlfromm *et al.* (1992) who reported similar results from their SEM and EDS analyses. It is surprising to note that the endothermic temperature associated with the melting of β-spodumene is lower than that of AT and peaked in the range 1317-1324°C. The melting temperature of β-spodumene is well-known to occur at 1399°C (Knickerbocker, Tuzzolo and Lawhorne 1989). This result suggests that in the AATS samples β-spodumene formed a eutectic with AT, thus drastically lowering its melting point. The broad endotherm further suggests that melting of β-spodumene occurred gradually and probably commenced at temperatures well below 1300°C.

6.2.3 Dilatometry

Dilatometry data were collected over the temperature range 20-1500°C (section 3.4.2). Figure 6.6 shows the *in-situ* thermal expansion and contraction results. The temperatures associated with the onset of densification and the maximum shrinkage are also shown in Figure 6.6.

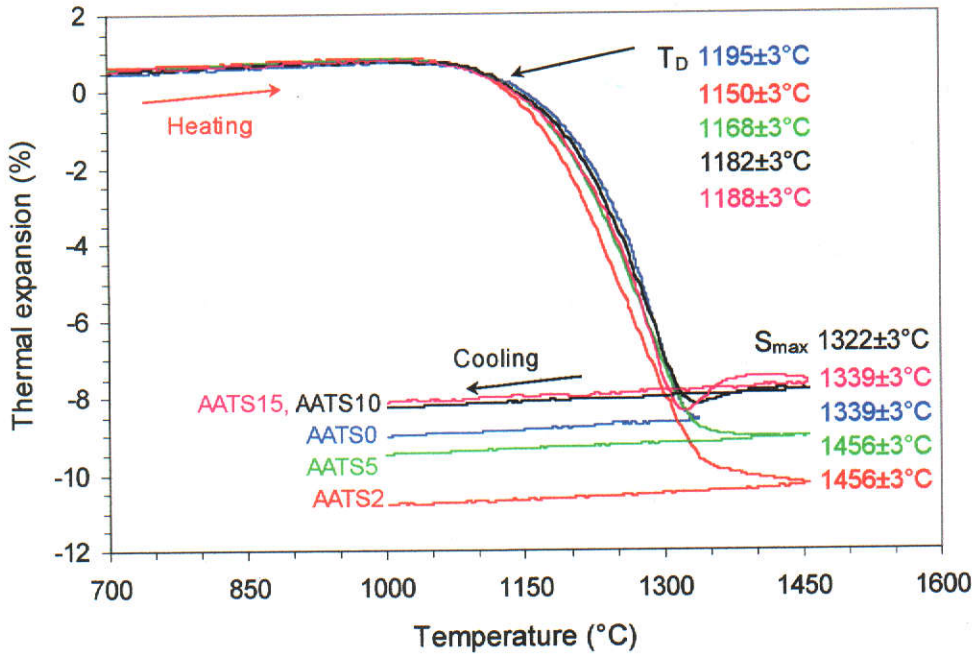

Figure 6.6. Dilatometric analyses of samples AATS0, AATS2, AATS5, AATS10 and AATS15. The temperatures associated with the start of densification (T_D) and maximum shrinkage (S_{max}) are highlighted.

The thermal expansion and contraction behaviour of all samples was similar up to 1100°C, with slight differences being noticeable beyond 1100°C. When compared to the control which had a maximum shrinkage of ~8.5%, samples AATS2 and AATS5 had greater shrinkage whereas samples AATS10 and AATS15 had lower shrinkage. In contrast to other samples which showed continuous shrinkage during heating, samples AATS10 and AATS15 displayed a discontinuity in shrinkage at ~1330 and 1320°C respectively and underwent thermal expansion

thereafter. This distinct display of shrinkage to expansion transition at ~1330°C for sample AATS10 and ~1320°C for sample AATS15 can be attributed to the melting of spodumene and the concomitant formation of glassy phase which expanded during heating. This display of discontinuity during shrinkage was also reported by Thomas, Stevens and Gilbart (1991) for AT dispersed with 5 wt% ZrO_2.

Values of densification temperature (T_D), maximum shrinkage (S_{max}) and the average thermal expansion coefficient ($\bar{\alpha}$) for AATS samples in the range 20–1000°C are shown respectively in Figures 6.7, 6.8 and 6.9.

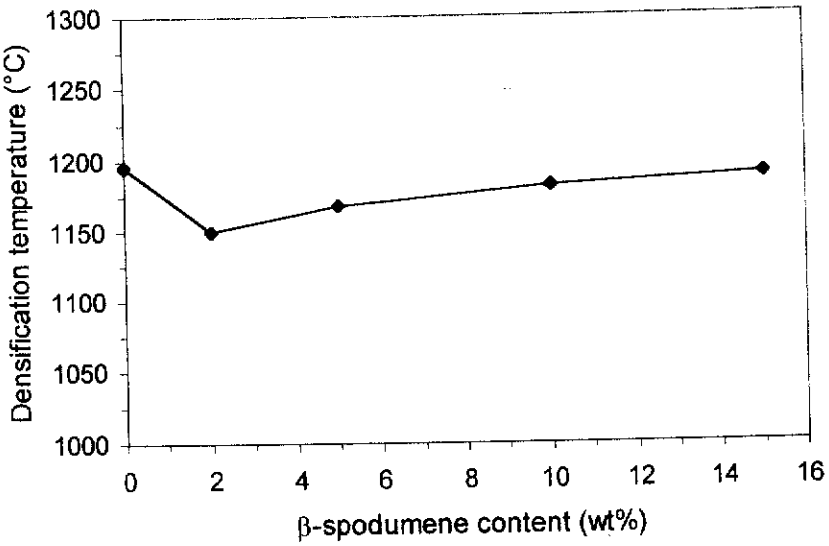

Figure 6.7. Variation of densification temperature (T_D) for AATS0, AATS2, AATS5, AATS10 and AATS15 as a function of β-spodumene content.

The densification temperature decreased from sample AATS0 to sample AATS2 indicating that the presence of a small concentration of β-spodumene lowered the starting temperature for densification. However, the densification temperature increased with an increase of β-spodumene content (AATS2 to AATS15), indicating that the presence of excess β-spodumene would not assist the densification process.

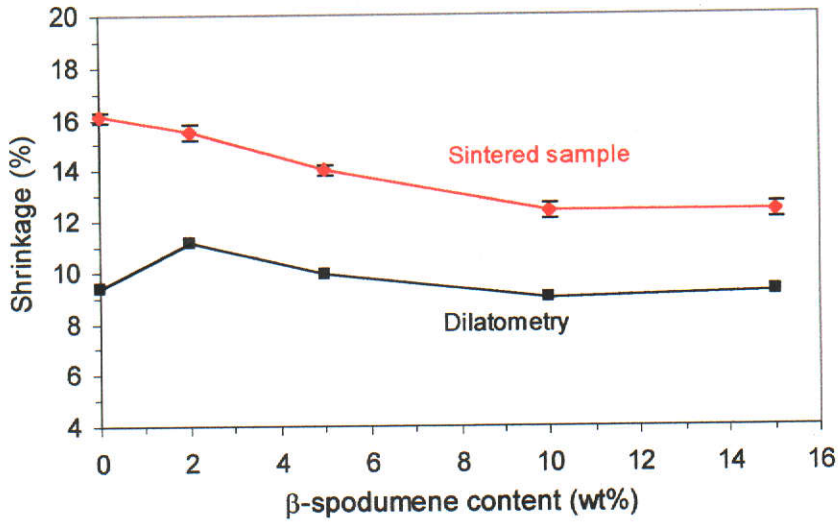

Figure 6.8. Variation of shrinkage for AATS0, AATS2, AATS5, AATS10 and AATS15 as a function of β-spodumene content as measured by dilatometry (up to 1456°C) compared to sintered sample (up to 1600°C). Error bars indicate two estimated standard deviations (2σ).

Figure 6.8 shows that shrinkage values from dilatometry are lower than those of sintered samples. This is consistent with the values from dilatometry were dynamically measured only up to ~1450°C whereas the values for the sintered samples were obtained following 3 h sintering at 1600°C.

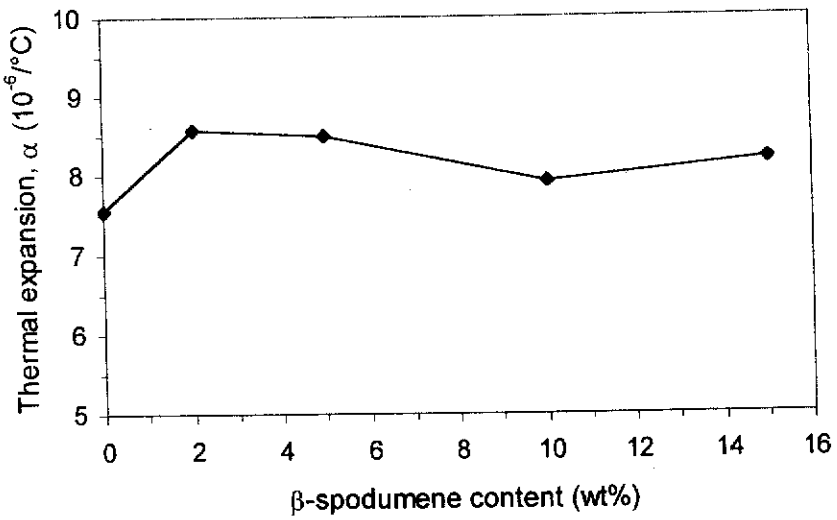

Figure 6.9. Average thermal expansion coefficient for AATS0, AATS2, AATS5, AATS10 and AATS15 in the range 20-1000°C as a function of β-spodumene content.

If a solid material is heated to higher temperatures the atom vibrates over a range centred on the equilibrium atomic spacing. The average atomic spacing accumulates over a macroscopic distance in the material and then produce a dimensional increase. In isotropic materials, this effect is the same in all directions but different in anisotropic materials. From Figure 6.9, the average thermal expansion coefficient ($\bar{\alpha}$) in the temperature range 20-1000°C increased from 7.55 to 8.57 × 10^{-6}/°C. Generally the presence of β-spodumene can cause a small increase in the thermal expansion coefficient and the highest value of $\bar{\alpha}$ was found in sample AATS2.

6.2.4 *In-situ* Study of Phase Development by Neutron Diffraction

In-situ neutron diffraction measurements were conducted using high temperature ND (HTND) to monitor phase development in sample AATS15 as described in section 3.3.3. Since the formation temperature of AT occurs at a peak value of ~1370°C (Figure 6.5), the study of phase development was monitored at

1200, 1290, 1310, 1330, 1350, 1370 and 1390°C. Figure 6.10 shows the measured ND patterns.

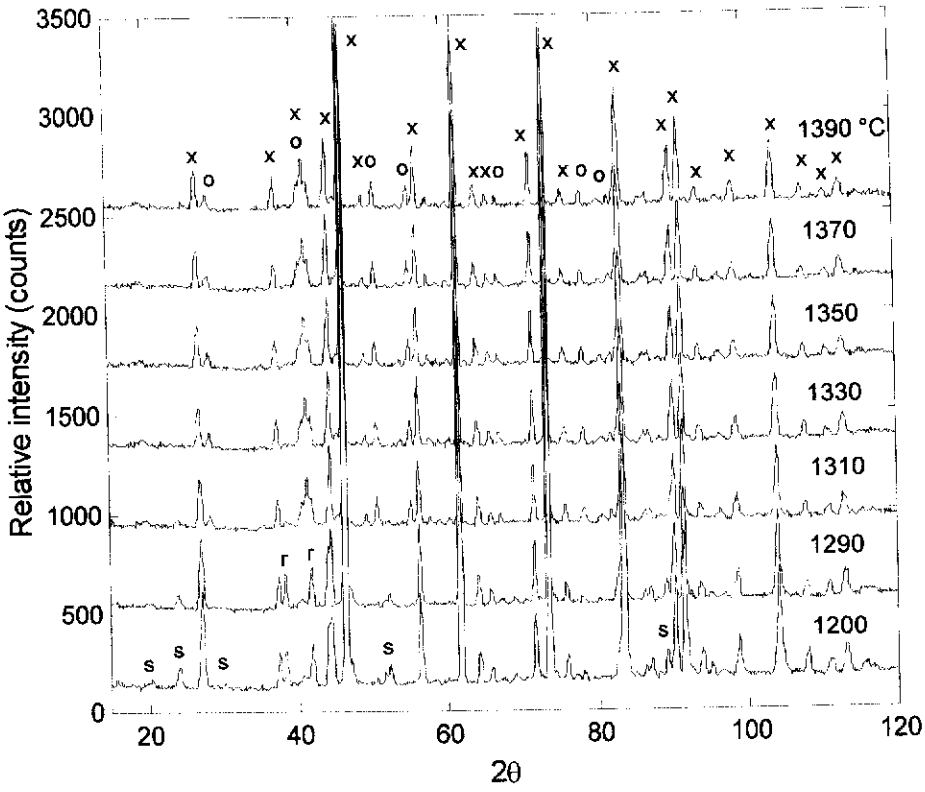

Figure 6.10. *In-situ* ND patterns for sample AATS15. The holding time at each temperature was 2 hours to increase the intensity statistic. Legend: x = alumina, o = AT, r = rutile, s = β-spodumene. Wavelength = 1.666 Å.

The presence of β-spodumene in the sample is clearly seen at 1200°C with peaks at 2θ of 20.34, 24.1, 30.1, 52.12 and 89.24°. When the temperature increased to 1310°C, those peaks disappear progressively indicating that β-spodumene started melting or underwent phase-separation with release of glassy phase. At 1330°C, these peaks have disappeared due to complete melting. This notion of melting over a temperature range is consistent with the display of a broad endotherm in the DTA plot described previously (Figure 6.4).

Like β-spodumene, the peaks due to the rutile phase (*ie.* 38.23 and 41.72°) decreased slowly with increase in temperature from 1200 to 1310°C. AT peaks started appearing at 1310°C at 28.46 and 50.61° and the peak intensities increased

gradually with temperature. It is interesting to note that AT formed at ~1310°C *prior* to the complete melting of β-spodumene at 1330°C, suggesting an overlap of their co-existence as indicated by their closely spaced endotherms (Figure 6.4).

Rietveld analysis was subsequently employed to calculate the relative abundance of the phases present using the model of Maslen *et al.* (1993) for alumina, Epicier *et al.* (1991) for AT, Howard, Sabine and Dickson (1991) for rutile and Clarke and Spink (1969) for β-spodumene. The Rietveld parameters refined were background and 2θ-zero, scale factors, peak profile, lattice, preferred orientation, asymmetry factors, mixing parameters and thermal parameters. Figure 6.11 shows a typical Rietveld difference plot for AATS15 at 1310°C after refinement. The crystalline phase concentrations were normalised to 100% and the relative phase abundances are shown in Figure 6.13.

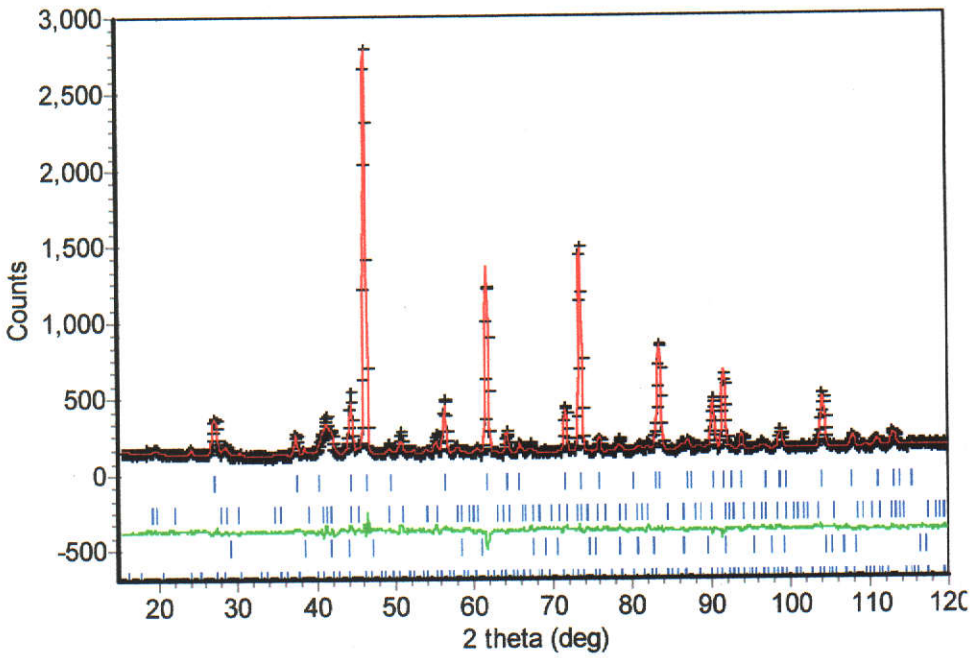

Figure 6.11. Neutron diffraction profile plot for sample AATS15 at 1310°C. The measured and calculated patterns are indicated by crosses (black) and solid lines (red). The difference plot is shown in green. Vertical bars (blue) represent the Bragg peak positions for each of the phases (from top to bottom: alumina, AT, rutile and β-spodumene. Wavelength = 1.666 Å.

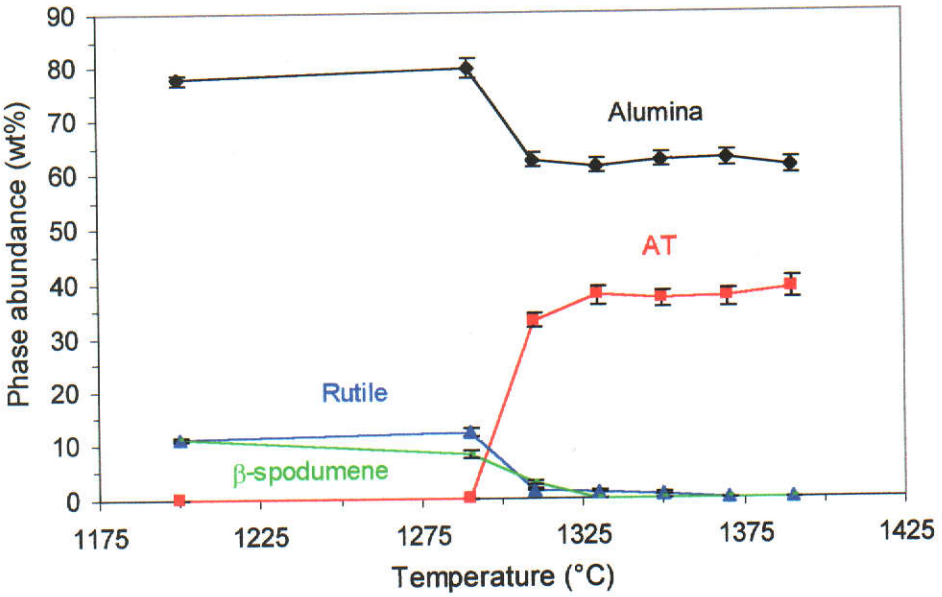

Figure 6.12. Relative phase abundances (wt%) for sample AATS15 from 1200 to 1390°C. Error bars indicate two estimated standard deviations (2σ).

Figure 6.12 shows the relative abundance of each of the phase is temperature-dependence. At 1200°C the phase abundance of β-spodumene is at a maximum. When the temperature increases from 1200 to 1290°C, the alumina and rutile phases both increase slightly whereas β-spodumene decreases due to initial melting or phase separation. Unusual phase changes appear to occur at temperature in the range 1290-1310°C. The phase abundances of rutile and alumina decrease rapidly from ~12 to 1.5 wt% and ~80 to 62 wt%, respectively. At the same time, AT formed with an initial content of ~ 3 wt%. A similar behaviour was observed for β-spodumene which reduced its content from ~8 to 3 wt%. This implies that not all β-spodumene melted completely but underwent a gradual phase separation with the release of a glassy phase. It is likely that β-spodumene began to decompose by phase separation and partial melting at 1290°C, followed by complete melting at 1330°C. Formation of AT was observed to occur at 1310°C and its abundance then increased with temperature. The presence of β-spodumene did not appear to react with alumina or rutile to form additional phases.

6.3 CHARACTERISATION BY X-RAY DIFFRACTION

Phase Compositions

Room temperature XRD data were used to examine the phase composition of the AATS samples containing 0-15 wt% β-spodumene. Details of sample preparation were described in section 3.2.3. Figure 6.13 shows the XRD patterns after sintering at 1600°C for 4 h. Analysis of phase identification was conducted using PDF files numbers 43-1848 for α-Al_2O_3, 41-0258 for AT, 21-1276 for TiO_2 and 35-0797 for β-spodumene.

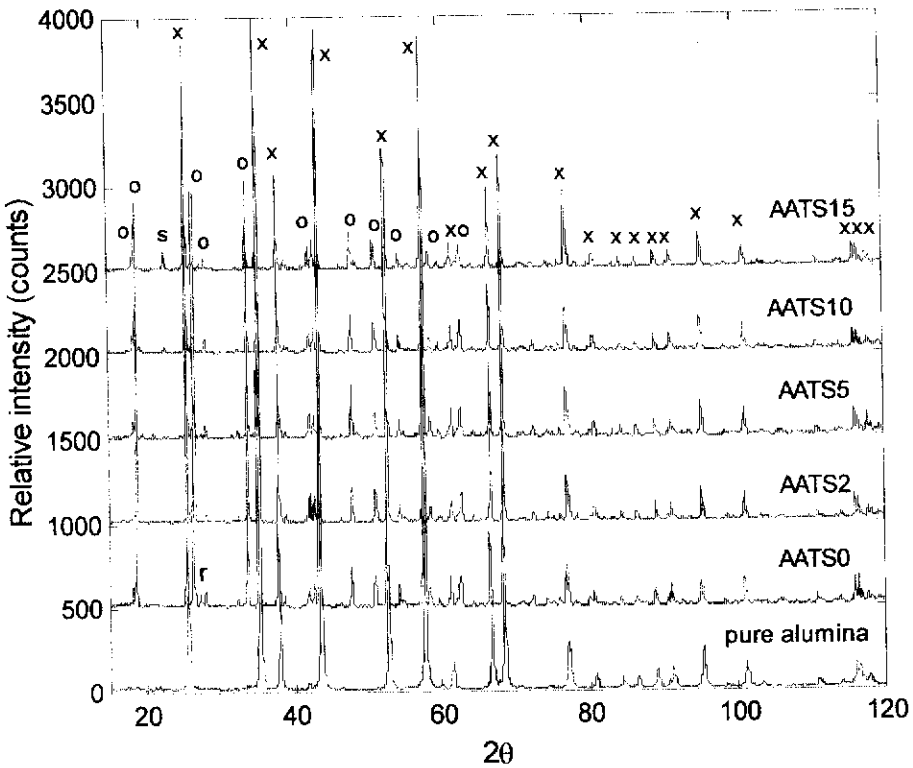

Figure 6.13. XRD patterns for samples AATS0 – AATS15 sintered at 1600°C. The peaks for β-spodumene are evident in samples AATS10 and AATS15. The pattern of pure alumina is shown for comparison. Legend: x = alumina, o = AT, r = rutile and s = β-spodumene. Wavelength = 1.5418 Å.

Weak rutile peaks were detected in sample AATS0 at 2θ of 27.15° but not in other samples. The presence of recrystallised β-spodumene (2θ = 22.62°) was

detected in samples AATS10 and AATS15 but not in AATS2 and AATS5. Although not obvious, a considerable amount of glassy phase is expected to form in all samples, especially AATS 10 and AATS15 where the excess recrystallised as β-spodumene.

Rietveld analysis was conducted to calculate the relative phase abundance of AT using *Rietica* (Hunter 1997). The refinement procedure and models used are the same with ND data as explained in the section 6.2.4. Figure 6.14 shows a typical difference plot for sample AATS15. The calculated pattern is overlaid on the measured pattern. The corresponding relative abundances for the AATS samples are shown in Figure 6.15.

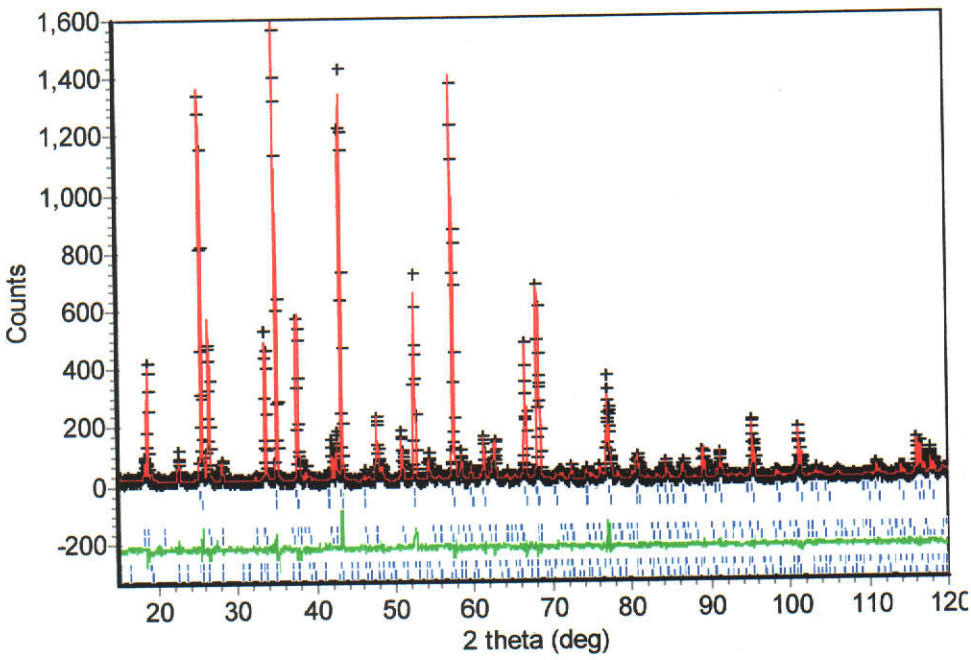

Figure 6.14. XRD Rietveld difference plot for sample AATS15 sintered at 1600°C. The measured and calculated patterns are indicated by crosses (black) and solid lines (red). The difference plot is shown in green. Vertical bars (blue) represent the Bragg peak positions for each of the phases (from top to bottom: alumina, AT and β-spodumene. Wavelength = 1.5418 Å.

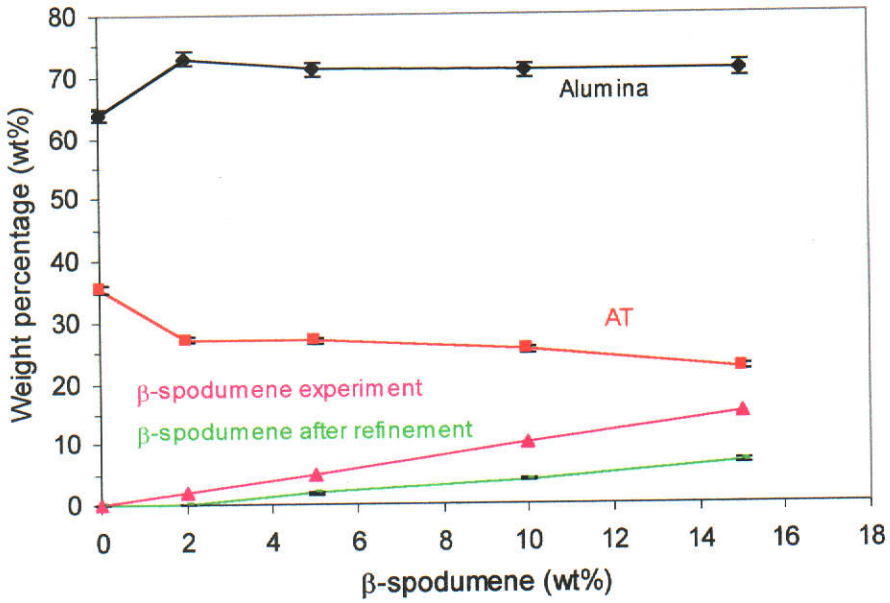

Figure 6.15. Relative weight percentage (wt%) of phases from Rietveld refinement for the AATS samples. Error bars indicate two estimated standard deviations (2σ).

Phase analysis shows that there was less than 1 wt% rutile in sample AATS0 whereas in other samples, this phase was not detected. No β-spodumene was detected in sample AATS2 probably due to its complete melting in forming a glassy phase. The addition of more β-spodumene appeared to cause an increase in the content of alumina but a decrease for AT. Besides, the presence of β-spodumene is believed to have caused the formation of residual glassy phase within the samples through phase-separation. Bayususeno, Latella and O'Connor (1999) reported the presence of a considerable amount of glassy phase in alumina ceramics containing 15 wt% β-spodumene.

In this experiment, the presence of β-spodumene is appeared to enhance the sintering of AATS ceramics through the formation of a liquid phase. For samples AATS5, AATS10 and AATS15, the phase abundance of recrystallised β-spodumene was 2, 4 and 7 wt% respectively, indicating that β-spodumene had resulted in the formation of residual glassy phase (see also TEM results in Figures 6.18-6.20).

6.4 MICROSTRUCTURE EVALUATION

6.4.1 Optical and Electron Microscopy

The microstructure of as-received β-spodumene powder is shown in Figure 6.16. The irregular shape of the grains and rough texture is clearly evident. Fine particles of ~1 μm have agglomerated to form larger grains.

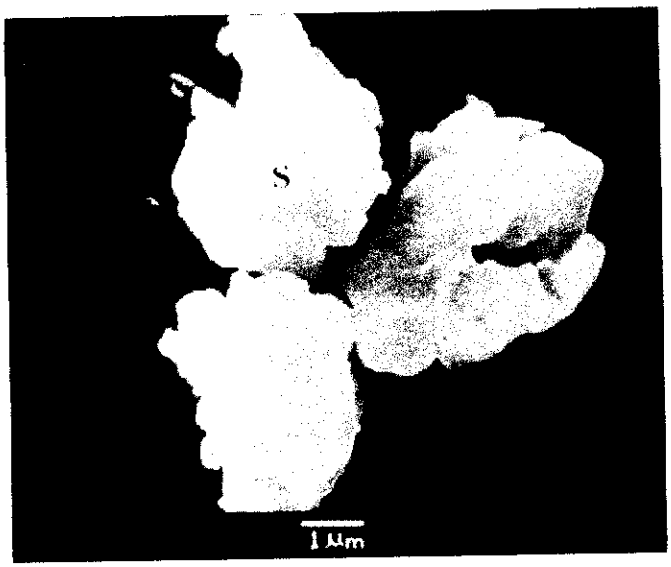

Figure 6.16. SEM micrograph of as-received β-spodumene powder. The grain size is ~ 4 μm.

Optical micrograps were taken on polished samples using an Olympus PMG3 microscope (section 3.3.7). Figure 6.17 shows the optical micrographs for samples AATS0, AATS2, AATS5, AATS10 and AATS15. The presence of β-spodumene appears to have a strong influence on the resultant microstructures (compared to Figure 5.16 in the section 5.6). When the content of β-spodumene is small (*ie.* ≤ 2 wt%), the distribution of whitish AT grains is finely-dispersed with no evidence of agglomeration. In contrast, the AT grains appear to have agglomerated and coarsen quite considerably when ≥ 5 wt% β-spodumene is present.

The dark regions in the microstructures are either due to grain pullout from polishing or residual porosity. The relatively weak grain boundaries between AT and alumina by virtue of large thermal expansion mismatch may have caused the preferential pull-out of AT grains during polishing. The highly pronounced thermal expansion anisotropy of AT may also have a role in this mechanism. This phenomenon has also been observed in AT-alumina particulate composites (Wohlfromm *et al.* 1991; Runyan and Bennison 1991). The presence of β-spodumene may serve to acerbate this problem.

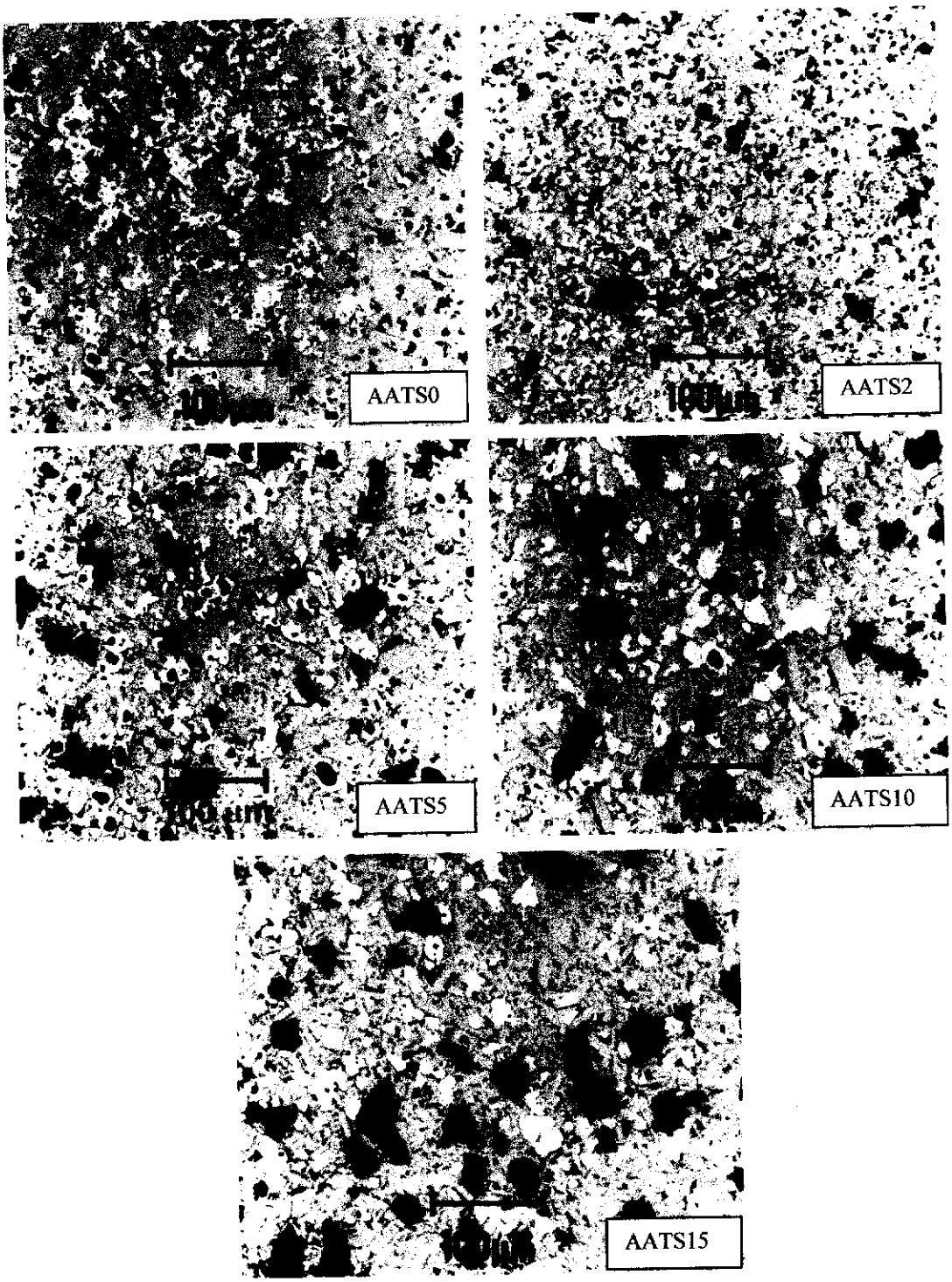

Figure 6.17. Optical micrographs of polished AATS samples. Grey and white phases are alumina and AT respectively. Dark regions represent porosity or grain pull-outs.

6.4.2 Transmission Electron Microscopy (TEM)

The presence of glassy phase in the AATS samples as alluded previously in section 6.4.1 was verified by transmission electron microscopy. Several processes associated with the presence of β-spodumene are believed to have occurred during sintering at 1600°C. At elevated temperatures, β-spodumene undergoes phase separation with the release of glassy phase. Only a small amount of glassy phase is required for sintering and the excess will recrystallise to form β-spodumene upon cooling. The presence of glassy phase in sample AATS10 is clearly revealed in Figures 6.18 (a), (b), and (c) showing, respectively, a bright-field image, the selected area diffraction (SAD) image, and the corresponding energy dispersive spectroscopic (EDS) chart. The presence of glassy phase is confirmed by the diffuse or amorphous diffraction pattern. The EDS chart also shows that the relative intensity of Si is much higher than Ti indicating that the area is rich in glassy phase.

The presence of the recrystallised β-spodumene within the glassy phase is shown in Figures 6.19 (a), (b) and (c). The relative intensities of Al, Si, O, and Ti are higher than the values for the glassy phase (Figure 6.18c).

The morphology of a typical AT crystal is shown in Figure 6.20 (a), (b), and (c). The presence of the AT crystallite is verified by the corresponding SAD pattern (Figure 6.20b). The EDS chart in Figure 6.20c affirms the absence of the Si element in the structure of AT.

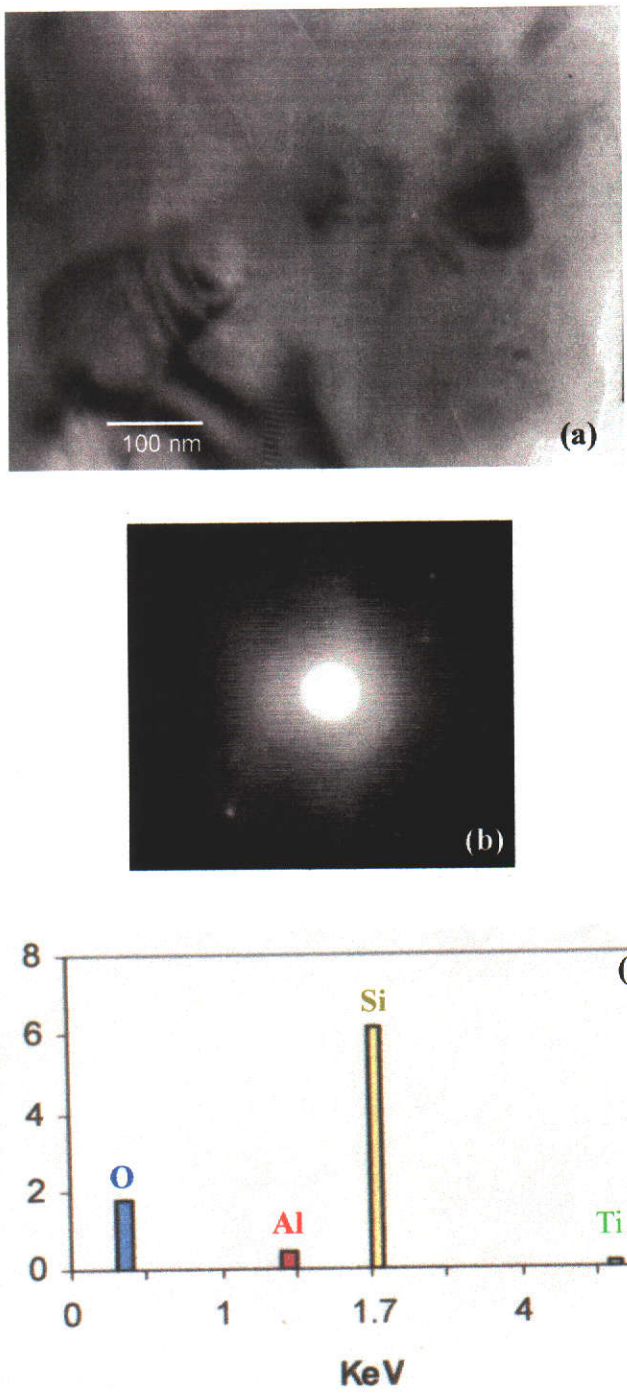

Figure 6.18. TEM analysis of sample AATS10 showing (a) bright-field imaging of glassy phase, (b) the selected area diffraction (SAD) pattern and (c) the corresponding energy dispersive spectroscopic (EDS) chart.

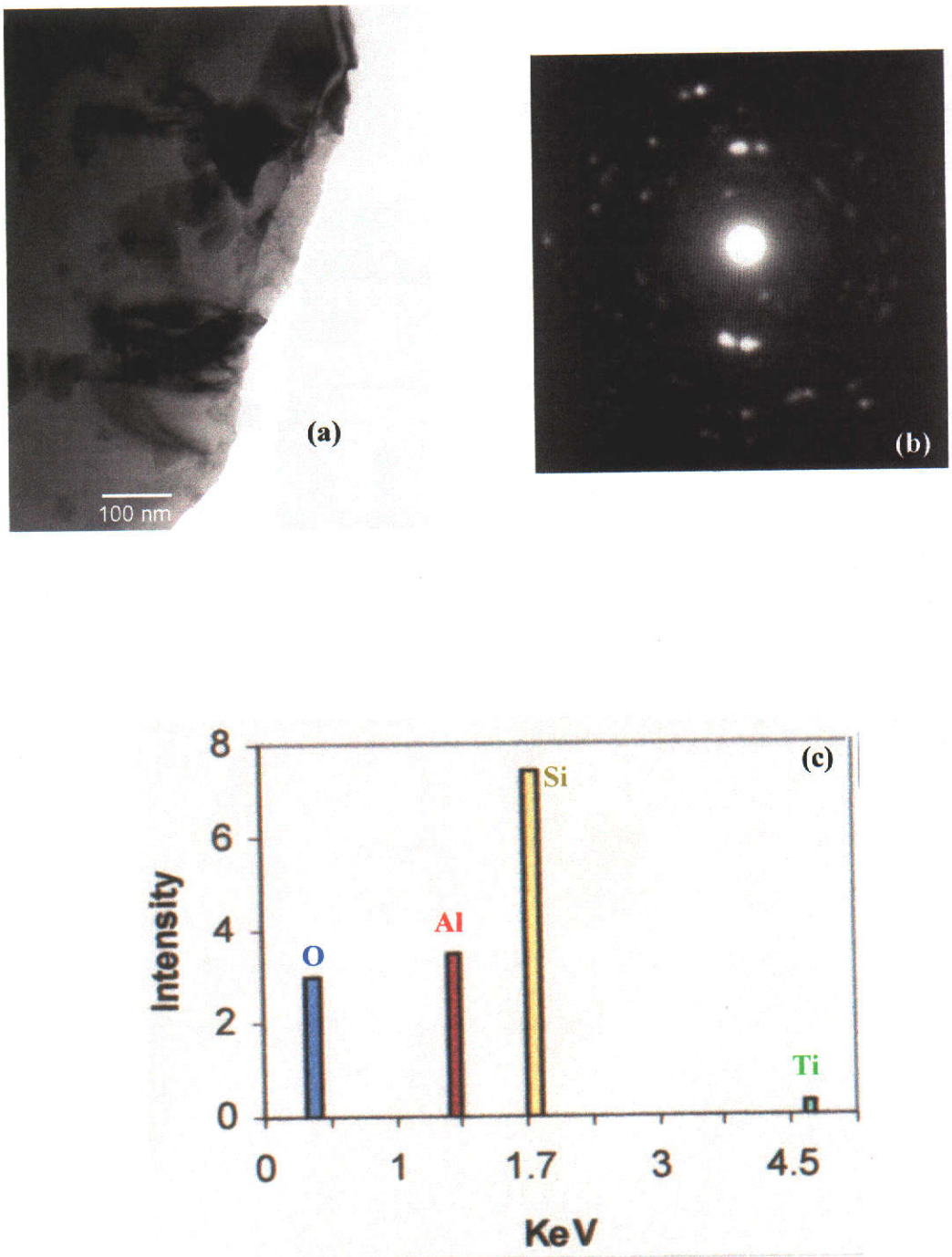

Figure 6.19. TEM analysis of sample AATS10 showing (a) bright-field imaging of recrystallised β-spodumene within a glassy matrix, (b) the SAD pattern, and (c) the corresponding EDS chart.

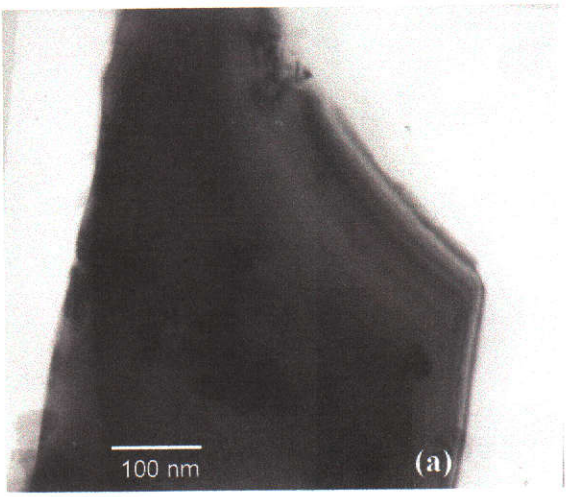

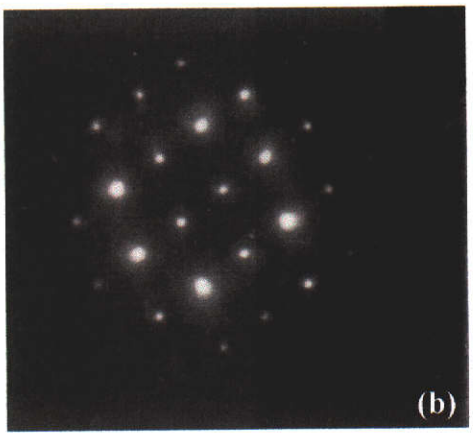

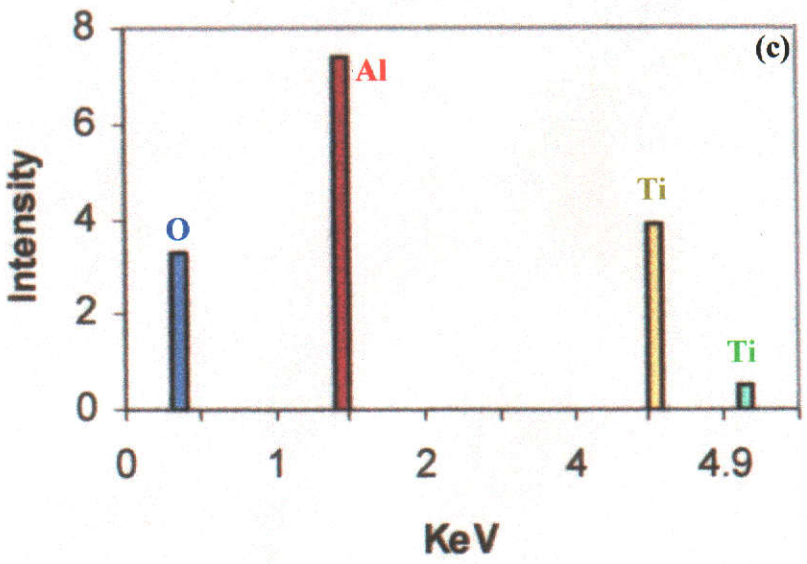

Figure 6.20. TEM analysis of sample AATS10 showing (a) bright-field imaging of a typical crystal of AT, (b) the SAD pattern, and (c) the corresponding EDS chart.

6.5 MECHANICAL PROPERTIES

The specimens used for the indentation tests were prepared by polishing with diamond paste to achieve a surface finish of 1 μm. Three indents were made for each load. The half-diagonal lengths of Vickers indent and the radial crack lengths were measured for the computation of hardness and fracture toughness (Evans and Charles 1976). The effects of β-spodumene addition on the hardness and fracture toughness of AAT ceramics are shown in Figures 6.21 and 6.22.

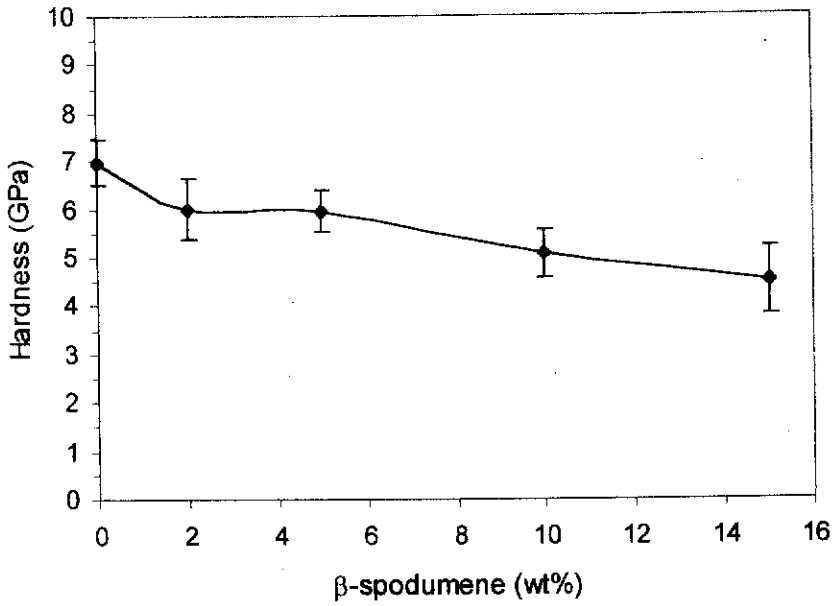

Figure 6.21. Variation of hardness as a function of β-spodumene content in AATS samples. Error bars indicate two mean deviations (±).

The results show that the hardness decreases with β-spodumene content. This is consistent with β-spodumene being a relatively soft phase and therefore its presence would naturally cause a reduction in hardness. Moreover, the formation of excess glassy phase due to the phase separation of β-spodumene would cause a further reduction in hardness.

The effect of β-spodumene addition on the fracture toughness of AATS samples is shown in Figure 6.22 and the fracture decrease with β-spodumene. Again, this is consistent with β-spodumene being intrinsically very brittle and its presence in large concentrations can cause the formation of excess glassy phase in the microstructure. The presence of brittle glassy phase along the grain-boundaries would inevitably lead to the lowering of fracture resistance. From the design prospective, it is necessary to use less than 5 wt% β-spodumene as a sintering additive to avoid a drastic reduction in mechanical properties such as hardness, strength and fracture toughness.

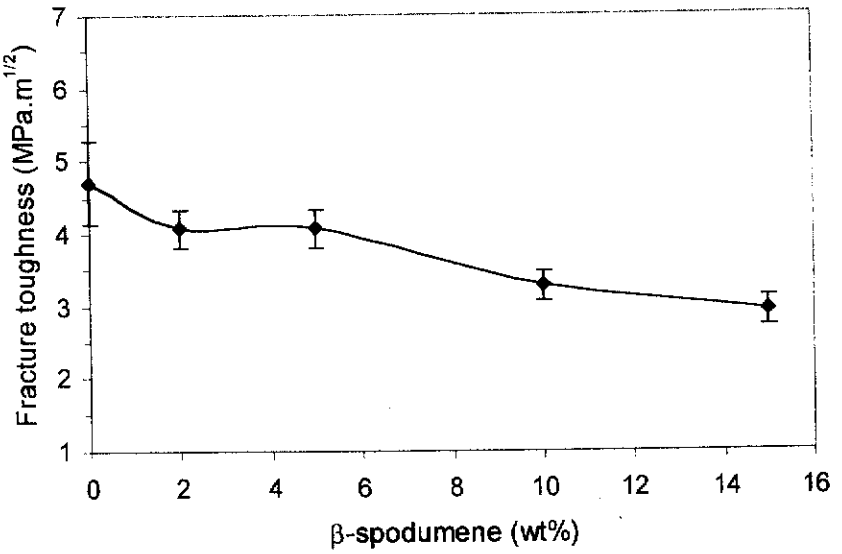

Figure 6.22. Variation of fracture toughness as a function of β-spodumene content in AATS samples. Error bars indicate two mean deviations (±).

6.6 SUMMARY

The effects of β-spodumene addition on the densification, phase relations, microstructure and properties of AATS composites have been investigated. The addition of 5 wt% β-spodumene gave rise to the best densification through liquid-phase-sintering.

DTA data show that the formation temperature of AT was dependent on the content of β-spodumene. The presence of ≤ 5 wt% β-spodumene caused an increase in the formation temperature of AT.

Based on the dilatometry results, the presence of ≤5 wt% β-spodumene gave rise to greater shrinkage, but lower shrinkage for samples containing ≥10 wt% β-spodumene. The latter samples also displayed a discontinuity in shrinkage at ~1330 and 1320°C respectively and underwent thermal expansion thereafter. This unique display of shrinkage to expansion transition was attributed to the melting of spodumene and the concomitant formation of glassy phase which expanded readily during heating.

Phase analyses by XRD showed that the presence of β-spodumene had not reacted with the matrix to form additional phases. Phase separation of β-spodumene during sintering caused the formation of glassy phase in the microstructure and its recrystallisation during cooling.

The dynamic phase relations in sample AATS were studied by high temperature neutron diffraction (HTND). At 1290°C, the melting and phase separation of β-spodumene commenced and then continued until at 1330°C. The formation of AT commenced at 1310°C and the concentration increased with temperature. Rutile was still present when AT formed and it disappeared only at 1370°C.

The presence of β-spodumene has a profound influence on the microstructure. At low concentrations of β-spodumene (≤5 wt%), the AT grains were finely and uniformly dispersed within the matrix. As the content of β-spodumene increased (ie. ≥10 wt%), there was a strong tendency for AT grains to agglomerate and coarsen probably due to high glassy phase content. The existence of glassy phase and the recrystallisation of β-spodumene have been verified by TEM imaging and reconfirmed by the EDS and SAD analyses.

The presence of β-spodumene caused a reduction in both the hardness and fracture toughness as a result of glassy phase formation within the microstructure. For optimum physical and mechanical properties, it would be necessary to use ≤ 5 wt% β-spodumene as sintering aid for the fabrication of AATS composites.

CHAPTER SEVEN

INFILTRATION PROCESSING OF ALUMINA/ALUMINIUM TITANATE COMPOSITES

7.1 INTRODUCTION

Liquid-phase infiltration of preforms has emerged as an extremely useful method for the processing of composite materials. This process involves the use of low viscosity liquids such as sols, metal- or polymer- melts. Using this infiltration process, it is possible to design new materials with unique microstructures (*eg.* graded, multiphase, microporous) and unique thermomechanical properties (graded functions, designed residual strains and thermal shock).

Liquid infiltration into dry porous materials occurs due to capillary action. The mechanism of infiltrating liquids into porous bodies has been studied by many researches in the fields of soil physics, chemistry, powder technology and powder metallurgy. However, the processes and kinetics of liquid infiltration into a powdered preform are rather complex and have not been completely understood. Based on Darcy's fundamental principle and the Kozeny-Carman equation (Carman 1956), Semlak and Rhines (1958), and Yokota *et al.* (1980) have developed infiltration rate equations for porous glass and metal bodies. These rate equations can be used to describe the kinetics of liquid infiltration in porous ceramics preforms, but a single capillary model will result in the pore size measured from the experimental infiltration rates, being an order of magnitude smaller than the pore sizes seen from SEM and porosimetry measurements (Dullien, El-Sayed and Batra 1977 and Einset 1996). Buckley, Manurung and Low (2000) have shown that a combination of the Washburn model (Washburn 1921) and Dulliens analysis (Dullien, El-Sayed and Batra 1977) is able to reconcile the infiltration rates and the pore sizes determined from SEM and porosimetry measurements for the infiltration of water and $TiCl_4$ into alumina preforms.

In this chapter, the effects of pre-sintering temperature, types of infiltrant, vacuum and multiple infiltrations on the rate of infiltration into porous alumina preforms are described. Initial attempts to model the observed infiltration kinetics

using various rate equations are also described. The deficiencies of the existing models to describe the infiltration kinetics in this study are discussed.

This chapter also focuses on the use of infiltration to fabricate functionally-graded alumina/AT ceramics and the determination of their physical, microstructural, and mechanical characteristics. This method has been well demonstrated in other graded ceramic systems such as alumina/mullite (Marple and Green 1993), mullite/ZTA (Low *et al.* 1993a; Low *et al.* 1993b), AT/ZTA (Low *et al.* 1996; Pratapa and Low 1996; Pratapa, Low and O'Connor 1997), alumina/AT (Low 1998; Skala 2000), and alumina/calcium hexaluminate (Asmi *et al.* 1999; Asmi 2001). The effects of graded AT composition on the physical and mechanical properties have been evaluated using X-ray diffraction (XRD), grazing incidence synchrotron radiation diffraction (GISRD), scanning electron microscopy (SEM), optical micrograph, differential thermal analysis (DTA) and Vickers indentation.

7.2 RESULTS AND DISCUSSION

7.2.1 Studies on Infiltration Kinetics

After the preforms were pre-sintered, the bulk density and porosity were measured using Archimedes principle (Australian Standard 1989). Tables 7.1 and 7.2 list the physical properties of the preforms and infiltrants. It was found that the porosity values of the preforms sintered at 900, 1000 and 1100°C for 2 h were quite similar. This suggests that pores were not eliminated at these sintering temperatures. However, the pore sizes are expected to become smaller in preforms pre-sintered at higher temperatures.

Table 7.1. Porosity and bulk density properties of pre-sintered preforms.

Sintering temperature (°C)	Porosity (%)	Bulk density (g/cm^3)
900	45.0(1.2)*	2.125(30)
1000	45.9(1.5)	2.123(31)
1100	44.6(1.5)	2.193(32)

*Number in parentheses is estimated standard deviation (σ).

Table 7.2. Surface tension and viscosity properties of infiltrants.

Infiltrant (at 23°C)	Surface tension, γ (x 10^{-2} N/m)	Viscosity, η (x 10^{-4} Ns/m^2)
H_2O	7.225(42)*	9.5(7)
$TiCl_4$	7.046(41)	53.1(4.2)

*Number in parentheses is estimated standard deviation (σ).

Mercury porosimetry was performed on the alumina preform, which had been sintered at 1000°C. Figure 7.1 shows a bimodal pore size distribution with neck diameter, D_n = 0.15 μm according to the equation:

$$D_n = \frac{4\gamma \cos\theta}{P} \tag{7.1}$$

where γ is the surface tension of mercury, 0.485 N/m, θ is the contact angle for mercury, 130° and P is the pressure of the mercury infiltrant.

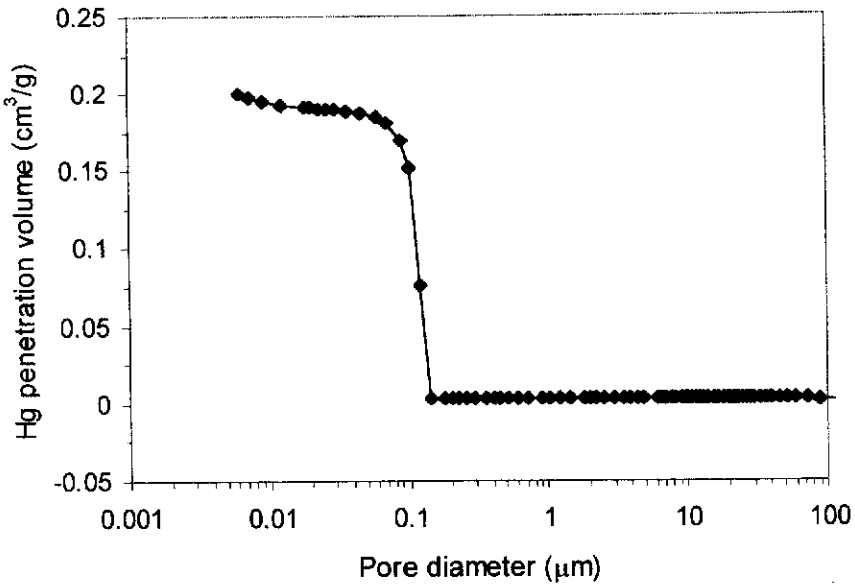

Figure 7.1. Mercury porosimetry measurements for a partially sintered (1000°C) alumina preform. The pore-neck diameter, D_n is ~ 0.15 μm.

As a comparison with the pore-sizes and distribution of the preform measured by porosimetry, SEM micrographs were taken before (Figure 7.2) and after infiltration (Figure 7.3). Based on SEM examination, the pores in the preform before infiltration ranged in size from r ~0.1-0.5 μm (Figure 7.2). Assuming an average pore radius of 0.3 μm, this radius is approximately four times larger than the pore-neck radius (D_n = 0.15 μm, so pore radius = 0.075 μm) determined by mercury porosimetry.

It is interesting to note that the pore sizes appear to remain virtually unchanged following the infiltration process. This suggests that (i) the capillary forces involved did not appear to cause any shrinkage or size reduction of the pores, and (ii) the infiltrant had not filled-up the pores but only formed a thin layer deposit on the walls of pores. The small particles entering the grains are believed to arise from the infiltrant which had entered the pore-channels and adhered to the walls of the pores following drying (Figure 7.3).

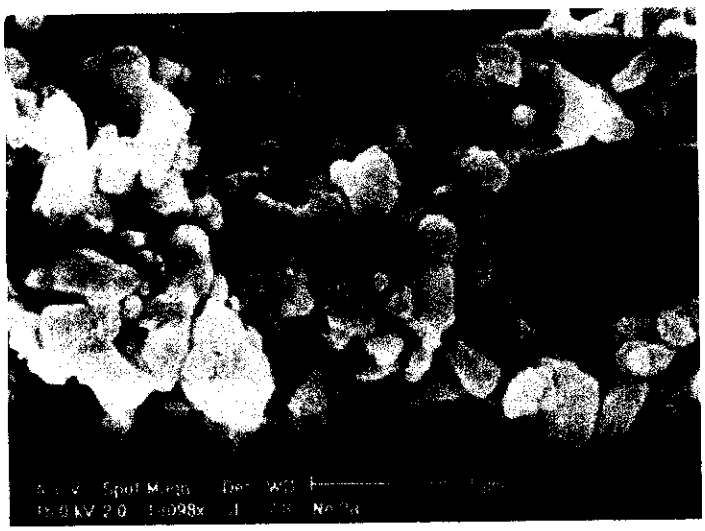

Figure 7.2. SEM micrograph of the partially-sintered alumina preform (1000°C) showing pores of various sizes (r ≈ 0.1-0.5 μm).

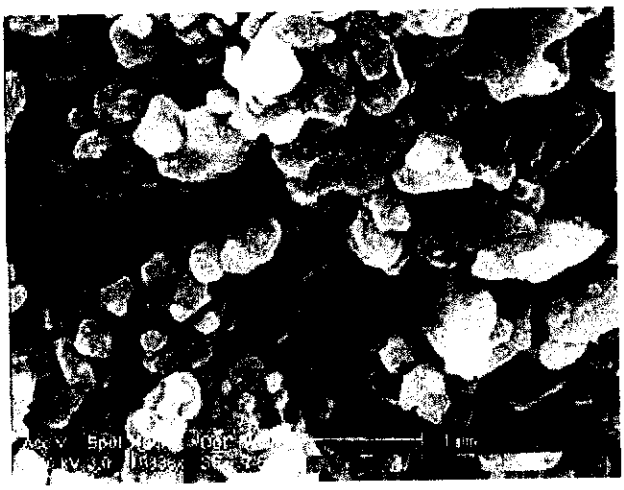

Figure 7.3. SEM micrograph of the partially-sintered alumina preform (1000°C) after infiltration with $TiCl_4$. The pore sizes appeared to remain unchanged. Some small particles attached to alumina grains are clearly seen.

In order to successfully model the infiltration kinetics in terms of the effects of pre-sintering temperature, type of infiltrant, infiltration environment, and multiple infiltrations, the pore-radius of alumina preform (presintered at 1000°C) was measured using water as infiltrant, since the viscosity and surface tension of water are well known. The pore-radius of the alumina preform was calculated from the Washburn model (Equation 2.2).

By assuming a contact angle $\theta = 0°$ (Einset 1996; Ligenza and Bernstein 1951) the pore radius of the preform can be calculated if the height and time of infiltration are known. The rate of infiltration is determined from the slope in Figure 7.4 and then from this slope, the pore radius can be found. From the measurements (without vacuum), it was found that the pore-radius of the alumina preform is 0.015 ± 0.001 μm. Similarly the pore-radius found from alumina preform infiltrated with $TiCl_4$ is 0.018 ± 0.002 μm. The errors in the radii only reflect the experimental uncertainty in the measured values for surface tension and viscosity. However, the measured pore radius is an order of magnitude smaller than the pore radius determined from porosimetry and SEM (Figures 7.1 and 7.2).

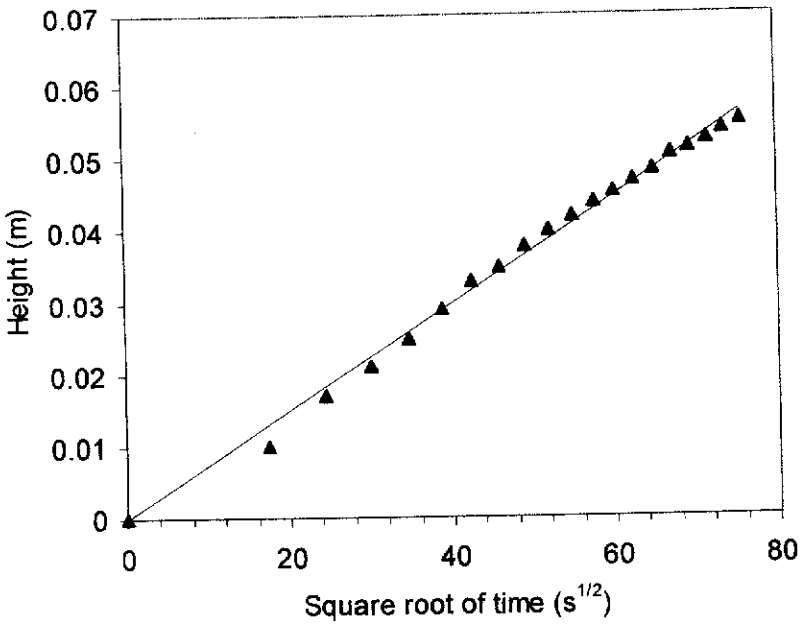

Figure 7.4. Height of infiltration of water into alumina preforms (sintered at 1000°C) as a function of square root of time.

The pore-radius determined from infiltration kinetics can be reconciled to the experimentally determined radii from SEM and porosimetry, by assuming a two-pore size model (pore-neck and pore-bulge), instead of a single capillary pore-size (Dullien, El-Sayed and Batra 1977; Einset 1996). The schematic diagram for this two-pore size model is shown in Figure 7.5.

Dullien (1979) have considered the rate of capillary rise of a fluid in a model three-dimensional network pore structure consisting of a repeating pore element with step changes in diameter. The effective diameter, D_{eff} model is given by:

$$D_{eff} = \frac{1}{3}\left[\sum_k D_k\right]^2\left[\sum_k D_k \sum_j \left(\frac{D_k}{D_j}\right)^3\right]^{-1} \qquad 7.2$$

where the summations are over the number of segments of the repeating pore unit.

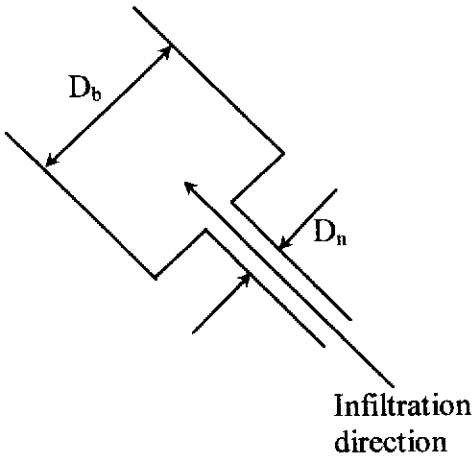

Figure 7.5. A schematic of the two-size single-capillary. D_b is the pore-bulge diameter and D_n is the pore-neck diameter.

The effective pore-diameters are therefore smaller than the individual diameters of the pore segments. Consider a two pore-size repeating unit model in equation (7.2) is j = 1, 2 and k = 1, 2 for pore-necks and pore-bulges as shown in Figure 7.5. Thus D_b can be calculated by substituting D_{eff} (determined from the slope in Figure 7.4) and D_n (determined from mercury porosimetry in Figure 7.1) into equation (7.2). The results are 0.27(3) and 0.18(4) μm for water and $TiCl_4$ respectively. The calculated value of D_b for both infiltrants is in reasonable agreement with the average pore-diameter estimated from SEM (Figure 7.2).

7.2.2 Effects of Various Parameters on Infiltration Kinetics

Contact Angles

This model describes the influence of contact angle (θ) on the infiltration kinetics of water into the preform using Equation (2.2) with pore-radius, r of 0.015 μm. The first assumption for θ is 0° which remains fixed during the experiment. The second assumption uses θ of 30° which also remains fixed during the experiment. The effect of contact angle for 0 and 30° on the rate of infiltration is shown in Figure 7.6.

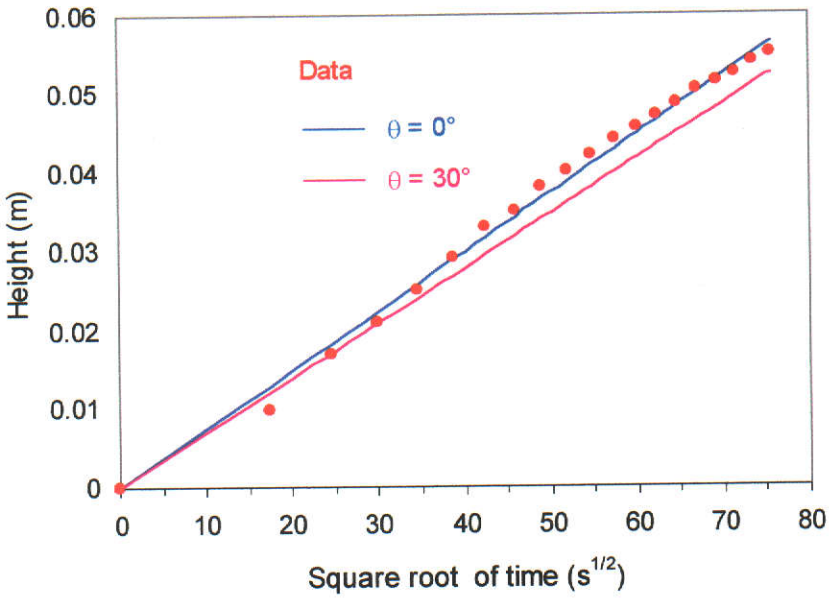

Figure 7.6. Height of infiltration as a function of time according to experimental data and equation (2.2) for the infiltration θ = 0° (blue) and 30° (magenta).

Figure 7.6 shows the predictions of infiltration behaviour based on the Washburn (1921) equation for contact angle (θ) of 0° and 30°. The graph represents the kinetics of water infiltration into the preform with pore- radius, r of 0.015 μm. However, for θ of 30° the model matches well up to time of ~1500 sec and height ~3 mm. Thereafter the model deviates from the data. This suggests that the contact angle did not remain constant but became smaller with an increase of time. Following this revised assumption, the contact angle, θ is replaced with a linear function in time such that θ decreases linearly from 30° to 0° according to $\theta_t = \theta_0 (1- t)$ where θ_t is contact angle at time t and θ_0 is the contact angle at $t = 0$. The revised graph is shown in Figure 7.7.

Further refinement of the model uses the contact angle which varies with time exponentially (Yokota *et al.* 1980) *ie.* $\theta_t = \theta_0 \exp(-0.0021t)$. Assuming 30° for θ_0 and the graph is also shown in Figure 7.7.

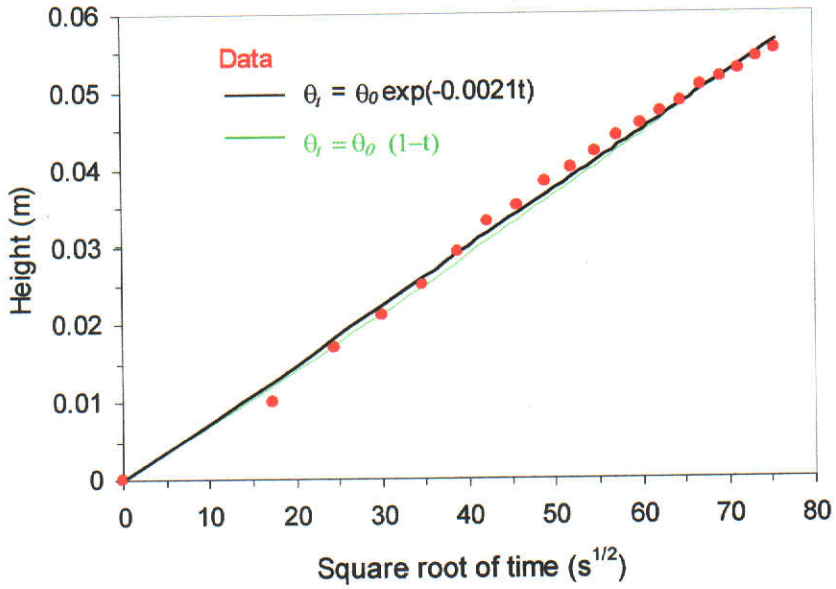

Figure 7.7. Height of infiltration as a function of time according to experimental data and equation (2.2) for the infiltration $\theta_t = \theta_0 (1- t)$, in green colour and $\theta_t = \theta_0 \, exp(-0.0021t)$, in black colour with θ_0 =30°.

Figure 7.7 shows that the revised model, $\theta_t = \theta_0 (1- t)$ matches the data well both at the beginning and at the end. A close examination reveals that this revised model resembles that proposed for Figure 7.6. In other words, the model using the fixed contact angle of 0° is very similar to the model that uses a time-dependent contact angle.

This refined model, $\theta_t = \theta_0 \, exp(-0.0021t)$ is most promising and best resembles the match shown in Figure 7.6. Hence, by using a time-dependent contact angle that varies exponentially, the initial and the middle portions of curve match well with the data. This model is obviously better than previous ones.

Effect of Pre-sintering Temperature

The effect of pre-sintering temperature on the infiltration kinetics can be seen in Figure 7.8. The results show that the rate of infiltration for the preform sintered at 1000°C is higher than the infiltration rate of the preforms sintered at 900 and 1100°C. One would expect that preforms sintered at the lower temperatures would have a higher porosity, which should then increase the infiltration rate.

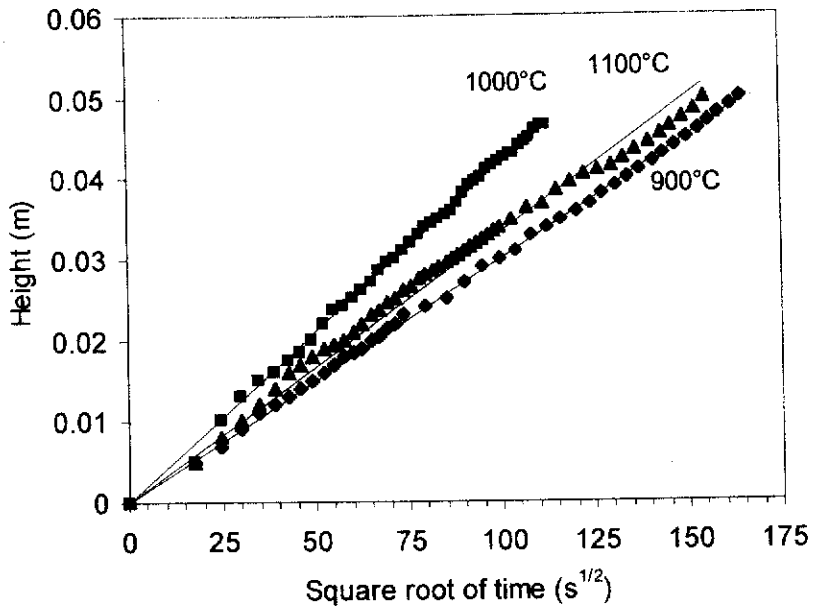

Figure 7.8. Effect of pre-sintering temperature at 900, 1000 and 1100°C. These lines represent the best fit between height and square root of time. The alumina preforms were immersed with $TiCl_4$ at atmospheric pressure.

Table 7.1 shows that the porosities of the preforms sintered at the above temperatures are similar within experimental errors. The difference in the infiltration rates maybe due to differences in tortuosity as explained in section 2.5.4 within the three alumina preforms. The results indicate that other factors (such as permeability and pore structure) apart from porosity also influence the infiltration rates of alumina preforms pre-sintered at temperatures in the range of 900 – 1100°C.

Effect of Infiltrants

The effect of infiltrant on the infiltration kinetics was studied by comparing the infiltration rates for water and $TiCl_4$. From Table 7.2 it can be seen that the values of surface tension for both liquids are quite similar, but the viscosity of water is ~ 6 times smaller than that of $TiCl_4$.

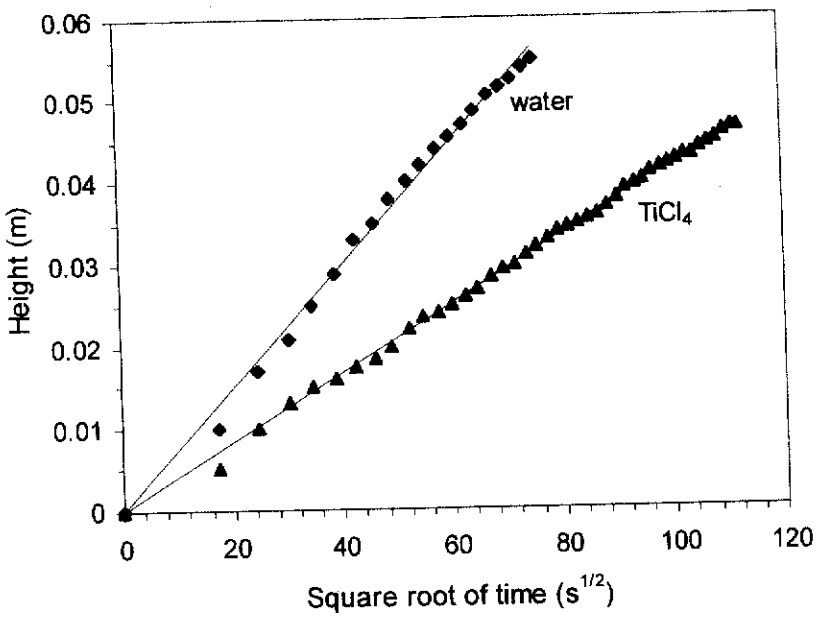

Figure 7.9. Effect of infiltrants using water and titanium trichloride ($TiCl_4$). These lines represent the best fit between height and square root of time. Note that the viscosity of water is ~6 times smaller than that of $TiCl_4$. Pre-sintering temperature was 1000°C.

Figure 7.9 indicates that rate of infiltration for water is higher than that for $TiCl_3$, and based on equation (2.2) this is what would be expected, since the rate of infiltration is inversely proportional to the viscosity of the infiltrant.

Effect of Vacuum

The effect of vacuum on the rate of infiltration is presented in Figure 7.10. It is clear that the rate of infiltration increases under vacuum. Therefore infiltration under vacuum is a means of experimentally enhancing the kinetics of infiltration of water and $TiCl_4$ into porous alumina preforms.

The effect of vacuum on the infiltration rate can be explained by Equations (2.4) and (2.5). Gravity does not have a measurable effect on the rate of capillary rise for this system, since the infiltration height is <6 cm, therefore its contribution can be neglected in Equation (2.5).

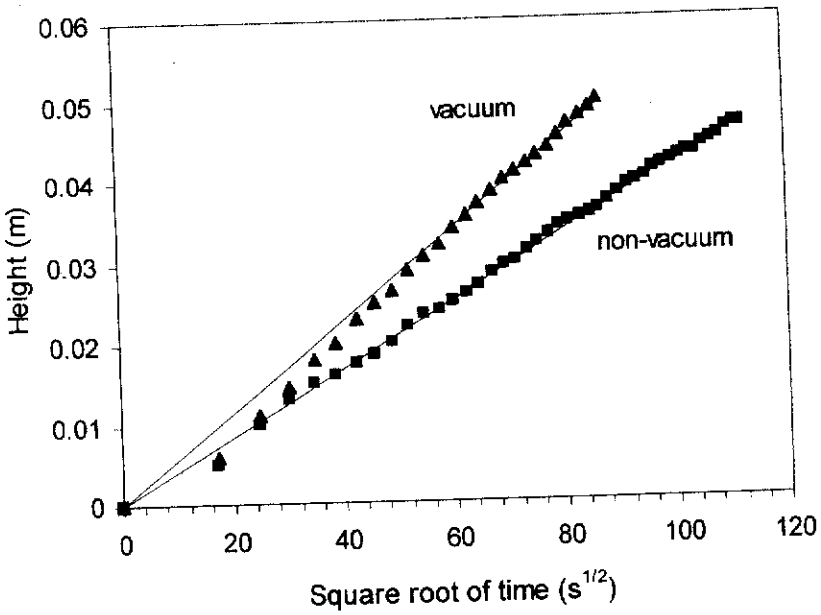

Figure 7.10. Effect of vacuum on the rate of infiltration. The infiltrant is $TiCl_4$. These lines represent the best fit between height and square root of time. Pre-sintering temperature was 1000°C.

When the system is under a vacuum P_{net} increases as compared to the situation when the system is at atmospheric pressure, therefore from Equation (2.4) the rate of infiltration increases, which agrees with the experimental results (see Figure 7.10).

Effect of Multiple Infiltrations

The effect of multiple infiltrations is presented in Figure 7.11. The results show that the rate remains linear and increases for each subsequent cycle. Equation (2.3) shows the relationship between the rate and T, the totuosity, p, the porosity, and C_s, the shape factor. If it is assumed that $TiCl_4$ leaves a coating on the walls of pores after each subsequent cycle, two scenarios result.

1) The pore radius will decrease, therefore the rate of infiltration should decrease on subsequent cycles according to Equation (2.3), and

2) The angle of wetting may increase (since we have assumed previously that $\theta = 0$, the angle cannot be negative), therefore $\cos\theta$ will decrease, hence from Equation (2.3) the rate will decrease.

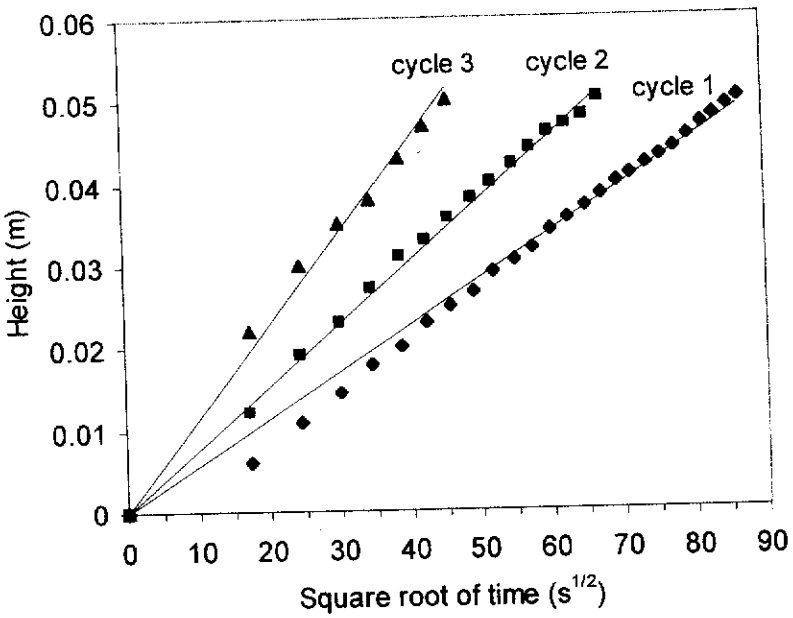

Figure 7.11. Effect of multiple infiltrations with $TiCl_4$ under vacuum. These lines represent the best fit between height and square root of time. Preform was sintered at 1000°C.

Neither of these 2 scenarios occurs experimentally. Figure 7.11 shows an increase in the rate for subsequent cycling. Therefore a combination of the rates from Figure 7.11 and Equation (2.3) suggest that $TiCl_4$ does not leave a coating on the pores during subsequent cycling.

A more likely reason as to the rate increase during subsequent cycles can be attributed to a decrease in the tortuosity. The path that the infiltrant takes during each cycle is smoothed by the preceding infiltration cycle. Therefore the tortuosity is decreased. Inspection of Equation (2.3) shows that the infiltration rate will increase if the tortuosity is decreased. From cycle 1 to cycle 3, the rate approximately increases by a factor of 2. The tortuosity would have to decrease by a factor of ~2, if the rate increase was attributed entirely to a decrease in tortuosity. This is unlikely, therefore

it is suggested that there may be a slight increase in the pore radius and shape factor during subsequent cycling, as well as a decrease in tortuosity. It is suggested that the major cause in the rate increase in going from cycle 1 to cycle 3 can be attributed to a decrease in the tortuosity.

7.2.3 Concluding Remarks on the Modelling of Infiltration Kinetics

The experimental results show that the kinetics of infiltrating water and titanium trichloride into an alumina preform is parabolic with time. It has been shown that the viscosity of infiltrants influences the rate of infiltration and that the rate of infiltration is pressure dependent. The experimental result of faster kinetics in a vacuum as opposed to that in one atmosphere agrees with Travitzky's (1988) model. The pre-sintering temperature has a strong influence on the kinetics of $TiCl_4$ in alumina preforms and multiple infiltrations increase the rate of infiltration. According to Yokata *et al.* (1980) the increase in the infiltration rate due to multiple cycling is predominantly attributable to a decrease in the tortuosity of the preform during subsequent cycles.

Based on the results obtained from the study of infiltration kinetics, several pore models for alumina preform can be summarized as follows.

- Based on SEM results, the radius pore ranges from 0.1 to 0.5 μm.
- The Washburn model gives an average pore radius, r of 0.0147 μm.
- From mercury porosimetry the pore-neck diameter, D_n, is 0.15 μm which is approximately five times larger than that predicted by the Washburn model.

7.3 STUDIES ON DIFFERENTIAL THERMAL ANALYSIS (DTA)

The sample for DTA studies was prepared by mixing alumina powder in $TiCl_4$ for 24 h. The experimental details were described in section 3.4.5. The DTA data were collected between room temperature and 1500°C using a Netzsch STA 409 C instrument. Figure 7.12 shows the DTA plots for the powder at different heating rates. The purpose of collecting data at different heating rates was to calculate the activation energy using an analytical method (Kissinger 1957).

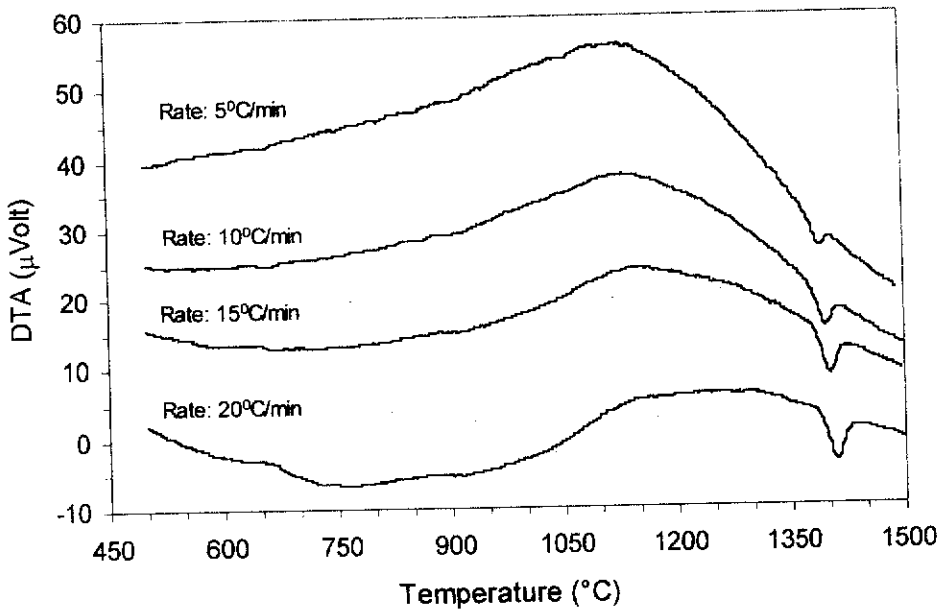

Figure 7.12. DTA thermograms of an alumina/AT (AAT) sample with ~30 wt% AT prepared by mixing alumina powder in $TiCl_4$.

The results in Figure 7.12 show that the shape and position of endotherms due to AT formation temperature are dependent on heating rate. Figure 7.13 depicts the formation temperature of AT at various heating rates.

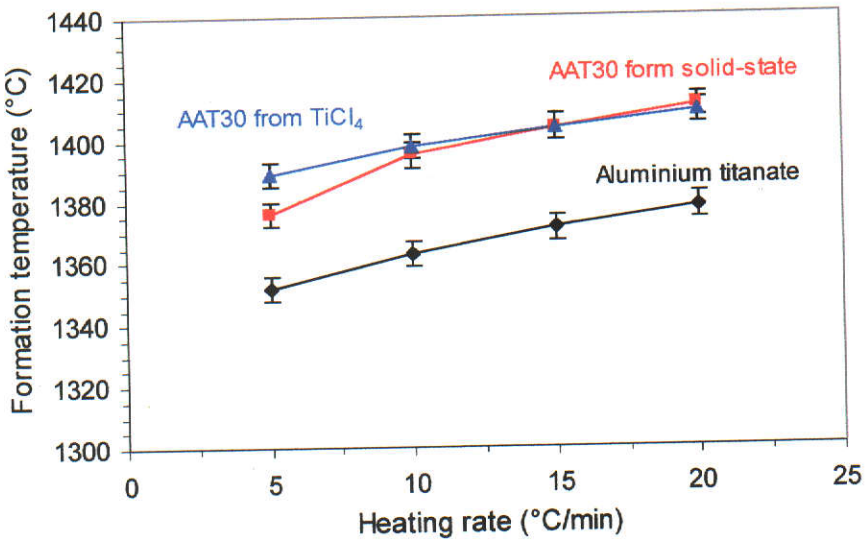

Figure 7.13. The formation temperature of AT from $TiCl_4$ infiltration compared to AAT30 and AT from solid-state-reaction at different heating rates.

From Figure 7.13, the formation temperature of AT occurs at between 1389 and 1409°C. The formation temperature increases with heating rate. The time required to form AT at a slow heating is longer than for fast heating. As a aconsequence, the formation temperature is lower and the endotherm is weaker and more diffuse.

The position of the endotherm peak also varies with heating rate. Generally, the peak temperature shifts to lower temperature with a decrease of heating rates and the peak shape becomes broader with an increase in crystal growth. The activation energy calculated using Equation (4.6) (Bansal *et al.* 1983) with the crystal growth dimension, $m = 3$ as explained in section 4.2.1 is shown in Table 7.3. The Table also contains the activation energy values of AT from the other authors (Sakabe *et al.* 1970; Dos-Santos and Kiminami 1977; Kato, Kobayashi and Daimon 1979; Yamaguchi, Hitoshi and Shimizu 1981) and this study for comparison.

Table 7.3. Activation energy of AT in alumina/aluminium titanate powders.

Additives	Method	Activation Energy (kJ/mol)	Reference
None	DTA	531(2)*	This study (30 wt% AT from α-Al_2O_3 + $TiCl_4$)
None	DTA	295(2)	This study (30 wt% AT from α-Al_2O_3 + TiO_2)
None	DTA	389(2)	This study (100 wt% AT from α-Al_2O_3 + TiO_2)
0.5-7 mole % Fe_2O_3	Kinetic	205.8	Sakabe *et al.* (1970)
None	Kinetic	279.1	Kato, Kobayashi and Daimon (1979)
None	DTA	370.7	Yamaguchi, Hitoshi and Shimizu (1981) (from Al and Ti alkoxides)
Mullite	DTA	243 to 282	Dos-Santos and Kiminami (1977)

*Number in parentheses is mean deviation based on the best-fit data and model.

The activation energy obtained for this route is higher than values for AAT and AT obtained by other workers using the solid-state reaction. Kato *et al.* (1979) obtained an activation energy of 279.1 kJ/mole for pure AT. The methods of preparation can also give different values. Yamaguchi *et al.* (1981) found an activation energy of 380.7 kJ/mole for AT prepared from mixed powder of Al and Ti alkoxides. The presence of additive can also affect the activation energy. Sakabe *et al.* (1970) obtained an activation energy of 205.8 kJ/mole for AT containing (0.5-7 mole%) Fe_2O_3. The higher value obtained in this work (Table 7.3) can be attributed to the presence of alumina which acted as constraint to the crystallisation of AT.

7.4 STUDIES ON PHASE COMPOSITION

7.4.1 Mass Increment

The samples for this study were prepared by full infiltration of the preform. Immersion was conducted either once or twice. The porosity of alumina preforms was ~45-50% (Table 7.1). The mass increments for the samples with one infiltration (T_1, T_2) and two infiltrations (T_3, T_4) are shown in Table 7.4.

Table 7.4. The comparison of mass increments between single and multiple infiltrations.

Sample	Mass increments wet, Δm_w (%)	Mass increments dry (60°C), Δm_d (%)	Mass increments Sinter, Δm_s (%)
T_1	18.2(5)*	6.9(4)	4.1(3)
T_2	18.0(6)	7.0(5)	4.2(2)
T_3 (2x)	22.4(4)	10.1(3)	5.6(3)
T_4 (2x)	22.3(5)	10.2(3)	5.6(1)

* Number in parentheses is estimated standard deviation (σ).

The results in Table 7.4 show that the mass increment for single infiltration is 18 %, whereas for double infiltrations it is 22%. The difference in mass between single and double infiltrations is 4%. Thus, it is expected that the AT content in samples T_3 and T_4 will be higher than in the samples T_1 and T_2.

After drying, all the samples were sintered at 1600°C for 4 h. Table 7.4 shows the increment in mass after sintering. The mass increment of samples which were infiltrated once is 4.15% and twice is 5.64%. The mass increment of sintered samples between single and double infiltrations is ~1.5%. This additional amount could significantly increase the phase abundance of AT in the twice-infiltrated samples.

7.4.2 Depth Profiling by XRD

The samples prepared from the above-mentioned infiltration process are expected to show a graded concentration behaviour where the outer surface is AT-rich whereas the inner body is poor in AT. The formation of AT is believed to occur as follows:

$$TiCl_4 + 4H_2O \rightarrow Ti(OH)_4 + 4HCl \qquad 7.3(a)$$

$$Ti(OH)_4 \rightarrow TiO_2 + 2H_2O \qquad 7.3(b)$$

$$TiO_2 + Al_2O_3 \rightarrow Al_2TiO_5 \qquad 7.3(c)$$

In order to examine the graded compositional profiles, samples T_1 and T_3 were cut into thin slices with the thickness of ~1 mm. The depth corresponding to

each slice is shown in Table 7.5. The corresponding XRD patterns for the slices are shown in Figure 7.14 and 7.15.

Table 7.5. The depth of slices for samples T_1 and T_3.

Samples	Slice No.	Depth (mm)
T_1 Single infiltration	1	0
		0.9
	2	1.3
		2.1
	3	2.5
		3.4
T_3 Double infiltrations	1	0
		0.8
	2	1.2
		2.0
	3	2.4
		3.1

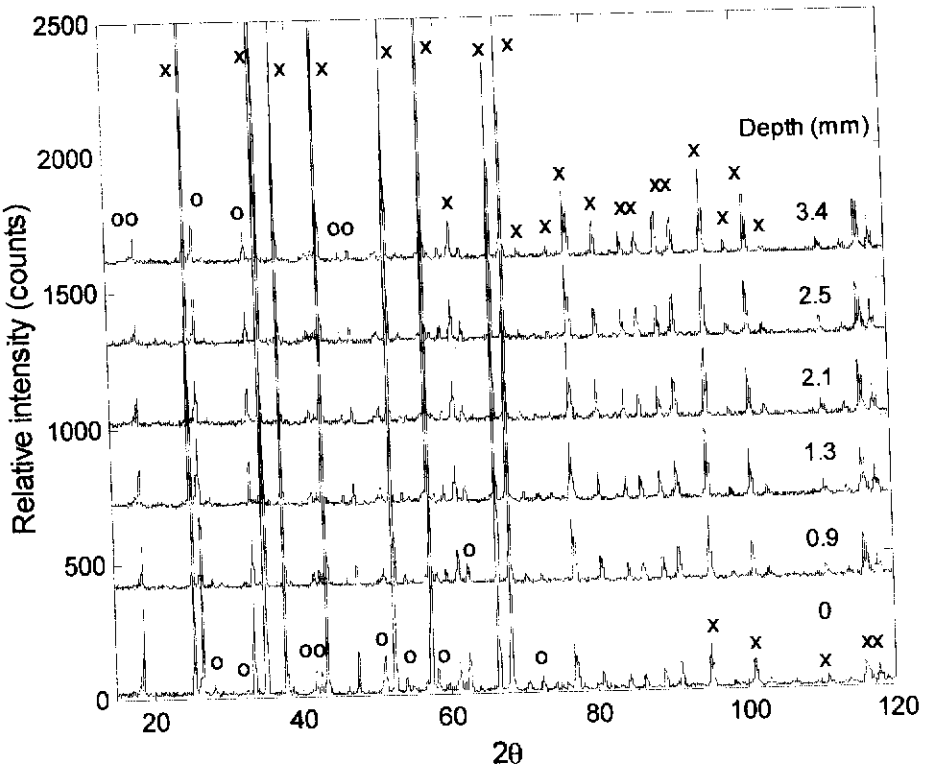

Figure 7.14. XRD patterns for sample T_1 at various depths. Depth 0 corresponds to the top of the surface. Legend: x = alumina and o = aluminium titanate. Wavelength = 1.5418 Å.

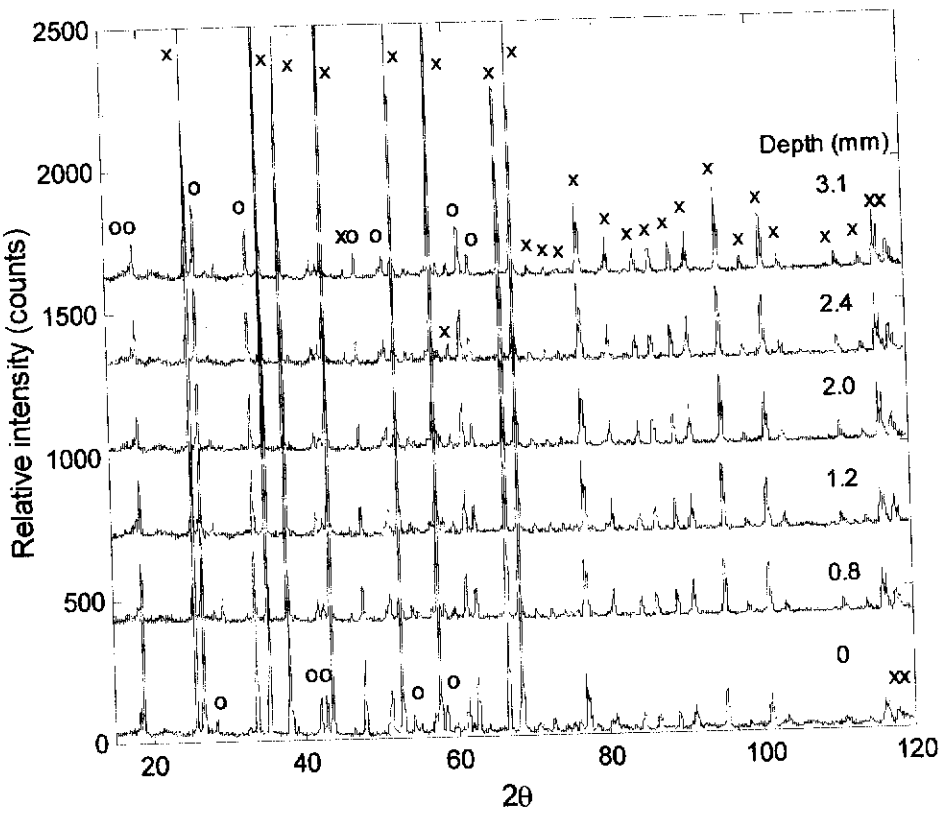

Figure 7.15. XRD patterns for sample T_3 at various depths. Depth 0 corresponds to the top of the surface. x = alumina and o = aluminium titanate. Wavelength = 1.5418 Å

The AT peaks for sample T_3 are considerably more intens than in sample T_1 thus indicating a higher content of AT in the former. The XRD patterns for both samples T_1 and T_3 show that only two major phases were present *ie.* alumina and AT. The *Rietica* software package program (Hunter 1997) was used to analyse the relative phase abundances by Rietveld pattern-fitting. The graph of AT content versus depth for both samples is shown in Figure 7.16.

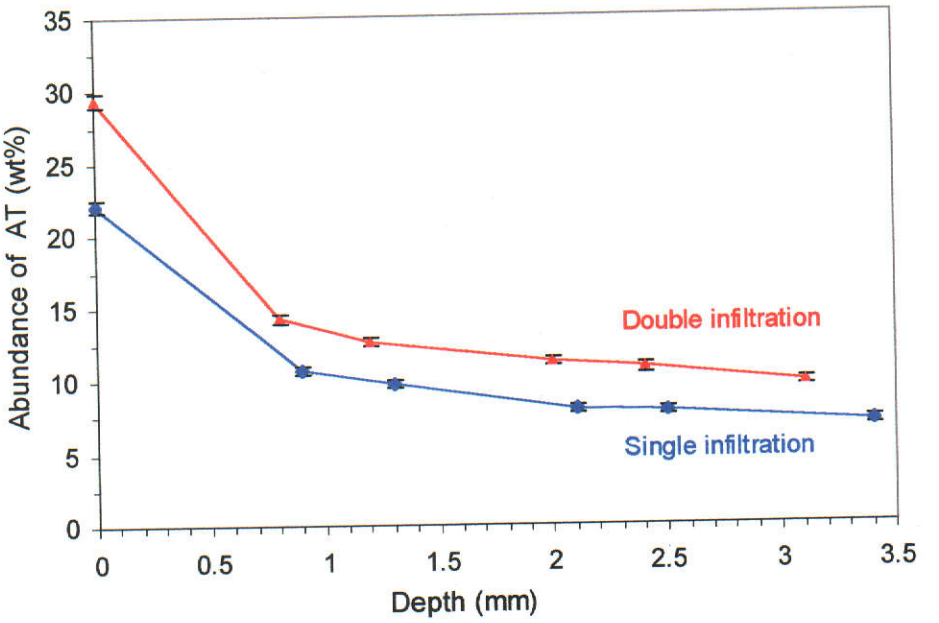

Figure 7.16. Abundance of AT as a function of depth for samples T_1 (♦) and T_3 (■). Error bars indicate two estimated standard deviations (σ).

The results in Figure 7.16 show that the abundance of AT in sample T_3 is clearly higher than in sample T_1. This agrees well with the mass increment results shown in Table 7.4. Hence multiple infiltrations can offer an easy process to increase the phase abundance of AT in the sample. Prolonging the infiltration time would further enhance the rate of infiltration and thus the content of AT.

The AT content decreases gradually with depth (Figure 7.16). From the surface to a depth of 1 mm, the AT content decreases sharply to approximately 50%. Beyond the depth of 1 mm, the AT content decreased gradually. The same behaviour was also observed for alumina/calcium-hexaluminate composites prepared by infiltration (Asmi *et al.* 1999).

7.4.3 Depth Profiling by GISRD

Grazing incidence synchrotron radiation diffraction (GISRD) was used to depth-profile the phase abundance behaviour at the near-surface (section 3.3.4). Many authors have suggested using GISRD to analyse depth-profiles of phase composition at the near-surface of graded ceramics (Skala 2000; Pratapa 1997). GISRD data were collected at the Photon Factory in Tsukuba, Japan using the BIGDIFF diffractometer. Figure 7.17 shows the GISRD patterns for sample T_1 at various grazing incidence angles (α).

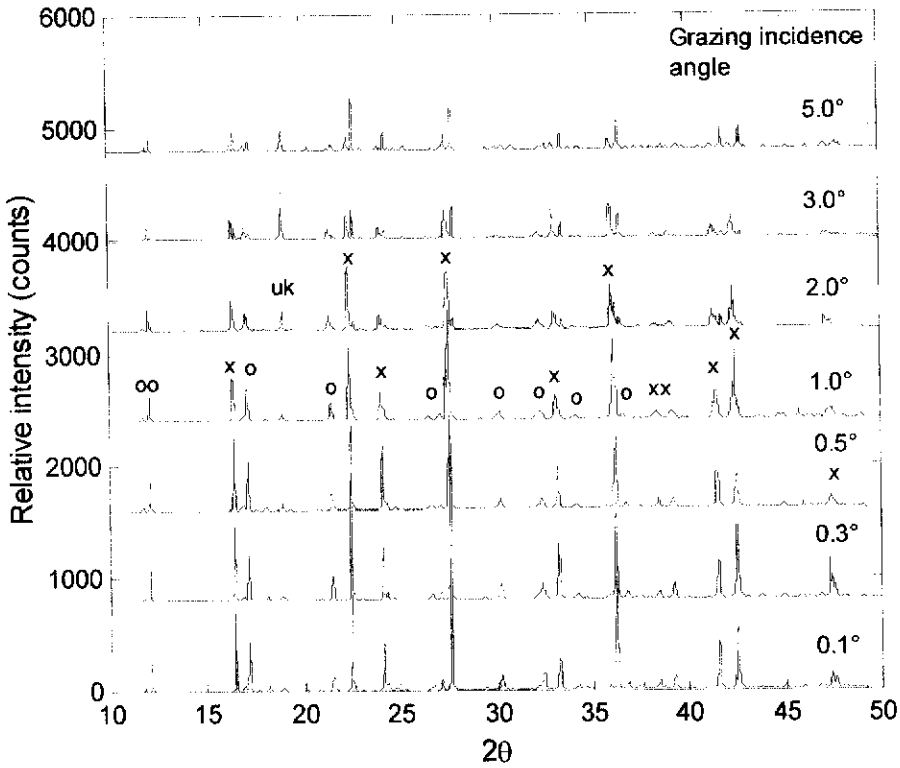

Figure 7.17. GISRD patterns of sample T_1 on slice 1 (top surface) at the grazing incidence angles 0.1, 0.3, 0.5, 1.0, 2.0, 3.0 and 5.0°. Legend: o, x, and uk are AT, alumina and unknown phases, respectively. Wavelength = 1 Å.

When the grazing incidence angle is small *ie.* 0.1°, the sample area bombarded by photons is wide but the beam only penetrates to a very shallow depth (*ie.* tens of nanometers). That means the photons received by the detector will be almost the same as the incidence beam. As the grazing incidence angle increases *eg.* 0.3°, the beam will hit a smaller area but penetrates deeper. When the grazing incidence angle is increased further to a larger value *eg.* 5.0°, the beam will hit an even smaller area and penetrate much deeper. Thus the depth-profile phase abundance of a sample can be readily characterised by varying the grazing-incident angle (α). The variation of peak intensity ratio between AT (*110*) and alumina (*104*) as a function of grazing-incidence angle is shown in Figure 7.18.

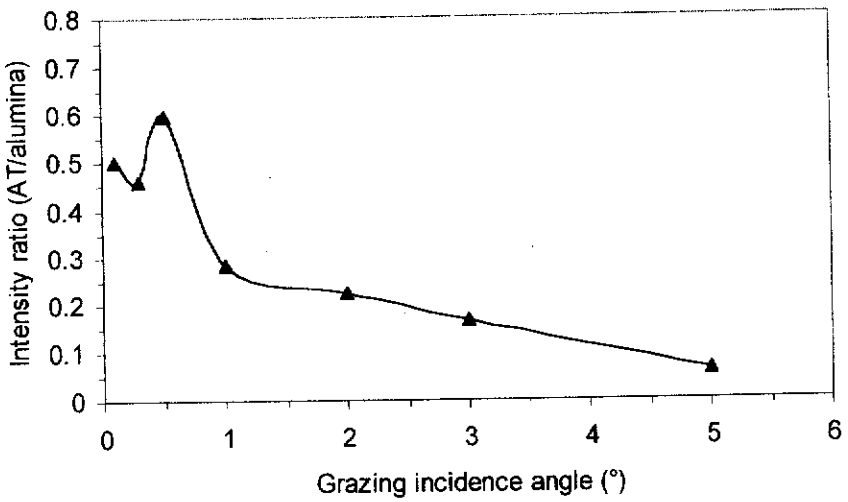

Figure 7.18. Variation of peak intensity ratio between AT (*110*) and the alumina (*104*) as a function of grazing-incidence angle.

The results in Figure 7.18 clearly show the gradation of AT intensity within the near surface. Furthermore, the results show that the content of AT peaked *not* on the surface but at several micrometres below the surface. Assuming that the intensity represent the phase abundance, it is evident that the phase abundance of AT decreases with sample depth or grazing incidence angle. Since the grazing incidence angle is related to the penetration depth, hence the phase abundance of AT decreases

with depth. However, before describing the penetration depth, the critical angle, α_c should be determined first

Case of $\alpha < \alpha_c$ (Below the Critical Angle)

For angles below the critical value, α_c the penetration depth, l can be calculated from (Vineyard 1982):

$$l \cong \frac{\lambda}{2\pi(\alpha_c^2 - \alpha^2)^{1/2}} \tag{7.4}$$

where λ is the wavelength of the radiation. Critical angle, α_c can be approximated by (Barner 1992):

$$\alpha_c = 1.6 \times 10^{-3} \rho\lambda \tag{7.5}$$

where α_c is in radians, ρ is density in g/cm^3 and λ is the wavelength in Å. From Figure 7.16, the weight percentage of AT at the surface is 22 wt%. For this composition, the theoretical density is 3.920 g/cm^3. Figure 7. 19 shows the calculated penetration depth from Equations (7.4) and (7.5) versus α.

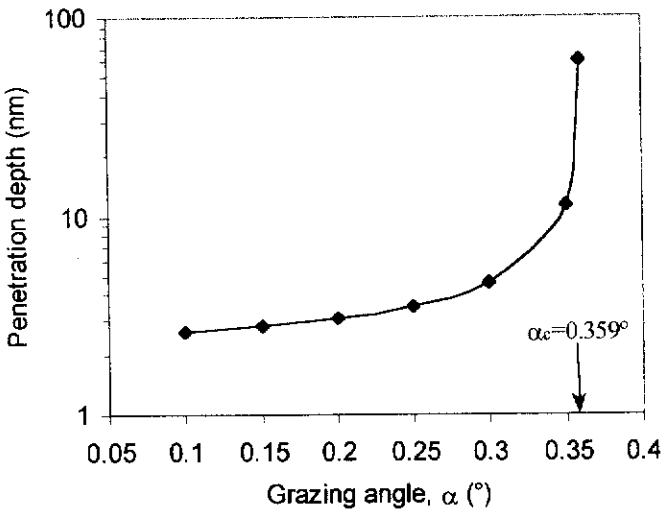

Figure 7.19. Penetration depth below the critical angle for 22 wt% AT in the AAT composite. Wavelength = 1 Å.

Case of $\alpha > \alpha_c$ (Above the Critical Angle)

The penetration depth, l increases very sharply according to the formula:

$$l \cong \frac{2\alpha}{\mu} = \frac{2\alpha}{(\mu_m \rho)} \tag{7.6}$$

where μ is the linear absorption coefficient of matter, μ_m is the mass attenuation coefficient and ρ is the phase density. For a compound or mixtures, μ_m is:

$$\mu_m = \sum_i w_i \mu_{mi} \tag{7.7}$$

where w_i and μ_{mi} are the weight fraction and mass absorption coefficient, respectively, for element i. For Al, Ti and O, the μ_{mi} values are 13.5, 58.6 and 3.5 cm^2/g respectively at 1Å (Liebhafsky *et al.* 1972). The μ_m for 80 wt% Al_2O_3 and 20 wt% Al_2TiO_5 can be calculated using Equation (7.7) and result 11.2 cm^2/g. The density of AAT containing 22 wt% AT is 3.926 g/cm^3, and then the value of μ is 44.0/cm. The calculated penetration depth above the critical angle are shown in Figure 7.20. The results show that the penetration depth increases with the grazing incidence angle.

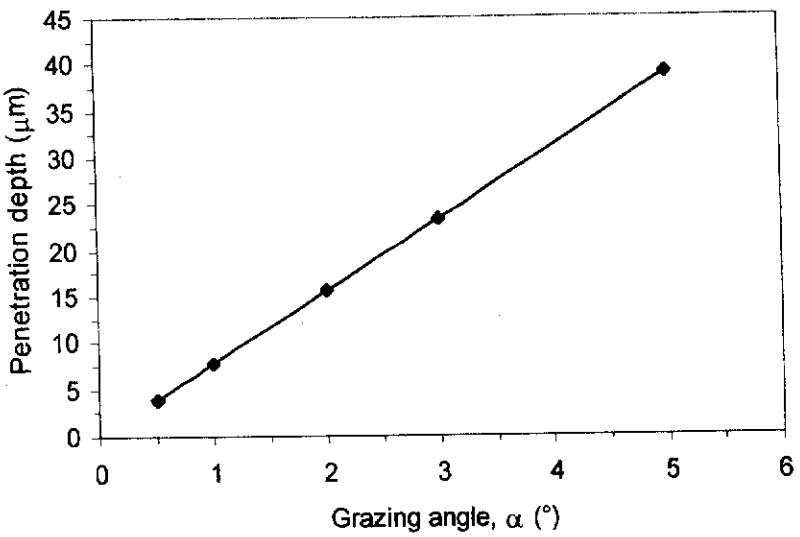

Figure 7.20. Penetration depths above the critical angle for the graded AAT sample (22 wt% AT in AAT). Wavelength = 1 Å.

The penetration depth increases much more rapidly with grazing angle above the critical angle (see results in Figure 7.20). The phase abundance of AT clearly decreases with depth but reaches a peak at a depth of ~4 μm below the surface. In order to confirm the graded compositional behaviour, a polished cross-section of the sample was viewed using SEM with backscattered imaging (Figure 7.21). The white areas represent Ti that formed in Al_2TiO_5. The graded compositional behaviour is evident in Figure 7.21.

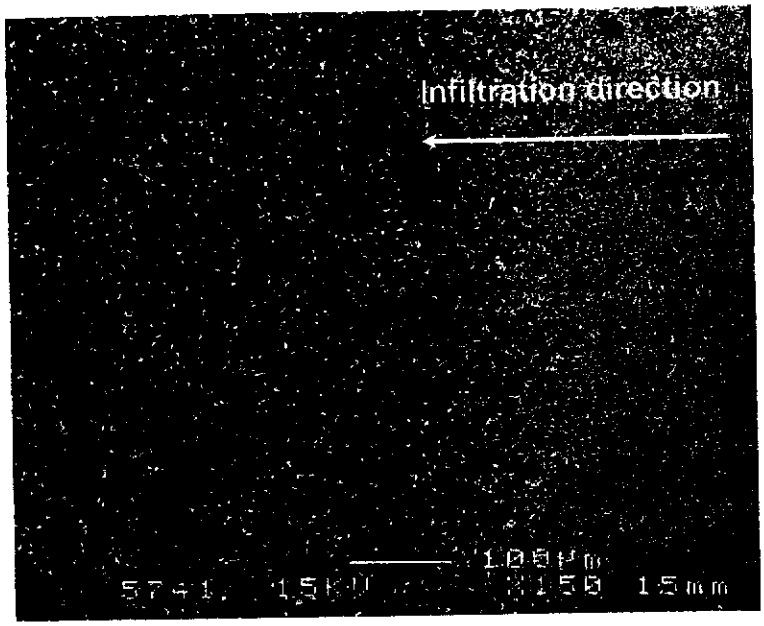

Figure 7.21. Back-scattered scanning electron micrograph showing the gradation of AT distribution within the sample. Direction of infiltration is from right to left.

7.5 DEPTH PROFILLING OF GRADED Al_2O_3/AT SAMPLES INFILTRATED IN ONE DIRECTION

7.5.1 Mass and Shape Change

Before infiltrating with $TiCl_4$, the cylindrical alumina preforms were weighed to ascertain the mass change before and after infiltration. The sides of preforms were shielded with plastic tape to allow the infiltrant to diffuse only from top to bottom. The depth profile results, presented in section 7.4.2 for fully-infiltrated samples, showed that the concentration of AT decreased rapidly, and after ~1 mm depth its concentration decreased slowly. This was the result of full immersion of preform to the infiltrant without shielding where the infiltrant diffused into the preform from all directions.

For comparison purposes, samples were also infiltrated twice. The mass changes in the samples after double-infiltration are shown in Table 7.6. Two samples were prepared with the same procedure where sample one (FGM_1) was used for XRD depth profiling and sample two (FGM_2) for SEM examination and hardness measurement.

Table 7.6. Mass change after drying in oven and sintering at 1600°C.

Sample	Mass increment after drying, Δm_{dry} (%)	Mass increment after sintering, Δm_{sin} (%)
FGM_1	9.7(6)*	7.5(3)
FGM_2	10.0(3)	7.8(4)

*Number in parentheses is estimated standard deviations (σ).

The density and porosity of the sintered samples, measured according to Australian Standard (1989), are given in Table 7.7. The samples show excellent densification as indicated by their low porosity (~ 1%). The measured density lies between the theoretical densities for pure alumina (3.987 g/cm^3) and AT (3.700 g/cm^3).

Table 7.7. The density and porosity of samples after sintering at 1600°C.

Sample	Density (g/cm^3)	Porosity (%)
FGM_1	3.705(62)	1.2(2)
FGM_2	3.803(73)	1.1(1)

The shrinkage behaviour is a criterion for ascertaining the presence of graded concentration in the sintered samples. Figure 7.22 shows the shape of samples after sintering at 1600°C for 6 h. The figure shows top and side views respectively.

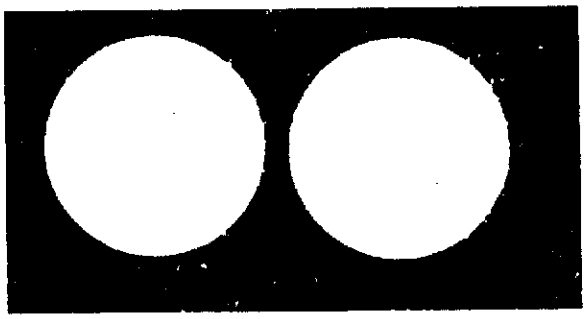

(a) Top view

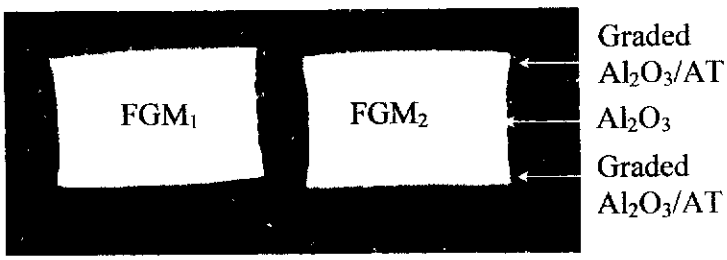

(b) Side view

Figure 7.22. Shape of samples FGM_1 and FGM_2 after sintering at 1600°C for 6 h. (a) top view and (b) side view (hourglass shape).

The shape of the fired samples reflects the differential shrinkage due to densification variations. The alumina region shrank more than the graded Al_2O_3/AT region because the latter has a high content of AT near the surface which hindered the kinetics of sintering and densification. Furthermore, the AT phase is less dense phase than alumina. Similar non-uniform shrinkage can also arise from variations in green density within the sample (Figure 7.23).

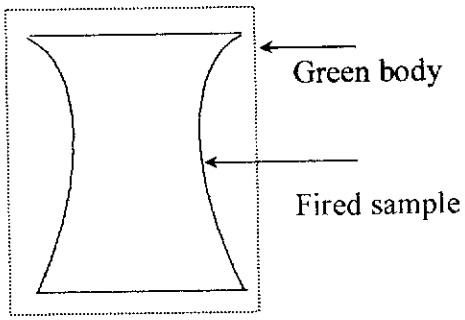

Figure 7.23. Pressed cylindrical sample before and after firing. Firing shrinkage of pressed sample with differential shrinkage due to green density variations (After Kingery, Bowen and Uhlmann 1976).

A major cause of warping during firing is density variations in the green body. The density after firing is nearly uniform, and there is higher shrinkage for the parts that had a low density than for the parts that had a high density in the green body. The presence of temperature gradients can also be a source of warping behaviour during firing. Another source of warpage in firing is the preferred orientation of platy grains during the forming process. The alumina preform in this experiment was pressed to 100 MPa using sodium stearate as lubricant to minimise the build-up of graded density in the green body. However, during the infiltration process, the preform will absorb the infiltrant in different amounts and form the less dense AT phase near the top and bottom surfaces, causing the middle section of the sample to shrink more.

7.5.2 Depth Profiling of Phase Composition by XRD

Depth profiling of phase abundance was conducted on thin-slices (~1 mm) cut from the sample (section 3.3.2). The corresponding XRD patterns are shown in Figure 7.24. Search/match analysis was employed to identify the individual peak in each pattern. Alumina, AT, and rutile, and no other phases, were detected. Alumina and AT phases were observed at each depth but the rutile phase appeared only at depths of 1.9 and 2.3 mm. The content of rutile increased with depth which may be attributed to an incomplete reaction or decomposition of AT during furnace cooling through the 900 - 1200°C range. Unassigned peaks were not detected at each depth indicating that the qualitative phase analysis was acceptable.

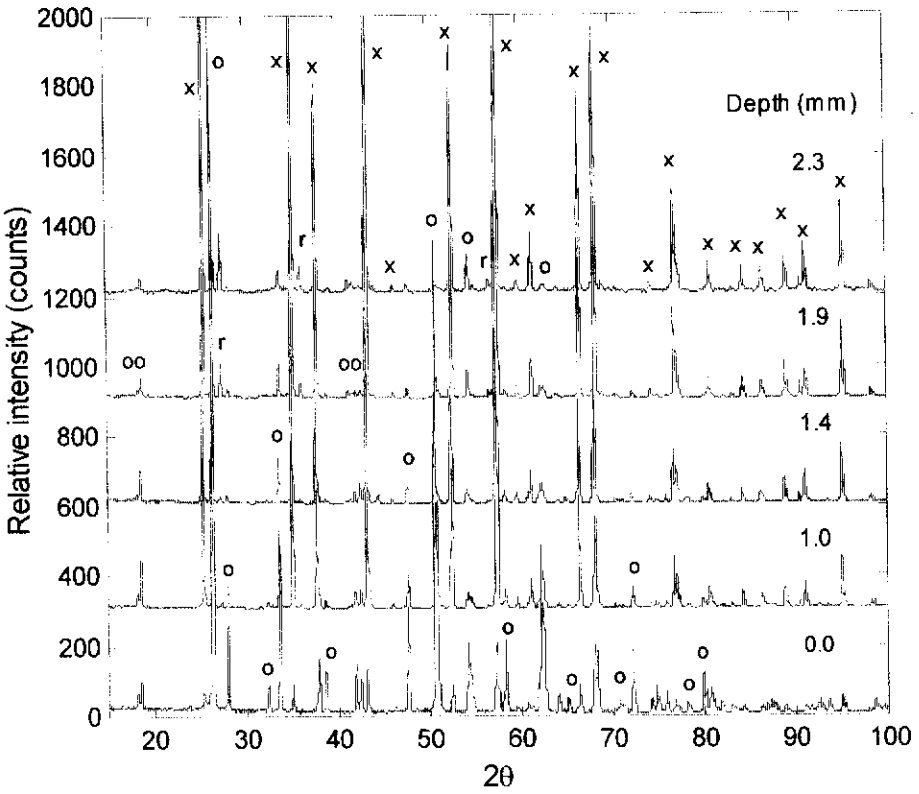

Figure 7.24. X-ray diffraction patterns of graded sample for various depths. o = AT, x = alumina and r = rutile. Wavelength = 1.5418 Å.

Generally the AT peaks decreased gradually from the surface to the inner body. This behaviour is particularly obvious for the Bragg peaks at 2θ of 18.4 and 18.8°. Rietveld refinement using *Rietica* program (Hunter 1977) was conducted to

examine the phase abundance and the results are listed in Table 7.8. The surface of the sample appeared to display some preferred orientation. In this refinement, the preferred orientation was used March model at *hkl (200)*.

Table 7.8. Relative phase abundances for sintered AAT sample (FGM_1) at various depths.

Depth (mm)	Rwp	GOF	Phase abundance (esd, σ)		
			Alumina	AT	Rutile
0.0	21.8	4.8	12.24(30)	87.76(82)	0
1.0	13.2	2.4	73.54(48)	26.46(23)	0
1.4	16.5	2.5	82.08(64)	17.92(24)	0
1.9	12.7	2.4	88.48(50)	9.74(16)	1.78(5)
2.3	13.7	2.1	90.97(55)	6.54(19)	2.48(7)

Note: esd = estimated standard deviation.

The relative phase abundance of alumina increased with depth, while that the AT phase decreased. It is interesting to note that the rutile phase was not detected up to the depth of 1.4 mm, and then was detected at 1.9 mm and its content increased to ~ 2.5 wt% at 2.3 mm depth. Table 7.8 clearly confirms the presence of graded phase abundance as result of infiltration processing. Figure 7.25 shows a comparison of the depth profile of the AT phase observed by various researchers.

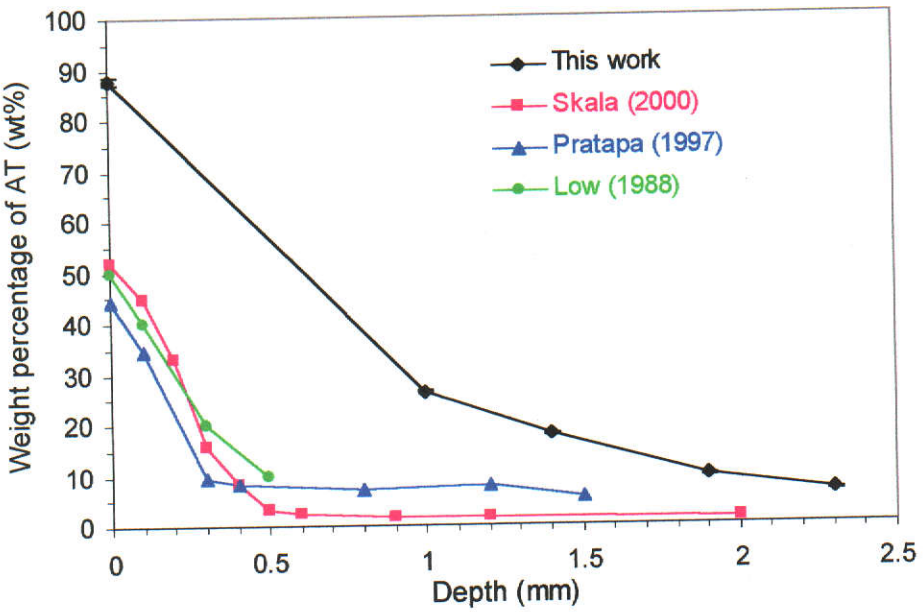

Figure 7.25. Depth profiles for the AT phase in graded AAT obtained by various researchers, including this study. Error bars indicate two error estimated deviations (σ).

The XRD depth profile shows that the top surface region is very rich in AT (~ 88 wt%) with the concentration decreasing slowly as the depth increases towards the middle region of the sample. The amount of AT formed here is very large when compared to other workers. For instance, Pratapa (1997) found 46 wt% AT phase on the surface of graded AT/ZrO_2-alumina system, with the value decreasing substantially to 7 wt% at a depth of 0.8 mm. Low (1998) found 50 wt% AT on the surface of graded AAT composites and decreased to 10 wt% at the depth of 0.5 mm. Similarly Skala (2000) obtained 52 wt% on the surface which decreased to only 3 wt % at the depth of 0.5 mm in AAT composite. This suggests that uni-directional and double-infiltrations with the aid of plastic-shield is an effective method for increasing the content of AT near the surface and for preventing a very rapid decrease in the graded AT content.

7.5.3 Microstructural Studies

The graded microstructures of the FGMs was examined using field-emission scanning electron microscopy. Sample FGM_2 was cut diagonally from top to bottom

using a precision diamond-blade cutter. The cross-section was then polished to a 1 μm surface finish. The sample was then thermally-etched at 1300°C for 15 min to reveal the microstructure.

Figure 7.26 shows SEM micrograph of the region rich until lack in AT. Based on XRD phase analysis of the top surface (Table 7.8), the major phase is AT (~ 88 wt%). Microcracking within some of the AT grains are clearly evident. This cracking behaviour is due to the display of thermal expansion anisotropy of AT upon cooling to room temperature (Bennison and Lawn 1989). In addition, the presence of AT within a ceramic matrix c

an prevent the grain-coarsening (Runyan and Bennison 1991).

Figure 7.26 also shows the microstructure of the bottom surface which is rich in AT. The AT grains here do not appear to show microcracks probably due to their fine size. Based on the XRD phase analysis described earlier, the AT content decreased sharply with depth. The microstructures at the middle region that is poor in AT are shown in Figures 7.26. Very few AT grains are observed here and the alumina grains appear to grow larger in size due to the lack of AT to hinder grain growth. The size of the alumina grains appears to coarsen as the content of AT present decreases.

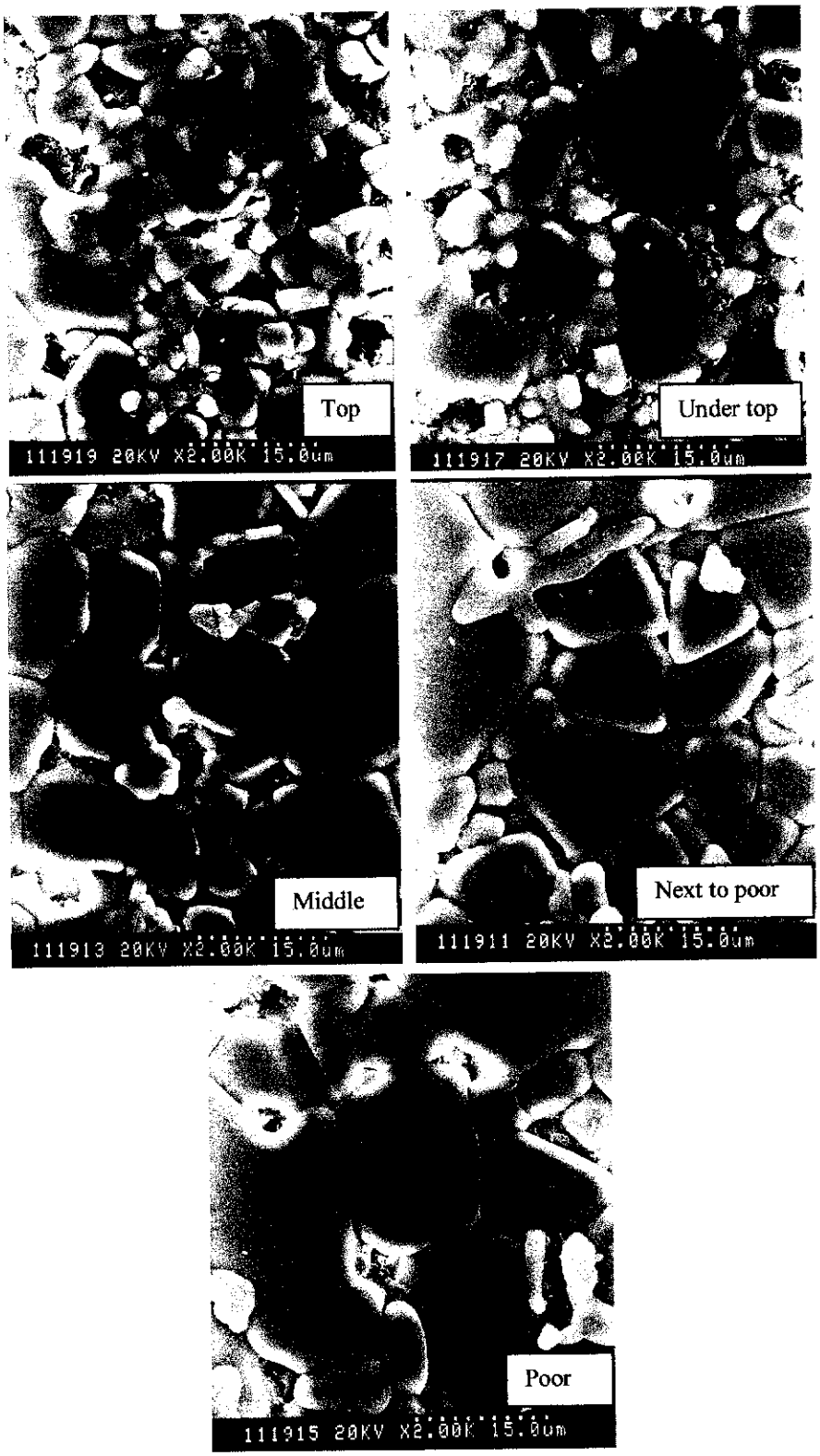

Figure 7.26. Cross section SEM for FGM from the top to bottom regions (rich until lack in AT). The arrow indicates the microcrack along an AT grain. Note that the grain sizes of Al_2O_3 from the top to bottom regions are ~ 9(1), 13(4), 13(3), 13(2) and 15(4) μm, respectively.

Figure 7.27 shows the variations of alumina grain size in the graded AAT sample due to the presence of AT. It is very clear that the grain size of alumina in AT-rich region is relatively small whereas in AT-poor region the grain size is considerably larger indicating that the grain growth of alumina is effectively controlled by the presence of AT.

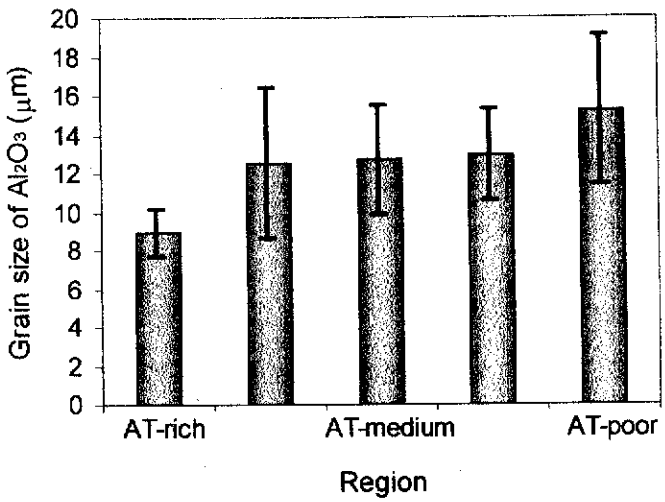

Figure 7.27. The grain size of alumina for regions containing various concentrations of AT, *ie*. AT-rich, AT-poor or AT-medium. Error bars indicate two estimated standard deviations (2σ).

7.6 STUDIES OF MECHANICAL PROPERTIES

7.6.1 Hardness

The Vickers hardness was measured according to the procedure outlined in section 3.4.6. The hardness profile was measured along a polished cross-section of the FGM. The purpose of this measurement was to examine the effect of the graded microstructure and hence the depths on the variation of hardness. Hardness was measured at depths of 0.52, 1.39, 1.60, 1.96, 2.20 and 2.43 mm with a load 3 kg. The Vickers hardness as a function of depth is shown in Figure 7.28.

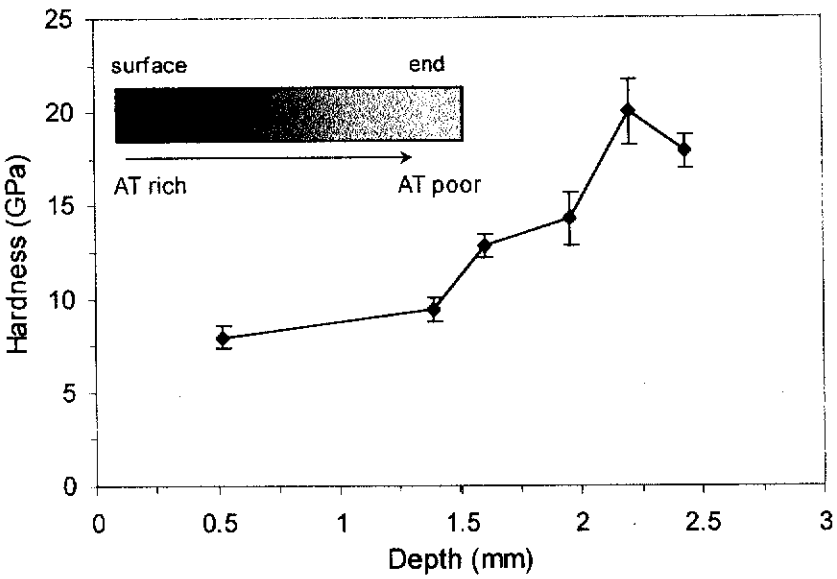

Figure 7.28. Vickes hardness of alumina/AT (AAT) FGM as a function of depth with load of 3 kg. Error bars indicate two mean deviations (±).

It is clear that the hardness increased with depth. This result is consistent with the results for AAT composites prepared by solid-state reaction where hardness decreased with an increase of AT content (Figure 5.13 in section 5.5). The highest hardness of ~ 20 GPa was obtained at 2.2 mm depth which contains ~ 8 wt% AT (see Figure 7.25). This value is higher than the hardness of AAT prepared by solid-state reaction (Chapter 5.5) which is of ~ 11 GPa. This superior hardness is attributed to unique microstructure of this material. The same trend of hardness was also found in PSZ materials prepared by plasma spraying (Fukushima, Kuroda and Kitahara

1990) where the hardness increased with ZrO_2 (8% Y_2O_3) content. Skala (2000) also showed that the hardness of a graded AAT system increased as the depth within the sample increased. Pratapa and Low (1998) and Asmi (2001) also reported the same behaviour in graded AAT/zirconia and alumina/calcium-hexaluminate systems, respectively.

7.6.2 Fracture Toughness

The fracture toughness of a ceramic material may be determined from the length of the crack propagation path formed at the corners of Vickers indentations. Unlike more classical brittle materials, the functionally-graded AAT system exhibited no cracks at any of the corners of the indentation site. Instead, it was found that a large degree of localised microcracking and a well-contained damage zone was formed in and around each of the indentation sites. Figure 7.29 shows several indentation sites for a graded AAT sample at 0.52, 1,39, 1.96 and 2.43 mm depths prepared by single direction infiltration. The optical micrographs show some short cracks not only at the corners but also at the sides of indent. The absence of any long propagating cracks emanating from the corners of Vickers indent implied that the graded sample is damage resistant or flaw-tolerant.

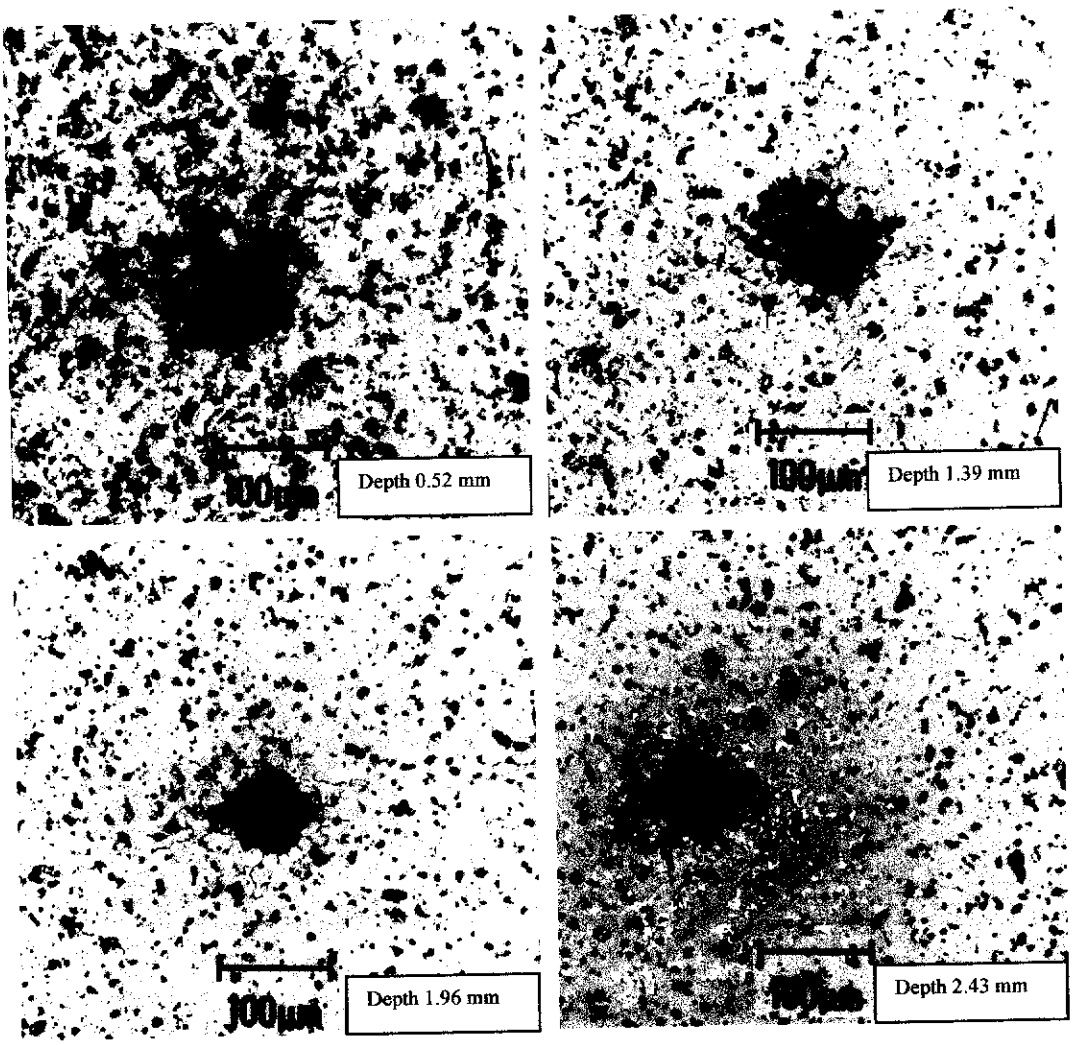

Figure 7.29. Optical micrograph of Vickers indentation on the polished surface for graded AAT sample. The white phase is AT and grey phase is alumina. Dark regions represent porosity or grain pullout from polishing. Load used = 3 kg.

From the optical micrographs, it was very difficult to locate long propagating cracks due to Vickers indentation. In view of this, it was impossible to quantitatively determine the fracture toughness of this material using the Vickers microhardness test (Skala 2000; Partapa and Low 1998). It is worth noting that the ability of this graded material to tolerate damage is reminiscent of other damage-tolerant ceramic-based systems such as alumina/AT (Runyan and Bennison 1991; Padture *et al* 1991; Bartolome *et al.* 1996), mica/glass (Cai, Kalceff and Lawn 1994), Ti_3SiC_2 (El-Raghy

et al. 1997; Low *et al.* 1998), alumina/calcium hexaluminate (An and Chan 1996; An *et al.* 1996).

7.7 SUMMARY

A new, relatively simple infiltration method was used to fabricate functionally-graded AAT ceramic. The process involved the use of a low viscosity liquid to infltrate the alumina preforms. The alumina preforms were pre-sintered at 900, 1000, and 1100°C for 2 h to give sufficient porosity (~ 45%) for subsequent infiltration. The infiltration kinetics was studied to gain a better understanding of the complex processes involved.

The contact angle of zero was chosen for modeling the kinetics of infiltration. The Washburn model (1921) gave a pore-radius of 0.015 μm with water and 0.018 μm with $TiCl_4$ as infiltrant. These radii were confirmed with mercury porosimetry measurements and scanning electron microscopy. However, the results from SEM and mercury porosimetry gave a pore-radius an order of magnitude larger than that predicted by the model. A refined model based on a time-dependent contact angle which varied exponentially gave the best fit to the experimental data.

The effects of pre-sintering temperature, vacuum, types of infiltrants and multiple infiltrations have also been studied. Even though the porosity of the preforms at different pre-sintering temperatures was similar, the rates of infiltration for those preforms were different. It is proposed that other factors apart from porosity had an over-riding influence on the rate of infiltration in alumina preforms. The rate of infiltration was higher for water than for $TiCl_4$ by virtue of a much lower viscosity for water. The use of vacuum significantly increased the rate of infiltration due to an increase of net pressure. Multiple infiltrations also significantly increased the infiltration rate. Two scenarios were used to explain this behaviour *ie.* a decrease in pore radius and an increase in contact angle. A more likely reason was a decrease in the tortuosity as a result of the preceding infiltration cycle.

The formation temperature for AT in the AAT system varied from 1389 to 1409°C depending on the heating rates. A slow heating rate gave a lower formation temperature and vice versa for a fast heating rate. When compared to solid-state derived AT (sectionr 4), the activation energy of AT synthesized from Al_2O_3 and $TiCl_4$ was higher.

XRD depth-profiles showed that the graded AAT system had the highest AT content on the infiltrated surface but decreased rapidly with depth. The converse was true for alumina. Similar results were observed from depth-profiles measured by GISRD where the intensity ratio between AT and alumina decreased grazing incidence angle. The content of AT was found to peak at ~3 μm below the surface. The graded microstructure was confirmed by backscattered SEM imaging.

A significant change in microstructure was observed due to the presence of dispersed AT. The grain size of alumina in the AT-rich region was smaller when compared to those in the region poor in AT. The presence of AT appeared to be effective in arresting the coarsening of alumina grains.

The hardness of graded AAT sample was depth-dependent and increased with depth which is consistent with the depth-profiling results from XRD, GISRD and electron microscopy.

The graded material displayed a high degree of damage tolerance according to Vickers indenttaion results. A damage zone with substantial microdamage due to interphase debonding and grain push-outs formed in the vicinity of the indent. There was no evidence of major crack formation.

CHAPTER EIGHT

CONCLUSIONS AND FURTHER WORK

8.1 CONCLUSIONS

The fabrication of alumina/AT (AAT) composites was studied using both solid-state reaction and infiltration. Analysis and characterisation of the phase assemblages, microstructure, physical and mechanical properties of AAT systems revealed that the properties vary as a function of aluminium titanate (AT) content. In functionally-graded AAT materials, the properties vary as a function of the depth.

The major findings from the study were as follows:

1. The use of rutile in processing AAT ceramics using solid-state reaction yielded materials with varying densities, shrinkages and porosities. As the content of AT increased, the porosity increased and the hardness decreased. The presence of AT resulted in lowering the densification temperature and the thermal expansion coefficient. The fracture toughness improved in samples containing 15–30 wt% AT.
2. The formation temperature and activation energy of AT depended on the methods of preparation and the starting material. The formation temperature of AT in AAT composites was heating-rate dependent. The activation energy of pure AT was higher than that of the AAT system.
3. The formation of AT in AAT was not instantaneous but occurred gradually. The formation of AT commenced at 1310°C and did not reach completion until 1370°C.
4. The use of β-spodumene in processing AAT ceramics using solid-state reaction yielded materials with varying densities, shrinkages, porosities, and formation temperatures. The hardness and fracture toughness decreased with increase in β-spodumene level. The incorporation of β-spodumene resulted in the formation of glassy phase as a result of phase separation. The existence of glassy phase was confirmed by TEM examination and analysis. AT formed at ~1310°C *prior* to the complete melting of β-spodumene at 1330°C. The

addition of β-spodumene (2–15 wt%) increased the lattice parameters and thermal expansion coefficient but the densification temperature decreased.

5. *In-situ* neutron diffraction showed that the rate of decomposition of pure AT at 1100°C was relatively fast. Decomposition commenced within the first 2 h and the AT abundance reduced to 28.5% after 5 h in air. Decomposition of AT in air was a bulk process whereas in vacuum it was surface-initiated. Controlled decomposition of AT in vacuum may offer a novel approach for the design of functionally-graded Al_2O_3-AT systems.
6. The addition of MgO was effective in stabilising AT against thermal decomposition at 1100°C both in air and in vacuum. Decomposition in both environments decreased the lattice parameters of AT relative to as-fired MgO-AT.
7. Experimental results showed that the infiltration rate of water and $TiCl_4$ in alumina preform was parabolic with time. Both the pressure and the viscosity of the infiltrant strongly influenced the rate of infiltration. The rate of infiltration was also found to be dependent on variables such as pre-sintering temperature of preforms and multiple infiltrations.
8. Depth-profiling of phase compositions and microstructure by XRD, GISRD and SEM has verified the existence of graded phase in the functionally-graded AAT system. The hardness was found to be depth-dependent with low values in the graded region and high values in the non-graded alumina layer. The presence of AT has imparted considerable improvement in damage-tolerance as evidenced by the absence of indentation cracking and the pronounced display of microdamage both within and in the vicinity of the indent.

8.2 FURTHER WORK

This research project has investigated the structure-property relationships of AAT ceramics synthesized by both solid-state and infiltration methods. A great deal of information regarding the character of AAT system has been revealed during the study. However, further research should be undertaken to better understand the interplay between preparation, composition, microstructure and mechanical

properties. This is essential if the full potential of these materials are to be utilised in various applications.

The major recommendations from the study are as follows:

1. The tortuosity of preforms pre-sintered at various temperatures should be investigated. This is essential for more precise modelling of the infiltration kinetics in relation to the pore-size and pore distribution. This would provide valuable information for precise control of the infiltration process.
2. The use of additives such as MgO or Fe_2O_3 should be considered for the sintering and thermal stabilisation of AAT composites.
3. The study of thermal shock resistance of AAT composites should be undertaken. This information is important for various engineering applications especially in situations where the environments demand a high degree of thermal shock resistance.
4. The feasibility of using controlled vacuum heat-treatment to fabricate functionally-graded AAT composites deserves further investigation. The chemistry of decomposition in vacuum needs to be fully understood to enable the precise control of the graded microstructures in terms of layer thickness and phase abundance.

REFERENCES

Aboudi, J., Pindera, M.J. and Arnold, S.M. (1999). Higher-Order Theory for Functionally Graded Materials, *Composite Part B*, **30**, 777-832.

Adamson, A.N. (1970). *Alumina Production: Principles and Practice*. Chemical Engineer, London, **239**, 156-171.

Ajit-Prasad, S.L., Mayuram, M.M. and Krishnamurthy, R. (1999). Response of Plasma-Sprayed Alumina-Titania Composites to Static Indentation Process. Materials Letters, 41, 234-240.

An, L., Chan, H.H. and Chan, H.M. (1998). High-Strength Alumina/Alumina Calcium Hexaluminate Layer Composites. *J. Am. Ceram. Soc.*, **81**, 3321-3324.

An, L., Chan, H.M., Padture, N.P. and Lawn, B.R. (1996). Damage-Resistance Alumina-Based Layer Copmposites. *J. Mater. Res.*, **11**, 204-207.

Anderson, H., Besch, W and Haberland, D. (1977). Investigation about Methods of Quantitative Evaluation of DTA Curves, *J. Thermal Anal.*, **12**, 59-68.

Asmi, D. (2001). *Microstructural Design and Characterisation of Alumina/Calcium-Hexaluminate Composites*. Curtin University of Technology Thesis.

Asmi, D. and Low, I.M. (1998). Processing of an In-situ Layered and Graded Calcium Hexaluminate/Alumina Composite. I. Physical Characteristics. *J. Europ. Ceram. Soc.*, **18**, 2019-2024.

Asmi, D., Low, I.M., Kennedy, S. and Day, R.A. (1999). Characteristics of a Layered and Graded Alumina/calcium-Hexaluminate Composite. *Mater. Lett.*, *40*, 96-102.

Asmi, D., Shi, C.G., Low, I.M. and Day, R.A. (1998). Physical and Microstructural Characteristics of β-Spodumene Modified Alumina/Calcium-Hexaluminate Composites, *J. Aust. Ceram. Soc.*, **34**(2), 155-160.

Austin, A.E. and Schwartz, C.M. (1953). The Crystal Structure of Aluminum Titanate. *Acta Crystallographica*, **6**, 812-813.

Australian Standards. (1989). Refractories and Refractory Materials-Physical Test Methods, Method 5: The Determination of Density, Porosity and Water Adsorption: **1774.5**, *Standards Australia*.

Avrami, M. (1939). Kinetics of Phase Change I, *Journal of Chemical Physics*, **7**, 1103-1112.

Bansal, G.K. Duckworth, W.H. and Niesz, D.E. (1976). Strength-Size Relations in Ceramic Materials: Investigation of an Alumina Ceramic. *J. Am. Cram. Soc.*, **59(11-12),** 472-478.

Bansal, N.P., Doremus, R.H., Bruce, A.J. and Moyhinan, C.T. (1983). Kinetics of Crystallisation of ZrF_4-BaF_2-LaF_3 Glass by Differential Scanning Calorimetry, *Journal of The American Ceramic Society*, **66(4),** 233-238.

Barner, P. (1992). Dynamic Diffraction Studies on the Synthesis of Ceramics Using Synchrotron Radiation. *Trans. J. Br. Ceram. Soc.*, **91(1),** 26-29.

Bartolome, J.F., Requena, J., Moya, J.S., Li, M. and Guiu, F. (1996). Cyclic Fatigue Crack Growth Resistance of Al_2O_3-Al_2TiO_5 Composites. *Acta Mater*, **44(4),** 1361-1370.

Bayer, G. (1971). Thermal Expansion Characteristics and Stability of Pseudobrookite Type Compound, Me_2O_5. *J. Less-Common Met.*, 24(129-138.

Bayususeno, A., Latella, B. A. and O'Connor, B. H. (1999). Resistance of Alumina-Spodumene Ceramics to Thermal Shock, *J. Am. Ceram. Soc.*, **82(4)**, 819-824.

Becher, P.F. (1991). Microstructural Design of Toughened Ceramic. *J. Am. Ceram. Soc.*, **74(2),** 255-269.

Bennison, J. and Lawn, B.R. (1989). Role of Interfacial Grain-Bridging Sliding Friction in the Crack-Resistance and Strength Properties of Nontransforming Ceramics. *Act. Metall.*, 37(10), 2659-2671.

Bhattacharyya, B.N. and Sudhir Sen. (1963). Aluminium Titanate. *Cent. Glass Ceram. Inst. Bull.*, **10(4)**, 115-23.

Boch, P., Chartier, T. and Huttepain, M. (1986). Tape Casting of Al_2O_3/ZrO_2 Laminated Composites. *J. Am. Ceram. Soc.*, **69(8),** C191-C202.

Bragg, W.H. and W.L. Bragg. (1916). *X-rays and Crystal Structure*. Bell and Sons, London.

Braun, L.M. Bennison, S.J. and Lawn, B.R. (1992). Objective Evaluation of Short-Crack Toughness Curves Using Indentation Flaws: Case Study on Alumina-Based Ceramic. *J. Am. Ceram. Soc.*, **75,** 3049-3054.

Brook, R.J. (1976). Controlled Grain Growth. In *Treatise in Materials Science and Technology* (Ed. Wang, F.F.Y). Academic Press, New York, 331-364.

Buckley, C.E., Manurung, P. and Low, I.M. (2000). Modelling the Liquid Infiltration Kinetics in Alumina Preforms. *J. Aust. Ceram. Soc.*, **36(1),** 127-134.

Buessen, W.R., Thielke, N.R. and Sarakauskas, R.V. (1952). Thermal Expansion Hysterisis of Aluminium Titanate, *Ceramic Age*, **60(5)**, 38-40.

Buscaglia, V., Caracciolo, F., Leoni, M., Nanni, P., Viviani, M. and Lemaitre, J. (1997). Synthesis, Sintering and Expansion of $Al_{0.8}MgO_{0.6}Ti_{1.6}O_5$: A Low-Thermal-Expansion Material Resistant to Thermal Decomposition, *J. Mater. Sci*, **32(24)**, 6525-6531.

Buscaglia, V., Delfrate, A.M., Leoni, M., Bottino, M. and Nanni, P. (1996). The Effect of $MgAl_2O_4$ on the Formation Kinetics of Al_2TiO_5 from Al_2O_3 and TiO_2 Fine Powders, *J. Mater. Sci*, **31(7),** 1715-24.

Buscaglia, V. and Nanni, P. (1998). Decomposition of Al_2TiO_5 and Al_2(1-x)MgxTi(1+x)O_5 Ceramics. *J.Am.Ceram.Soc.*, **81(10),** 2645-2653.

Bush, E.A. and Hummel, F.A. (1959). High-Temperature Mechanical Properties of Ceramic Materials: II. *J. Am. Ceam. Soc.*, **42(8),** 388-391.

Caglioti, G., Paoleyyi, A. and Ricci, F.P. (1958). Choice of Collimators for a Crystal Spectrometer for Neutron Diffraction, *Nuclear Instruments*, **3**, 223-228.

Cai, H., Kalceff, M.A. and Lawn, B.R. (1994). Deformation and Fracture of Mica Containing Glass-Ceramics in Hertzian Contacts. *J. Mater. Res.*, **9**, 762

Cannon, R., Rhodes, W.H. and Heuer, A.H. (1980). Plastic Deformation of Fine-Grained Alumina (Al_2O_3): I, Interface-Controlled Diffusional Creep. *J. Am. Cram. Soc.*, **63(53-58),** 46-53.

Carman, P.C. (1956). *Flow of Gaseous through Porous Media.* Butterworths Scientific Publications, London.

Chen, P.L. and Chen, I.W. (1992). *In-situ* Alumina/Aluminate Platelet Composites. *J. Am. Cram. Soc.*, **75(9),** 2610-2612.

Chung, G.Y., McCoy, B.J., Smith, J.M. and Cagliostro, D.E. (1992). Chemical Vapour Infiltration: Modeling Solid Matrix Deposition for Ceramic Composites Reinforced with Layered Woven Fabrics, *Chem. Eng. Sci.*, **47(2),** 311-323.

Clarke, P.T. and Spink, J.M. (1969). The Crystal Structure of β-spodumene, $LiAlSi_2O_6$-II. *Kristallphysik*, **130**, 420-426.

Claussen, N. (1976). Fracture Toughness of Al_2O_3 with an Unstabilized ZrO_2 Disphersed Phase. *J. Am. Ceram. Soc.*, **59(1-2),** 49-51.

Coble, R.L. (1961). Sintering of Crystalline Solids II. Experimental Test of Diffusion Models in Porous Compacts. *J. Appl. Phys., 32(5),* 793-799.

Cutler, R.A., Mayhew, R.J., Prettyman, K.M. and Virkar, A.V. (1991). High-Toughness Ce-TZP/Al_2O_3 Ceramics with Improved Hardness and Strength. *J. The American Ceramics Society*, **74(1),** 179-186.

Demaestri, P.P., Giachello, A., Martinengo, P.C. and Majani, C. (1989). Influence of Some Oxides on the Thermal Characteristics of Stoichiometric Al_2TiO_5. *Euro-Ceramics*. **2**, 257-263.

Dollase, W.A. (1986). Correction of Intensities for Preferred Orientation in Powder Diffractometry: Application of the March Model, *Journal of Applied Crystallography*, **19**, 267-272.

Dorre, E. and Hubner, H. (1984). *Alumina: Processing, Properties and Application.* Springer, Heidelburg. Berlin.

Dos-Santos, J.L. and Kiminami, R.H.G.A. (1997). Study on the Sintering of Aluminium Titanate-Mullite by Using a Constant Heating Rate. *Key Eng. Mater.*, 132-136.

Dullien, F.A., El-Sayed, M.S. and Batra, V.K. (1977). Rate of Capillary Rise in Porous Media with Non-uniform Porous. *J. Colloids and Interface Science, 60*, 497-506.

Dullien, F.A.L. (1979). *Porous Media: Fluid Transport and Pore Structure.* Academic Press, New York.

Duran, A., Wohlfromm, H. and Pena, P. (1994). Study of the Behaviour of Al_2TiO_5 Materilas in Reducing Atmosphere by Spectroscopic Techniques. *J. Europ. Ceram. Soc.*, **13**, 73-80.

Dworak, W. and Fingerle, D. (1987). Ceramics Materials for Engines, *British Ceramics Transaction Journal*, **86**(6), 170-78.

Einset, E.O. (1996). Capillary Infiltration Rate into Porous Media with Application of Silicon Composite Processing. *J. Am. Ceram. Soc.*, **79(2),** 333-338.

Einset, E.O. (1998). Analysis of Reactive Melt Infiltration in the Processing of Ceramics and Ceramic Composites. *Chemical Engineering Science*, **53(5),** 1027-1039.

El-Raghy, T., Zavaliangos, A., Barsoum, M.W. and Kalidindi, S. (1997). Damage Mechanisms around Hardness Indentations in Ti_3SiC_2. *J. Am. Ceram. Soc.*, **80(2),** 513-516.

Epicier, T., Thomas, G., Wohlfromm, H. and Moya, J.S. (1991). High Resolution Electron Microscopy Study of the Cationic Disorder in Al_2TiO_5. *J. Mater. Res.*, **6**, 138-145.

Evans, A.G. (1990). Perspective on the Development of High-Toughness Ceramics. *J. Am. Ceram. Soc.*, **73(2),** 187-206.

Evans, A.G. and Charles, E.A. (1976). Fracture Toughness Determinations by Indentations. *Journal of the American Ceramic Society*, **59(7-8),** 371-372.

Fahrenholtz, W.G., Ewsuk, K.G., Loehman, R.E. and Lu, P. (1998), Kinetics of Ceramics-Metal Composite Formation by Reactive Metal Penetration. *J. Am. Ceram. Soc.*, **81(10),** 2533-41.

Fukui, Y. Yamanaka, N. and Enokida, Y. (1997). Bending Strength of an Al-Al_3Ni Functionally Grade Material, Centrifugal. *Composites Part B*, **28B**, 37-43.

Fukushima, T., Kuroda, S. and Kitahara, S. (1990*). Proc. 1st Int. Sympo. Functionally Gradient Materials,* Edit by Yamanouchi, M. Koizumi, M. Hirai, T. and Shiota, **I.**, 145-150.

Gani, M.S.J. and McPherson, R. (1973). The Enthalpy of Formation of Aluminium Titanate, *Thermochimica Acta*, **7**, 251-252.

Garret, R.F., Cookson, .J., Foran, G.J., Sabine, T.M., Kennedy, B.J. and Wilkins, S.W. (1995). Powder Diffraction Using Imaging Plates at the Australian National Beamline Facility at the Photon Factory. *Review of Scientific Instruments*, **66(2)**, 1351-1353.

Glass, S.J. and Green, D.J. (1987) Surface Modification of Ceramics by Partial Infiltration. *Advanced Ceramic Materials*, **2**, 29-31.

Green, D.J., Hannink, R.H.J. and Swain, M.V. (1989). *Transformation Toughening of Ceramic*. CRC Press, Boca Raton, Florida.

Gregory, C., Stangle and Miyamoto, Y. (1995). FGM Fabrication by Combustion Synthesis. *MRS Bulletin*, 52.

Grier, D. and McCarthly, G. (1991). ICDD Grant-in-Aid, North Dakota State University, USA.

Gutierrez-Alejandre, A., Gonzalez-Cruz, M., Trombetta, M., Busca, G. and Ramirez, J. (1998). Characterisation of Alumina-Titania Mixed Oxide Supports Part II: Al2O3-Based Supports. *Microporous and Mesoporous Materials*, **23**, 265-275.

Hamano, K. (1975). Aluminium Titanate Ceramic, *Taikabutu*, **27**, 520-527.

Hamano, K., Nakagawa, Z., Sawano, K. and Hasegawa, Y. (1981). Effects of Additives on Several Properties of Aluminium Titanate Ceramics, *J. Chem. Soc. Jpn.*, 1057-1059.

Hamano, K., Ohya, Y. and Nakagawa, Z. (1983). Microstructure and Mechanical Strength of Aluminium Titanate Ceramic Prepared from Mixture of Alumina and Titania. *J. Ceram. Soc. Jap.*, **91(2)**, 94-97.

Hamelin, M. (1958). Structure du Compose $TiO_2Al_2O_3$ Comparaison Avec la Pseudo-Brookite. *Bulletin de la Societe Chimique de France*, 1559-1566.

Harmer, M.P., Chan, H.. and Miller, G.A. (1992). Unique Opportunities for Microstructural Engineering with Duplex and Laminar Ceramic Composites. *J. Am. Ceram. Soc.*, **75(7)**, 1715-1728.

Hasselman, D.P.H. (1969). Unified Theory of Thermal Fracture Initiation and Crack Propagation in Brittle Ceramics. *J. Am. Ceram. Soc.*, **52(11)**, 600-604.

Hasselman, D.P.H., Donaldson, K.Y., Anderson, E.M. and Jhonson, T.A. (1993). Effect of Thermal History on the Thermal Diffusivity and Thermal Expansion of Alumina-Aluminium Titanate Composite, *J. Am. Ceram. Soc.*, **76**(9), 2180-84.

Hennicke, H.W. and Lingenberg, W. (1986). Formation of Aluminium Titanate, *J. de Phys.*, **2(47)**, 533-536.

Hill, R.J. and Howard, C.J. (1987). Quantitative Phase Analysis from Neutron Powder Diffraction Data Using the Rietveld Method. Journal of Applied Crystallography, **20**, 467-474.

Hirai T. (1996). Functional Gradient Materials. In: Brook RJ, editor, *Processing of Ceramics*-Part2, Weinheim, Germany: VCH Verlagsgesellschaft mbH Publishers, 293-341.

Hirai, T. (1995). CVD Processing. *MRS Bulletin*, 45-47.

Hirai, T. (1996). Functional Gradient Materials, *In Processing of Ceramics* **(Part 2)** Ed. Brook, R.J). VCH Verlagsgesellschafft mbH, Weinheim.

Hirai, T. and Sasaki, M. (1989). *Ceramic Data Book 89*, Kogyo-Seihin-Gijutsu-Kyokai, 51-55.

Hirai, T. and Sasaki, M. (1989). *Seramikkusu (Ceramics)*, **24**, 925-31.

Hiroshi, S. (1990). Manufacture of High-Temperature Aluminum Titanate Ceramics. *Jpn. Kokai Tokkyo Koho*, 1-5.

Holcombe Jr, C.E. and Coffey Jr, A.L. (1973). Calculated X-Ray Powder Diffraction Data for Beta Al_2TiO_5. *J. Am. Ceram. Soc.*, **56(4)**, 220-221.

Howard, C.J., Sabine, T.M. and Dickson, F. (1991). Structural and Thermal Parameters for Rutile and Anatase, *Acta Cryst. B*, **47**, 462-468.

Huang, Y.X., Senos, A.M.R. and Baptista, J.L. (2000). Thermal and Mechanical Properties of Aluminium Titanate-Mullite Composites. *J. Mater. Res.*, **15(2)**, 357-363.

Hübner, E.D.H. (1984). (Ed.). *Alumina Processing, Properties and Application.* Springer-Verlag, New York, 1-317.

Hummel, F.A. (1951). Thermal Expansion Properties of Some Synthetic Lithia Materials, *J. Am. Ceram. Soc.*, **34**(8), 235-239.

Hunter, B.A. (1997). *Rietica for 95/98/NT Version* **1.71**.

Hwang, C.S., Chang, Y.J. (1996). Effect of TiO_2 on the Microstructure and Mechanical Properties of Al_2O_3/ZrO_2 Composites. *J. Mater. Res.*, **11(6)**, 1545-1551.

Hwang, C.S., Nakagawa, Z. and Hamano, K. (1993). Microstructures and Mechanical Properties of TiO_2-Doped Alumina Ceramics Owing to Decomposition of Formed Al_2TiO_5. *J. Ceram. Soc. Japan*, **102**, 253-306.

Ilschner, B. and Cherradi, N. (1995). *FGM 94*, Processing of the Third International Symposium on Structural and Functional Gradient Materials, Switzerland.

Ishitsuka, M., Sato, T., Endo, T. and Shimada, M. (1987). Synthesis and Thermal Stability of Auminium Titanate Solid Solutions. *J. Am. Ceram. Soc.*, **70(2)**, 69-71.

Kamiya, S. and Bowen, H.K. (1988). Microstructural Control of Al_2O_3-TiO_2 Composites by Cyclic Annealing. *Ceramic Powder Science II.* Transactions Westerville, **1**, 978-985.

Kato, E., Daimon, K. and Takahashi, J. (1980). Decomposition Temperature of β-Al_2TiO_5. *J. Am. Ceram. Soc.*, **63(5-6)**, 355-56.

Kato, E., Kobayashi, Y. and Daimon, K. (1979). Decomposition Kinetics of Aluminum Titanate (Al_2TiO_5) in Powdered State. *Yogyo Kyokaishi*, **87(2),** 81-85.

Kenny, G.B. and Bowen, H.K. (1983). High Tech Ceramics in Japan: Current and Future Markets. *American Ceramics Society Bulletin*, **62(5)**, 590-596.

Kim, I. J., Zografou, C. and Kroenert, W. (1993). Synthesis and Characterisation of Submicrometer Monosized Ceramic Powders of Aluminium Titanate-Mullite Composite by Sol-Gel Process, *Int. J. Mater. Prod. Technol.*, **8**, 440-51.

Kingery, W.D., Bowen, H.K. and Uhlmann, D.R. (1976). *Introduction to Ceramics*. John Wiley & Sons, New York.

Kirchner, H.P. and Gruver, R.M. (1980). Fractographic Criteria for Subcritical Crack Growth Boundaries in 96% Al_2O_3. *J. Am. Ceram. Soc.*, **63(5-6),** 169-174.

Kisi, E.H. (1994). Rietveld Analysis of Powder Diffraction Patterns, *Materials Forum*, **18**, 135-153.

Kissinger, H.E. (1957). Reaction Kinetics in Differential Thermal Analysis. *Analytical Chemistry*, **29(11),** 1702-1706.

Knickerbocker, S., Tuzzolo, M.R. and Lawhorne, S. (1989). Sinterable β-Spodumene Glass-Ceramics. *J. Am. Ceram. Soc.*, **72**(10), 873-879.

Koizumi, M. (1997). FGM Activities in Japan, *Composites Part B*, **28B**, 1-4.

Koizumi, M. and Niino, M. (1995). Overview of FGM Research in Japan. *MRS Bulletin*, 19-21.

Kraus, W. and Nolze, G. (1999). *PowderCell for Windows Version 2.3.*

Krell, A. and Schädlich, S. (2001). Nanoindentation Hardness of Submicrometer Alumina Ceramics. *Materials Science and Engineering*, **A307**, 172-181.

Lang, S.M., Filmore, C.L. and Maxwell, L.H. (1952). The System Beryllia-Alumina-Titania: Phase Relations and General Physical Properties of Three-Component Porcelains, *J. Res. Nat. Bur. Stand.*, **48**, 298-312.

Latella, B.A. and O'Connor, B.H. (2000). Effect of Post-sintering Heat-treatments on the Erosive Wear Behaviour of Liquid-phase-sintered Aluminas. *J. Mat. Sci.*, **35**, 3505-3517.

Latella, B.A., Burton, G. R. and O'Connor, B.H. (1995). Use of Spodumene in the Processing of Alumina-Matrix Ceramics- Influence on Microstructure and Mechanical Properties, *J. Am. Ceram. Soc.*, **78**(7), 1895-1899.

Lee. H.L., Jeong, J.Y. and Lee, H.M. (1997). Preparation of Al_2TiO_5 from Alkoxides and the Effects of Additives on its Properties. *J. Mat. Sci.*, **32(21),** 5687-5695.

Lejus, A.M., Goldberg, D. and Revcolevschi, A. (1966). New Compounds Formed between Rutile, Tetanium Oxide and Oxides of Trivalent and Quadrivalent Metals. *C. R. Hebd. Seances Acad. Sci.*, Ser. **C263(20),** 1223-1226.

Levin, E.M., Robbins, C.R. and McMurdie, H.F. (1964). *Phase Diagrams for Ceramists*. The American Ceramic Soc., Inc.

Lewis, J., Schwarzenbach, D. and Flack, H.D. (1982). Electric Field Gradients and Charge Density in Corundum, α-Al_2O_3. *Acta Crystallographica*, **A38**, 733-739.

Liebhafsky, H.A., Pfeiffer, H.G., Winslow. E.H. and Zemany, P.D. (1972). *X-Rays, Electrons and Analytical Chemistry*. Wiley-Interscience, New York, 525-528.

Ligenza, J.R. and Bernstein, R.B. (1951). The Rate of Rice of Liquids in Fine Vertical Capillaries. *J. Am. Chem. Soc.*, **73**, 4636-4638.

Lin, Y.S. and Burggraaf, A.J. (1991). Modeling and Analysis of CVD Processes in Porous Media for Ceramic Composite Preparation, *Chem. Eng. Sci.*, 46, 3067-3080.

Liu, T.S. and Perera, D.S. (1998). Long-term Thermal stability and Mechanical Properties of Aluminium Titanate at 1000-1200°C. *J. Mat. Sci.*, **33(4),** 995-1001.

Loehman, R.E., Ewsuk, K. and Tomsia, A.I. (1996). Synthesis of Alumina-Al Composites by Reactive Metal Penetration. *J. Am. Ceram. Soc.*, **79(1),** 27-32.

Low, I.M. and Shi, C.G. (2000). Physical and Thermal Characteristics of Aluminum Titanate Dispersed with Spodumene and Zirconia. *Journal of Materials Science*. **35(24),** 6293-6300.

Low, I.M. (1998). Synthesis and Properties of in-situ Layered and Graded Aluminium Titanate/Alumina Composites. *Mater. Res Bull.* **33(10),** 1475-1482.

Low, I.M., Mathews, E., Garrod, T., Zhou, D., Phillips, D. N. and Pillai, X.M. (1979). Processing of Spodumene-Modified Mullite Ceramics. *J. Mater. Sci.*, **32**, 3807-3812.

Low, I.M., Skala, R. and Li, D.Y. (1993). Assessment of Residual Strains in Mullite/ZTA Composites using XRD. *J. Mater. Sci. Lett*, **13**, 1354-1356.

Low, I.M., Skala, R. and Perera, D.S. (1994). Fracture Properties of Layered Mullite/ZTA Composites. *J. Mater. Sci. Lett*, **13**, 1334-1336.

Low, I.M., Skala, R. and Zhou, D. (1995). Synthesis of Functionally-Gradient Aluminium Titanate/Alumina Composites. *J. Mater. Sci. Lett*, **15**, 345-347.

Low, I.M., Skala, R., Richard, R. and Perera, D.S. (1993). Synthesis and Properties of Novel Mullite-Zirconia-Toughened Alumina Composites. *J. Mater. Sci. Lett*, **12**, 1585-1587.

Low, I.M., Skala, R.D. and Zhou, D. (1996). Synthesis of Functionally Gradient Aluminium Titanate/Alumina Composites. *J. Mat. Sci. Lett.*, **15(4),** 345-347.

Low, I.M., Suherman, P.M. and Phillips, D.N. (1997). Synthesis and Properties of Spodumene-Modified Mullite Ceramics Formed by Sol-gel Processing. *J. Mater. Sci. Letter.* **16**, 982-984.

Lowell. S. and Shields, J.E. (1984), *Powder Surface Area and Porosity.* Chapman and Hall, New York.

Manurung, P., Low, I.M. and Buckley, C.E. (2000). An Investigation of Kinetic of Liquid into Porous Alumina Preforms under Various Experimental Conditions. *Proceeding of 2000 Powder Metallurgy World Congress*, Kyoto Japan. 124-127.

Markworth, A.J., Ramesh, K.S. and Park Jr, W.P. (1995). Review of Modelling Studies Applied to Functionally Graded Materials. *J. Mater. Sci.*, **30**, 2183-2193.

Marple, B.R. and Green, D.J. (1990). Mullite/Alumina Particulate Composites by Infiltration Processing: II, Infiltration and Characterisation. *J. Am. Ceram. Soc.*, **73(12),** 3611-3616.

Marple, B.R. and Green, D.J. (1991). Mullite/Alumina Particulate Composites by Infiltration Processing: III, Mechanical Properties. *J. Am. Ceram. Soc.*, **74(10),** 2453-2459.

Marple, B.R. and Green, D.J. (1991). Mullite/Alumina Particulate Composites by Infiltration Processing: III, Residual Stress Profiles. *J. Am. Ceram. Soc.*, **75,** 44-47.

Marple, B.R. and Green, D.J. (1993). Graded Compositions and Microstructures by Infiltration Processing. *Journal of Materials Science*, **28**, 4637-4643.

Martinez, J.J.M., Melendo, M.J., Rodriguez, A.D. and Wötting, G. (2001). High Temperature Mechanical Behaviour of Aluminium Titanate-Mullite Composites. *Journal of the European Ceramic Society*, **21**, 63-70.

Marturano, M., Aglietti, E.F. and Ferretti, O. (1997). α-Al2O3 Catalyst Supports for Synthesis Gas Production: Influence of Different Alumina Bonding Agents on Support and Catalyst Properties. *Mater. Chem. and Physics*, **47**, 252-256.

Maslen, E.N. Streltsov, V.A. Streltsova, N.R., Ishizawa, N. and Satow, Y. (1993). Synchrotron X-ray Study of the Electron Density in Alpha Al_2O_3. *Acta Crystallographica*, **B49**, 937-980.

Matusita, K and Sakka, S. (1980). Kinetic Study on Crystallization of Glass by Differential Thermal Analysis-Criterion on Application of Kissinger Plot, *Journal of Non-Crystalline Solids*, **38-39**, 741-746.

McMillan, P.W. (1964). *Glass-Ceramics*, Academic Press, London, UK, 225.

Morelli, C.E., Cutard, T., Schaller, R. and Bonjour, C. (1998). Processing and Characterization of Aluminium-Based MMCs Produced by Gas Pressure Infiltration. *Materials Science and Engineering A*, **251**, 48-57.

Morishima, H., Kato, Z., Uematsu, K., Saito, K., Yano, T. and Ootsuka, N. (1986). Development of Aluminum Titanate-Mullite Composite Having High Thermal Shock Resistance. *J. Am. Ceram. Soc.*, **69**, C226-C227.

Morosin, B. and Lynch, R.W. (1972). Structure Studies on Al_2TiO_5 at Room Temperature and at 600 °C. *Acta Crystallographica*, **B28**, 1040-1046.

Munro, R.G. (1997). Evaluated Material Properties for a Sintered α-Alumina. *J. Am. Ceram. Soc.*, **80(8)**, 1919-1928.

Nagano, M., Nagashima, S., Maeda, H. and Kato, A. (1999). Sintering Behaviour of Al_2TiO_5 Base Ceramics and Their Thermal Properties. *Ceramic International*, **25**, 681-687.

Nagendra, N. and Jayaram, V. (2000). Fracture and R-Curve in High Volume Fraction Al_2O_3/Al Composites, *J. Mater. Res*, **15(5)**, 1131-44.

Natl. Bur. Stand. (U.S.). (1984). Lithium Aluminum Silicate, β-$LiAlSi_2O_6$. *Monogr.*, 25, 21, 75.

Newnham, R.E. and DeHaan, Y.M. (1962). Refinement of the α-Al_2O_3, Ti_2O_3, V_2O_3 and Cr_2O_3 Structures. *Zeitschrift fuer Kristallographie*, **117(2-3)**, 235-237.

O'Connor, B.H., van Riessen, A., Carter, J., Burton, G.R., Garret, R.F. and Cookson, D.J. (1997). Characterisation of Ceramic Materials with BIGDIFF Synchrotron Radiation Debbye-Scherrer Powder Diffraction. *J. Am. Ceram. Soc.*, **80**, 1373-1381.

O'Connor, B.H. and Raven, M.D. (1988). Application of Rietveld Refinement Procedure in Assaying Powedered Mixtures. *Powder Diffraction*, **3**, 2-6.

O'Connor, B.H. and Li, D.Y. (2000a). Influence of Refinement Strategies on Rietveld Phase Composition Determinations. *Advance in X-ray Analysis*, **42**, 204-211.

O'Connor, B.H. and Li, D.Y. (2000b). Attaining 1% Accuracy in Absolute Phase Composition Levels by Rietveld Analysis. *Advance in X-ray Analysis*, **43**, 305-312.

Ohya, Y., Hamano, K. and Nakagawa, Z. (1983). Microstructure and Mechanical Strength of Aluminum Titanate Ceramics Prepared from Synthesized Powders. *Yogyo-kyokai-shi*, **91**, 289-297.

Ohya, Y., Hamano, K. and Nakagawa, Z. (1986). Effects of Some Additives on Microstructure and Bending Strength of Aluminum Titanate Ceramics, *Yogyo-kyokai-shi*, **94**, 665-670.

Ohya, Y., Nakagawa, Z. and Hamano, K. (1987). Grain Boundary Microcracking due to Thermal Expansion Anisotropy in Aluminium Titanate Ceramics. *J. Am. Ceram. Soc.*, **70(8)**, C184-C186.

Ostertag. W., Fischer, G.R. and Williams, J.P. (1968). Thermal Expansion of Synthetic β-Spodumene and β-Spodumene-Silica Solid Solutions, *J. Am. Ceram. Soc.*, **51**(11), 651-654.

Ozawa, T. (1971). Kinetics of Nonisothermal Crystallisation. *Polymer*, **12**, 150-158.

Padture, N., Bennison, S.J., Runyan, J., Chan, H.M. and Lawn, B.R. (1991). Flaw Tolerant Alumina-AT Composite. *Ceramic Transaction*, **19**, 715-721.

Padture, N.P., Bennison, S.J. and Chan, H.M. (1993). Flaw-Tolerance and Crack-Resistance Properties of Alumina-Aluminium Titanate Composites with Tailored Microstructures, *J. Am. Ceram. Soc.*, **76(9)**, 2312-2320.

Parish, W. and Hart, M. (1985). Synchrotron Experimental Methods for Powder Structure Refinement, *Transaction of The American Crystallographics Association*, **21**, 51-55.

Parker, F.J. (1990). Al_2TiO_5-$ZrTiO_4$-ZrO_2 Composites: A New Family of Low-Thermal-Expansion Ceramics. *J. Am. Ceram. Soc.*, **73(4)**, 929-932.

Parker. F.J. and Rice, R.W. (1989). Correlation between Grain Size and Thermal Expansion for Aluminum Titanate Material. *J. Am. Ceram. Soc.*, **72**, 929-935.

Partington, J.R. (1955). *An Advanced Treatise on Physical Chemistry*, The Properties of Liquids, Longmans, Green and Co, London. **2**, 76.

Partington, J.R. (1955). *An Advanced Treatise on Physical Chemistry*, The Properties of Liquids, Longmans, Green and Co, London. **2**, 188.

Pauling, L. and Hendricks, S.B. (1925). The Crystal Structures of Hematite and Corundum. *J. Am. Ceram. Soc.*, **47**, 781-790.

Pratapa, S. and Low, I.M. (1998). Infiltration-Processed Functionally-Graded AT/Alumina-Zirconia Composites. II. Mechanical Properties. *J. Mater. Sci.*, **33**, 3047-3053.

Pratapa, S., Low, I.M. and O'Connor, B.H. (1997). Infiltration-Processed Functionally-Graded AT/Alumina-Zirconia Composites. I. Microstructural and Physical Properties. *J. Mater. Sci.*, **33**, 3037-3041.

Rabinovich, E.M. (1985). Review: Preparation of Glass by Sintering. *J. Mater. Sci*, **20**, 4259-4297.

Rahaman, M.N. (1995). *Ceramic Processing and Sintering*, Marcell Dekker, Inc., New York, 6-24.

Rietveld, H.M. (1969). A Profile Refinement Method for Nuclear and Magnetic Structures, *Journal of Applied Crystallography*, **2**, 65-71.

Rhodes, W.H. (1981). Agglomerate and Particle Size Effect on the Sintering of Yttria Stabilizes Zirconia, *J. Am. Ceram. Soc.*, **64**, 19-23.

Runyan, J.L. and Bennison, S.J. (1991). Fabrication of Flaw-Tolerant Aluminium Titanate-Reinforced Alumina. *J. Euro. Ceram. Soc.*, **74**, 93-96.

Sakabe, T., Inagaki, K., Tanaka, Y. and Nakamura, M. (1970). Effect of Ferric Oxide Addition on Sintering and Formation of Aluminium Titante, *Ind. Res. Inst.*, **6**, 97-104.

Sakai, H., Matsuhiro, K. and Furuse, Y. (1991). Mechanical Properties of SiC Platelet Reinforced Ceramic Composites. *Ceramic Transaction*, **19**, 765-771.

Sarkar, P., Datta, S. and Nicholson, P.S. (1997). Functionally Grade Ceramic/Ceramic and Metal/Ceramic Composites by Electrophoretic Deposition. *Composites Part B*, **28B**, 49-56.

Sawada, H. (1995). An Electron Density Residual Study of Magnesium Aluminium Oxide Spinel. *Mater. Res. Bull.*, **30(3)**, 341-345.

Schneider, S.J. (1994). *Engineered Materials Handbook.* **4**, ASM International.

Schwartz, M.M. (1984). *Composite Materials Handbook*, McGrawHill, New York.

Segadaes, A.N., Morelli, M.R. and Kiminami, G.A. (1998). Combustion Synthesis of Aluminium Titanate. *J. Europ. Ceram. Soc.*, **18**, 771-781.

Sekar, M.M.A. and Patil, K.C. (1994). Synthesis and Properties of Tialite, β-Al_2TiO_5. *British Ceramic Transaction*, **93(4)**, 146-149.

Semlak, K.A. and Rhines, F.N. (1958). The Rates of Infiltration of Metals. *Transaction of The Metallurgical Society of AIME*, **212**, 325-331.

Sheelak, K. and Shob, K. (1998), Reactive Infiltration of Aluminium into Molybdenum Disilicate Preform. *J. Am. Ceram. Soc.*, **81(3)**, 730-732.

Shi, C.G. and Low, I.M. (1998). Effect of Spodumene Additions on the Sintering and Densification of Aluminium Titanate, *Mater. Res. Bulletin*, **33**(6), 817-824.

Shi, C.G. and Low, I.M. (1998). Use of Spodumene for Liquid-Phase-Sintering of Aluminium Titanate, *Mater. Lett.*, **36**, 118-122.

Skala, R.D. (2000). Development of a Functionally-Graded Aluminium Titanate/Alumina Composite. *Curtin PhD Thesis.*

Skamser, D J., Jennings, H.M. and Johnson, D.J. (1997). Model of Chemical Vapor Infiltration using Temperature Gradients. *J. Mater. Res.*, **12(3)**, 724-737.

Skamser, D J., Thomas, J.J., Jennings, H.M. and Johnson, D.J. (1995). A Model for Microwave Processing of Compositionally Changing Ceramic Systems. *J. Mater. Res.*, **10(12)**, 3160-3178.

Slepetys, R.A. and Vaughan, P.A. (1969). Solid Solution of Aluminium Oxide in Rutile Dioxide. The *Journal of Physical Chemistry.* **73**, 2157-2162.

Smoke, E.J. (1951). Ceramics Compositions Having Negative Linier Expansion, *J. Am. Ceram. Soc.*, **34**(3), 87-90.

Suvorov, S.A., Makarov, V.N., Filatova, N.M., Makhortova, M.F. and Kolomeitsev, V.V. (1987). Phase Composition, Microstructure and Thermal Properties of Magnesium Aluminate-Aluminium Titanate ($MgAl_2O_4$-Al_2TiO_5) Composite. *Ogneupory*, **12**, 14-18.

Swanson, H.E., Cork, M.I., Isaacs, T. and. Evans, E.H. (1953). *Standard X-ray Diffraction Powder Patterns*. National Bureau of Standards, USA, **2**.

Tai, N.H. and Chou, T.W. (1989). Analytical Modeling of Chemical Vapor Infiltration in Fabrication of Ceramic Composites, *J. Am. Ceram. Soc.*, **72**, 414-420.

Tai, N.H. and Chou, T.W. (1990). Modeling of an Improved Chemical Vapor Infiltration Process for Ceramic Composites Fabrication, *J. Am. Ceram. Soc.*, **73**, 1489-1498.

Takahashi, H. (1993). Mechanical Properties of Functionally Gradient Materials of Titanium-Apatite and Titanium-Zirconia for Dental Use. *J. Jap. Soc. Dent. Mater.*, **12**, 595-612.

Takahashi, W., Watari, F. and Nishimura, F. (1992). Study of Functionally Gradient Materials for Dentals Use. *Proc. 'Int. Symp. Ti in Dentistry', Soc.* Ti Alloy in Dentistry, Tokyo, 64.

Takahashi, W., Watari, F. and Nishimura, F. and Nakamura, H. (1992). Study of Functionally Gradient Materials of Titanium-Apatite and Titanium-Silica for Dental Use, *J. Jap. Soc. Dent. Mater.*, **11**, 426-468.

Takanori, W., Shin-ichiro, S., Toshio, T. and Yasuo, I. (1999). Reactive Infiltration of Magnesium Vapor into Alumina Powder Compacts. *J of the European Ceramic Society*, **19**, 1889-1893.

Thomas, H.A.J., Stevens, R. and Gilbart, E. (1991). Effect of Zirconia Additions on the Reaction Sintering of Aluminium Titanate, *J. of Mater. Sci.*, 26(13), 3613-3616.

Tilloca, G. (1991). Thermal Stabilization of Aluminium Titanate and Properties of Aluminium Titanate Solid Solution, *J. Mater. Sci.*, **26**, 2809-2814.

Tomsia, A.P., Saiz, E., Ishibashi, H., Diaz, M., Requena, J. and Moya, J.S. (1998). Powder Processing of Mullite/Mo Functionally Graded Materials. *Journal of the European Ceramic Society*. **18(9),** 1365-1371.

Travitzky, N.A. and Shlayen, A. (1998). Microstructure and Mechanical Properties of Alumina/Cu-O. *Material Science and Engineering*, **A224**, 154-160.

Tsuchida, Y., Kirihara, S., Tomota, Y. and Tsujimoto, T. (1998). Ti/Ti_3Sn Functionally Graded Coating by Reaction Diffusion and Eutectic Reaction. *Journal of the Japan Institute of Metals*, **62(11),** 992-998.

Tu, W.C. and Lange, F.F. (1995). Liquid Precursor Infiltration Processing of Powder Compact: II, Fracture Toughness and Strength. *J. Am. Ceram. Soc.*, **78(12),** 3283-3289.

Vineyard, G.H. (1982). Grazing-incidence Diffraction and the Distorted-wave-Approximation for the Study of Surfaces. *Physiscal Review B*, **26(8),** 4146-4158.

Wadley, H.N.G, Hsiung, L.M. and Lankey, R.L. (1995). Artificially Layered Nanocomposites Fabricated by Jet Vapor Deposition, *Composites Engineering*, **5(7),** 935-940.

Warren, B.E. (1969). *X-ray Diffraction*, Addison-Wesley Publishing Company Inc., United State of America.

Washburn, E.W. (1921). *Principles of Physical Chemistry*. McGraw-Hill, New York.

Wasmuht, C., Recht, R. and Kroenert, W. (1991). Thermal-Shock Resistance of Refractory Materials Based on Partially Stabilised Zirconium Dioxide and Aluminium Titanate. *Ceram. Crist.*, **31(108),** 31-32.

Wefers, K. and Misra, C. (1987). *Oxides and Hydroxides of Aluminum*. Alcoa Laboratories, Pittsburgh.

Wei, G.C. and Becher, P.F. (1985). Development of SiC-Whisker-Reinforced Ceramics. *Am. Ceram. Soc. Bull.*, **64(2),** 298-304.

Wendlandt, W. (1964). *Thermal Methods of Analysis*. Wiley Interscience.

Wohlfromm, H., Pena, P., Moya, J.S. and Requena, J. (1992). Al_2TiO_5 Formation in Alumina/Titania Multilayer Composites, *J. Am. Ceram. Soc.*, **75(12),** 3473-3476.

Wohlfromm, H., Pena, P., Moya, J.S., Tomsia, A.P. and Thomas, G. (1989). Joining of Aluminium Titanate with Niobium. *Euro-Ceramics*, **3**, 429-435.

Wook, K.S., Jik, L.H. and Lim, H.L. (1999). Effect of Bicomponent Additives on Thermal Decomposition of Al_2TiO_5. *Yoop Hakhoechi*, **36(6),** 632-639.

Xu, X.J. Ray, C.S. and Day, D.E. (1991). Nucleation and Crystallization of $Na_2O.2CaO.3SiO_2$ Glass by Differential Thermal Analysis. *Journal of The American Ceramic Society*, **74(5),** 909-914.

Yamaguchi, O., Hitoshi, T. and Shimizu, K. (1981). Formation Process of Alkoxy-Derived β-Al_2TiO_5. *Sci. Eng. Rev. Doshisha Univ.*, **22(1)**, 26-32.

Yasuoka, M., Hirao, K., Brito, M.E. and Kanzaki, S. (1995). High-Strength and High-Toughness Ceramics in the $Al_2O_3/LaAl_{11}O_{18}$ Systems. *J. Am. Ceram. Soc.*, **78(7)**, 1853-1856.

Yokota, M., Hara, A., Ohata, M. and Mitani, H. (1980). Infiltration Process of Liquids into Porous Bodies. *Trans. Jap. Inst. Of Metals*, **21(10),** 652-659.

Yokota, M., Moto-oka, N., Hara, A. and Mitani. H. (1980). Some Considerations on the Process of Penetration of Liquids into Capillary Tubes. *Trans. Jap. Inst. Of Metals*, **21(10),** 645-651

Young, R.A. (1993). *The Rietveld Method*, International Union of Crystallography, Oxford University Press, Great Britain.

Young, R.A. and Wiles, D.B. (1982). Profile Shape Functions in Rietveld Refinements, *Journal of Applied Crystallography*, **15**, 430-438.

Zografou, C., Dhupia, G.S., Kroenert, W. Staudt, T. and Rehfeld, G. (1988). Thermal Durability of Aluminium Titanate Ceramics Prepared from Electrofused Powders. *Sci. Ceram.*, **1**, 757-762.

APPENDIX 1

LIST OF PUBLICATIONS ARISING FROM THE THESIS

Refereed Publications

Buckley, C.E., Manurung, P. and Low, I.M. (2000). Modelling the Liquid Infiltration Kinetics in Alumina Preforms. *J. Aust. Ceram. Soc.*, **36(1),** 127-134.

Manurung, P., Low, I.M. and Buckley, C.E. (2000). An Investigation of Kinetic of Liquid into Porous Alumina Preforms under Various Experimental Conditions. *Proceedings of 2000 Powder Metallurgy World Congress*, Kyoto Japan. 124-127.

Low, I.M., Skala, R.D., Asmi, D., Manurung, P. and Singh, M. (2000). Infiltration Processing of Novel Functionally-Graded Ceramic Materials. *Proceedings of 2000 Powder Metallurgy World Congress*, Kyoto Japan. 1465-1468.

Low, I.M., Manurung, P., Smith, R.I. & Lawrence, D. (2002). A novel processing method for the microstructural design of functionally-graded ceramic composites. *Key Engineering Materials* **224-226,** 465-470.

Low, I.M., Singh, M., Manurung, P., Wren, E., Sheppard, D.P. & Barsoum, M.W. (2002). Depth profiling of phase composition and texture in layered-graded Al_2O_3- & Ti_3SiC_2- based systems using x-ray and synchrotron radiation diffraction. *Key Engineering Materials* **224-226,** 505-510.

Skala, R.D., Manurung, P. & Low, I.M. (2002). Depth profiling and indentation responses of functionally graded alumina/ aluminium-titanate composites. *Proc. Int. Conf. On Structural Integrity & Fracture 2002 (Eds. Dyskin, Hu &* Sahouryeh), 25-28 Sept. 2002, Perth, WA. pp.403-408.

Singh, M., Manurung, P. & Low, I.M. (2002). Depth profiling of near-surface information in a functionally-graded Al_2O_3/Al_2TiO_5 composite using grazing-incidence synchrotron radiation diffraction. *Mater. Lett.* **55,** 344-349.

Manurung, P., Low, I.M. and O'Connor, B.H. (2002) Effect of β–Spodumene on Phase Development in Alumina/Aluminium Titanate Ceramics. *J. Aust. Ceram. Soc.*, **38(1),** 78-82.

Conference Proceedings

Manurung, P. and Low, I.M. (1999). Preparation and Characterisation of Alumina/Aluminium Titanate Composites by Sol-Gel Route. *Proceeding 1999 Joint WASEM and AXAA Conference* (Ed. B.J. Griffin), September 17-19, Mandurah, WA, p.25.

Manurung, P., Low, I.M. and Buckley, C. (1999). Infiltration Kinetics of Titanium Trichloride into Alumina Preform.Proceeding *Seventh Australian Institute of Physics (AIP) Postgraduate Research Conference*. 29 September – 1 October 1999, Pinjarra, WA, p.27.

Asmi, D., Skala, R., Manurung, P., Low, I.M., O'Connor, B. and Buckley, C. (2000). Depth-Profiling of Phase Compositions in Functionally-Graded Alumina-Based Composites Using Synchrotron Radiation Diffraction. *AUSTCERAM 2000 Transaction*, p. 273.

Manurung, P., Low, I.M., Kennedy, S. and O'Connor, B.H. (2000). Effect of β-Spodumene on the Phase Development of Alumina/Aluminium Titanate Ceramic. *Proceeding 2nd AINSE Symposium on Neutron Scattering Powder Diffraction*, 22 June 2000, AINSE, p.19.

Manurung, P., Low, I.M. and O'Connor, B.H. (2002) Effect of β–Spodumene on Phase Development in Alumina/Aluminium Titanate Ceramics. Pp.177-178 in *Proc. of AUSTCERAM 2002* (Eds. I.M. Low & D.N. Phillips), 30 Sept – 4 Oct. 2002, Perth, WA, p.177.

APPENDIX 2

CRYSTALLOGRAPHIC DATA

1. Alpha-Alumina

Phase	: Alumina (Al_2O_3)
Symmetry	: Trigonal
Space group	: R-3CH
Formula unit	: Al_2O_3
Formula units per cell	: 6
Unit cell volume	: 0.2541 nm^3
Unit cell molecular weight	: 101.96 g/mol

Cell parameters

a = 0.4754 nm	b = 0.4754 nm	c = 1.2982 nm
$\alpha = 90°$	$\beta = 90°$	$\gamma = 120°$

Atomic positions

Atom	Wyckoff Site	x	y	z	Occupancy
Al	12c	0	0	0.35223	0.3333
O	18e	0.69378	0	0.25000	0.5000

Reference:
Maslen, E.N., Streltsov, V.A., Streltsova, N.R., Ishizawa, N. and Satow, Y. (1993), Synchrotron X-ray Study of the Electron Density in Alpha-Al_2O_3. *Acta Crystallographica*, **B49**, 973-980.

2. Aluminium Titanate

Phase	: Aluminium Titanate (Al_2TiO_5)
Symmetry	: Orthorhombic
Space group	: C M C M
Formula unit	: Al_2TiO_5
Formula units per cell	: 4
Unit cell volume	: 0.3263 nm^3
Unit cell molecular weight	: 181.86 g/mol

Cell parameters

a = 0.3591 nm	b = 0.9429 nm	c = 0.9636 nm
$\alpha = 90°$	$\beta = 90°$	$\gamma = 90°$

Atomic positions

Atom	Wyckoff Site	x	y	z	Occupancy
Ti_1	4c	0	0.1863	0.2500	0.08333
Al_1	4c	0	0.1863	0.2500	0.16667
Al_2	8f	0	0.1351	0.5613	0.33333
Ti_2	8f	0	0.1351	0.5613	0.16667
O_1	4c	0	0.7590	0.2500	0.25000
O_2	8f	0	0.0480	0.1180	0.50000
O_3	8f	0	0.3170	0.0750	0.50000

Reference:
Epicier, T., Thomas, G., Wohlfromm, H. and Moya, J.S. (1991). High Resolution Electron Microscopy Study of the Cationic Disorder in Al_2TiO_5. *Journal of Materials Research*, **6**. 138-145.

3. Beta-spodumene

Phase	: Beta-spodumene ($AlLiO_6Si_2$)
Symmetry	: Tetragonal
Space group	: P 43 21 2
Formula unit	: $AlLiO_6Si_2$
Formula units per cell	: 4
Unit cell volume	: 0.5198 nm^3
Unit cell molecular weight	: 186.08 g/mol

Cell parameters

a = 0.7534 nm	b = 0. 7534 nm	c = 0.9158 nm
$\alpha = 90°$	$\beta = 90°$	$\gamma = 90°$

Atomic positions

Atom	Wyckoff Site	x	y	z	Occupancy
Si_1	8b	0.3322	0.1223	0.2388	0.6670
Al_1	8b	0.3322	0.1223	0.2388	0.3330
Si_2	4a	0.4174	0.4174	0	0.3335
Al_2	4a	0.4174	0.4174	0	0.1666
O_1	8b	0.4426	0.1216	0.3947	1.0000
O_2	8b	0.1243	0.1153	0.3001	1.0000
O_3	8b	0.3654	0.3048	0.1468	1.0000
Li	8b	0.0826	0.1982	0.4944	0.5000

Reference:
Clarke, P.T. and Spink, J.M. (1969). The Crystal Structure of Beta Spodumene, $AlLiO_6Si_2$ II. *Kristallphysik*, **130**, 420-426.

4. Rutile

Phase	: Rutile (TiO_2)	
Symmetry	: Tetragonal	
Space group	: P 42/M N M	
Formula unit	: TiO_2	
Formula units per cell	: 2	
Unit cell volume	: $0.0624nm^3$	
Unit cell molecular weight	: 79.89 g/mol	
Cell parameters		
a = 0.4594 nm	b = 0.4594 nm	c = 0.2959 nm
$\alpha = 90°$	$\beta = 90°$	$\gamma = 90°$

Atomic positions

Atom	Wyckoff Site	x	y	z	Occupancy
Ti	2a	0	0	0	0.1250
O	4f	0.30478	0.30478	0	0.2500

Reference:
Howard, C.J., Sabine, T.M. and Dickson, F. (1991). Structural and Thermal Parameters for Rutile and Anatase, *Acta Crystallographica*, **B47**, 462-468.

APPENDIX 3

CELL VOLUME CALCULATIONS

The following equations give the volume V of the unit cell.

Cubic: $V = a^3$ (A.1)

Tetragonal: $V = a^2c$ (A.2)

Hexagonal: $V = \frac{\sqrt{3}}{2} a^2 c = 0.866\, a^2 c$ (A.3)

Rhombohedral: $V = a^3 \sqrt{1 - 3\cos^2\alpha + 2\cos^3\alpha}$ (A.4)

Orthorhombic: $V = abc$ (A.5)

Monoclinic: $V = abc\ sin\beta$ (A.6)

Triclinic: $V = abc\sqrt{1 - \cos^2\alpha + \cos^2\beta - \cos^2\gamma + 2\cos\alpha\cos\beta\cos\gamma}$ (A.7)

Where a, b and c are the axes in direction of x, y and z respectively. Meanwhile α, β and γ are the angles between (x,y), (y,z) and (z,x) respectively.